Manufacture, characterisation and novel investigations of superhydrophobic surfaces

By

Haonan Xu

A thesis submitted in partial
fulfilment of the requirements for
the degree of Doctor of Philosophy
University of Liverpool
School of Engineering

September 2017

Declaration

I hereby declare that this dissertation is a record of work carried out in the School of Engineering at the University of Liverpool during the period from March 2014 to February 2017.The dissertation is original in content except where otherwise indicated.
September 2017

.....

(Haonan Xu)

Acknowledgements

I would like to take this opportunity to thank everyone who supported me during my PhD work in the University of Liverpool. Above all, I would like to thank Prof Rob Poole for his invaluable guidance and support throughout this thesis. Thanks to him for always being so patient with all my errors and mistakes. His encouragements and precious suggestions with his rich experience and knowledge in this work and the fluid mechanics helped and motivated me a lot during the work.

I would like to thank Prof Jonathan Rothstein from University of Massachusetts Amherst who generously provided his original idea of creating the "hot-embossed" superhydrophobic surfaces and many valuable suggestions for this thesis.

I would like to thank Dr Colin Crick from the Department of Chemistry who provided the TiO_2 surfaces, and helped in setting up the water bouncing experiments. His kind help extended the borders of this work.

I would also like to thank Dr David Dennis, Dr Volfango Bertola and Dr Robert Birch for their kind help and suggestions in my experiments.

I would like to acknowledge Mr Christopher Hinchcliffe and Mr Derek Neary for their technical support. Many thanks to Mr Dave Atkinson, without his generous and kind help regarding the furnace and microscope, this work would not have been as smoothly as expected. I would also like to thank Dr Karl Dawson from Nanoinvestigation Centre for the help with SEM imaging.

Many thanks to my colleagues in our office: Dr Henry Ng., Mr Allysson Domingues, Mr Oguzhan Der, Mr Mahdi Davoodi, Mr Bayode Owolabi, Mr Rishav Agrawal, Dr

Waleed M. Abed and Dr Tiago de Jesus Henriques. Thanks for their time with me both in academic and daily life to make my life more easy and enjoyable in Liverpool.

Thanks to Mr Jack Carter-Hallam for his excellent administrative support and all the football nights in Everton park.

Especially Thanks to Dr Chaofan Wen, Mr Simeng Chen and Mr Yue Zhang. We are not only colleagues but also roommates. I will miss all the nights we spent on the hotpot, all the football games we watched and all the fights on the Summoner's Rift.

Finally, sincerely thanks to my family, my parents and my wife, for your love, support, understanding, patience and optimism.

Abstract

In this thesis, a method which can manufacture “large” superhydrophobic surfaces in an easy and inexpensive way is provided. Fine stainless steel meshes with a wire diameter around 30 microns were used to “hot-embossed” onto the hydrophobic polytetrafluoroethylene (PTFE) surfaces. The negative of the mesh structure is then printed onto the PTFE surfaces to create superhydrophobicity. Five types of meshes were attempted in this thesis and a high static contact angle and low contact angle hysteresis were measured being around 150° and 15° respectively.

These surfaces’ properties were then characterised carefully. The static contact angles and contact angle hysteresis were measured. The surfaces’ structures were investigated via scanning electron microscopy (SEM). Finally, the water bouncing experiments and “slip-length” measurements were implemented to evaluate their superhydrophobicity and drag reduction respectively. The “slip-length” is independent of the precise flow over the surface and can be used to describe the slip effect of the surface. Due to its small value, a well-designed flow set-up, a sensitive and accurate experimental equipment are required for this measurement. In this thesis, the “slip-length” for water of the xPTFE surfaces were measured as around 30 μm. The measurements were implemented carefully using two types of laminar flows: rotating-disk method and channel-flow method. These methods were selected due to analytical results being available under these laminar flow conditions. After that, the resilience to fluid shear-stress of these superhydrophobic surfaces were studied via a commercial rheometer. The loss of superhydrophobicity could be classified as two types: a temporary loss and a permanent loss. For a temporary loss, the surface has no change after the workload

but temporarily losses their superhydrophobicity which can be recovered or partial recovered by cleaning. In the case of permanent loss, the surface was damaged by workload and could not be recovered. In this thesis, a pulse of high workload was used to determine the minimum fluid shear stress to cause a temporary loss. Then the surfaces were exposed to a designed fluid shear-stress for an extended period of time to study the resulting permanent loss. The static contact angles and slip-lengths were measured to examine the loss of their superhydrophobicity. Then the variation of their surface structures was investigated using SEM imaging.

Finally, complex viscoelastic fluids interacting with superhydrophobic surfaces were investigated by studying drops moving on the surfaces. A novel phenomenon was observed viscoelastic fluid drops move on the surface at a significantly reduced velocity in comparison with the Newtonian fluid drops which have the same volume, static contact angle, viscosity, density and surface tension. In addition, complex branch-like patterns, beads-on-a-string-like phenomenon, are left behind on the surfaces. Studying this phenomenon may help improve applications of superhydrophobic surfaces in the chemical, food and pharmacy industries in which viscoelastic fluids are common.

Publications

Xu, H., Clarke, A., Rothstein, J.P. & Poole, R.J., (2016). Sliding viscoelastic drops on slippery surfaces. *Applied Physics Letters*, 108(24), p.241602.

Xu, H., Clarke, A., Rothstein, J.P. & Poole, R.J., (2018). Viscoelastic drops moving on hydrophilic and superhydrophobic surfaces. *Colloid and Interface Science*, 513 p53-61.

Xu, H., Clarke, A., Rothstein, J.P. & Poole, R.J., Sliding viscoelastic drops on slippery surfaces. The XVIIth International Congress on Rheology (ICR2016), Kyoto, Japan, August 2016.

Xu, H., Clarke, A., Rothstein, J.P. & Poole, R.J., Sliding viscoelastic drops. AERC2017 and the 26th Nordic Rheology Conference, Copenhagen, Denmark, April 2017.

Contents

List of figures

List of tables

Nomenclature

A = Area, m^2

b = Slip-length, m

Bo = Bound number

Ca = Capillary number

D = Diameter, m

D_r = Drag reduction

F_{app}= Macroscopic pinning force, N

F_{EV} = Extensional viscosity, N

F_g= Gravitational force, N

F_h= Contact angle hysteresis force, N

F_p= Pinning forces, N

F_v= Viscous force, N

f_g = Gas fraction

f_s = Solid fraction

g = Gravitational acceleration, m/s^2

G = Elastic modulus, Pa

h = Gap distance, m

h_t = Trim distance, m

H = Height, m

k = Probability of Boger fluid attaching on the pillars of the surface structure

L = Length, m

l_g = Thickness of the gas layer, m

M_w = Molecular weight, g/mol

P = Pressure, Pa

ΔP = Pressure drop, Pa

ΔP_{slip} = Pressure drop with slip, Pa

P_l = Liquid pressure over a gas, Pa

Q = Flow rate, m^3/s

r = Radius, m

r_f = Roughness ratio of the wet surface

r_s = Roughness factor

R = Radius of rotation geometry, m

R_{mid} = Radius of mid-point, m

s = Length scale of surface structures, m

s^+ = Non-dimensional spacing between surface structure

s_f = Geometric factor of cone-and-plate system

t = Time, s

t_b = Thickness of "blade-like" surface structure, m

T = Torque, N·m

T_0 = Torque without slip, N·m

T_s = Torque with slip, N·m

Tr = Trouton ratio

u = Velocity, m/s

U = Velocity of drop, m/s

u_0= Slip velocity, m/s

V = Volume, m^3

V_τ= Friction velocity, m/s

vw = Width of surface structure valley, m

w = Width, m

Wi = Weissenberg number

α = Angle of inclined plate, Degrees

α_c = Angle of cone, Degrees

γ = Shear rate, 1/s

$\dot{\varepsilon}$ = Extension rate

η_E = Extensional viscosity, Pa·s

θ = Contact angle, Degrees

θ_{adv} = Advancing contact angle, Degrees

θ_{hi} = Contact angle of hydrophilic surface, Degrees

θ_{ho} = Contact angle of hydrophobic surface, Degrees

θ_{rec} = Receding contact angle, Degrees

θ_C = Threshold contact angle between Wenzel and Cassie-Baxter states, Degrees

θ_{CB} = Contact angle of Cassie-Baxter state, Degrees

θ_Y = Young's contact angle, Degrees

θ_W = Contact angle of Wenzel state, Degrees

λ = Relaxation time, s

μ = Dynamic viscosity, Pa·s

μ_{ap} = Apparent dynamic viscosity, Pa·s

μ_{ba} = Baseline dynamic viscosity, Pa·s

μ_l = Dynamic Viscosity of liquid, Pa·s

μ_a = Dynamic Viscosity of air, Pa·s

ν = Kinematic viscosity, m^2/s

ρ = Density, kg/m^3

τ = Shear stress, Pa

τ_b = Filament break-up time, s

τ_c = Time for the drop to reach to the next pillar, s

τ_i = The shear stress on the interface of liquid and gas, Pa

σ = Surface tension, N/m

σ_{LG} = Surface tension of liquid-gas, N/m

σ_{SG} = Surface tension of solid-gas, N/m

σ_{SL} = Surface tension of solid-liquid, N/m

ω = Angular velocity, rad/s

Acronyms

BCH	Brucite-type Cobalt Hydroxide
BCH-LA	Lauric Acid-Coated Brucite-type Cobalt Hydroxide
CaBER	Capillary Break Up Extensional Rheometer
DRIE	Deep Reactive Ion Etching
EHD	Electrohydrodynamics
FE-SEM	Emission Scanning Electron Microscope
FODMS	Fluorooctylmethyldimethoxysilane
FPs	Fluoropolymer
HFCVD	Hot Filament Chemical Vapor Deposition process
i-PP	Isotactic Polypropylene
LBL	layer-by-layer process
MODMS	Methyloctyldimethoxysilane
MTEOS	Methyltriethoxysilane
PAA	Poly acrylic acid
PAH	Allylaminehydrochloride
PDMS	Poly dimethysiloxance
PEG	Polyethylene Glycol
PEO	Polyethylene Oxide
PS/DMF	Polystyrene in Dimethylformamide
PTFE	polytetrafluoroethylene

SEM	Scanning Electron Microscopy
STP	Standard Temperature and Pressure
TEM	Transmission Electron Microscopy
WSA	Water Shedding Angle
μ-PIV	Microparticle Image Velocimetry

Chapter 1 Introduction

1.1 Background of superhydrophobic surfaces

On a rainy day, the rain drops hit and stick on the glass window making your vision fuzzy, but when you look through the window, the leaves of trees and other plants are still clean and without water attached. This phenomenon is the well-known "lotus-effect" (Neinhuis and Barthlott (1997)). Some plant leaves, like lotus and rice leaves, are highly water-repellent, small water drops can stand on such surfaces in an almost perfect spherical shape and very easily roll off, as seen in Figure 1.1. Inspired from nature, these kind of surfaces, also called "superhydrophobic" surfaces have attracted a great deal of attention in recent decades because of their numerous potential applications such as "self-cleaning" surfaces (Cheng and Rodak (2005) and Neinhuis and Barthlott (1997)), friction-reduced surfaces for drag reduction (e.g., for hydrodynamically efficient ship design and "drag-reducing" pipe flows) and icephobic (Nosonovsky and Hejazi (2012)) surfaces for wind turbine blades. However, it is typically difficult to experimentally measure how easily water will slip past the surface, or how much the drag will be reduced, because the size of available superhydrophobic surfaces are small, and their resilience to wear is low (Voronov et al. (2008)).

Figure 1.1. An image of “lotus effect”,
http://www.naturesraincoats.com/Plants_Lotus.html

Superhydrophobic surfaces can be characterized using several wetting properties. The most convenient one, which is also subject to much discussion (details are discussed in Section 4.1.1), is the static contact angle, as illustrated in Figure 1.2. The contact angle is the angle which is measured through the liquid, where a liquid–vapor interface meets a solid surface. For a surface having a contact angle lower than 90°, the surface is called a hydrophilic surface, otherwise it is a hydrophobic surface. Superhydrophobic surfaces can be simply defined as a surface which has a very high contact angle (typically > 150°) and low contact angle hysteresis, Tian et al. (2016)).

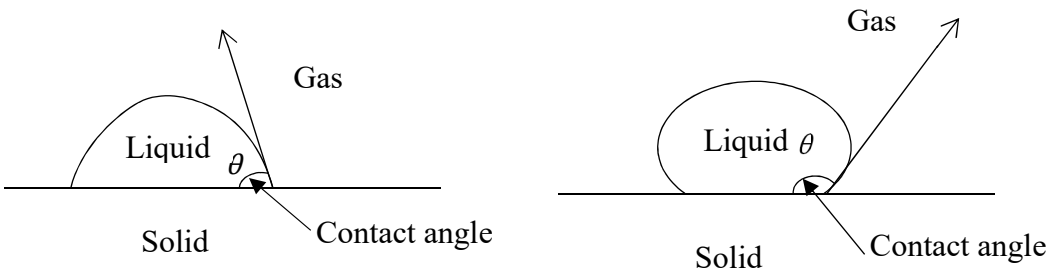

Figure 1.2. A schematic of contact angles of hydrophilic and hydrophobic surfaces.

The wetting properties of a surface depend mainly on two factors: (1) the surface free energy, determined by the chemical nature of the surface material, of the interaction between the liquid and the top most solid molecular layer, and (2) the surface roughness, (Feng et al. (2002)). Superhydrophobicity arises from a combination of these two factors, and the latter is the dominant factor, an artistic image of the superhydrophobic surface structure is shown in Figure 1.3. After decades of study, a number of conceptual models have been proposed to describe the superhydrophobic effects, such as the well-known Wenzel (Wenzel (1936)) and Cassie–Baxter (Cassie & Baxter (1944)) models. If a liquid fully fills the surface structure this state is called the Wenzel state. If the drop stands on top of the surface structure and gas is trapped between the solid and liquid to form a liquid-gas-solid interface between the drop and the surface, this state is called the Cassie-Baxter state (more details will be discussed in Section 2.1.1). Studies of these models helped people to understand superhydrophobic surfaces and manufacture them artificially.

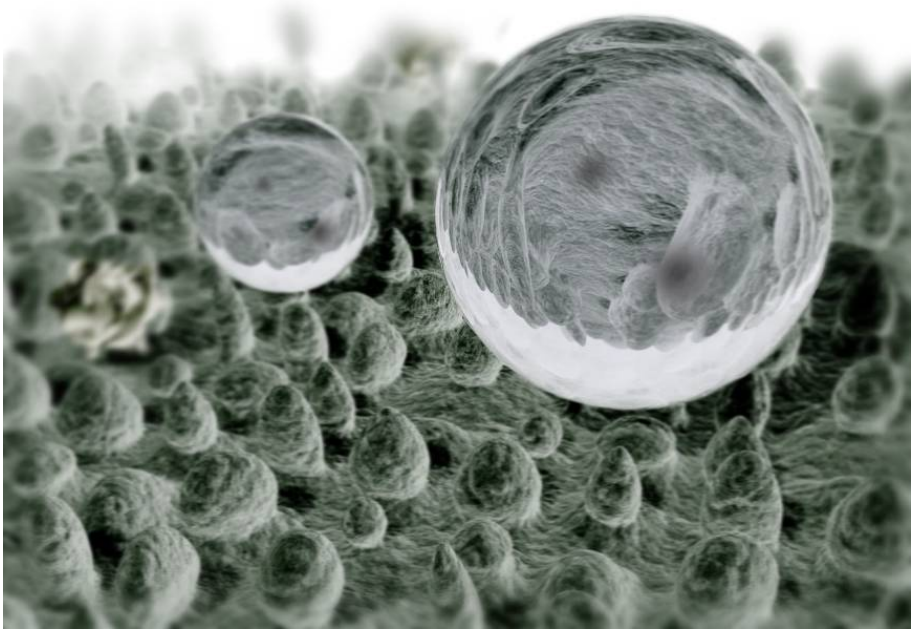

Figure 1.3. An artistic rendering of the surface of a lotus leaf. Image from William Thielicke at http://www.visionlearning.com/blog/2015/08/24/self-cleaning-leaf-superhydrophobic-lotus/

Many methods have been developed to manufacture superhydrophobic surfaces such as using physical methods, chemical methods, plasma methods, laser methods and photolithography methods, more precise details will be described in the literature review in Section 2.2. Nowadays, a few of commercial methods are available and have achieved some success despite their shortcomings such as lack of resilience, UV sensitivity and high cost of manufacture "large" surfaces. In this work, a cheap and repeatable method of fabricating relatively large superhydrophobic surfaces was achieved, details will be introduced in Chapter 3.

Besides the water-repellence and high static contact angle of the superhydrophobic surfaces, the potential for flow drag reduction is one of the most attractive potential industrial applications. Drag reduction can occur for a superhydrophobic surface which maintains a Cassie-Baxter state forming the liquid-solid-gas interface, as seen in Figure 1.4. Obviously, the drag between the gas and liquid is significantly lower than that between liquid and solid. This phenomenon has potential for enormous economic and technological applications in fluids engineering. Navier (1823) first proposed the concept of a "slip-length" to describe the drag provided by a "slip" boundary condition which is unlike the normal "no-slip" boundary condition. Under this boundary condition, the flow velocity at the boundary is not zero. The slip boundary is defined as an extrapolated distance relative to the wall where the tangential velocity component is equivalent to zero, (Lee et al. (2016)), full details are introduced in Section 2.3.1. Nevertheless, the value of slip-lengths is very small for most surfaces and difficult to measure. There are limited slip-length measurements for superhydrophobic surfaces in existing studies.

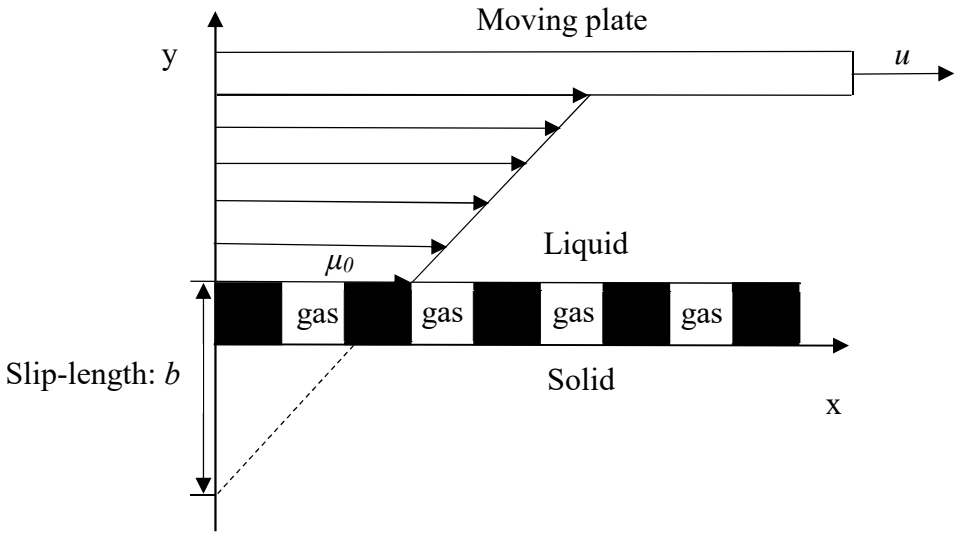

Figure 1.4. A schematic diagram of the drag reduction from superhydrophobic surface.

In general, after decades of study, much progress has been made in the development of superhydrophobic surfaces. They are moving out of the laboratory into the real world. However, there remain a number of questions about superhydrophobic surfaces such as: 1) how to create large superhydrophobic surfaces in an inexpensive way; 2) how to quantify the drag reduction on superhydrophobic surfaces; 3) how to create a robust superhydrophobic surface and how to quantify its resilience; and 4) what will occur when more complex fluids instead of water interact with such superhydrophobic surfaces. Attempts to answer all of these questions are made in this work.

1.2 Motivation

Although superhydrophobic surfaces have numerous potential applications in many aspects, there are many problems preventing them becoming a reality. Following the questions raised in the previous section, the motivation of this work is to try to solve them and help to better understand superhydrophobic surfaces. The first question is the cost of manufacturing superhydrophobic surfaces. Fabrication of a sufficiently large

surface area for practical applications in currently not economical. This fact encourages us to find a method which can produce “large” superhydrophobic surfaces in an easy and inexpensive way. In addition, a comprehensive characterisation beyond static contact angles can aid for understanding of the nature of superhydrophobic surfaces. (Zhang et al. (2008), Shirtcliffe et al. (2010), Verho et al. (2011), Simpson et al. (2015) and Lee et al. (2016)) Many studies focus on the measurement of static contact angle, but it is difficult to describe all the properties of superhydrophobic surfaces using the static contact angle alone. For example, the slip-length or drag reduction of the surface cannot be predicted via the static contact angle. Furthermore, there is a fundamental contradiction of the superhydrophobic surface: a finer surface structure gives a higher superhydrophobicity but it also means a weaker surface which loses its hydrophobicity easier. This problem is a significant issue for applications of superhydrophobic surfaces. But, there are not many studies regarding the resilience of superhydrophobic surfaces and investigating them in a systematic way under an “in-use” condition. Finally, the majority of existing studies only investigated Newtonian fluids interacting with superhydrophobic surfaces. The different behaviour of complex non-Newtonian fluids should be studied because of the potential applications of superhydrophobic surfaces in many relevant industrial areas such as the chemical and food industries where such fluids are common.

1.3 Aim and objectives

The aim of this thesis is to manufacture, characterise and investigate novel superhydrophobic surfaces.

The first objective of this work is to find a method which is easy, inexpensive and can manufacture “large” surfaces. This is a fundamental aspect of this work, and gives the possibility to meet the other objectives.

The second objective is to characterise the superhydrophobic surface in a quantifiable way. To meet this objective, static contact angle measurements, microscopy imaging, a water bouncing method which can provide a clear and convenient definition of superhydrophobicity, and “slip-length” measurements which can predict the drag reduction in different applications were all performed.

The third objective is to provide a systematic and quantifiable method to evaluate the resilience of the superhydrophobicity. This is an essential issue for any potential industrial applications.

Finally, this work also aims to investigate the behaviour of complex non-Newtonian fluids on the superhydrophobic surface. This subject is novel and very few studies focus on it. But understanding such interactions is important for the development of superhydrophobic surfaces in many applications in food, chemical and pharmaceutical industries which deal with such non-Newtonian fluids.

1.4 Outline of thesis

In this work, a number of contributions were made to the development of the superhydrophobic surfaces and their applications. In Chapter 2, a literature review is provided. Firstly, the development of the superhydrophobic surfaces is introduced. The basic concepts regarding wetting, contact angles, the relationship between the superhydrophobicity and the surface roughness are described. Then, the manufacturing methods are introduced under different categories. Following that, the slip on the

superhydrophobic surfaces and how to measure it are presented. Finally, the resilience of superhydrophobic surfaces are discussed.

In Chapter 3, a method which is easy, inexpensive and can provide “large” surfaces is introduced. The superhydrophobic surfaces are created by “hot-embossing” a fine wire mesh onto a hydrophobic polytetrafluoroethylene (PTFE) surface. The negative of the mesh structure is printed onto the PTFE surface to create superhydrophobicity with an advancing contact angle above ~150° and low contact angle hysteresis.

In Chapter 4, the static contact angles and contact angle hysteresis of these superhydrophobic surfaces were measured. Scanning electron microscopy (SEM) images are used to investigate their surface structure. After that, their superhydrophobicity is investigated using water bouncing experiments. Finally, their slip was measured by using the concept of “slip-length”.

In Chapter 5, the resilience of the superhydrophobic surfaces are quantifiably examined. The method can be simply described as: the contact angles and slip-lengths of the surfaces were measured to evaluate the superhydrophobicity after a designed exposure to fluid shear-stress applied via rotating plates on a rheometer.

In Chapter 6, a novel phenomenon regarding a so-called Boger fluid, a constant-viscosity dilute elastic liquid, drops moving on superhydrophobic surfaces was studied. A Boger fluid drop moved on various surfaces caused by sudden surface inclination. For smooth or roughened hydrophilic surfaces, there are minor difference between these elastic liquids and a Newtonian comparator fluid. In contrast for superhydrophobic surfaces, profound differences are observed: the elastic drops slide at a significantly reduced rate and complex branch-like patterns, beads-on-a-string-like phenomenon, are left on the surface.

In Chapter 7, general conclusions of this work are provided, and ideas for future works are also suggested.

Chapter 2 Literature review

Superhydrophobic surfaces have drawn a great deal of attention in recent decades (Shirtcliffe et al. (2010)) because of their potential technical applications such as "self-cleaning" surfaces (Nosonovsky and Hejazi (2012)), friction-reduced surfaces (e.g. for hydrodynamically efficient ship design and "drag-reducing" pipe flows) and icephobic surfaces for wind turbine blades (Cheng and Rodak (2005)). In this chapter, a historical overview and the current state-of-the art of superhydrophobic surfaces is presented which includes the wetting properties and the theoretical models of superhydrophobic states; the relationship between surface roughness and superhydrophobicity; the various manufacturing methods; drops moving and hitting on superhydrophobic surfaces; the slip on superhydrophobic surfaces and their resilience.

2.1 Surface roughness and hydrophobicity

2.1.1 Superhydrophobic states

Ollivier (1907) first reported contact angles of nearly 180° on a surface coated with hydrophobic powders. Coghill and Anderson (1923) found that stearic acid drops can achieve a contact angle as high as 160° on a rough surface of galena. This study showed the connection between wetting properties and surface roughness. It is well known that the contact angle of water on flat hydrophobic solid surfaces is typically in the range of 100 to 120°. But surface roughness can significantly enhance the contact angle to 150°

or higher, see Section 2.2 for a detailed discussion. It is remarkable because this wetting property is not generated by the surface chemistry only but also the surface structure itself, (Lafuma and Quéré (2003)). Since those early studies, a number of conceptual models have been proposed to explain and aid understanding of this connection, such as the well-known Wenzel (Wenzel (1936)) and Cassie–Baxter (Cassie and Baxter (1944)) models. From this relationship, many studies have shown that superhydrophobicity can be produced by creating a micro or nano-scale roughness on surfaces.

Young (1805) proposed the relationship between contact angles of solid, liquid and gas phases, as shown in Figure 2.1 below.

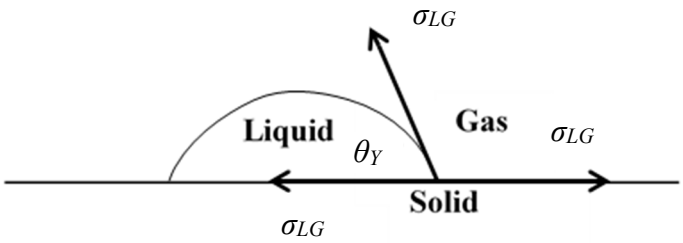

Figure 2.1. Schematic of Young's force balance between surface tensions.

A force balance between surface tensions when a liquid drop stands on a smooth solid surface surrounded by gas is given by:

$$\sigma_{SG} = \sigma_{SL} + \cos\theta_Y \cdot \sigma_{LG} \qquad 2.1$$

where σ_{SG} , σ_{SL} and σ_{LG} are the surface tension of solid-gas, solid-liquid and liquid-gas respectively. θ_Y is the contact angle detemined by the Young's equation (Equation 2.1).

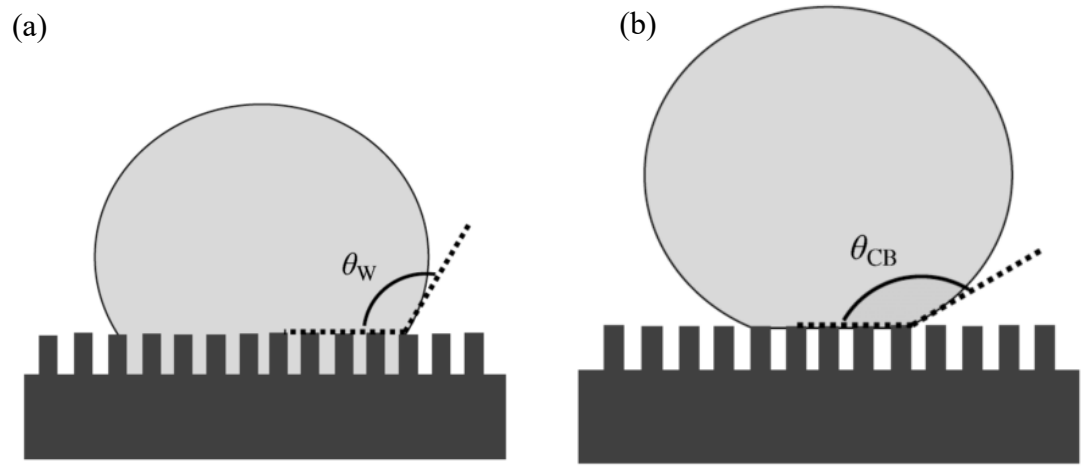

Figure 2.2. Wenzel (a) and Cassie–Baxter state (b) of a liquid drop stands on a rough surface.

When a liquid drop stands on a rough surface, if we assume the liquid fully fills the surface structure this state is called the Wenzel state, as illustrated in Figure 2.2 (a). If we define a roughness factor, r_s , as the ratio of the actual surface area over its nominal (apparent) surface area, the contact angle for the Wenzel state θ_W can be calculated as follows:

$$\cos\theta_W = r_s \cos\theta_Y . \qquad 2.2$$

Where θ_Y is the Young's contact angle as defined for an ideal surface. For a rough surface, r_s is larger than unity, thus θ_W is larger than θ_Y. The Wenzel model describes most cases of drops on hydrophilic surfaces. However, it does not describe the physical observed contact angle hysteresis. (i.e. when a drop moves on the surface, the contact angle at the forward and rearward side are different.) In most hydrophobic surface cases, especially for superhydrophobic surfaces, the drop stands on top of the surface structure and gas is trapped between the solid and liquid to form a liquid-gas-solid interface between the drop and the surface, as shown in Figure 2.2 (b). This state is called the

Cassie-Baxter state. From Young's relationship and the force balance, the contact angles for this state are as follows.

$$\cos\theta_{CB} = r_f f_s \cos\theta_Y + f_g \cos\theta_{LG} = -1 + f_s(1 + r_f \cos\theta_Y) \qquad 2.3$$

Where θ_{CB} is the apparent drop contact angle in the so-called Cassie–Baxter state. f_s and f_g are the fractions of solid and gas contacting the liquid. The contact angle for gas-liquid θ_{LG} is π and ($r_f f_s + f_g = 1$). Here r_f is the roughness ratio of the wet surface area and f_s is the fraction of solid surface area wet by the liquid. Whyman et al. (2008) provided an analysis that illustrates the transition between these two states: when f_s =1 and $r_f = r_s$, the Cassie–Baxter equations becomes the Wenzel equation. Increasing surface roughness decreases f_s, which results in a large increase in θ_{CB} (becoming much larger than θ_W). More details can be seen in Johnson and Dettre (1964).

In general, for the Wenzel state, roughness geometrically increases the surface contact area which enhances the hydrophobicity. For the Cassie–Baxter state, the air trapped in the surface structure leads to a superhydrophobic behaviour (Lafuma and Quéré (2003)). The contact angle for ideal Wenzel or Cassie-Baxter states can be calculated via surface free energy arguments (Shirtcliffe et al. (2010)). In practice, a drop can be fully in the Wenzel state, the Cassie–Baxter state, or in a state in-between them. The relationship between apparent contact angle θ^* and Young's contact angle on a flat surface θ_Y in these two states is plotted in Figure 2.3. The threshold value θ_C between two states should be given by equating equations 2.2 and 2.3, and is physically fixed by surface structure design.

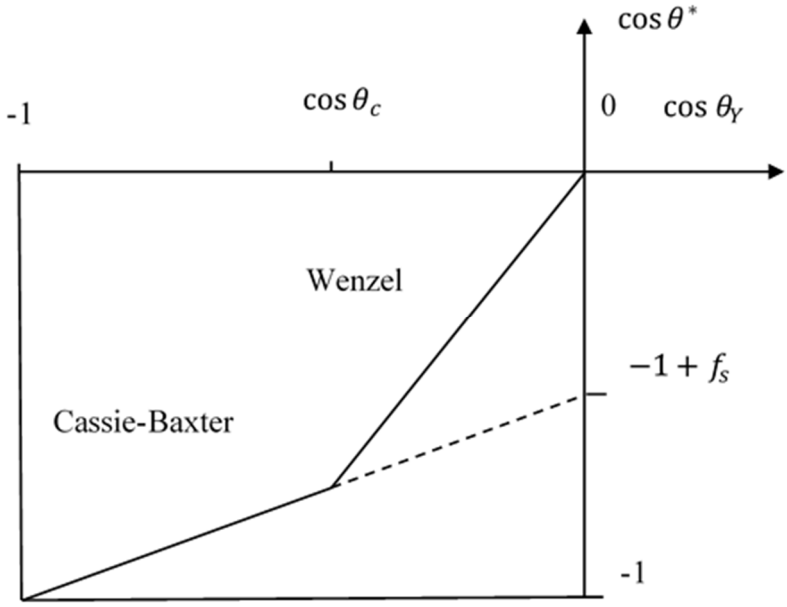

Figure 2.3. The two models of superhydrophobicity, following Lafuma and Quéré (2003).

For a moderate hydrophobic surface ($90° < \theta_Y < \theta_C$), the apparent contact angle θ^* should be given by the Wenzel model (equation 2.2). If $\theta_Y > \theta_C$ air remains trapped below the drop, which sits on a composite surface made of solid and air (Cassie-Baxter state, equation 2.3). However, it has often been reported that the Cassie-Baxter state can also be observed for $\theta_Y < \theta_C$, due to a higher surface free energy. This metastable situation is represented by a dashed line in Figure 2.3. Papadopoulos et al. (2013) studied the Cassie-to-Wenzel transition of water drops evaporating on arrays of hydrophobic micropillars dynamically using a laser scanning confocal microscope. Depending on the surface structure geometry, impalement of a droplet into the surface features can extend over several minutes. The downward velocity of the meniscus depends on the evaporation rate. When the drops recede, single depinning events and the formation of finger-like necks were observed, as illustrated in Figure 2.4.

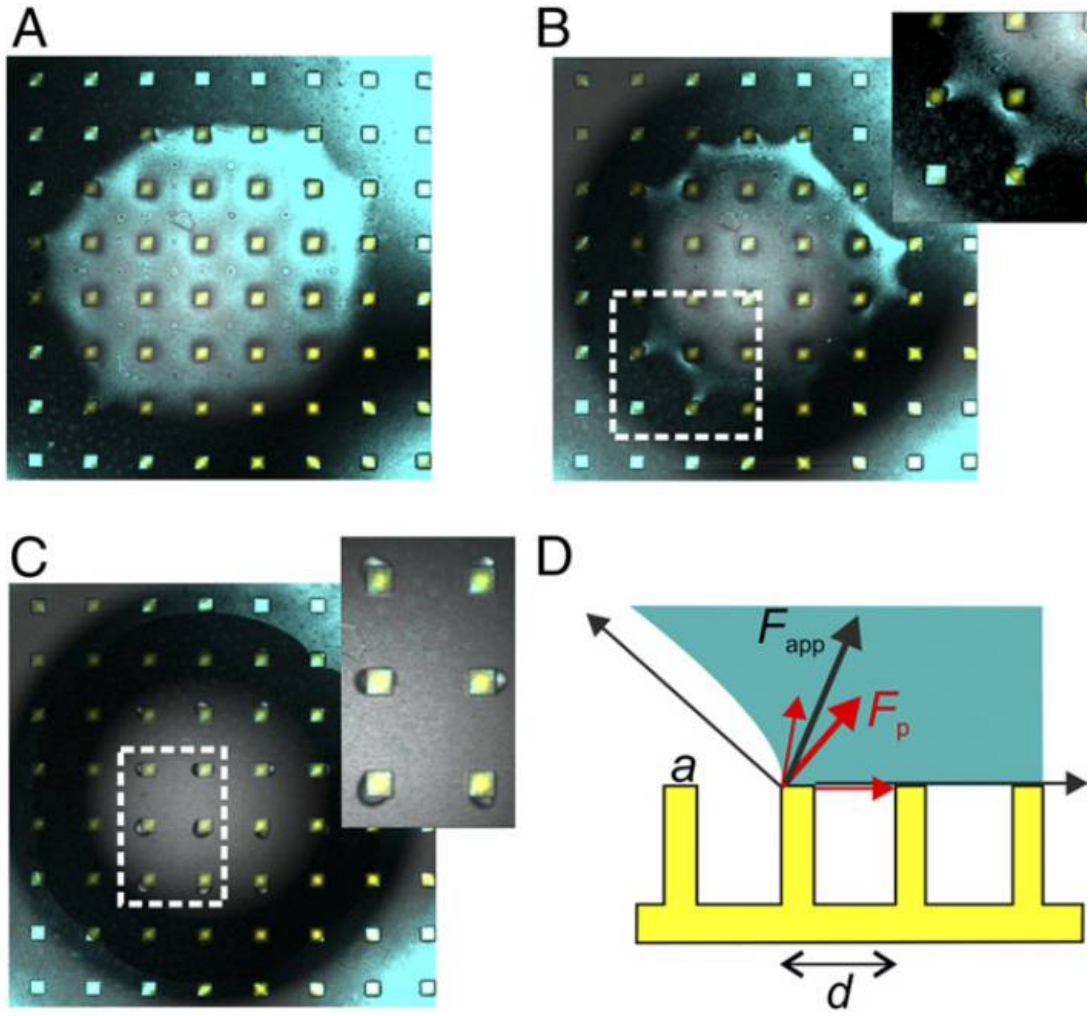

Figure 2.4. Drop depinning during evaporation. (A) Superposition of transmission (bluish) and the reflection from the drop–air cushion interface (cyan) on sub pillars (yellow) (d = 200 μm, a = 50 μm, h = 25 μm) just after deposition. (B) Rim of the drop just before the impalement transition. (Inset) Pinning-induced necks of the drop. (C) Horizontal section recorded just after the impalement transition. (Inset) Air bubbles are visible at the backside of the pillars. (D) Macroscopic pinning force "F_{app}" at the receding part of the drop rim (black arrows). Its horizontal component must be equal to the sum of horizontal components of pinning forces "F_p" at the pillars (red arrows). It is assumed that the mean curvature of the drop is zero. Taken from Papadopoulos et al. (2013).

It should be noted that there are also some arguments about these ideal models, as discussed in Shirtcliffe et al. (2010). The space between surface structures and the shape

of the droplet contact line determines whether the droplet penetrates into the surface structure. McHale (2007) suggested that if axial symmetry is observed, then these models will be reasonable approximations. If the surface structure had a strong symmetry, such as parallel grooves structure, in this case, the contact angle would be different parallel and perpendicular to the grooves and the droplet would become distorted compared to standing on an axially-symmetric structure surface.

2.1.2 Drops on superhydrophobic surfaces

One of the most famous and obvious phenomenon of superhydrophobic surfaces, the so-called “lotus effect” (Onda et al. (1996) and Neinhuis and Barthlott (1997)), is that small liquid drops can stand on such surfaces as a virtually perfect spherical shape and very easily roll off. The static contact angle of a water drop standing on a plant leaf is in excess of 150° and quite common in nature (Shirtcliffe et al. (2010)). The phenomenon of water drops moving or interacting on superhydrophobic surfaces are two of the fundamental problems for studying superhydrophobicity. For example, the most basic problem regards how a drop advances and recedes on a superhydrophobic surface. As introduced in Section 2.1.1, the advancing contact line of a moving droplet on the superhydrophobic surface including three phases and the contact line has to overcome an air gap between the surface structures. Schellenberger et al. (2016) used laser scanning confocal microscopy to get the first microscopic videos, stills of which as shown in Figure 2.5, of water drops moving on a superhydrophobic array of micropillars. From the videos it can be observed that, on the advancing side, the droplet surface bends down until it touches the next micropillar, and the apparent advancing contact angle is 180°, in contrast to what was previously believed (Schellenberger et al. (2016)). On the receding side, the apparent receding contact angle is determined by the pinning on the top surface of the micropillars. For the reason that the advancing

contact angle is 180° for different surfaces, Schellenberger et al. (2016) suggested using receding contact angle to quantify the degree of the superhydrophobicity on a surface instead of the advancing contact angle and the contact angle hysteresis.

(a)

(b)

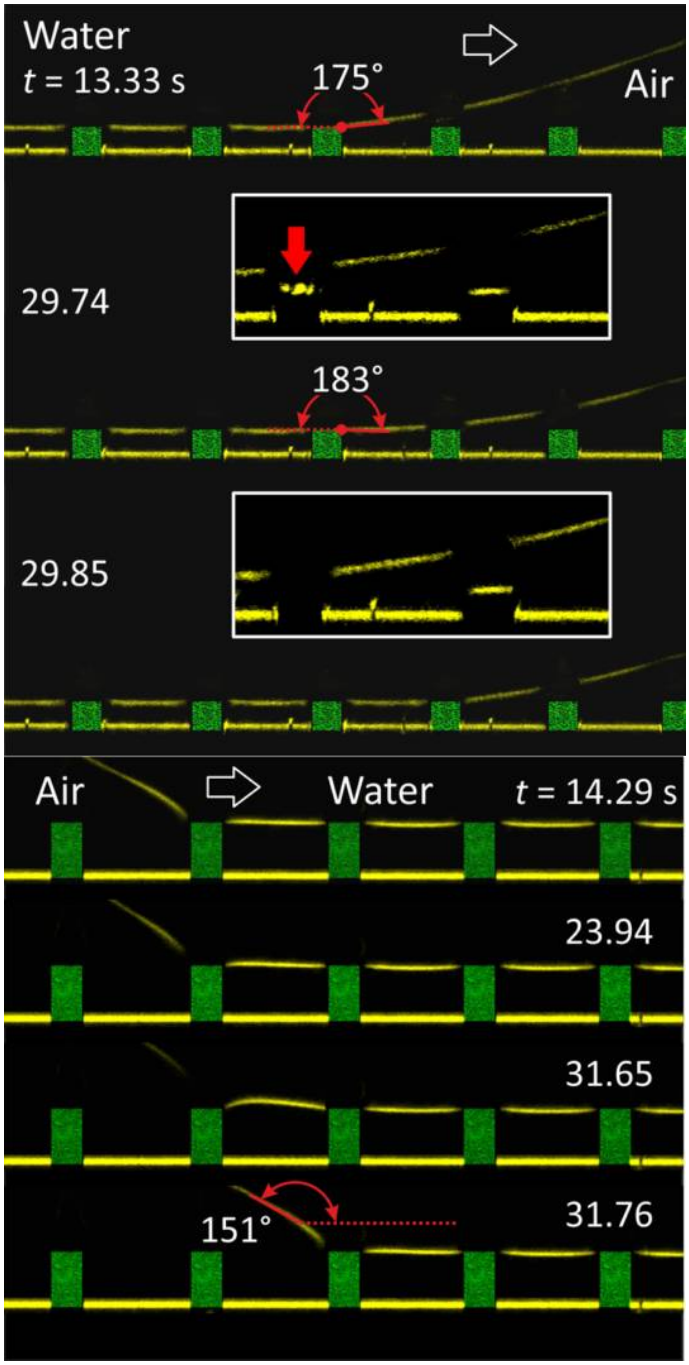

Figure 2.5. Laser scanning confocal microscopy images of (a) advancing, (b) receding drops on superhydrophobic surfaces. Taken from Schellenberger et al. (2016).

Another concern regarding drops standing on superhydrophobic surfaces is that of the effect of the volume of the drops. Afferrante and Carbone (2014) studied the relationship between the contact angle and the volume of the drop by a simple theoretical approach, based on homogenization techniques. For a drop which is gently placed on a micro-structured superhydrophobic surface, the apparent contact area is linear with the volume of the drop, and the macroscale apparent contact angle is negligibly affected by the drop volume, as shown in Figure 2.6.

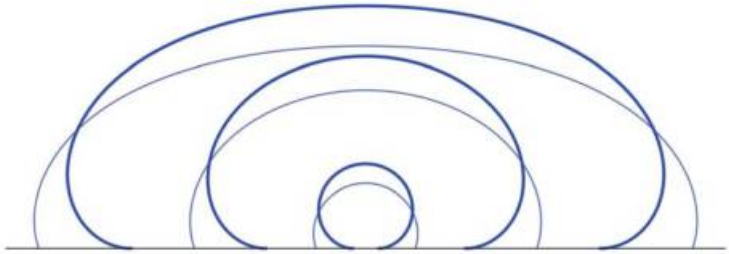

Figure 2.6. Comparison between the shapes that a liquid drop stands on a flat uniform surface (thin line) and a microtextured surface with conical pillars. Taken from Afferrante and Carbone (2014).

Besides droplets moving on superhydrophobic surfaces, drops hitting and bouncing on such surfaces has also been studied widely. As very commonly seen on rainy days, rain drops hit plant leaves which are superhydrophobic and some rain droplets can bounce up from the surface. Crick and Parkin (2011) studied water drops hitting and bouncing on superhydrophobic surfaces using a high-speed camera. A remarkable linear relationship of contact angle and number of water drop bounces was found. The water drop bouncing on a rounded micro-structure only occurs when the contact angle is greater than 151°, as shown in Figure 2.7. They suggested that whether bouncing occurs or not could be used as a definition of superhydrophobicity.

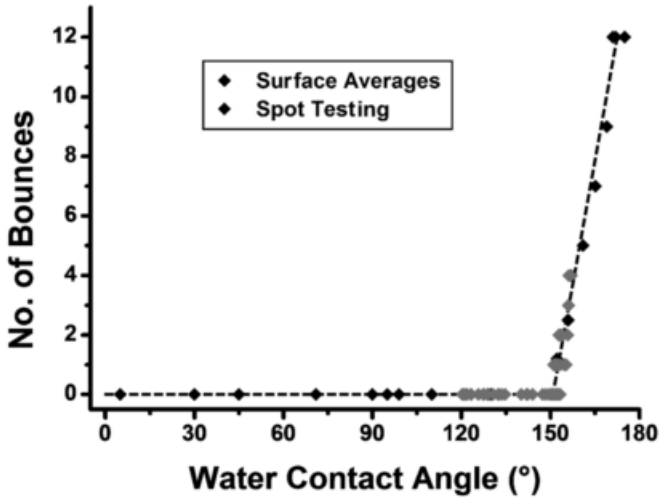

Figure 2.7. Relationship between contact angle and number of water drop bounces, taken from Crick and Parkin (2011).

Following this initial work, Crick and Parkin (2013) extended their study for different shapes of surface structure. For rounded surfaces, the initial water bouncing occurs for a static water contact angle of 151°. For sharp surfaces it was 156° and for extremely sharp (needle-like) surfaces it was 171°. Meanwhile the effects of the surface tension and fluid density were studied as well, and it was proved that the number of water bounces was directly related to both of these fluid properties. Higher droplet densities tended to produce fewer bounces. The number of bounces reached a maximum for a droplet with surface tension of 75 $mN \cdot m^{-1}$, which is very close to the surface tension of water at room temperature.

Another interesting phenomenon introduced here is the spontaneous jumping/bouncing of water droplet standing on superhydrophobic surfaces during freezing or condensing (Schutzius et al. (2015)). They showed that in a low-pressure environment, while droplets experience a high vaporization rate, the droplet could be frozen into a supercooled state that triggers a sudden increase in vaporization, which in turn boosts the pressure of the gas trapped between the drop and the surface structure. This

increased pressure could lift the drop and leads to a “trampolining” phenomenon. This mechanism can aid understanding of self-cleaning, anti-icing and condensation control via superhydrophobic surfaces.

2.2 Manufacturing of superhydrophobic surfaces

As introduced in the previous Section 2.1, superhydrophobicity is produced by a combination of surface roughness and a low surface free energy material. From the early part of the 20th century, scientists and engineers started to manufacture superhydrophobic surfaces using different methods which basically attempted to create micro/nano structure on surfaces. In this section, various methods of manufacturing superhydrophobic surfaces are introduced in different categories.

2.2.1 Physical methods

Zhang et al. (2004) introduced a simple method to create superhydrophobicity by stretching Polytetrafluoroethylene (PTFE) films. Teflon tape with 50–60 mm (length), 10–12 mm (width), 0.1 mm (thickness) were used. Stretching was achieved via a velocity of 1mm/min at room temperature. The surface structure size is about 10 to 50 μm, as shown in Figure 2.8. This very simple and inexpensive method can provide contact angles as great as 165°.

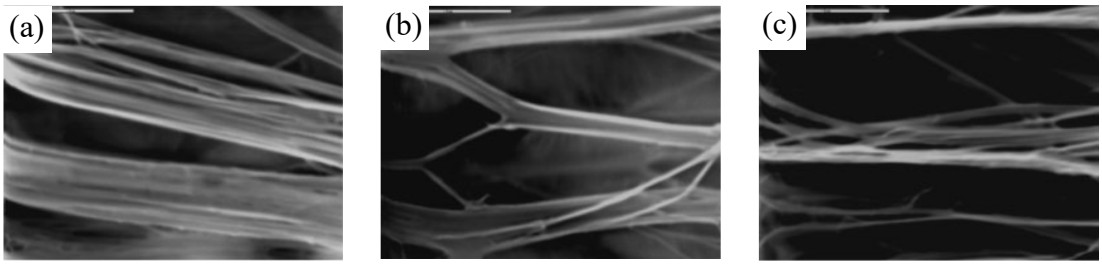

Figure 2.8. (a) No extension original length PTFE sheet, (b) 1.9 times of original length PTFE, (c) 2.9 times of original length PTFE, the scale bar is 5 μm. Taken from Zhang et al. (2004).

Nilsson et al. (2010) also used a very simple method to modify the roughness of PTFE sheet surface to become superhydrophobic. They used very fine sand paper to sand the PTFE sheet surface tens of times. Using of 320-grit sandpaper, the contact angle is higher than 151°. The roughness on the surface is about 10 μm, as can be seen in Figure 2.9. One problem of using this method is that the superhydrophobicity cannot remain for an indefinite amount of time in use (no more than a few hours).

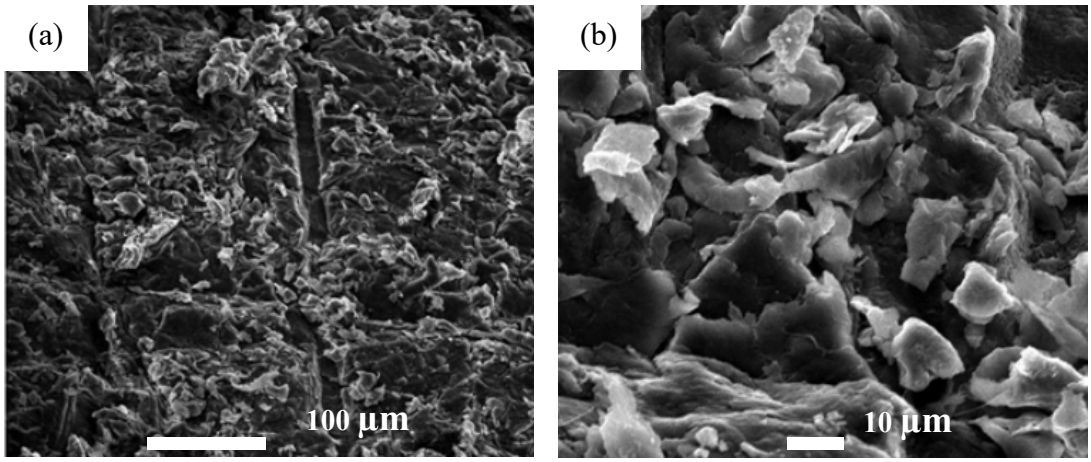

Figure 2.9. SEM images of sanded PTFE surfaces using 320-grit sandpaper. (a) at 200x; (b) at 1000x. Taken from Nilsson et al. (2010).

Bixler & Bhushan (2013) used liquid platinum silicon as a negative model to try to replicate the superhydrophobic structure such as rice, lotus leaves and sharkskin surface. The model was then used to cast the surface by PDMS (Poly (dimethysiloxance)) or urethane polymer. The replicated surface has a contact angle higher than 150°, as shown in Figure 2.10.

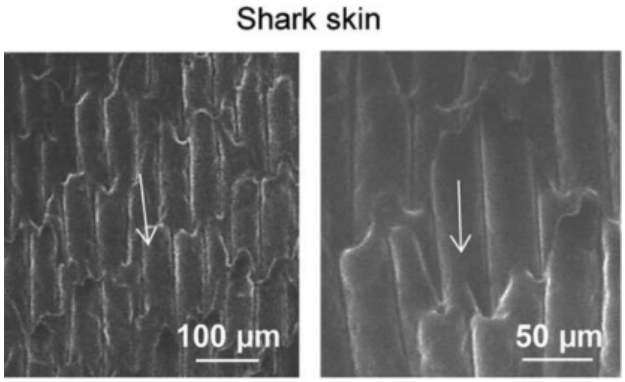

Figure 2.10. Replica of the sharkskin, taken from Bixler & Bhushan (2013)

These physical methods are relatively easy to use in practice. They can provide large and inexpensive superhydrophobic surfaces. However, the disadvantages of these methods are: they cannot control the shape of the surface structure precisely, consequently no regular or well-designed surface patterns can be produced, and the quality of the sample may vary with different batches of manufacture.

2.2.2 Plasma methods

Plasma can provide random patterns onto a material surface by plasma etching or plasma deposition. Plasma etching experiments were performed by using a parallel plate reactor, with the samples located on the water-cooled grounded electrode. Morra et al. (1989) used the plasma to etch the fluoropolymer to create superhydrophobic surfaces. The plasma parameters were the following: excitation frequency 13.56 MHz, power 100 W, pressure 2 Pa, gas flow rate 8 cm^3 (STP)/min. SEM images of plasma-treated fluoropolymer is shown in Figure 2.11. The surface structure size is about 1~20µm, and the contact angle can reach nearly 150°. Shiu et al. (2004) used a combination of nanosphere lithography and oxygen plasma treatment method on the fluoropolymer. This method can increase the contact angle to be as large as 158°.

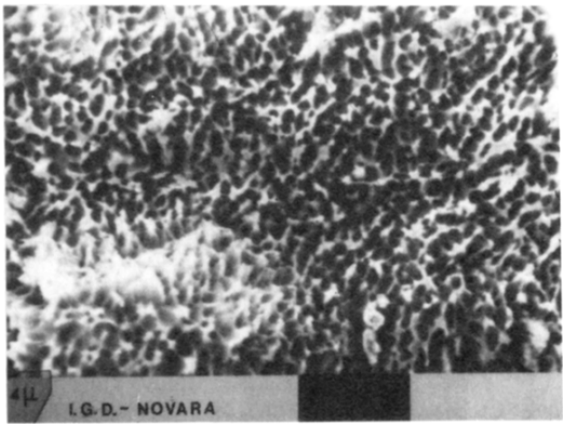

Figure 2.11. Plasma treated fluoropolymer surface, taken from Morra et al. (1989).

Kim et al. (2005) used a mixture of CF_4, H_2, and He gases in-line atmospheric radio frequency (rf) glow-discharge plasma process to modify surfaces to become superhydrophobic with contact angles ranging from 163 to 172°. The atmospheric radio frequency glow-discharge plasma system was constructed with a custom-made plasma generator head and a 13.56 MHz rf supply with an L-C matching unit. Helium was used as a carrier gas (5∼10 lpm) and a mixture of CF_4 and H_2 was used as a reactive gas (20∼80 sccm). A mixture of CF_4 and H_2 was used as a reactive gas (20∼80 sccm). The rf power was controlled in the range of 300∼400 W. The effective plasma area was 1 cm wide and 16 cm long. Samples were translated about 0.5cm below the plasma source along the plasma width direction. The two most important parameters were the speed at which the sample was moved under the plasma head and the use of hydrogen.

Ryan et al. (1996) and Coulson et al. (2000) used Pulsed Plasmachemical Deposition and Atomised Spray Plasma Deposition to create superhydrophobic surfaces on different substrate such as glass, plastic and cloth. Their surfaces have achieved commercial success and are used to protect the surfaces of products worldwide including footwear, clothes, mobile phones and other small devices. (Resound (2012))

Plasma methods can work directly on a low surface free energy material to create micro scale structures. Some of these methods require expensive equipment and a few hours to create square centimetre size surfaces. They provide an easy method to create superhydrophobicity and achieved some success in water-repellent surface coating.

2.2.3 Chemical methods

Jiang et al. (2004) and Acatay et al. (2004) used the electrohydrodynamics (EHD) technique to create a porous microsphere structured surface which produced contact angles higher than 160°, SEM images are shown in Figure 2.12. In a typical EHD process, polystyrene in dimethylformamide (PS/DMF) solutions are pumped through a nozzle to which a high voltage is applied relative to a grounded metal plate (collector) to form an electrically charged jet of solution. The solution jet solidifies with accompanying evaporation of solvent and forms a film on the collector.

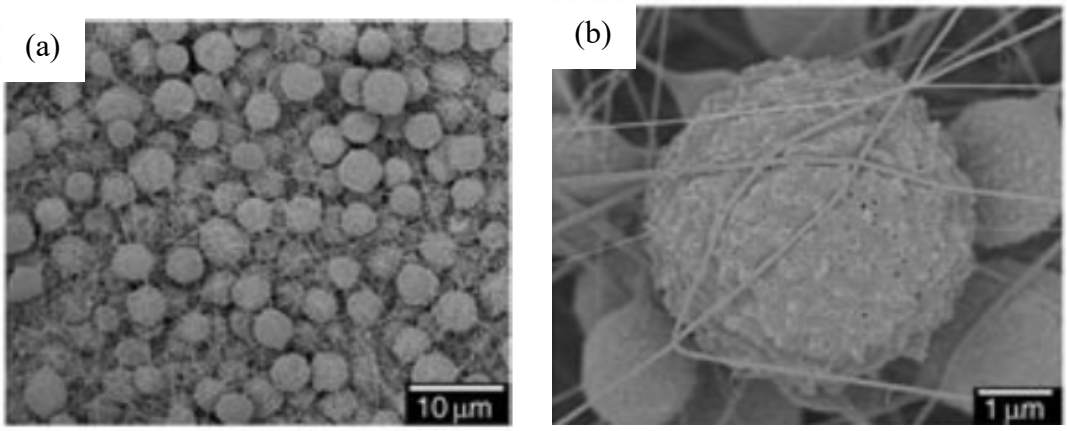

Figure 2.12. (a) 3D Network microsphere structure. (b) Nanostructure of a single porous microsphere, taken from Jiang et al. (2004).

Electrochemical deposition can also be used to fabricate superhydrophobic surfaces, which was shown in Shirtcliffe et al. (2004), Kunugi et al. (1993) and Han et al. (2005). For example, on copper film, flat copper surfaces were prepared by sputtering a thin layer of titanium on to glass cover slips and then sputtering copper on top. Photoresist

was patterned on to some of the copper on glass samples. The mask used was made up of tessellating squares with a circle of one half the side length with one corner being open. Sub patterns were produced using the same mask. Copper growth was carried out using copper sulphate in sulfuric acid. Superhydrophobicity with contact angle about 160° was achieved using a wash in solution designed for waterproofing breathable fabrics, the resulting SEM images of the copper surface with squat pillars structure are shown in Figure 2.13 below.

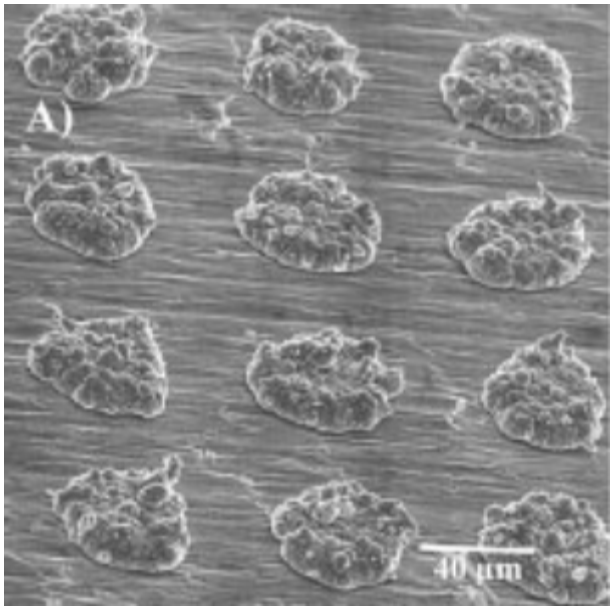

Figure 2.13. Rolled copper surface with squat pillars, 40µm diameter and separation, 4µm in height, taken from Shirtcliffe et al. (2004)

A chemical bath method is a commonly-used method to change surface structure. Hosono et al. (2005) used a chemical bath to fabricate superhydrophobic surfaces. They dissolved $CoCl_2$,$6H_2O$ (0.15 mol/dm^3) and NH_2CO (5 g) in water (25 mL) as a bath solution. Commercial borosilicate glass slides 1 mm in thickness were used as the substrates for deposition. The substrates were put into bottles filled with the solutions, sealed, and kept at 60°C for 24h in a drying oven. Following the deposition, the deposited brucite-type cobalt hydroxide (BCH, $Co(OH)1.13Cl0.09(CO_3)0.39$,

$0.05H_2O$) film were rinsed with ethanol and then dried at room temperature. The BCH films were then put into bottles filled with sodium laureate aqueous solutions (0.1 mol/dm^3) to coat the BCH surfaces with lauric acid, sealed, and kept at 60°C for 5 hours in a drying oven. After immersion, the fabricated films (BCH-LA, lauric acid-coated) were rinsed with ethanol and then dried at room temperature, as can be seen in Figure 2.14.

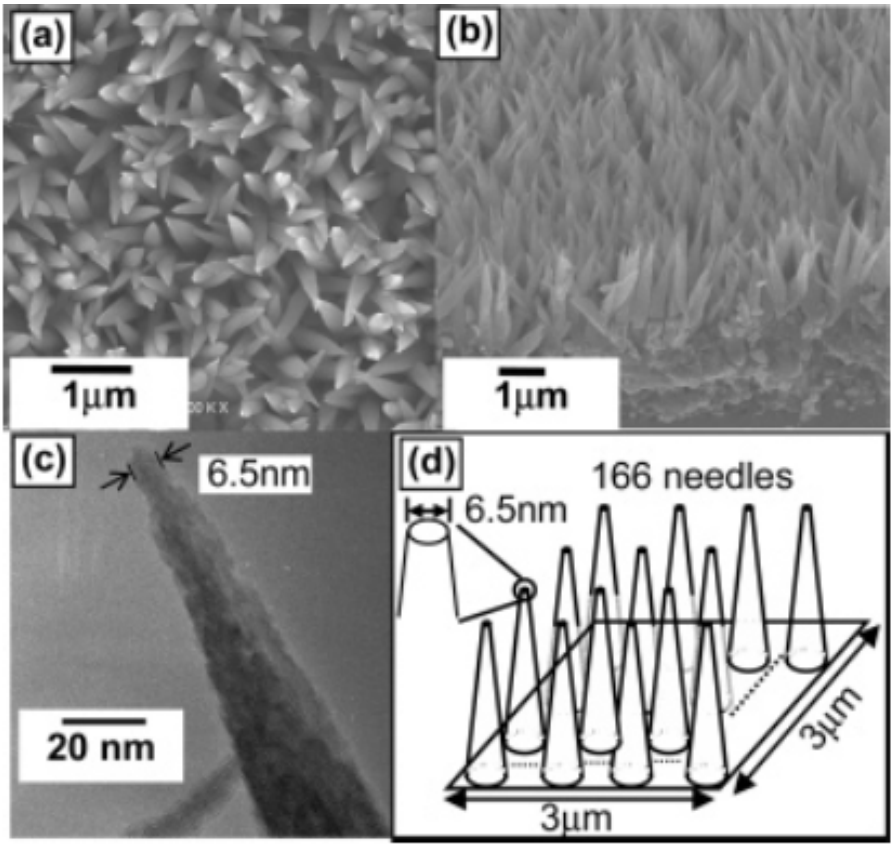

Figure 2.14. (a,b) FE-SEM images of the BCH-LA films observed from the top and side, respectively. (c) TEM images of the BCH-LA films. (d) A simple model of the film with the fractal structure. Taken from Hosono et al. (2005)

Chemical etching, used by e.g. Qian and Shen (2005) and Shirtcliffe et al. (2005), is a widely-used method to modify the surface structure to produce superhydrophobicity. Some metals, such as aluminium, copper or zinc specimens were etched to create superhydrophobic surface with contact angle about 150°. Aluminium specimens were

etched by immersing in a Beck's dislocation etchant in a polyethylene bottle close to room temperature (about 14°C). The etchant was prepared by mixing 40 mL of 37 wt% HCl, 12.5 mL of H_2O, and 2.5 mL of 40 wt % HF. The etching time was varied from 5 to 15 s. After etching, the specimens were immediately rinsed ultrasonically with water and dried at 80°C in air. Copper specimens were etched by mixing 0.06 mL of 37 wt % HCl, 0.02 mL of CH_3COOH, and 53.92 mL of H_2O. The etching time was varied from 8 to 24 hours. Zinc specimens were etched with 50 mL of 4.0 mol/L HCl solution in a glass beaker at room temperature. The etching time was varied from 30 to 90 s. The surface texture is shown in Figure 2.15, and the contact angle for these etched surfaces reached as high as 154°, 145° and 149° for aluminium, copper and zinc respectively.

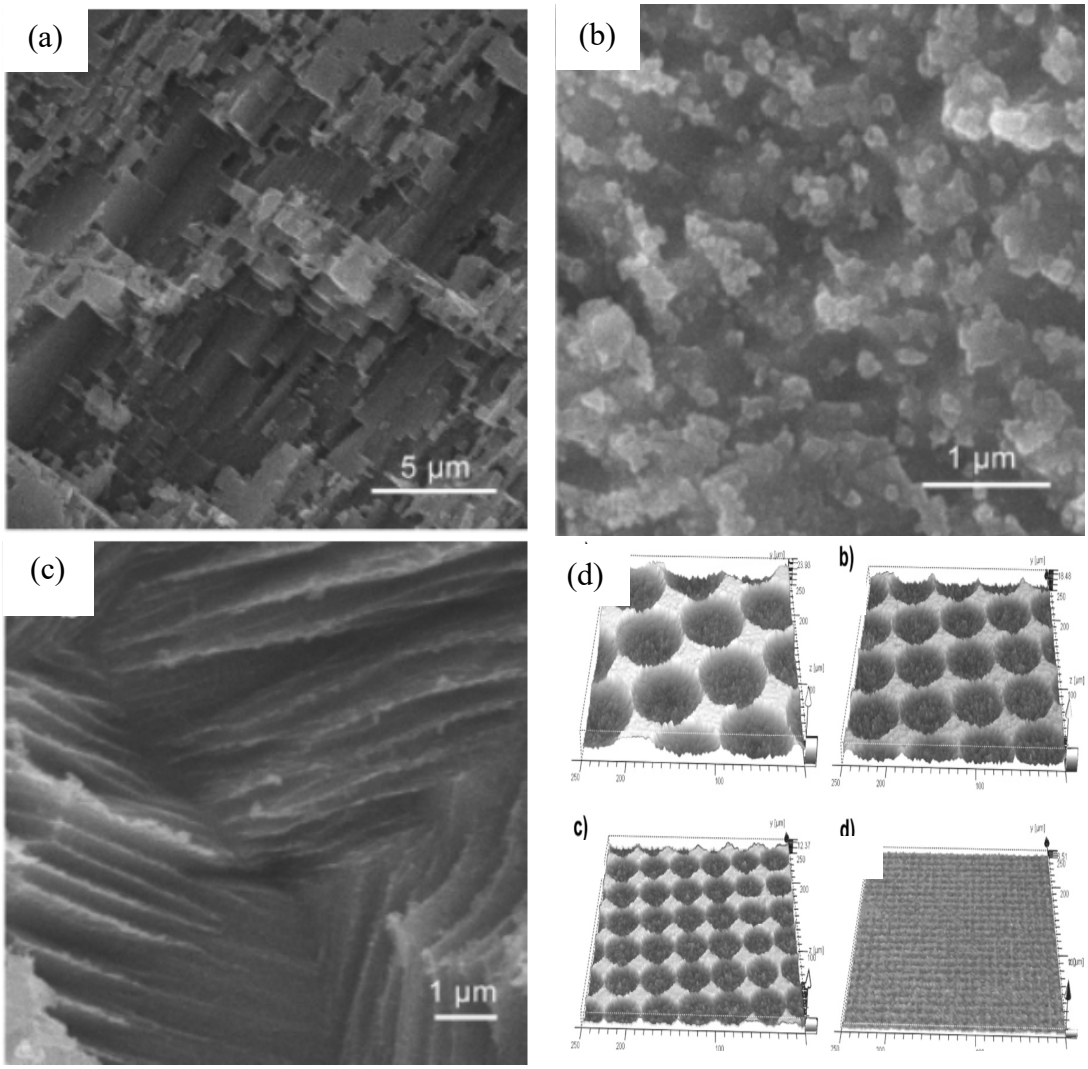

Figure 2.15. (a) Aluminium etched by 10s; (b) Copper etched by 24h; (c) Zinc etched by 90s; Taken from Qian and Shen (2005). (d) Controlled copper profiles of etched copper surfaces Shirtcliffe et al. (2005).

Zhao et al. (2006) further developed the methods originally proposed by Turska and Janeczek (1979) and Guo et al. (2004) using organic solvent to control the crystallization process of polycarbonate to create lotus-leaf-like structure. The smooth polycarbonate plate was coated with a thin layer of acetone, then some coagulator with water and methanol was sprayed onto the surface before acetone evaporated completely. The highest water contact angle reached about 159.7°±1.1°. Cui et al. (2012) used a similar simple single-step method to produce large-area superhydrophobic surfaces.

The polycarbonate sheet was partly dissolved whilst being immersed in acetone, then the crystallization process of the polymer while drying leads to the formation of a hierarchical structure with nano-scale fibers, as shown in Figure 2.16. The water contact angle of this kind of surface is reported as 152°±2°.

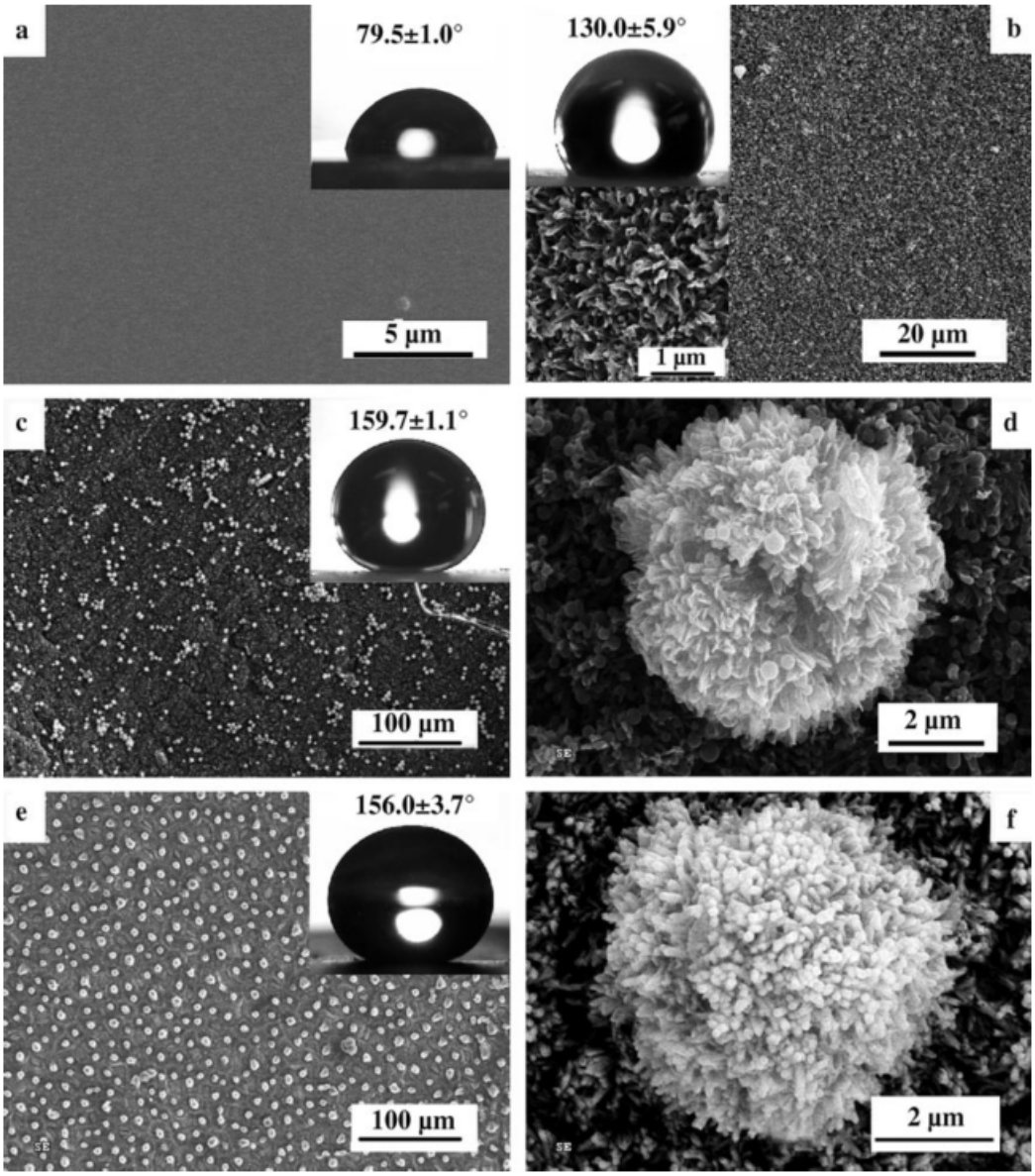

Figure 2.16. SEM images of PC plate (a) amorphous, (b) after SINC by acetone, (c) after being swelled by acetone first and then precipitated by methanol, (d) enlarged view of a single particle from image c and SEM images of (e) lotus leaf and (f) a single micron-sized protrusion on lotus leaf. Inset is the static water contact angle of each surface. Taken from Zhao et al. (2006).

Lu et al. (2015) created an ethanolic suspension of perfluorosilane-coated with dual-scale (~60 to 200nm and ~21 nm) titanium dioxide (TiO_2) nanoparticles, as shown in Figure 2.17, that forms a paint that can be sprayed, dipped, or extruded onto both hard and soft materials. The contact angles of these surfaces are observed to be between 156° to 168°. A highlight of these surfaces is their mechanical robustness and the resistance to oil contamination. These surfaces will be referred to as TiO_2 surfaces in the remaining of this thesis where they will be used as a comparator superhydrophobic surfaces.

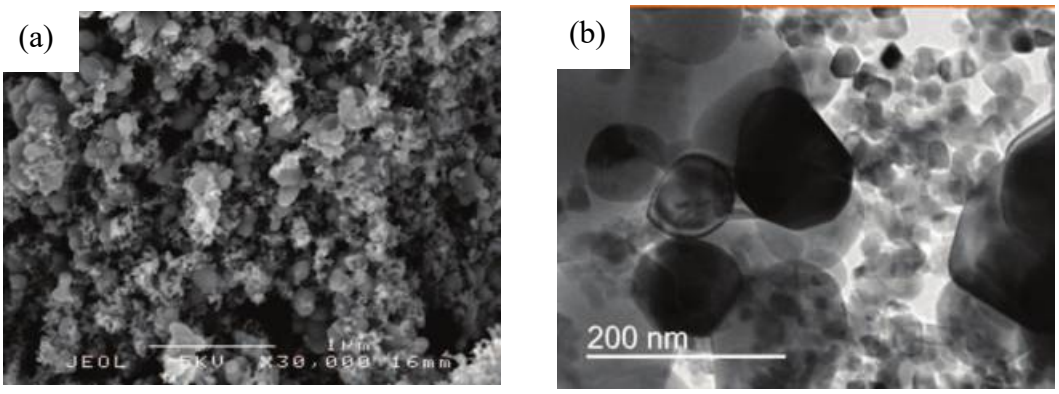

Figure 2.17. Scanning electron microscopy (SEM) and transmission electron microscopy (TEM) of nanoparticles TiO_2 in the paint. Taken from Lu et al. (2015).

Compared to the other methods, chemical methods are much more complicated. They require more equipment and manufacture procedures. However, using chemical methods, i.e., chemical etching, a large and robust superhydrophobic metal oxide surface can be produced. It can be used to make the surface of pipes or containers of industrial use to be superhydrophobic. Hence, they have an enormous potential for industrial applications.

2.2.4 Laser methods

Khorasani et al. (2005) used a high laser abrasion process on PDMS, to create a superhydrophobic surface with contact angle higher than 160°. Both sides of the

sample's surfaces were laser treated and the laser pulses in nitrogen atmosphere scanned the whole surface. No additional chemicals or photo sensitizers were used. The laser used was a line-tunable CO_2-pulsed laser (TEA CO_2 laser lumonics 103-2) which provides laser beams of wavelengths from 9.1 to 10.6 mm. The pulse duration was 100 ns. Each sample was exposed to the laser pulses under these selected conditions: fluency 0.5–5 J/cm^2, wavelengths 9.1–10.6 mm. After each exposure, the samples were washed first with acetone: mixed in distilled water (50/50, v/v) at 80°C for 48h. The extracted samples were dried in a vacuum oven at 50°C to constant weight. After the laser process, they applied solid particles to the final layer (NaCl/PDMS weight ratio is between 1/1 and 5/1) and volatilized the solvent in the final layer and then placed the sheet and the shell into an oven maintained at 135°C for 10 min for drying, the SEM images of these surfaces are shown in the Figure 2.18 below.

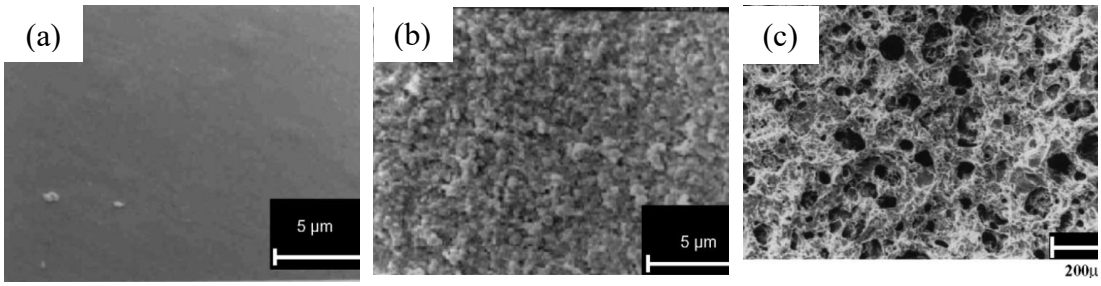

Figure 2.18. SEM images of (a) untreated PDMS surface, (b) laser treated surface, (c) laser and salt treated surface. Taken from Khorasani et al. (2005)

Song et al. (2005) introduced a method called "high power laser beam etching and self-assembly". They polished silicon wafers in a detergent solution and acetone for 30min first. Then they submerged them in a freshly-prepared mixture of H_2SO_4 (98%) and H_2O_2 (30%) at volume ratio of 7:3. Next the silicon wafers were heated at 80°C for 1h to remove organic contaminants. Then they were cleaned with Milli-Q water and dried with N_2. After that, they used a Quik-Laze II laser etching machine (New Wave

Research, U.S.) to roughen the silicon surface. The laser pulse produced grooves on a micrometer scale onto the silicon surface. Finally, the silicon surfaces were covered by a 10mL 50mM silane precursor solution at 47°C for 10min to 4h. Chemical vapor then was used for deposition on the silicon surface. A vessel containing methyloctyldimethoxysilane (MODMS) or fluorooctylmethyldimethoxysilane (FODMS) and silicon substrates were put in an oven at 150°C for 3 or 6 hours. The MODMS or FODMS will self-assemble on the silicon substrates. The contact angle on this surface could be higher than 160°, and the surface structure are shown in Figure 2.19.

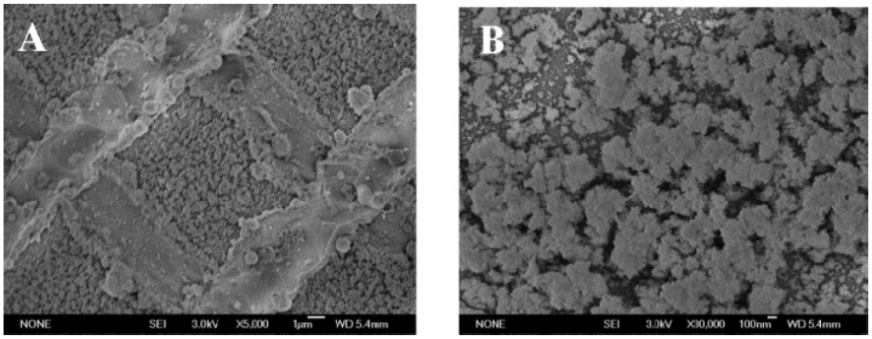

Figure 2.19. SEM images of etched silicon surfaces with laser-etching machine without modification. (A) Rough surface, (B) magnified image of the microconvex. Taken from Song et al. (2005)

Falah Toosi et al. (2015) used a femtosecond laser irradiation process modifying a PTFE surface to create superhydrophobicity. The resulting surface structure is shown in Figure 2.20. The PTFE surface was treated by ultra-short laser pulses with centre wavelength of 800 nm at a repetition rate of 1 kHz. Their study includes the laser fluence range from 5.7 to 51 J/cm^2 and scan speed form 0.25 mm/s to 2 mm/s to form the surface structure height from 10 to 360μm. For uniaxial laser scanning, the contact angle hysteresis is lower than 14° and the contact angle is higher than 160° when laser fluence is above 28 J/cm^2 and scan speed is below 0.5 mm/s. For biaxial scanning, when

using the first pass with laser fluence higher than 14 J/cm^2 and second pass with laser fluence of 7.1 J/cm^2, the contact angle achieved as high as 170° and the contact angle hysteresis decreases to only 3°.

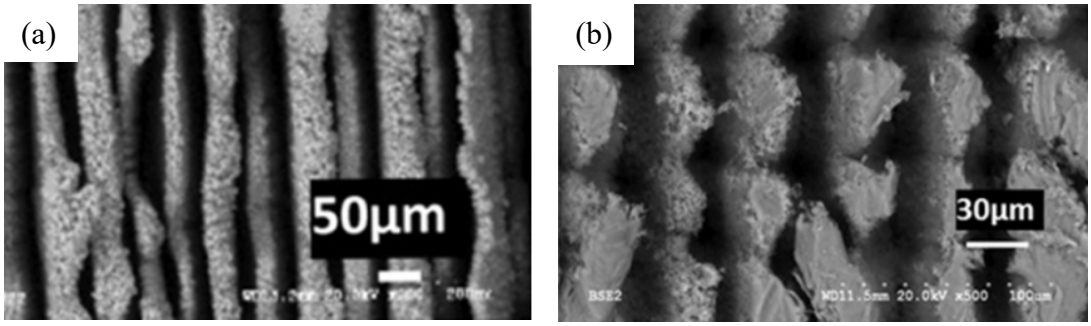

Figure 2.20. SEM images of (a) uniaxial laser scanned PTFE surface; (b) biaxial laser scanned PTFE surface. Falah Toosi et al. (2015)

Laser methods are similar to the plasma etching methods. They both use energy to modify the surface of low surface free energy material. Laser methods need expensive equipment, and take hours to manufacture a small area of superhydrophobic surface as well. Nevertheless, the laser methods can provide more regular and controllable surface structure than the plasma etching. This feature is a good point for laboratory study purposes.

2.2.5 Photolithography methods

Photolithography is one of the most popular methods used to create superhydrophobic surfaces. It uses light to transfer a geometric pattern from a photo mask to a light-sensitive chemical called the photoresist on to the substrate. A series of chemical treatments then engraves the exposed pattern into the material underneath the photo resist. This method can manufacture especially engineered and precise micro and nano-structures on to the surface. Muralidhar et al. (2011) used soft lithography to manufacture a well-designed superhydrophobic surface on PDMS and experimentally

studied the effect of slip boundary condition when flow passes over a cylinder. Many studies, e.g. Ou et al. (2004), Ou and Rothstein (2005), Choi et al. (2006), used this method to study the relationship between the surface structure geometry and superhydrophobicity. SEM images of superhydrophobic surfaces created using photolithography are shown in Figure 2.21.

Coating the polymer on the surface structure after the photolithography can provide a higher contact angle. Gu et al. (2003) used a nanosphere lithography method to coat a glass substrate with polystyrene and silica nanoparticles. The submicron-sized monodisperse polystyrene spheres and nanosized particles were ultrasonically dispersed into deionized water. A glass substrate was then immersed into the solution and withdrawn at a constant speed. By controlling the above process, the surface coated polystyrene and silica were formed. After the film was formed, it was dried in air and then calcined at 450°C to remove the polymer and to solidify the silica nanoparticles. Finally, the surface of the substrate was modified with a fluoroalkylsilane ($CF_3(CF_2)_7 CH_2 CH_2 Si(OCH_3)_3$) by thermal chemical vapor deposition, to render the surface hydrophobic with a contact angle higher than 150°.

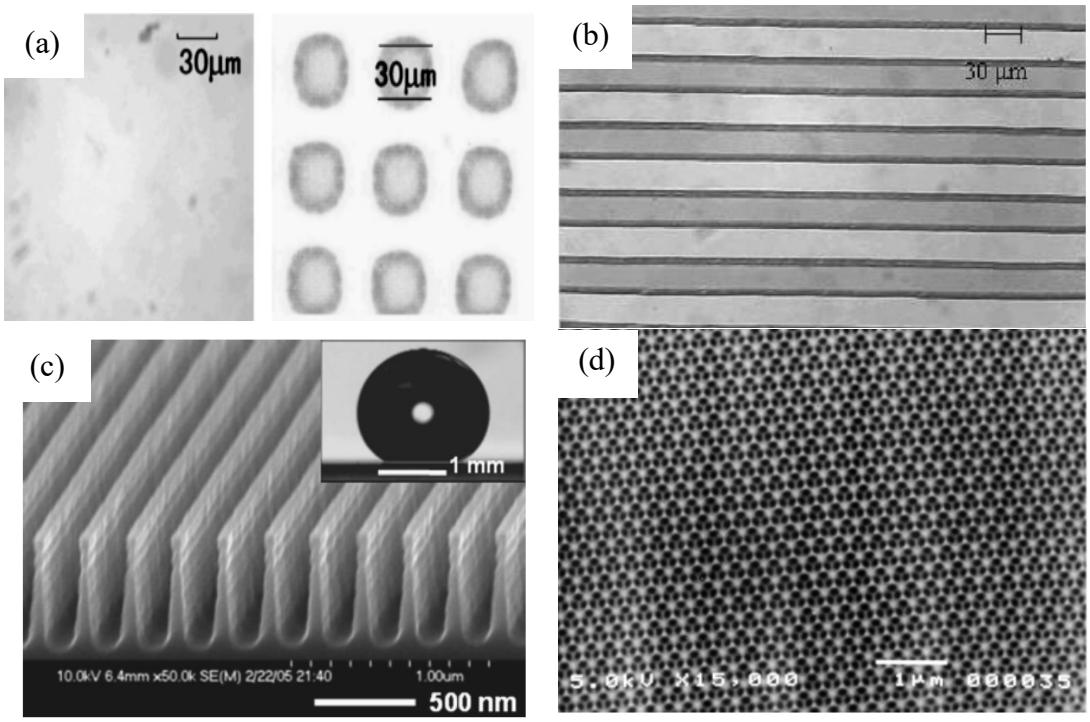

Figure 2.21. SEM images of superhydrophobic surfaces manufactured by photolithography methods. (a) Ou et al. (2004); (b) Ou and Rothstein (2005); (c) Choi et al. (2006); (d) Gu et al. (2003).

Photolithography methods can provide the most controllable and precise structure on the surface. They are the best methods to study the relationship between surface structure and superhydrophobicity. But the cost of equipment and time of this method are the most expensive. Hence, these methods are only for academic study purposes to date.

2.2.6 Polymer process methods

Lau et al. (2003) and Joseph et al. (2006) deposited a vertically-aligned carbon nanotube forest with a plasma enhanced chemical vapor deposition (PECVD) technique. First, the formation of nickel (Ni) catalyst islands on an oxidized (20 nm) silicon substrate through the sintering of a thin (5 nm) Ni film at 650°C is advised. Second, nanotube growth from these discrete catalyst islands in a DC plasma discharge (bias-600 V) of acetylene and ammonia, using flow rates of 75 and 200 sccm, respectively, at a partial pressure of 533.2 Pa. Finally, the PTFE coating is applied onto the forest of carbon

nanotubes through a hot filament chemical vapor deposition (HFCVD) process. The water contact angle is observed to be higher than 160°, and the SEM images are shown in Figure 2.22 below. Luo et al. (2008) studied another method to coat Nafion on carbon nanotubes by a solution process. The highest water contact angle can reach 165.3±9°.

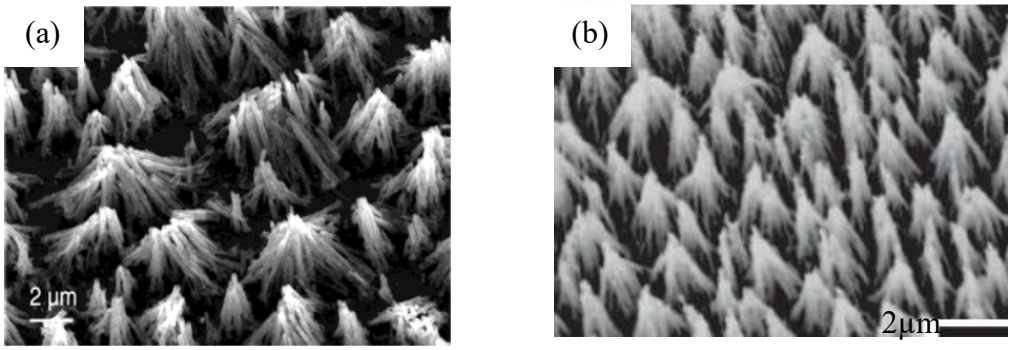

Figure 2.22. SEM images of vertically aligned carbon nanotube forest surface coated by PTFE. Taken from (a) Lau et al. (2003); (b) Joseph et al. (2006).

Shirtcliffe et al. (2003) used a sol-gel phase-separation process to create a frothy structure on a glass film. The contact angle of this surface can achieve 156°. The gel mixture which they used is 0.1255 mol (25 mL) of methyltriethoxysilane (MTEOS) (98%) which was added to 0.0018mol of HCl and 0.83 mol of water or 6.6 equiv (15 mL) of 0.12 MHCl (diluted from 37% HCl) and 0.327 mol (25 mL) of 2-propanol (Fisher p.a.) under rapid stirring using a magnetic stirrer. This mixture was sealed and allowed to react for 60 min at 22°C. Then the sol-gel solution formed micro scale structure on the glass film, as seen in Figure 2.23.

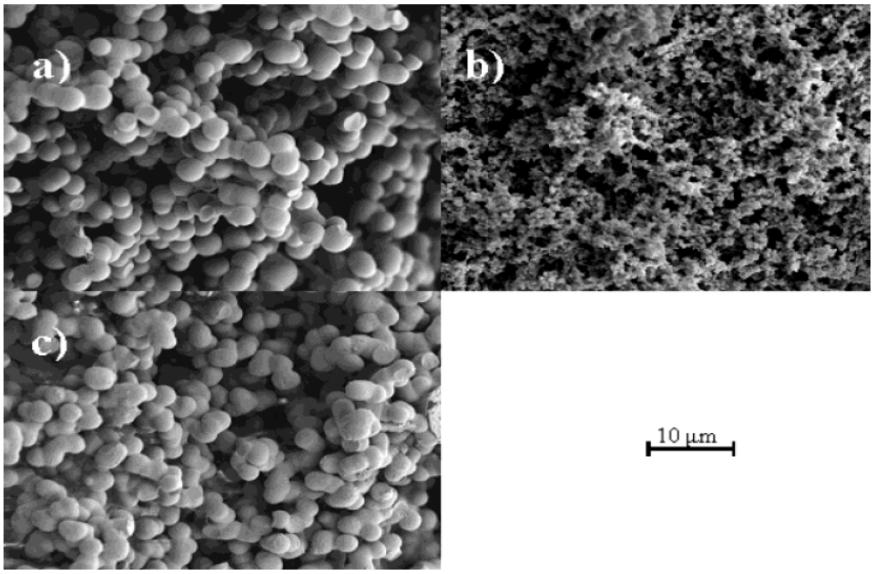

Figure 2.23. SEM images of MTEOS foams, taken from Shirtcliffe et al. (2003).

Erbil et al. (2003) used a carefully-controlled drying process of polypropylene to coat a glass plate to create a superhydrophobic surface with contact angle higher than 160°. They melted isotactic polypropylene (i-PP) between two glass slides at 200°C with subsequent crystallization at 100°C. Then they removed one of the glass slides and obtained a smooth surface and carefully controlled the solvent and the temperature during the drying process. Finally, the glass plate was coated with polypropylene which has a distinct microstructure, as shown in Figure 2.24.

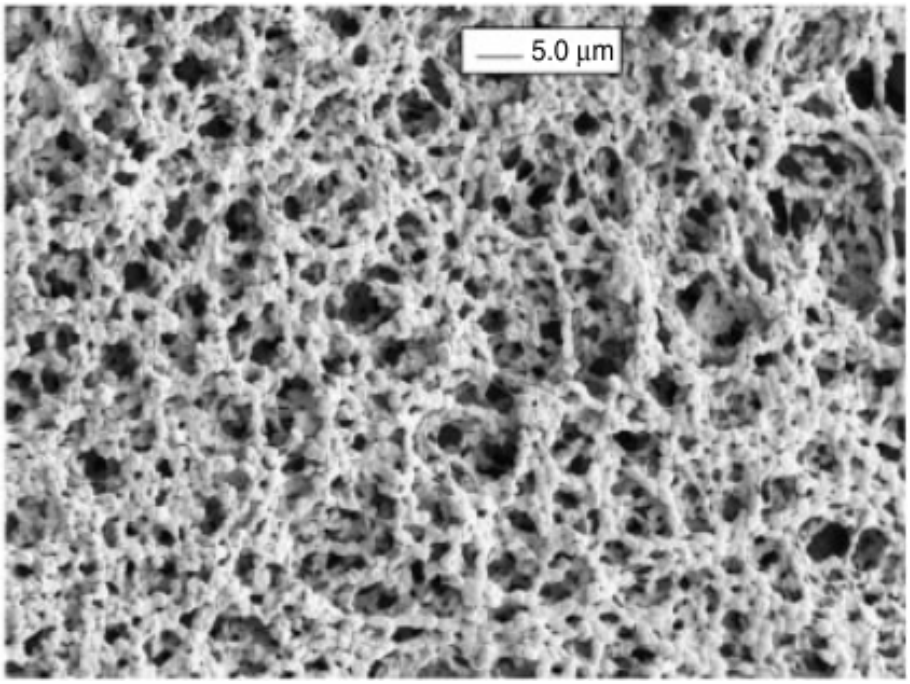

Figure 2.24. SEM image of glass slide coated with polypropylene. Taken from Erbil et al. (2003).

Zheng, et al. (2005) used Electrostatic Self-Assembly with layer-by-layer (LBL) deposition to create a superhydrophobic surface with contact angle about 140°. 0.5 mL of ZrO_2 colloid dispersion (20 wt%) was dropped into a poly (acrylic acid) (PAA) solution with a concentration of 0.07mol/L (with respect to monomer units). The PAA could adsorb for 20 min with periodic stirring. Prior to the first deposition of PAA-coated ZrO_2, five bilayers of allylaminehydrochloride (PAH) and PAA ($(PAH/PAA)_5$) were deposited onto the cleaned Si wafer to prepare the dense first ZrO_2 layer. The substrate was then dipped into PAA-coated ZrO_2 colloid solution for another 5 min and rinsed three times with ultrapure water. Then, 1.5 bilayers of silica nanoparticles/PAH were deposited on the (PAH/PAA-coated $ZrO_2)_n$ films. Then the sample was cleaned and dried, the final surface can be seen in Figure 2.25 below.

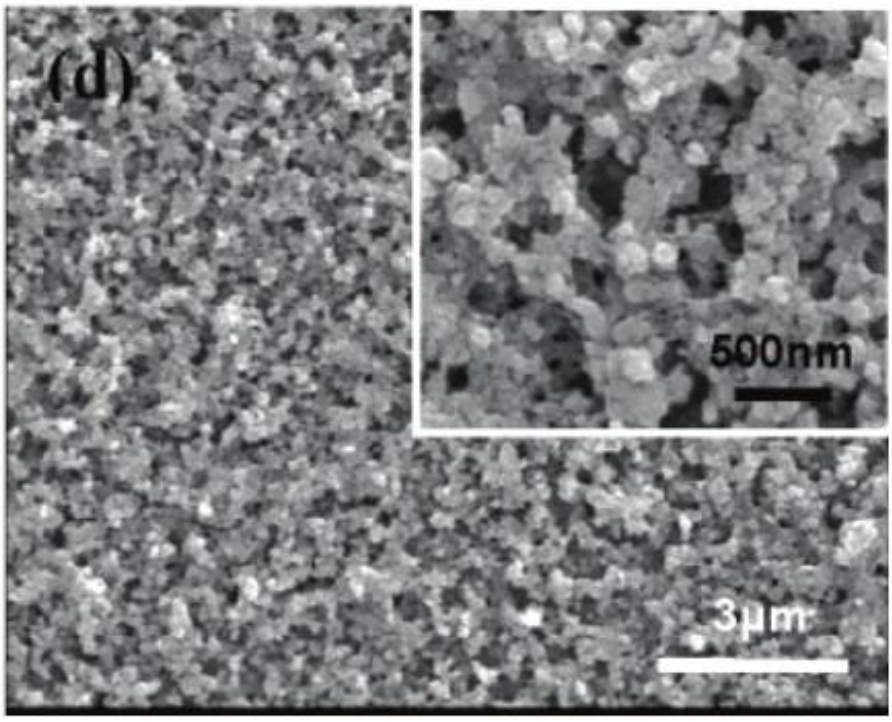

Figure 2.25. Self-Assembly with layer-by-layer (LBL) deposition surface. Taken from Zheng, et al. (2005).

Yabu & Shimomura (2005) used micro-phase separation of fluorinated block method to create a polymer superhydrophobic film. Their copolymer having equimolar amounts of fluorinated acrylate and methyl methacrylate monomers (molecular weight: 39 000 Da, Temperature of gas: 50.1°C), dissolved in a fluorinated solvent (AK-225, a mixture of $CF_3CF_2CHCl_2$/$CClF_2CHClF$, Asahi Glass Co., Japan). The fluorinated glass substrate was fixed to a moving substrate holder, which was smoothly controlled by a computer-driven system. A metal blade was fixed perpendicular to the substrate, and the gap between the blade edge and the substrate was adjusted to about 100 μm. Fifty microliters of the fluorinated copolymer solution was cast on the substrate, and the substrate was moved in a straight line at 2 mm/s. The fluorinated copolymer solution was supplied to the gap between the blade and substrate. Then, humid air (relative humidity ~ 60% at room temperature) was applied to the solution surface with a flow

rate of 10 L/min. After the water drop evaporated, honeycomb-patterns were observed on the surface. The pore size of the surface ranged from about 20 to 200 nm, and the contact angle is about 160°, as shown in Figure 2.26. The surface structure is very well arranged and the cost of this method is believed to be lower than either etching or lithography methods.

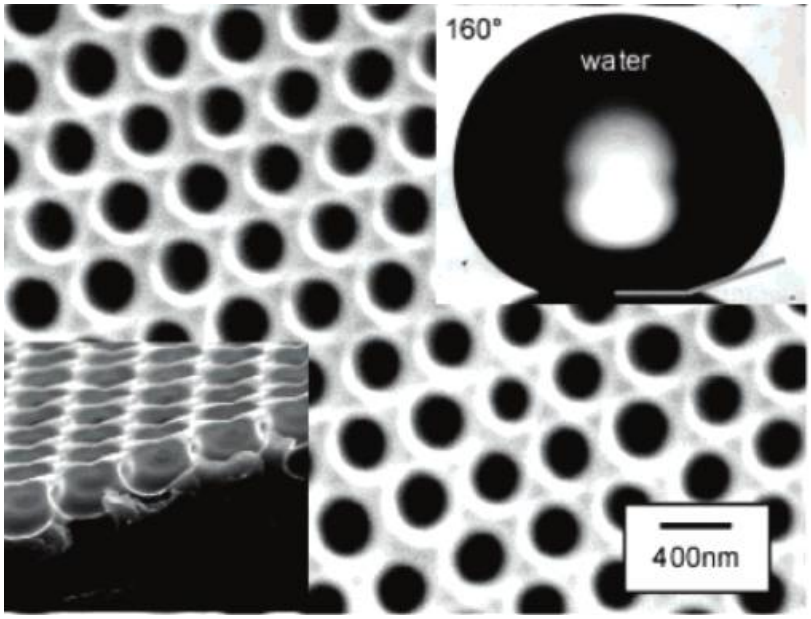

Figure 2.26. SEM image of honeycomb-patterned surface, and image of static contact angle (inset). Taken from Yabu & Shimomura (2005).

Gao and McCarthy (2006) provided a method to create superhydrophobicity with contact angle nearly 180°. They controlled composition mixtures of Me_nSiCl_{4-n} (n = 0-3) to try to reproduce surfaces. Silicon wafers were simply submerged in toluene solutions of $MeSiCl_3$ at room temperature, rinsed with toluene, ethanol, and water, and dried. Vessels were closed to the air during reaction but exposed (RH = 40-65%) during solution and sample introduction. A SEM image of this surface is shown in Figure 2.27 below.

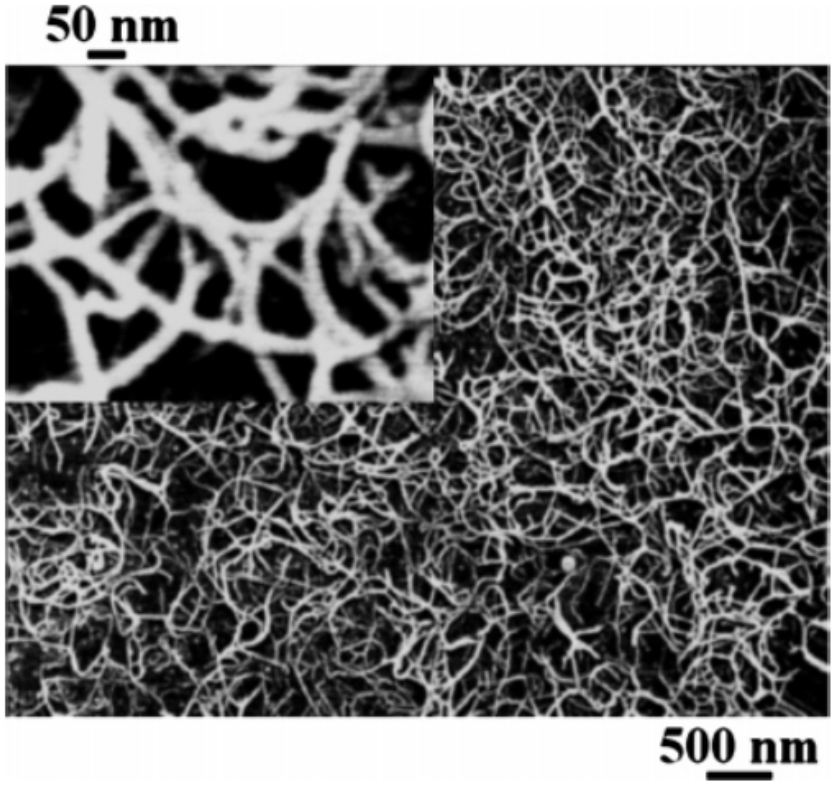

Figure 2.27. SEM images of a so-called “Lichao’s Surface”. Taken from Gao and McCarthy (2006).

A polymer spray is a popular and commercially used method to create superhydrophobicity due to the low cost and the possibility to cover sufficiently large surface areas. Choosing a low energy free material, polyimide or polytetrafluoroethylene, for example, and taking advantage of the spraying process to form micro/nano-scale structure on surface can achieve high contact angles. Guo et al. (2015) used a facile casting method to coat polyimide and polytetrafluoroethylene composite onto a glass surface. The composite coating was prepared by using ultrasound to disperse polyimide in anhydrous alcohol, then added to a polytetrafluoroethylene dispersion with controlled concentration. The water contact angle on the composite is larger than 150°. However, the water drops pin tightly on the surface. The SEM images are shown in Figure 2.28 (a), suggests that the composite

formed lotus-leaf-like structure but the top of papillae were not covered by the nano-scale polytetrafluoroethylene fibers. Srinivasan et al. (2011) used spraying of poly (methyl methacrylate) to create superhydrophobic surface, as see in Figure 2.28 (b). Different solution concentration and molecular weight of dissolved polymer are studied. The water drop contact angle can reach as high as 155°, and contact angle hysteresis is as low as 1°.

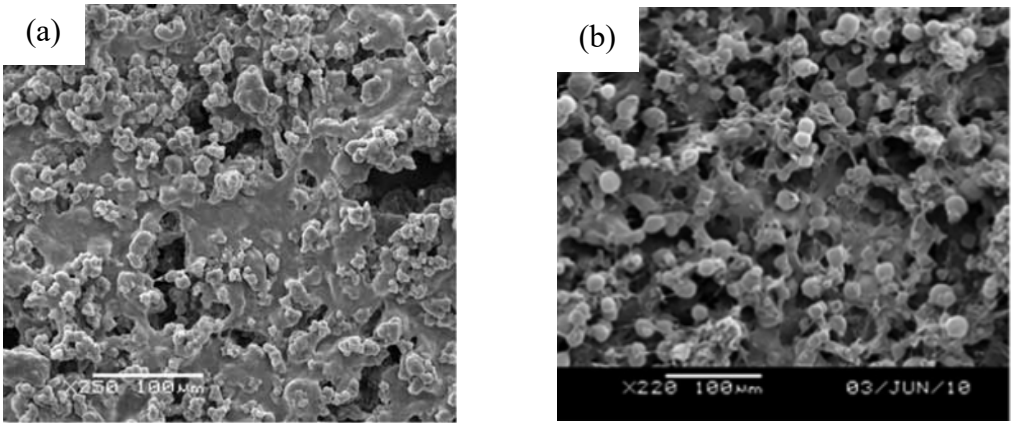

Figure 2.28. SEM images of superhydrophobic surface manufactured using polymer spray, (a) Guo et al. (2015), (b) Srinivasan et al. (2011).

Polymer process methods use chemical or physical procedures to control the polymer to form a micro scale structure, they can manufacture large scale surfaces in a relatively inexpensive way. They already have a few commercial products provided, i.e., superhydrophobic spray and superhydrophobic coating on footwear, clothes and other devices such as mobile phone. The problem they still need to overcome is the surfaces are not robust enough. Mechanical abrasion, chemical corrosion and even light could damage the surface in a very short time.

2.2.7 Discussion

Most of the methods introduced above are not economically viable for large surfaces and are presently only used for research purposes to cover very small areas. To

determine a method to fabricate a superhydrophobic surface in an easy and economical manner is the first step of this thesis. From previous studies and as suggested by Professor Jonathan Rothstein (Private communication) from University of Massachusetts Amherst, "Teflon" (Polytetrafluoroethylene, PTFE) is a material which has one of the lowest coefficients of friction against any solid, and good flexibility to follow any surface curvature. A very fine stainless steel mesh, the diameter of the mesh wire being tens of microns, was used to emboss the Teflon sheet as a model with suitable pressure at 315°C. This temperature is close to the melting point of Teflon (327°C), a regular micro-structure on the Teflon sheet is expected after this process, the details of this process will be discussed in Chapter 3.

2.3 Flow drag reduction of superhydrophobic surfaces

With the development of science and engineering, superhydrophobic surfaces are moving towards to real-world applications such as self-cleaning and anti-icing surfaces, bacterial resistance, drag reduction, and enhanced heat transfer, (Tian et al. (2016)). One of the most attractive applications is for drag reduction which has the potential to save enormous cost in industry, the development of this application will be introduced in this section both theoretically and experimentally.

2.3.1 Slip boundary condition and superhydrophobicity

The so-called no-slip boundary condition is accepted almost universally in fluid dynamics. But in some cases, a 'slip' has been observed in experiments: Watanabe et al. (1999), Barrat and Bocquet (1999), Lum et al. (1999), Tretheway and Meinhart (2004), Gogte et al. (2005), Lee et al. (2008), Daniello et al. (2009) and Srinivasan et al. (2013). An engineer can take advantage of such slip to reduce the drag, the force required to move an object through a fluid or move a fluid past a device, to save energy,

time and money. Navier (1823) firstly proposed the concept of the slip boundary condition which is shown in Figure 2.29 below. In a laminar Couette flow, the slip-length *b* was defined by equation 2.4 as:

$$u_0 = b\left|\frac{du}{dy}\right| \qquad 2.4$$

where *b* is the slip-length, u_0 is the slip velocity which means the fluid velocity on the surface, and $\left|\frac{du}{dy}\right|$ is the magnitude of the shear rate.

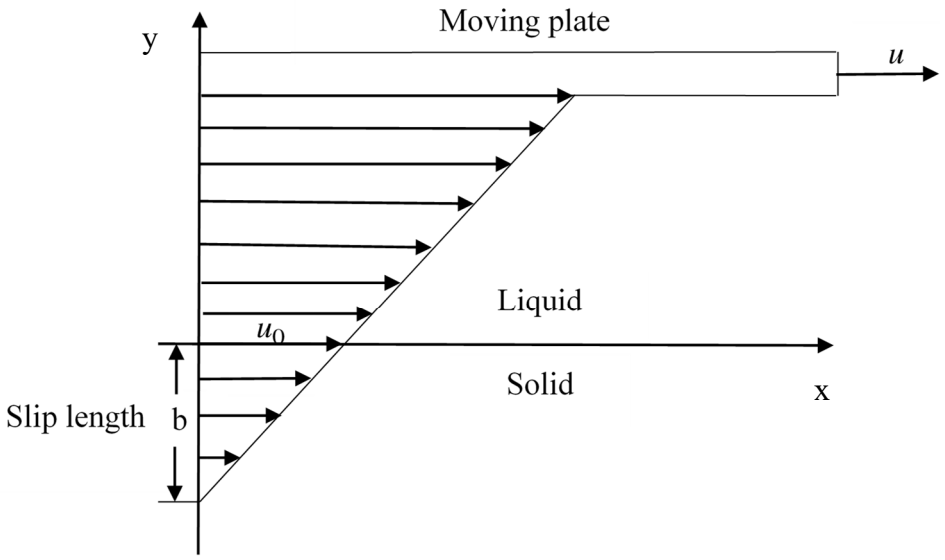

Figure 2.29. A schematic diagram of the slip-length concept.

Navier's calculation estimated the slip-length is on the order of the mean free path of liquid molecules. Thus, for almost all kind of macroscopic flows, the slip-length is so small, being on the order of 1nm, that slip effects can be neglected and the no-slip condition can be considered as accurate (Lee et al. (2016)).

In recent decades, some studies found superhydrophobic surface can produce a considerable slip to reduce the drag in both laminar and turbulent flow with increasing Reynolds number. As introduced in Section 2.1.1, superhydrophobicity was originally inspired by the water repellent natural leaves like lotus and rice leaves, where the contact angle, measured through the liquid-solid interface, of water on the surface is higher than 150° (Neinhuis and Barthlott (1997)). Thompson and Troian (1997) did a molecular simulation, which firstly showed that hydrophobicity can produce a slip-length larger than the mean free path. Their result showed that the slip-length became nonlinear with increasing shear rate and independent of the shear rate after a critical point. The critical shear rate decreased with a decrease of the surface energy. This result connected hydrophobicity to the slip-length concept. Barrat and Bocquet (1999), showed that the slip-length became constant and independent of the shear rate when the fluid-surface contact angle is higher than 140°, and the slip-length is larger than 40 molecular diameters.

From the studies which related the slip to the superhydrophobicity, a basic explanation of why superhydrophobicity can lead to slip is the micro or nano-structure on the surface. This feature can maintain air or water vapor to create a gas-liquid interface, the friction of this interface is significantly lower than a solid-liquid interface giving rise to an apparent slip. Tretheway and Meinhart (2004) examined the possible mechanism for the measured fluid slip, for water flowing over a hydrophobic surface. They extended the work of Lum et al. (1999), who suggest slip develops from a depleted water region or vapor layer near a hydrophobic surface, as shown in Figure 2.30. By modelling the presence of either a depleted water layer or nanobubbles as an effective air gap at the wall, they calculated slip-lengths for flow between two infinite parallel plates. The calculated slip-lengths are consistent with experimental values when the gas layer is

modelled as a continuum and significantly higher when rarefied gas conditions are assumed. Their results suggest that the apparent fluid slip observed experimentally at hydrophobic surfaces may arise from either the presence of nanobubbles or a layer of low viscosity fluid at the surface.

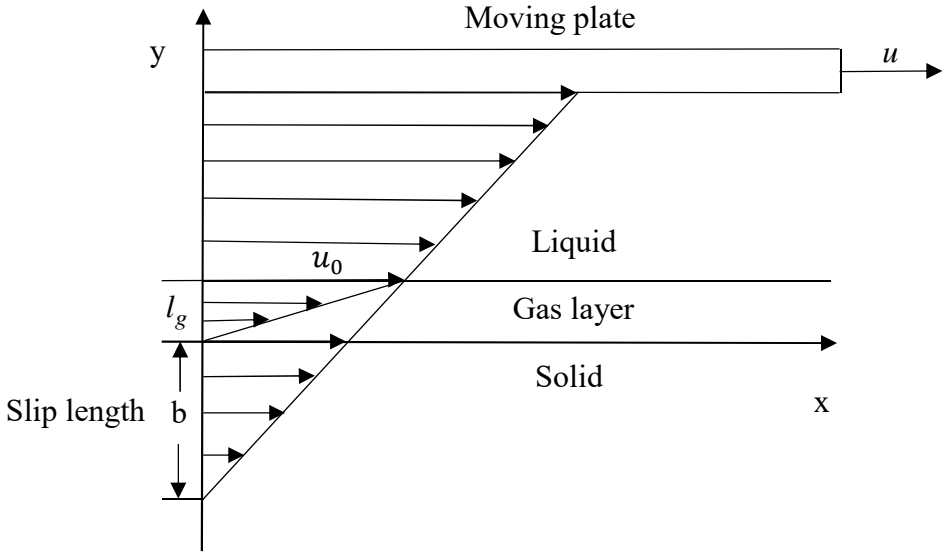

Figure 2.30. A schematic diagram of the slip-length from a gas layer.

The shear stress on the interface of liquid and gas is:

$$\tau_i = \mu_g \frac{u_0}{l_g} = \mu_l \frac{u_0}{b + l_g} \qquad 2.5$$

where τ_i and u_0 are the shear stress and the velocity of the liquid gas interface respectively. μ_g and μ_l are the viscosities of gas and liquid respectively. l_g is the thickness of the gas layer. Simplifying equation 2.5 above, the slip-length b is:

$$b = l_g \left(\frac{\mu_l}{\mu_g} - 1 \right). \qquad 2.6$$

The details of equation 2.6 can be seen in Vinogradova (1999). Realistically, it is difficult to maintain an ideal gas layer between the liquid and solid surface. The gas is trapped in the surface structure of superhydrophobic surface and the mass flow rate in the gas layer is zero. Therefore, the apparent slip-length is smaller than the value from equation 2.6, then has a limit in Couette flow and pressure driven pipe flow. The analytic results of the apparent slip length and optimum gas layer thickness were delivered by Busse et al. (2013). In this case, the slip-length could be determined by an analogous equation to equation 2.6, but the viscosity of liquid (μ_l) is divided by four ($b = l_g\left(\frac{\mu_l}{4\mu_g} - 1\right)$).

The slip-length was observed and measured by many studies experimentally. Ou et al. (2004) and Ou & Rothstein (2005) observed drag reduction on superhydrophobic surfaces by using direct velocity measurement, microparticle image velocimetry (μ-PIV). They did a series of experiments on water flowing past two kinds of superhydrophobic surfaces. These surfaces were created by photolithography and wet-etched silicon dioxide wafer which have a posts or ridges structure. The channel was 50mm long, 2.54 mm wide and had a 127 μm height cross section. They showed the drag reduction increased with the shear-free area ratio and up to a maximum of about 40% in laminar flow.

Choi and Kim (2006) studied a nanoengineered superhydrophobic surface and observed a slip-length of 20 μm for water and 50 μm for 30 wt% glycerine (its viscosity is around 2.5 mPa·s). Their surfaces were fabricated by a black silicon method on silicon wafer and spin coated by Teflon. The surface had a 1~2 μm height and 0.5~1 μm spacing needle-like structure. The contact angle of water-surface was measured as over 175°.

Their drag reduction experiments were undertaken on a rheometer which can measure a very small torque.

Choi et al. (2006) observed a slip-length for water of 100-200nm in the well-engineered "grates-like" (a series of parallelly-arranged bars) surface structure. The surface was fabricated by interference lithography and the grates were ~230nm pitch and 500nm deep. The contact angles of water-surface were measured as 145 to 150°. Their results shown a 20%~30% drag reduction in a 3 μm high channel-flow.

Daniello et al. (2013) investigated how the vortex shedding and separation on flow past superhydrophobic cylinders was modified. The cylinders were coated by sanded Teflon which was reported in Song et al. (2014). This simple method can provide a superhydrophobicity with contact angle of ~150°. A maximum slip-length for water observed on this surface was 20 μm. From their cylinder experiment results, the superhydrophobic surfaces increased the length and width of the recirculation region in the wake and decreased the lift coefficient by 15% to 20%.

These studies proved that superhydrophobic surfaces can provide a considerable slip-length which has a huge potential for drag reduction in the industrial applications. However, most of these studies were only implemented in the laboratory and need a lot of work before real-world applications which are economically viable.

2.3.2 Surface structure and slip-length

Gregory D. Bixler (2013) and Gregory D. Bixler and Bhushan (2013), (2013a), (2013b) studied shark-skin inspired microstructured surfaces on fluid drag reduction. They studied different geometries and configurations of the surface structures: "blade", "sawtooth" and "scalloped" which are shown in Figure 2.31 below. Their results optimized the microstructure design for the drag reduction and provide a new

explanation of the drag-reduction phenomenon in turbulent flow: the riblet structure can lift the streamwise vortex to reduce the collision, shown in Figure 2.32. For the "blade" geometry and "continuous" configuration, the optimal and scalable drag reducing riblets requires the design principles as low h, t_b/s, t_b, and vw; with $h/s = 0.5$, $s^+ \approx 15$, $H > 150$ wall units. Here h is the height of blade, s is the space between two blades, t_b is the thickness of a blade, vw is valley width, and $s^+ = \frac{sV_\tau}{v}$, is the non-dimensional spacing using the friction velocity $V_\tau (= \sqrt{\tau_w/\rho})$ and kinematic viscosity v the geometries are shown in Figure 2.31.

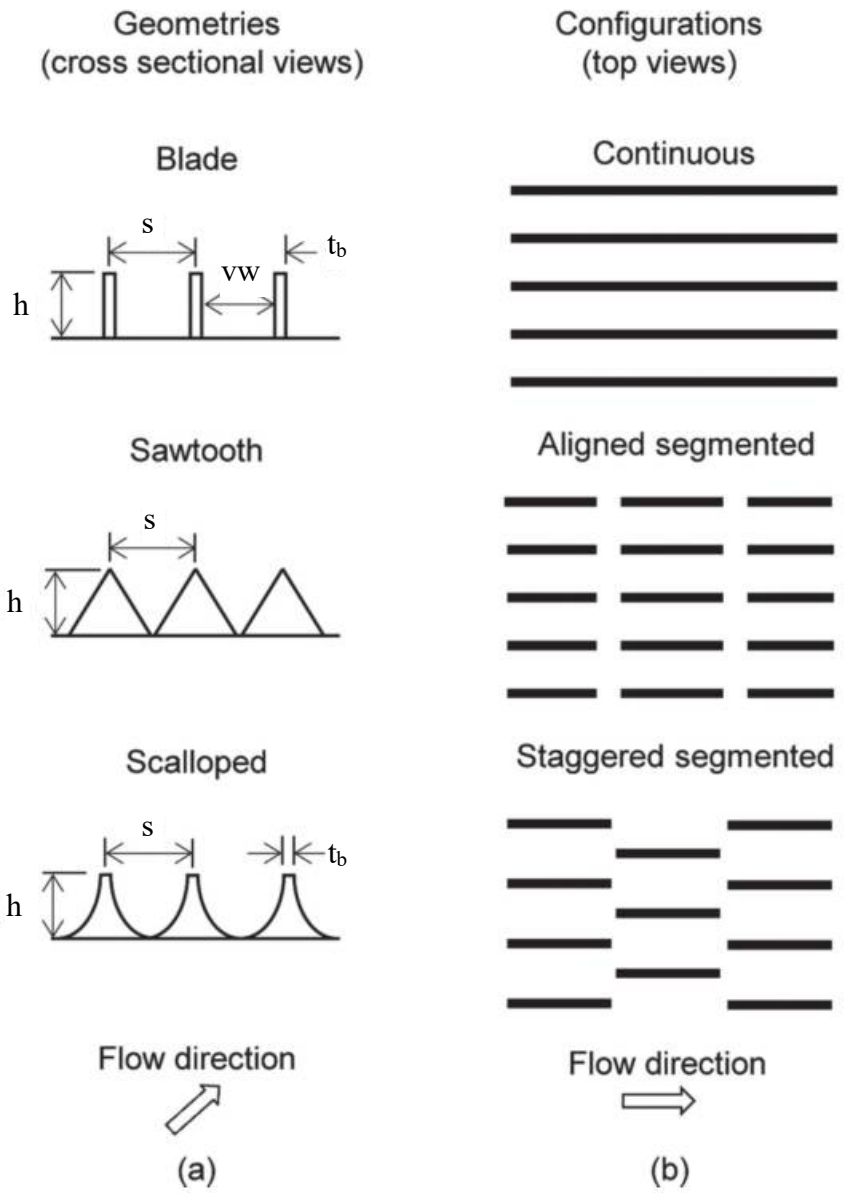

Figure 2.31. Surface geomeries and configurations, Bixler & Bhushan (2013).

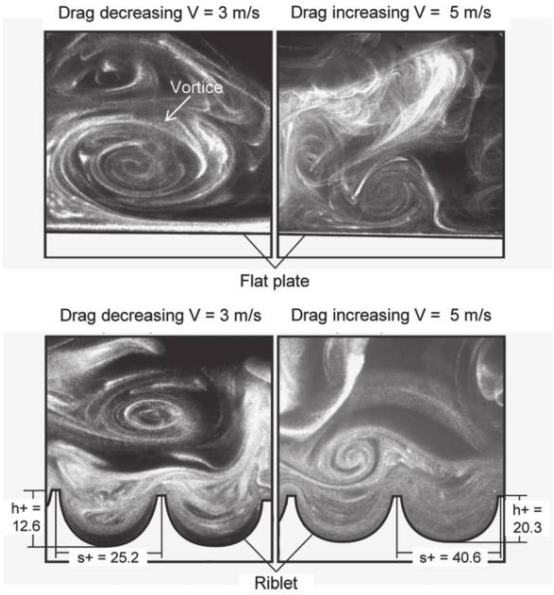

Figure 2.32. Visualized flow over riblets surface image by atomized oil burned in air, taken from Bixler & Bhushan (2013).

Lee et al. (2008) experimentally studied how the surface structure may affect slip-length. As introduced in Section 2.1, for a superhydrophobic surface to produce a large slip in practice requires that the surface maintains a dewetted Cassie-Baxter state. Firstly, Lee et al. (2008) proposed a maximum applied hydraulic pressure for a stable Cassie-Baxter state based on a force balance between surface tension and pressure across the interface. For a post surface structure:

$$P_l f_g \leq -4\sigma(1-f_g)\cos\theta / D \qquad 2.7$$

where P_l is the liquid pressure over a gas, f_g is the gas fraction, σ is the surface tension, θ is the contact angle of a liquid on a flat surface, and D is the diameter of the top of a post. For a grates surface structure:

$$P_l f_g \leq -2\sigma\cos\theta / s \qquad 2.8$$

where s is the space between grates. Using equation 2.7 and 2.8 for water under room temperature conditions, and assuming the material of the surface is PTFE which has a static water contact angle around 110°, they calculated the maximum applied pressure for the Cassie-Baxter superhydrophobic surfaces for different geometry and gas fraction, shown in Figure 2.33.

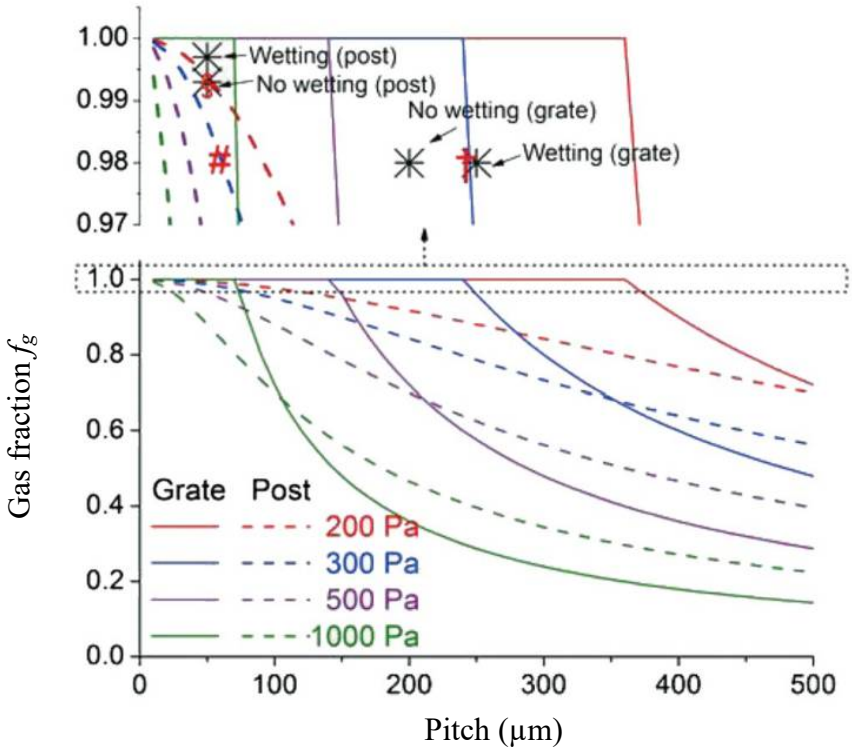

Figure 2.33. Maximum gas fraction for a stable Cassie-Baxter state surface condition for posts (dashed lines) and grates (solid lines), taken from Lee et al. (2008).

Well-regulated superhydrophobic surfaces were fabricated on silicon wafer by a photolithography method and coated with Teflon. The surfaces have fixed 50 μm pitch but varying gas fractions from 50% to 99.5% for a grates structure, and 50% to 98% for posts structure. The experimental results from Lee et al. (2008) agreed with the theoretical prediction, as shown in Figure 2.34, which describes the slip-length for both

"posts" and "grates" structures in equation 2.9 (Ybert et al. (2007)), and equation 2.10 (Lauga and Stone (2003)) respectively.

$$b \sim s \Big/ \sqrt{1-f_g} \qquad 2.9$$

$$b \sim s \log \sqrt{1-f_g} \qquad 2.10$$

In summary, Lee et al. (2008) verified that the slip-length on a structured surface increases exponentially with gas fraction and linearly with pitch. The data also approached the theoretical thermodynamic limits for a dewetting surface condition and demonstrated that theoretically large slip of up to 185 μm are possible.

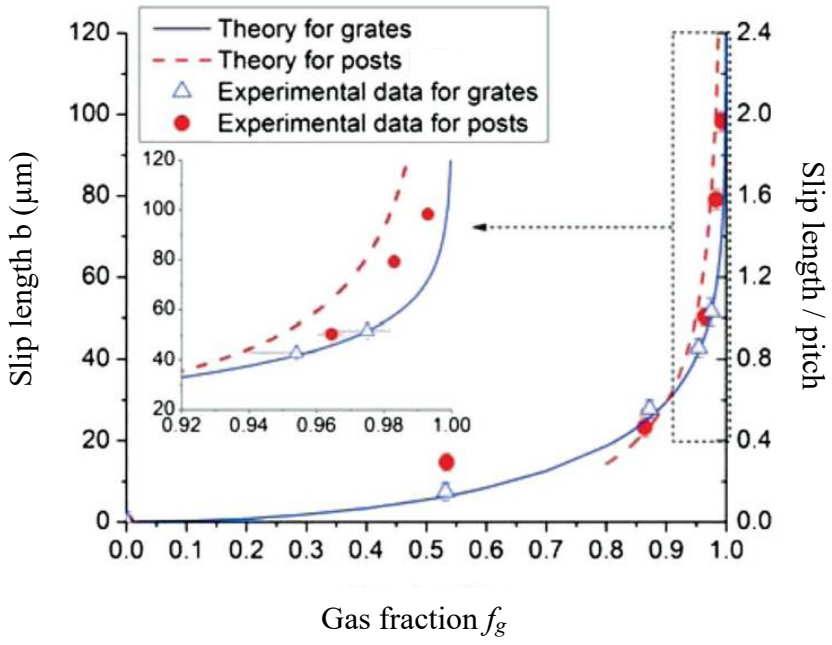

Figure 2.34. The effect of gas fraction on the slip-length with the pitch fixed at 50 μm, taken from Lee et al. (2008).

Following the original study discussed above, Lee et al. (2016) reviewed the experimental and numerical development in recent decades regarding drag reduction of superhydrophobic surfaces. Firstly, they suggested the apparent contact angle is the

most commonly used property to characterize superhydrophobicity, but this alone cannot be used to quantify the slip as a large apparent contact angle does not always mean large slip-length.

Secondly, they summarized tens of studies to plot the relationship between the surface structure and the slip-length, for both regular surface structures, shown in Figure 2.35 and Figure 2.36, and random surface structures, shown in Figure 2.37.

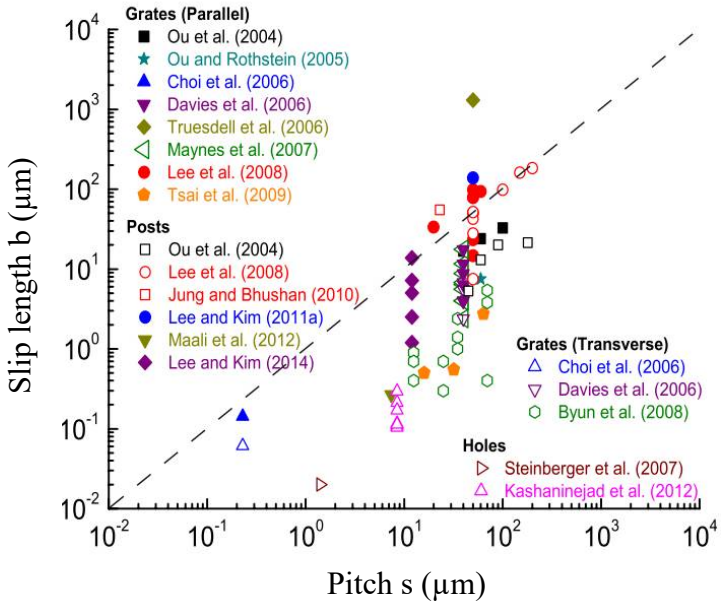

Figure 2.35. Measured slip-lengths on superhydrophobic surfaces with simple regular patterns. Slip-length as a function of the structural pitch. The broken line indicates the general trend of slip-length ~ pitch, taken from Lee et al. (2016).

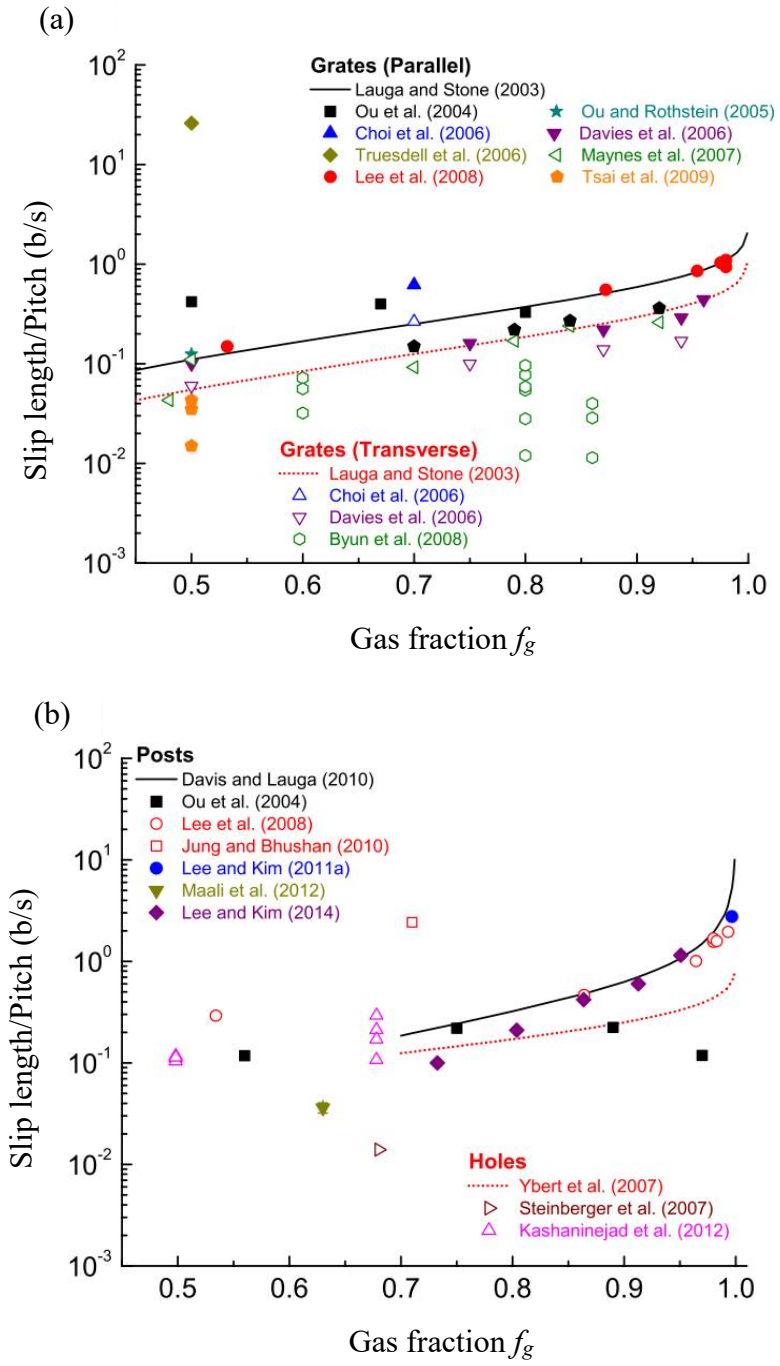

Figure 2.36. Measured slip-lengths on superhydrophobic surfaces with simple regular patterns. Non-dimensionalized slip-length (b/s) as a function of gas fraction fg. Lines represent the theoretical predictions (Eqation 2.10). (a) Slip-lengths on grates parallel and transverse to the liquid flow. (b) Slip-lengths on posts and holes, taken from Lee et al. (2016).

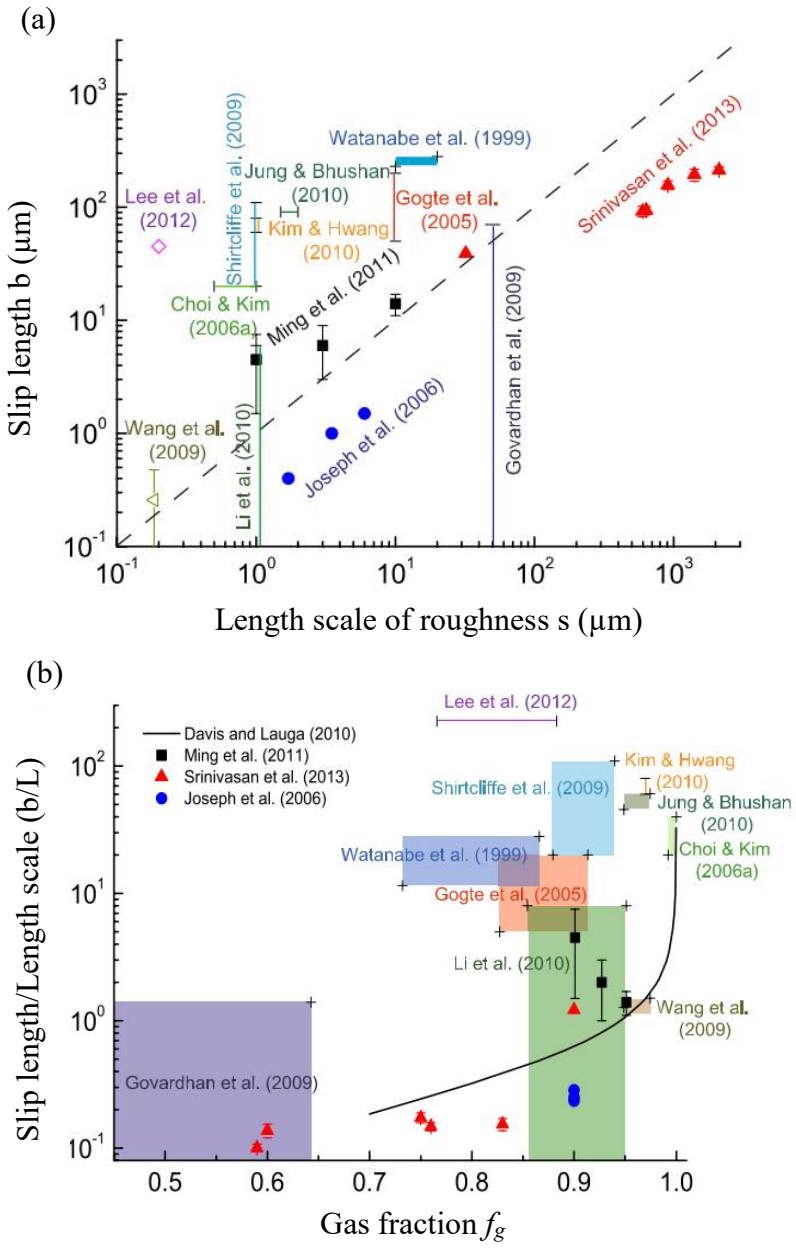

Figure 2.37. Estimated or measured slip-lengths on superhydrophobic surfaces with random surface structures. (a) Slip-length as a function of the length scale of roughness (s). The broken line indicates the general trend of slip-length ~ roughness scale. (b) Non-dimensionalized slip-length (b/s) as a function of gas fraction f_g. The black solid line shows the theoretical prediction for posts, taken from Lee et al. (2016).

From Figure 2.34, Figure 2.35 and Figure 2.36, with regular arrays of posts, most of the experimental data on patterned surfaces showed a qualitative agreement with the theoretical prediction, but the measured slip-lengths were often quantitatively lower.

Only at large gas fraction (f_g >0.9) does the slip-length become comparable to the surface structure pitch s, $b/s \sim 1$. Data for random structures highlights lots of data as being high way above the reference line $b = s$ (Figure 2.37) or the predicted slip-length for posts. Lee et al. (2016) summarized the reasons for the differences between these theoretical and experimental results.

2.4 Resilience of superhydrophobic surfaces

As introduced previously, there are many potential fields and industrial applications for superhydrophobic surfaces, e.g., marine engineering (Lee et al. (2016)). However, no significant commercial success has been reported yet. There are a few reasons which may be preventing the commercial success of superhydrophobic surfaces; (1) the manufacturing methods are too expensive for large scale surfaces. For example, the photolithography method needs expensive equipment and only centimeter scale surfaces can be produced by this method with a reasonable cost. (2) Another reason is that the trapped air could be expelled or the surface structures destroyed easily in practical conditions. The surface structures have to be at micro or nano-scale, and made from low surface free energy material, most of which are polymers which are not mechanically robust (Landel and Nielsen (1993)). Hence, there is an unavoidable natural contradiction for the superhydrophobic surface: the finer the surface structure is, the more hydrophobic but also frailer the surface is. These surface structures are highly susceptible to mechanical wear, chemical corrosion or even light, (Tian et al. (2016)). Identifying the resilience of superhydrophobic surfaces needs standardized methods and is important for applications outside of the laboratory.

Mechanical wear is considered the main reason for the degradation of superhydrophobic surfaces in realistic environments (Milionis et al. (2016)). Many

methods have been used to simulate mechanical wear and test the durability, or resilience, of superhydrophobic surfaces, including linear abrasion, circular abrasion, tape peeling, blade scratching, sand abrasion, ball on-disk sliding, oscillating steel ball, and water jet tests (Wang et al. (2011), Verho et al. (2011), Deng et al. (2012) and Milionis et al. (2016)).

Rubbing between two solid surfaces is an ordinary condition for a superhydrophobic surface in an industrial application. Using a solid surface and controlled abrasion stress to model this condition is a standardized method for the resilience test. In this method, the wear starts from one point on a superhydrophobic surface and moves parallel to another with a force normal to the surface. This tangential abrasion method is reported for many kinds of experimental set-ups including different abradant materials, for example: rough sandpapers of different grades, aluminium surfaces, A4 paper sheets, PDMS surfaces, glass surfaces, brushes, wipes, etc. All of these mechanical abrasions remove some material from the superhydrophobic surfaces and eventually lead to alteration of the surface structure and loss of the hydrophobicity. The simplest and widely accepted quantitative method is the linear abrasion test which uses a surface to move back and forth over the same line of contact, a typical setup is shown in Figure 2.38.

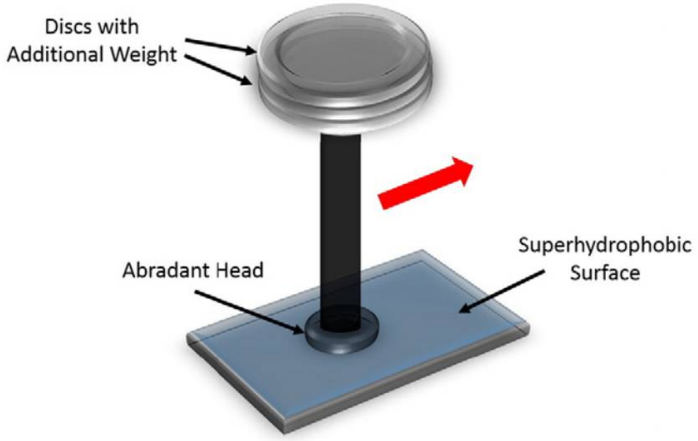

Figure 2.38. Typical linear abrasion setup, taken from Milionis et al. (2016).

Wu et al. (2014), prepared superhydrophobic polyester textiles by a dip-coating fluoropolymer (FPs) method (samples are referred to as FPs 1# ~ 4#, with slightly different preparation methods) and tested their resilience by using A4 paper sheets and very fine sandpaper (2000 grit) with a 5 kPa abrasion stress. Due to the macroscopical roughness of their surface, which is made of sponge and textiles, it is difficult to investigate the full drop profile for static contact angle measurement. Consequently, water shedding angle (WSA) was measured after a number of abrasion cycles. (The WSA measurement uses a certain volume of drop which falls down from a certain height to hit an inclined surface. The maximum inclination angle for the drop would not completely roll down from the surface is the water shedding angle.) From their test, the WSA increased with an increase of the number of abrasion cycles, and the surface was partially damaged by abrasion via sandpaper, as shown in Figure 2.39 and Figure 2.40. The WSA of one sample (FPs 4#) coated polyester textiles is still below 11° after 100 abrasion cycles and is obviously lower than the others. This result indicates that the micro and nano-scale surface structures are not essential but helpful in the resilience of superhydrophobicity.

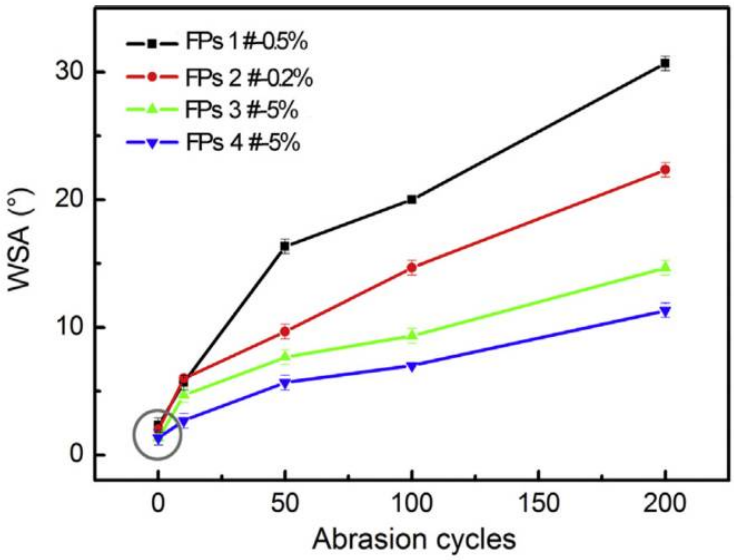

Figure 2.39. WSA changes depending on abrasion cycles using A4 paper as the abrasion partner, taken from Wu et al. (2014).

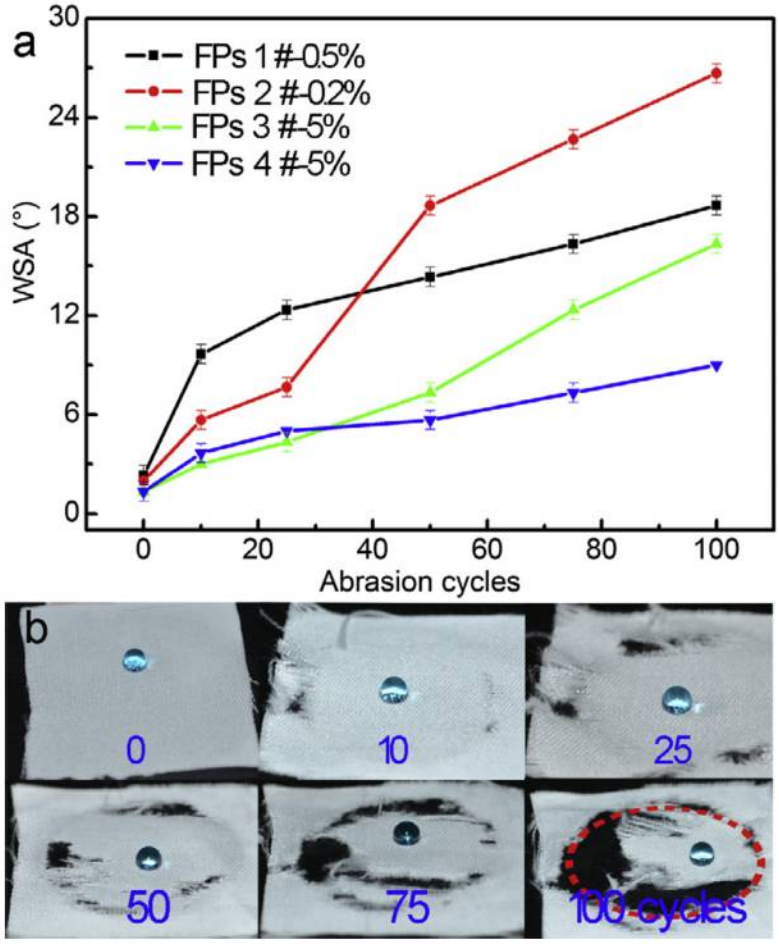

Figure 2.40. (a) WSA changes depending on abrasion cycles using sandpaper (2000 meshes) as the abrasion partner. (b) Digital images of water drops on the FPs 4# coated fabrics after different abrasion cycles against sandpaper, taken from Wu et al. (2014).

The circular abrasion method has the same concept as the linear abrasion, and uses similar experimental apparatus. The only difference is that the type of movement of the abradant surface. Compared to the linear abrasion, the setup is easier but the disadvantage of the circular abrasion is the abradant surface moves with different speed at different radii. Kondrashov and Rühe (2014) manufactured a number of superhydrophobic surfaces by using a Deep Reactive Ion Etching (DRIE) process on silicon wafers. Then circular abrasion tests were performed by a rheometer with 2cm

diameter metal disk. The disk contacted on the surface and rotated at a speed of 10 rpm for 30s, and different forces were applied from 1 to 20N. The abrasion changed the density of the surface structure and some breaking of the micro and nano cones on the surface was observed. The results and experimental schematic are shown in Figure 2.41 below.

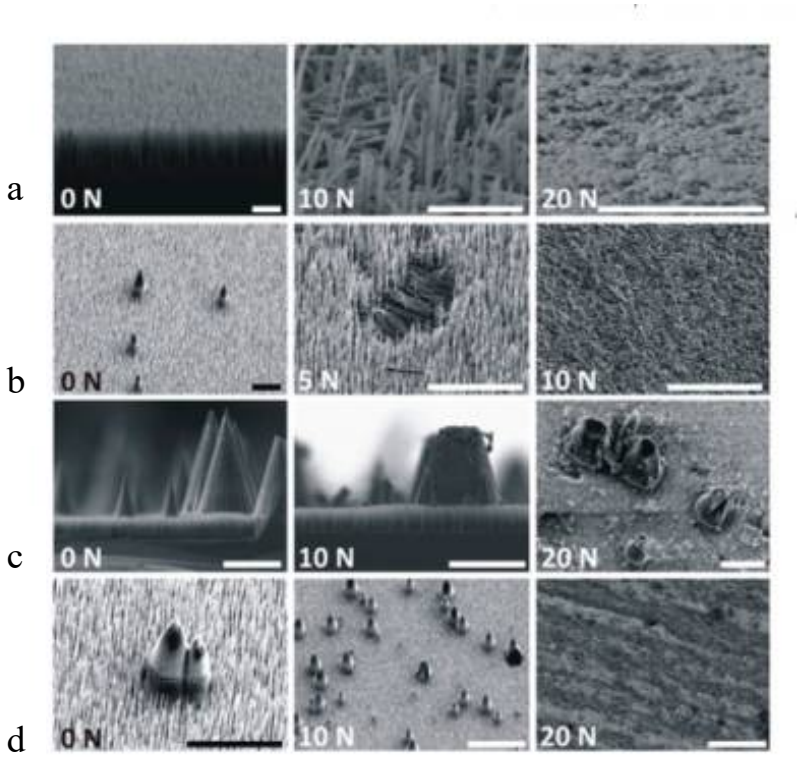

Figure 2.41. SEM images of various superhydrophobic surfaces before and after performing the circular abrasion with forces given in figure (a) nano-grass surface, (b, c, d) microcone and nano-grass combinations. Scale bar: (a) 5 μm, (b–d) 20 μm, taken from Milionis et al. (2016).

To investigate the consequences of contact with sharp objects (e.g. knives, pens, forks, etc.), a few studies used a blade/knife to test the resilience of superhydrophobic surfaces. These tests are practically similar to the linear abrasion test but rather than a flat abradant material a sharp blade is used instead. Wang et al. (2013) manufactured a few superhydrophobic surfaces by a 2-step dip-coating procedure. The superhydrophobic

samples were placed on a flat and smooth surface. A flat blade was mounted and the blade edge contacted the surface with a 0.8 kg load. Then the blade was dragged to move vertically on the surface with 100 drags of the blade being a “cycle”. The apparent contact angles were reported for the blade test. After one cycle, the apparent contact angle was slightly reduced to 150° for water, while for hexadecane was reduced to 120° and ethanol completely wetted the fabric. But remarkably, after heat treatment at 140°C for 30 min, the treated fabric recovered its extreme non-wetting properties for all liquids, as shown in Figure 2.42.

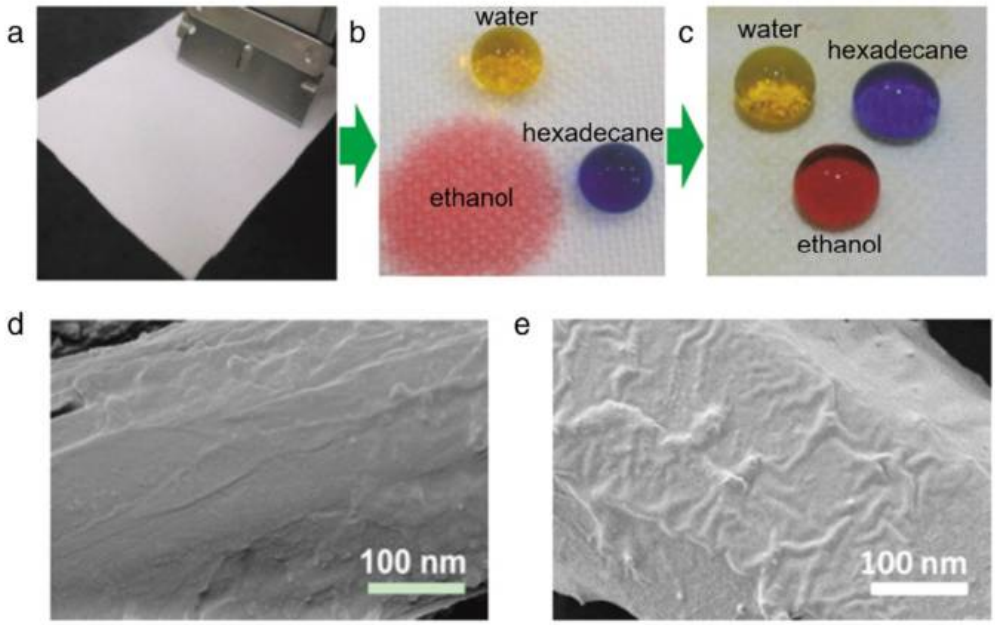

Figure 2.42. (a) The sharp blade test, (b, c) coloured water, hexadecane, and ethanol drops on the superhydrophobic surface (b) after the first blade scratching cycle (100 scratches) and (c) after blade scratching and heat treatment at 140°C. (d, e) SEM images of the coated fabric (d) after blade scratching (100 scratches) and (e) heat treatment, taken from Wang et al. (2013).

Another method to test the mechanical resilience is the oscillating steel ball method. Hensel et al. (2014) reported this test using a steel ball with a diameter of 1.5 mm which contacted with the sample surface and pressed down on the surface with a normal load.

The oscillation is generated laterally at a speed of 0.05 cm/s and a maximal displacement of 1 mm, and the normal load increased in a stepwise fashion until the surface features were damaged. As a result (shown in Figure 2.43), the mechanical resilience, which was able to deal with forces ranging from 1 to 75 mN depending on the pillar diameter, of the pillar structures surfaces was much lower compared to the membranes, which can resist 200 to 500 mN depending on the hexagonal structure wall width.

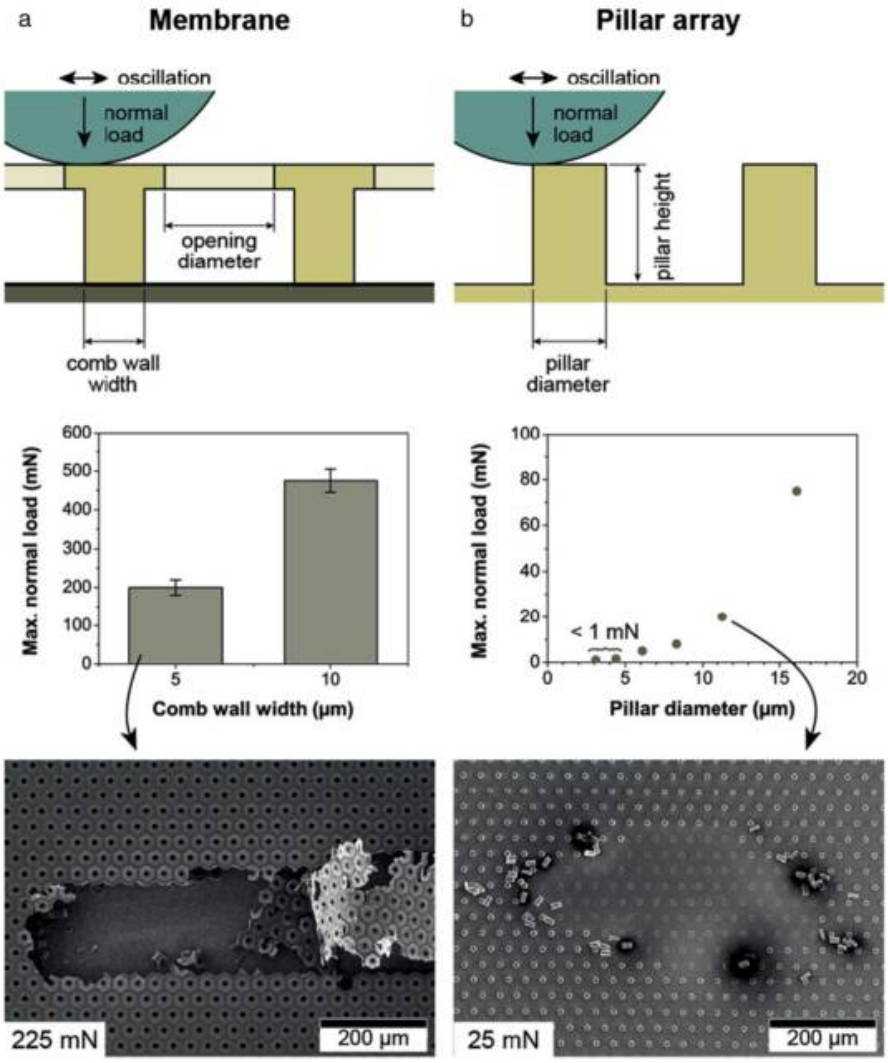

Figure 2.43. Oscillating steel ball tests on (a) polymer membranes in comparison to (b) pillar arrays: Schematic representation of the experimental setup consisting of an oscillating steel ball, pressed onto the structured surfaces. Experimental data on maximum normal loads the surfaces can resist without destruction and SEM images after failure, taken from Hensel et al. (2014).

Finally, a dynamic test method, the water-jet test, has also been used. In practical applications, e.g. non-wetting raincoat, a superhydrophobic surface commonly works in rainy weather. Such water-jet test can mimic an outdoor situation to examine the resilience of superhydrophobic surface from exposure to a realistic environment. In a heavy rain, the maximum diameter of a raindrop can be 4 to 5 mm, and the maximum speed can reach 7 to 9 m/s. The drop density on the ground with a frequency can be 3.88×10^5 drops/m^2 (Zhang et al. (2014)). Davis et al. (2014a and b) used a water-fed, spray setup to simulate a prolonged, high-impact rainy weather condition. The drops in the test have a traveling speed at 25 m/s with 1mm drop diameter. The pressure of the impacted droplets reached as high as 312 kPa. The testing samples were polyurethane/ fluoroacrylic/ organoclay superhydrophobic nanocomposites. The results are shown in Figure 2.44, and the apparent contact angle can remain higher than 140° after this harsh test. They also examined the impact from the inclination of the surface, and the samples retained slightly better hydrophobicity when they were tilted at a 40° inclination angle compared to vertical impact.

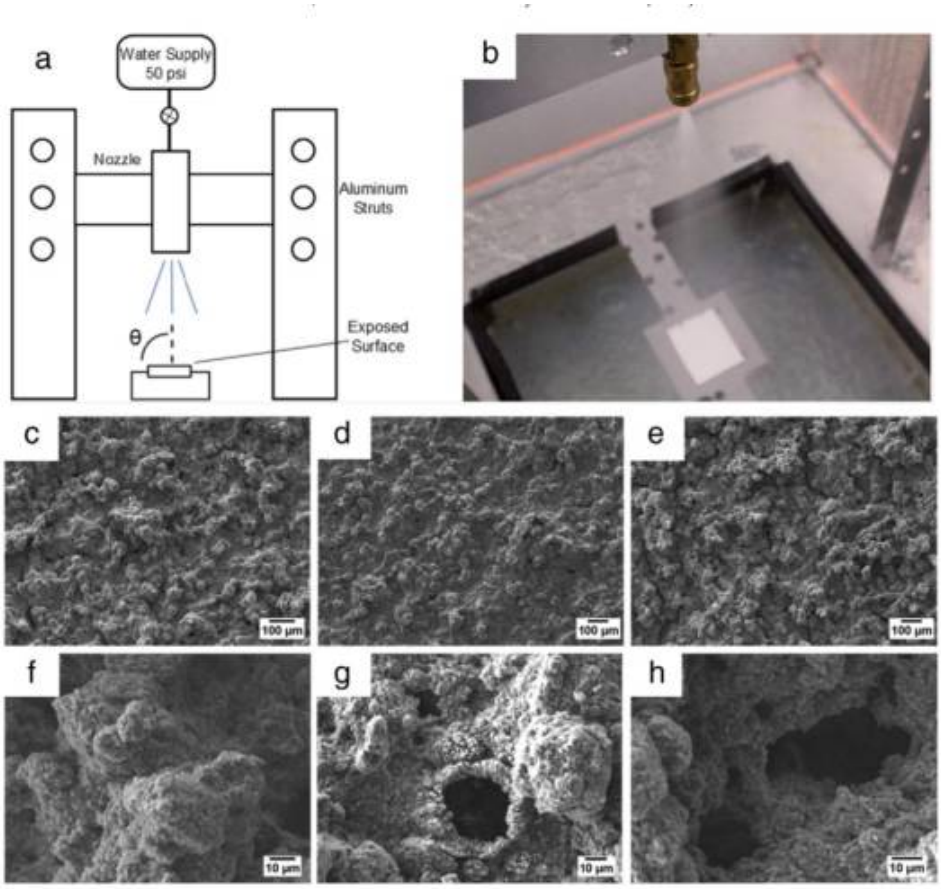

Figure 2.44. (a) Schematic and (b) photo of the spray impact setup used to investigate rain impact resistance of superhydrophobic surfaces. SEM images of surfaces (c) before exposure to rain- sized droplets, (d) after normal-impact exposure, and (e) after 40° exposure; (f–h) are higher magnification images, reproduced from Davis et al. (2014a)

In the last few years, increasingly robust superhydrophobic surfaces have been proposed and the viability of such surfaces in real-world applications is developed. With this development, the number of publications regarding the resilience tests are increased exponentially as well. In order to advance and help the development of the resilience of superhydrophobic surfaces, having standardized, simplified and prioritized evaluation methods is important. Linear abrasion is recommended as a well-accepted and straightforward method to evaluate the wear abrasion resistance. Moreover, a water

jet test is also recommended due to the advantage of simulating realistic outdoor weather conditions, Milionis et al. (2016). However, only few studies have carefully investigated wear by controlled fluid-imposed shear and this leaves a gap in the literature.

Chapter 3 Manufacture of a novel superhydrophobic surface

To find a method which is easy, inexpensive and can provide a "large" surface is a great challenge in the study of superhydrophobic surfaces. In this chapter, a method using "hot-embossing" a fine wire mesh onto a hydrophobic PTFE surface is introduced. The advancing contact angle for these surfaces is above 150° and contact angle hysteresis is lower than 15°. This method is relatively simple, inexpensive and has potential for large industrial scale manufacture and application.

3.1 Heat-press process

From the literature review in Section 2.2 many studies have shown that superhydrophobicity can be produced in two ways. One is to create a rough structure on a hydrophobic surface, which has a water contact angle great than 90°, and the other way is to modify a rough surface by materials with low surface free energy. Many of the methods introduced in the literature review are not economical and can only be used for research purposes to create very small samples. They are hardly able to provide a sufficiently large enough area which can be applied to host surfaces or expensive for large-scale applications. Therefore, to determine a method which is easy and economical is essential. PTFE is a potential material which has one of the lowest surface free energies, coefficients of friction against any solid (Dupont (1996)), and good flexibility to follow any surface curvature for industry applications e.g. turbine blades, cylinders etc. Several studies such as, Zhang et al. (2004), Yabu & Shimomura (2005), Erbil et al. (2003) and Nilsson et al. (2010) have proved that creating nano or micron-

scale features onto low surface free energy polymeric surfaces can produce superhydrophobicity. Here we follow a simple method suggested by a collabarator Professor Jonathan Rothstein from the University of Massachusetts (Rothstein (2014)). A very fine stainless steel mesh, the diameter of the mesh wire being tens of microns, was used to emboss native Teflon sheet using suitably high pressure and a temperature which was close to the melting point of Teflon (327°C, Starkweather et al. (1983)). Then the regular micro-structure on the Teflon sheet is expected to be embossed or "printed" onto the surface after this process. Fine stainless steel meshes are widely used in industry and are commercially available for a relatively low cost in the order of tens of pounds per square meter.

The first plan to implement this method was by "sandwiching" the stainless steel mesh and Teflon sheet between two flat plates and compressing this in a heat press, which is shown pictorially in Figure 3.1 and Figure 3.2 below.

Figure 3.1. Heat press (APV 3530/18, produced by Maschinenfabrik Herbert Meyer GmbH, Germany) located in the polymer lab of Harrison-Hughes Building, University of Liverpool

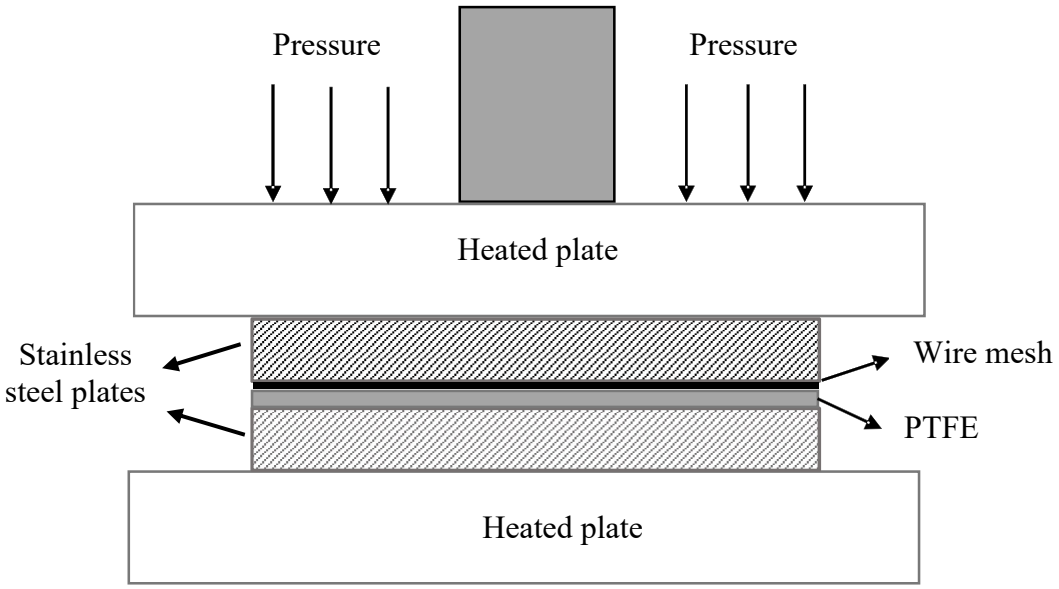

Figure 3.2. Schematic of heat press process.

Basically, the embossing process is affected by three factors: pressure, temperature and time which we can control. In the heat press process, the applied pressure and temperature can be controlled via the heat press, and time is controlled manually by the operator. The appropriate values of these parameters effect the results of the heat press embossing process significantly. Therefore, to optimize the heat press process, these three factors were studied independently and discussed in the each of the sub sections below.

3.1.1 Effects of pressure on heat-press process

To investigate how the variation of pressure affects the heat press process. Each PTFE sample was embossed by the mesh, the wire density of the mesh is 500 per inch and its wire diameter is 25μm (referred as mesh 50025) which is shown in Figure 3.3 below.

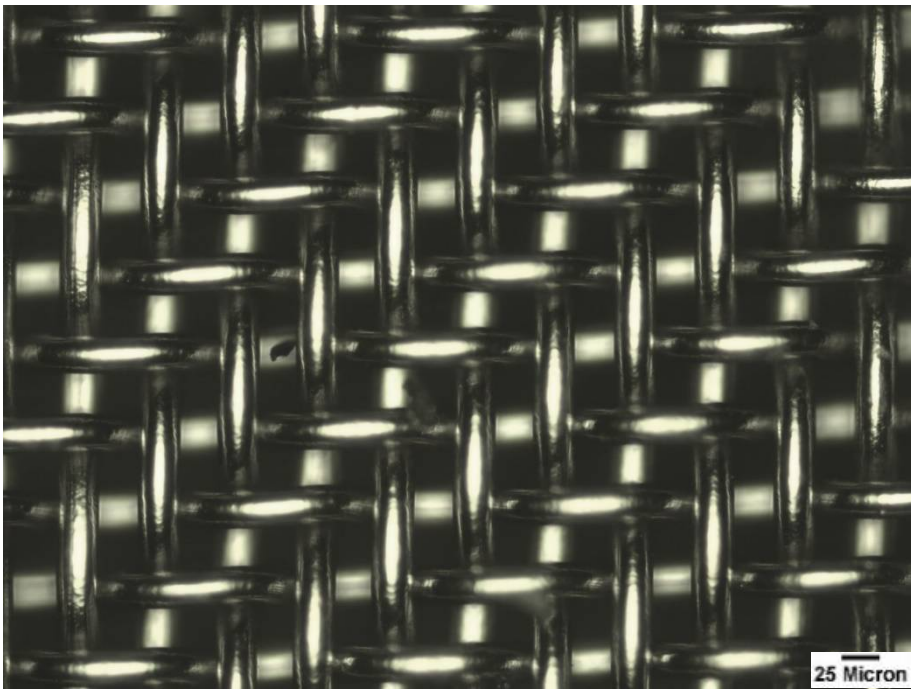

Figure 3.3 Optical image of 50025 stainless steel mesh with 25µm wire diameter at 200x magnification.

The pressure force can be varied by the heat press from 2832 N to 14159 N. This is equivalent to 177 kPa ~ 1415.9 kPa pressure on a 0.01m^2 (10cm by 10cm) surface which were utilised in our experiments. 5 different pressures (177 kPa ~ 887 kPa), listed in Table 3.1, were applied on the 10 by 10 cm skived virgin PTFE sample (purchased from Direct Plastic Limited) sheets with a thickness of 0.5 mm. All 5 samples were heated to 315°C and kept in this temperature for an hour then cooled to room temperature at ambient conditions. From repeating several experiments, it was observed that, increasing the pressure improves the quality of the embossing, providing a more regular structure and larger embossed area. Optical microscopy images of the samples, heat pressed under the lowest (177 kPa) and highest (885 kPa) pressures, were taken and shown in Figure 3.4 and Figure 3.5 respectively. The microscopy images were taken at 5 different points at the sample surface and very different embossing quality can be seen in these figures.

Table 3.1 PTFE samples heat pressed in different pressures.

Sample Number	A1	A2	A3	A4	A5
Sample thickness	0.5mm	0.5mm	0.5mm	0.5mm	0.5mm
Temperature	315°C	315°C	315°C	315°C	315°C
Time	1hour	1hour	1hour	1hour	1hour
Pressure	177kPa	354kPa	531kPa	708kPa	885kPa

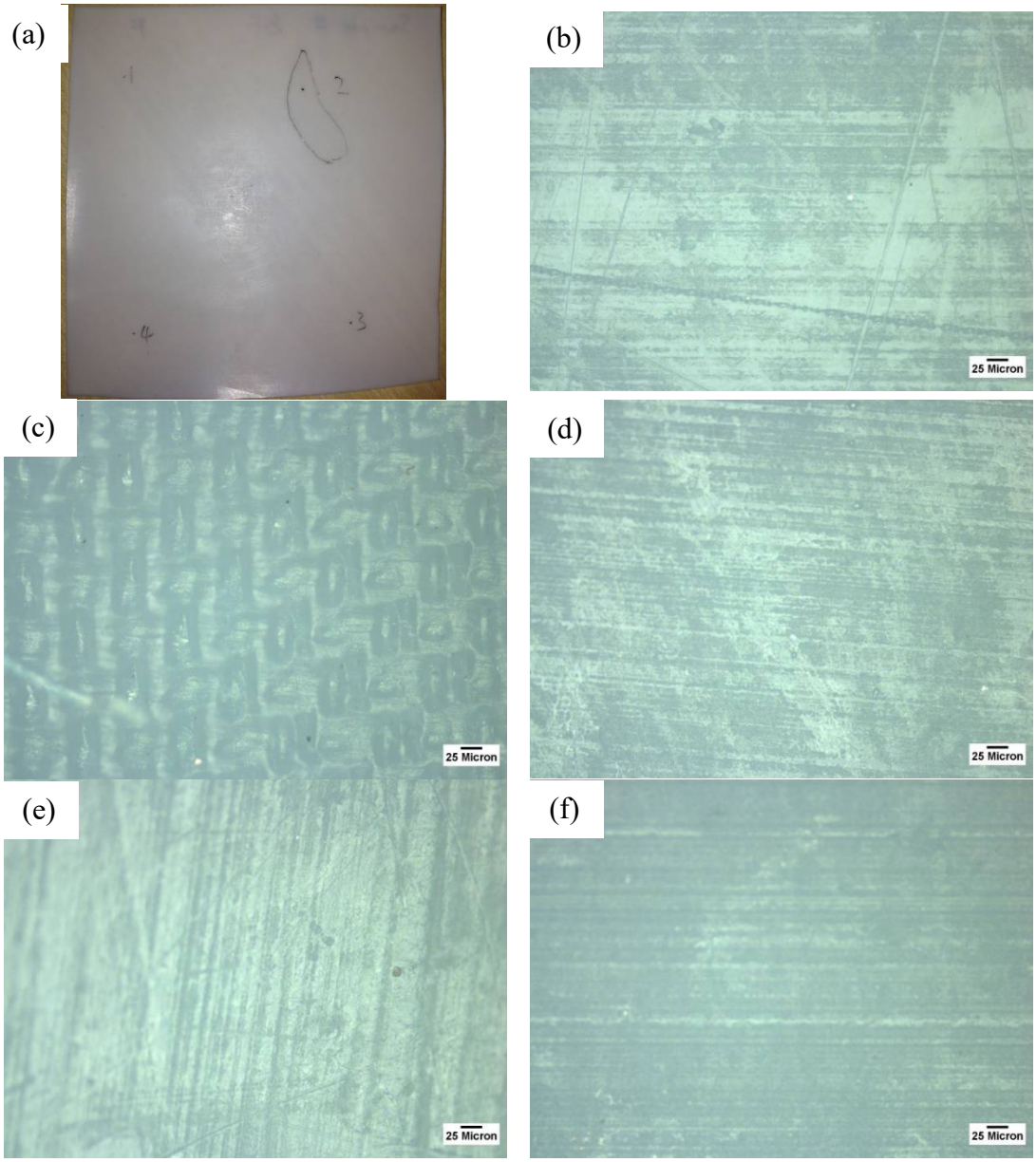

Figure 3.4. Images of PTFE sample (A1 in Table 3.1, heat pressed at 177 kPa. (a) Image of heat pressed sample (10 by 10 cm), area included in black line was well embossed. (b)-(f) Optical microscopy images of the point 1 to 5 on the sample.

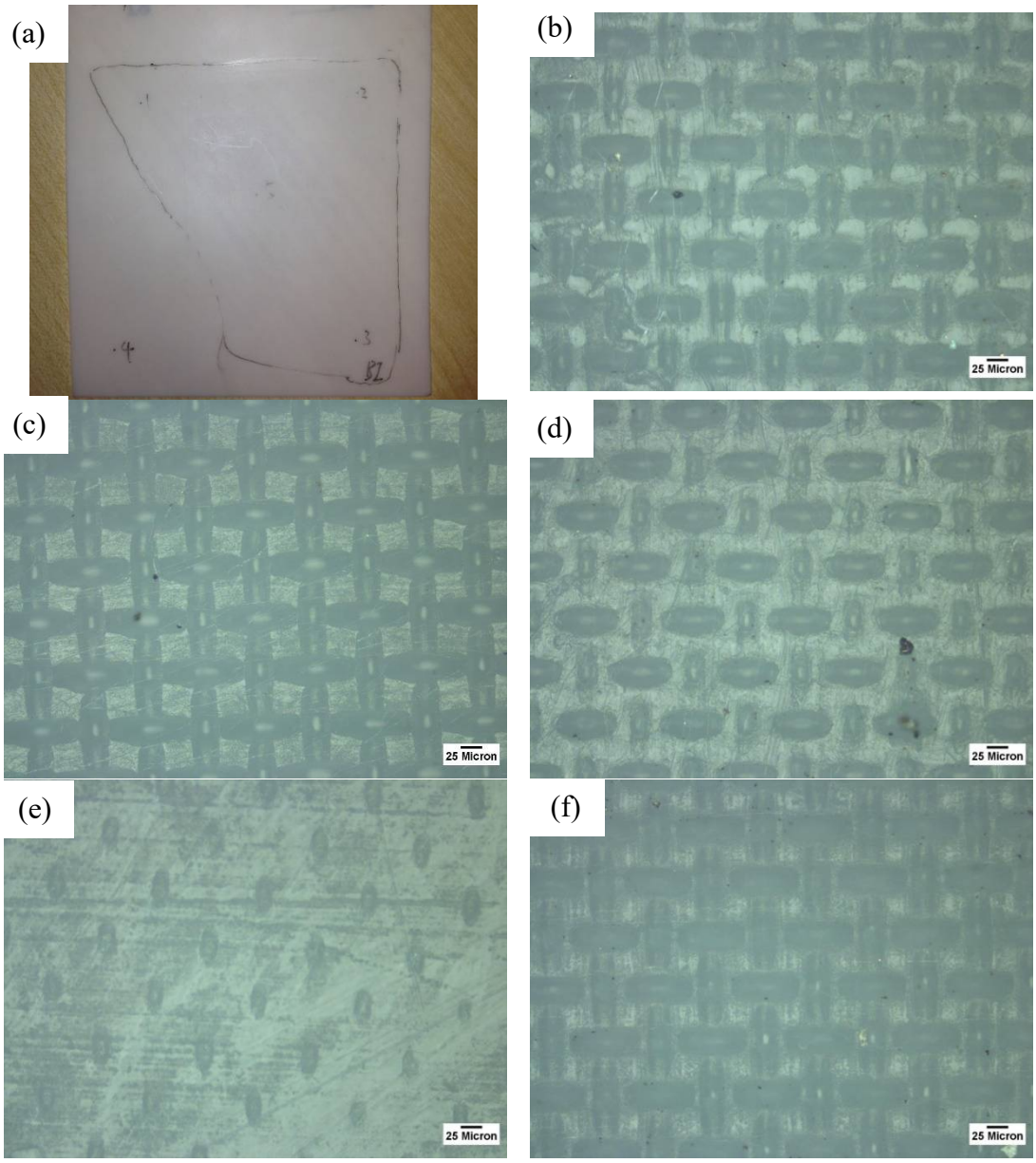

Figure 3.5. Images of PTFE sample (A5 in Table 3.1, heat pressed at 885 kPa. (a) Image of heat pressed sample (10 by 10 cm), area included in black line was well embossed. (b)-(f) Optical microscopy images of the point 1 to 5 on the sample.

From the images shown in Figure 3.4(a) and Figure 3.5(a), the embossed area on the sample A1 where the area is framed by a black line, is much smaller than the equivalent on sample A5, the microscopy images show there is no obvious change outside the framed area (indicated using black ink). That means the increase of pressure can significantly enlarge the embossed area. An optical microscope (Nikon Epiphot TME)

was used to examine the embossing quality inside the embossed area, shown in Figure 3.6. From the images which illustrate the best embossed section of each sample, it can be seen that, with increasing pressure the quality of embossing is significantly improved. At a low embossing pressure (sample A1 to A3), the mesh is not fully stamped into the PTFE surface, and the brick-like post structure is not clearly formed. When the pressure is high enough, the expected brick-like surface structure is produced from the shape of the stainless steel mesh and a typical shape is shown in Figure 3.6(e). Square posts with a size around 30μm are regularly arranged on the surface which is expected to produce superhydrophobicity (via a Cassie-Baxter like state). Although an appropriate area was created using the highest embossing pressure, the uniformity of the embossing was not as good as hoped for. From Figure 3.5(e), only a slight embossing and no brick structure were created, and different structural shapes can be seen in Figure 3.5 at different points of sample A5. From the above we can conclude that the heat-press process can create microscale brick-like structure on PTFE sheet surfaces, with a minimum pressure of about 700 kPa. Unfortunately, the uniformity of embossing is a significant problem of this method. To attempt to overcome this limitation, the effects of embossing time and temperature were investigated and are discussed in the following sections.

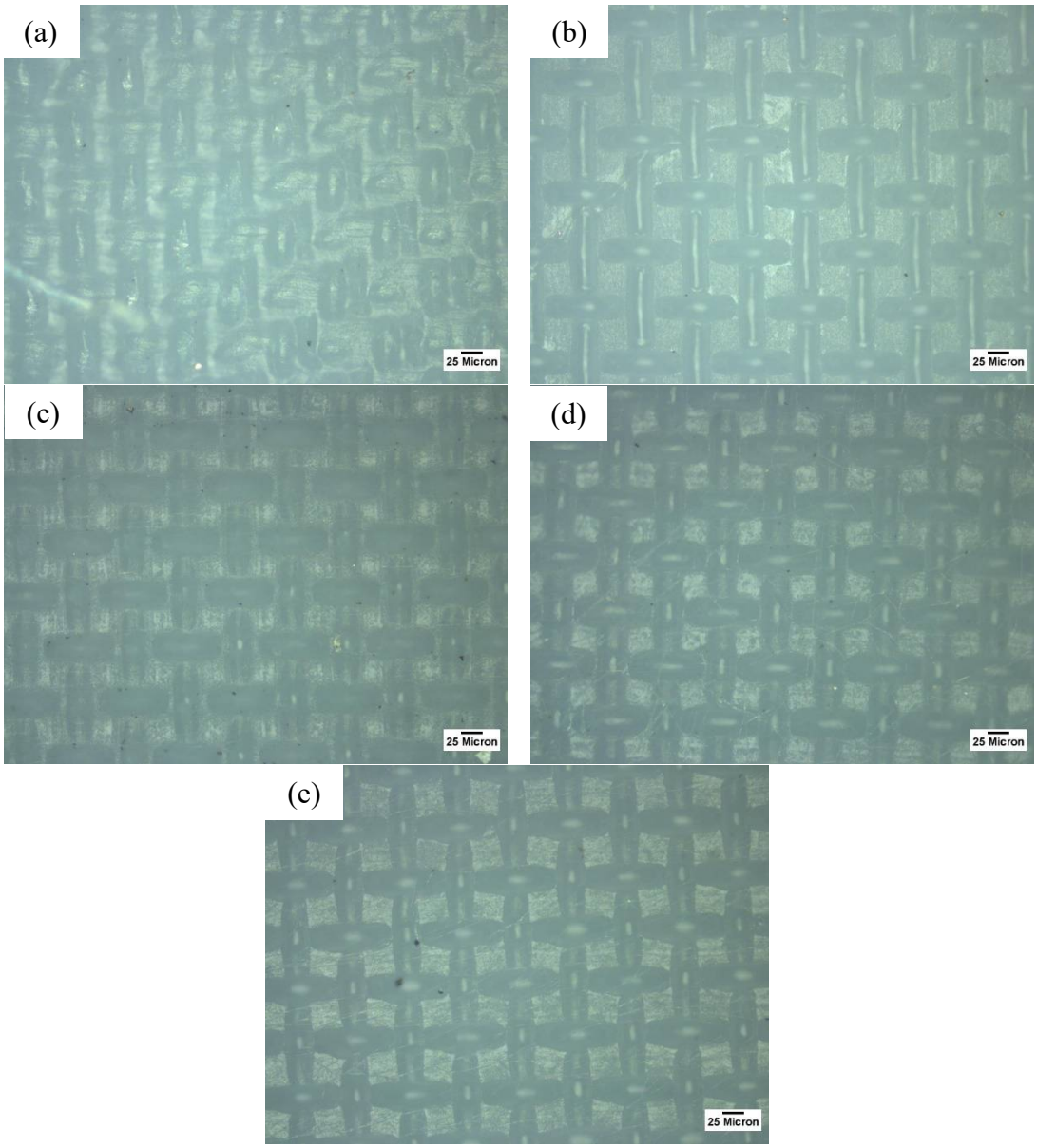

Figure 3.6. Optical microscopy images of the embossed point of the sample A1 (a) ~ A5 (e).

3.1.2 Effects of temperature on heat-press process

Temperature is another factor which can be controlled in the heat-press process. PTFE is a kind of thermoplastic polymer, and the melting point of PTFE is around 327°C (Dupont (1996)). When the term melting point is applied to polymers, it suggests not a solid–liquid phase transition but a transition from a crystalline or semi-crystalline phase

to a solid amorphous phase. PTFE decomposes above 375°C and may produce toxic gas (Starkweather et al. (1983)). Hence, the melting point can be basically recognised as a range of temperature. Three samples were heated at the same pressure (885kPa), but at different temperatures of 305°C, 325°C and 355°C, referred to as B1, B2 and B3 respectively.

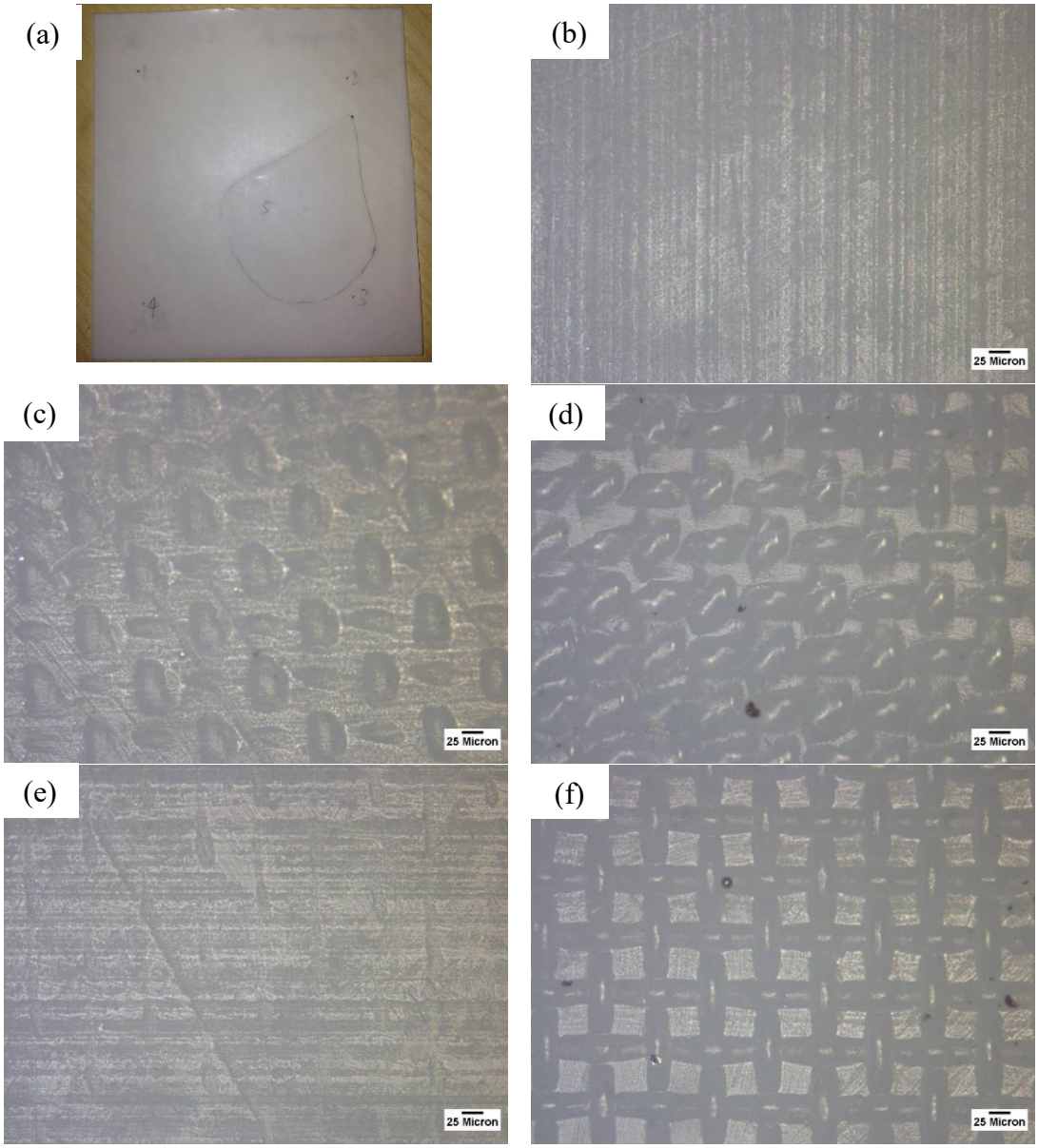

Figure 3.7. Images of PTFE sample B1 heat pressed at 305°C. (a) Image of heat pressed sample (10 by 10 cm), area included in black line was well embossed. (b)-(f) Optical microscopy images of the point 1(b) to 5(f) on the sample.

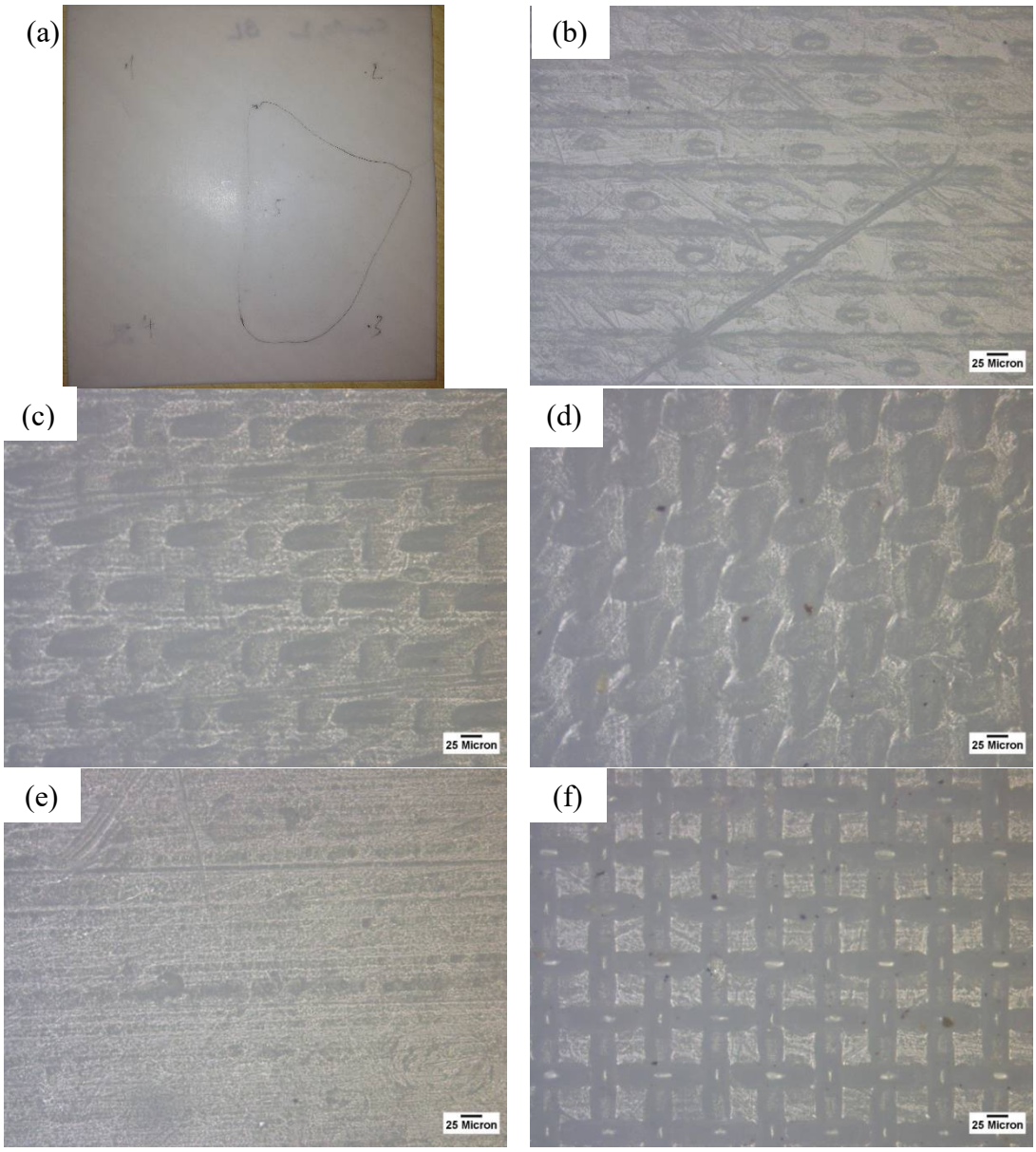

Figure 3.8. Images of PTFE sample B3 heat pressed at 355°C. (a) Image of heat pressed sample (10 by 10 cm), area included in black line was well embossed. (b)-(f) Optical microscopy images of the point 1(b) to 5(f) on the sample.

From the microscopy images shown in Figure 3.7 and Figure 3.8, the higher temperature is seen to be helpful for the embossing quality, but this is not a significant effect due to the narrow range which is possible. The regular “brick-like” post structure was created at the best embossed point. The area outside the black line was observed to

be not very well embossed. Considering safety reasons, the temperature should not be above 375°C. Hence, the heating temperature of 325°C ~ 375°C is chosen as an appropriate temperature for further experiments.

3.1.3 Effects of time on heat-press process

The embossing time is also essential for the heat-press process. Three samples were heated at 325°C and 885 kPa for 0.5 h, 1.5 h and 3 h, referred as C1, C2 and C3 respectively. Microscopy images are shown in Figure 3.9 (for 0.5 hour) and Figure 3.10 (for 3 hours). From Figure 3.9 (a) and (b), the embossed area is much smaller compared to the samples before, and the microscale posts are still connected to each other. Hence, 0.5 hour is not sufficient to produce a uniform embossing. From Figure 3.10, there is not much difference with the sample A5, as shown in Figure 3.5, which was heated for one hour. In addition, for the samples which were heated over 6 hours, it was found that the mesh become very difficult to separate from the PTFE sheet. When one sample was heated for over 12 hours, two stainless steel plates were tightly stuck together and could not be separated by any means. For these reasons, it can be concluded that, time is not a significant factor when it is over one hour, and further experiments should not be over 3 hours.

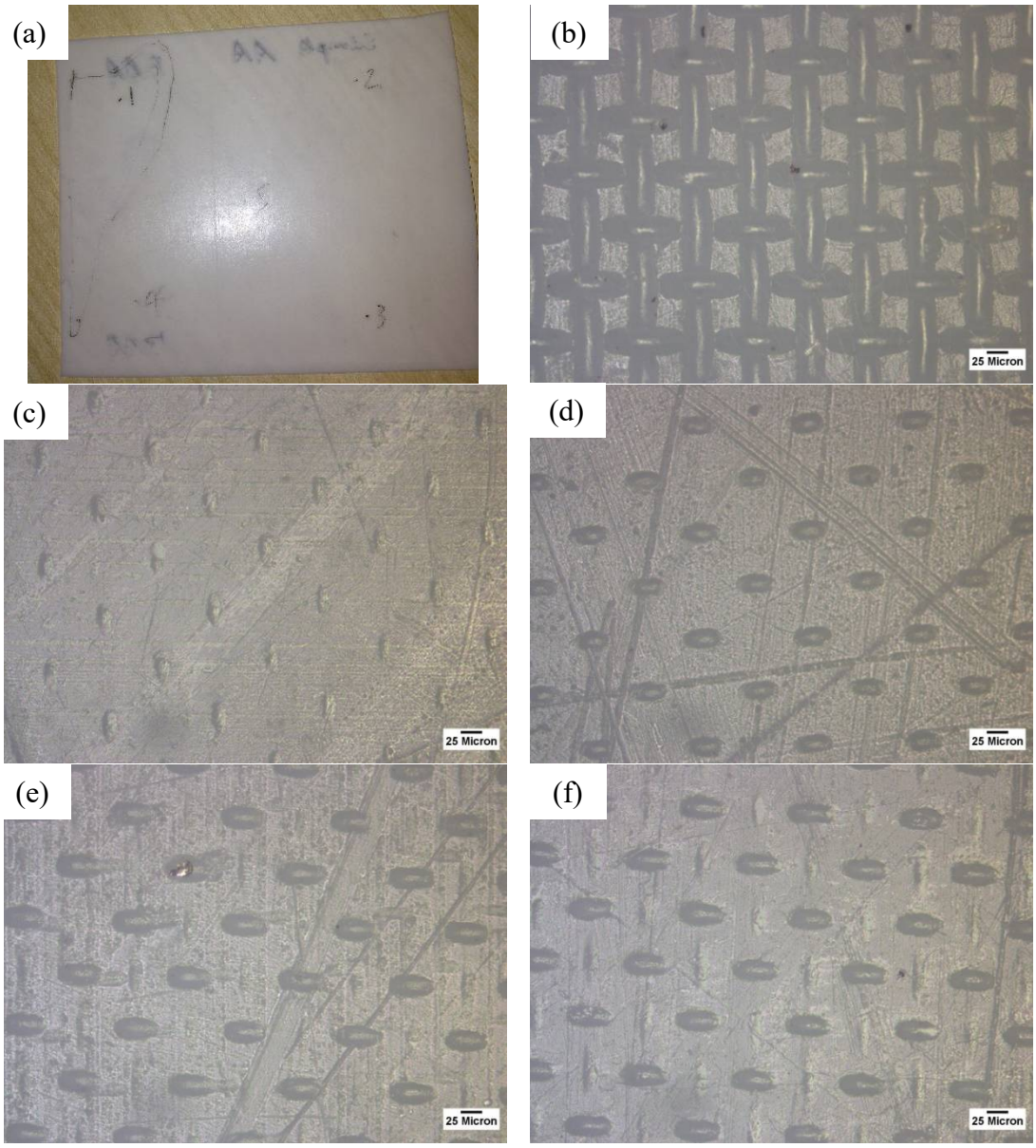

Figure 3.9. Images of PTFE sample C1 heat pressed for half an hour. (a) Image of heat pressed sample (10 by 10 cm), area included in black line was well embossed. (b)-(f) Optical microscopy images of the point 1(b) to 5(f) on the sample.

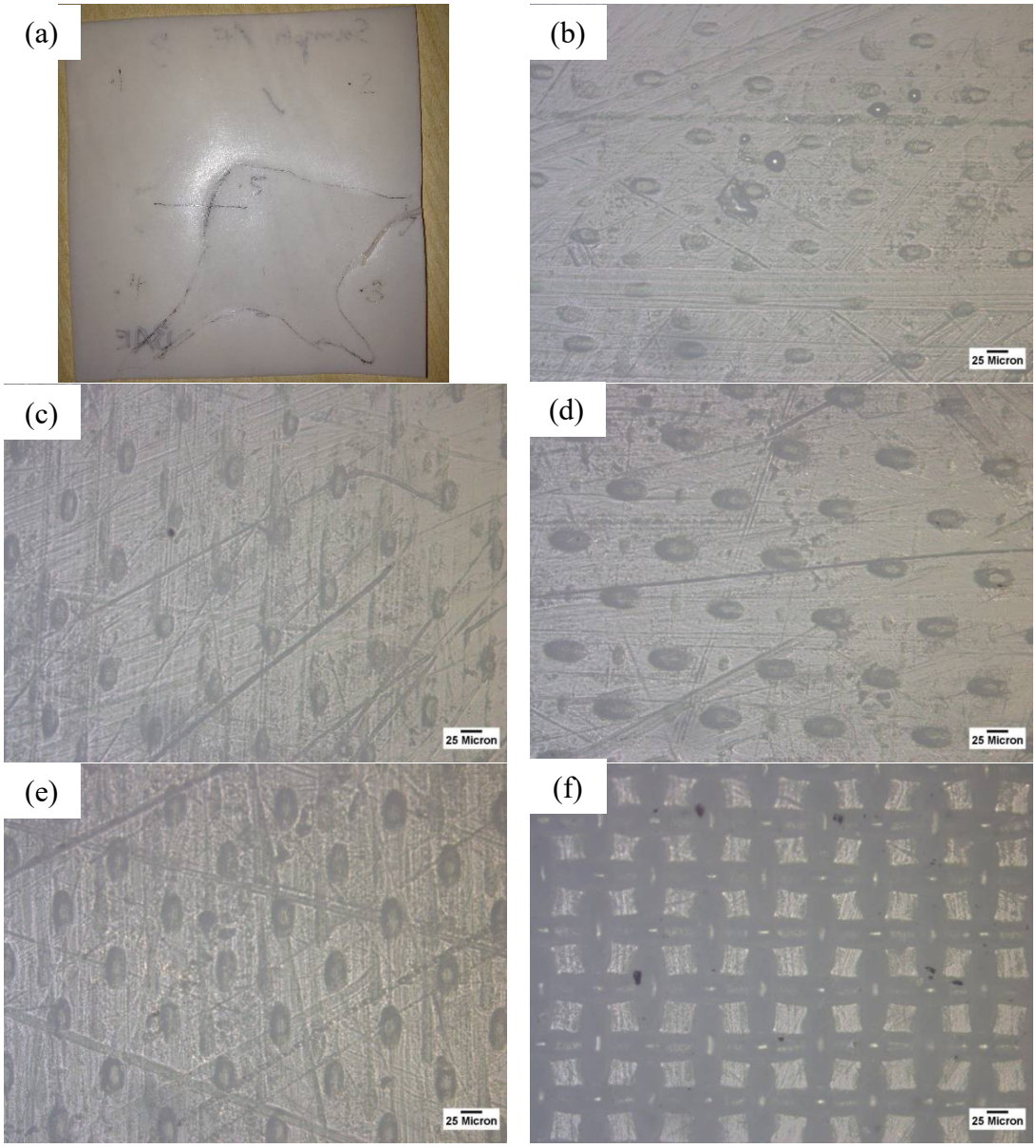

Figure 3.10. Images of PTFE sample C3 heat pressed three hours. (a) Image of heat pressed sample (10 by 10 cm), area included in black line was well embossed. (b)-(f) Optical microscopy images of the points 1(b) to 5(f) on the sample.

3.1.4 Discussion of heat-press process

Generally speaking, there are three factors: pressure, temperature and time which can be controlled during the heat-press process. The pressure can decrease the thermal contact resistance and increase the surface temperature and is probably the most important factor. Due to the melting point of the material, there is not too much scope

for variation of temperature. Time of the process seems to be not too significant at least when varied between 1 and 6 hours. The results show that, in some areas of the PTFE surface, it is well embossed by the mesh under the chosen experimental conditions, but the other areas are less. So, the major difficulty of the heat press process is the nonuniformity of the surface embossing. No matter how the conditions of the experiment were varied, the results were still disappointing. The patterns formed on some areas of the PTFE sheet are very well embossed and has the expected microstructure, but the mesh barely embossed the other area.

The highest static contact angle of embossed area on the PTFE sheet after the heat press process is about 146°. The pictures of distilled water drop on the embossed PTFE sheet, suitably cleaned by acetone, were taken by the microscope and are shown in Figure 3.11. Ten repeat tests were conducted for each volume-controlled sample to guarantee the reduce the random errors. Then the pictures were analysed and the static contact angles were measured by *ImageJ*.

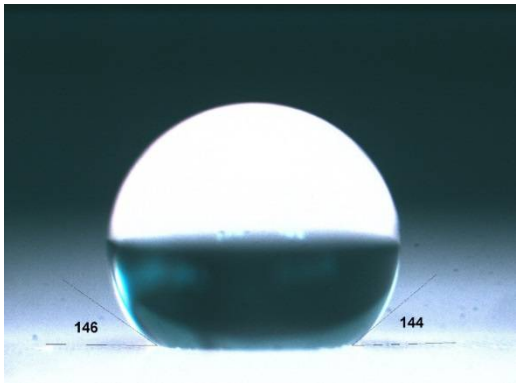

Figure 3.11. Contact angle measured of the water drop on the superhydrophobic surface.

The method to fabricate a superhydrophobic surface by embossing the PTFE sheets with the wire mesh was repeated numerous times. The heat press cannot provide a balanced and uniform force distribution on the sample leading to a nonuniform embossing. The probable reasons for this are suggested to be:

1. The compressed air system of the heat press needs to be calibrated, and the nominal pressure may not be correct;
2. The upper plate of the heat press may not be flat enough, and it cannot contact the sample uniformly which leads to a nonuniformity of the force distribution;
3. The heating elements of the heat press may not provide a uniform temperature field, providing a nonuniform heating of the sample. This difference in the PTFE surface temperature caused the nonuniformity of the embossing;
4. Although marks are made on both of the heat press and samples, the sample may not exactly be located in the central section of the heat press.

Due to the limitation of time and equipment, the heat-press process was abandoned. Instead, two plates held by G-clamps were heated in an oven. This method is straightforward and inexpensive. By using this approach, a maximum size of about 15 cm by 15 cm well-embossed PTFE sheets were fabricated, and large surfaces can be produced possibly by using a larger oven. This method will be discussed in following section.

3.2 Improved heat-press process using mechanical clamping

To achieve better uniformity of the PTFE sheet embossing process, several G-clamps were used instead of the heat-press to hold the wire mesh and PTFE sheet between two stainless steel gauge plates as shown schematically in Figure 3.13. These heavy-duty

G-clamps were bought from GoodHand UK Limited, and their model number is 3"GH-M75. Firstly, the PTFE sheet was sanded by sandpaper to soften the surface sufficiently for the embossing process. From several experiments, 180 grit sandpaper was found to be the best for this process. Then the mesh was placed onto the PTFE sheet and sandwiched in between two 12mm thick stainless steel plates. Based on preliminary results, it was found that the more G-clamps that were used, the better the force distribution that could be achieved. Because of the limitation of the size of the gauge plate and the oven, only 10 G-clamps could be applied on the 15 cm by 15 cm plates. The arrangement of clamps which can be seen in Figure 3.14 was found to be very important for a uniform pressure distribution. All the G-clamps were tightened by a torque wrench (Bedford, England) with the same torque which was around 50 N·m to make sure the pressure forces were the same for each clamp. Meanwhile for later experiments, oil was used to lubricate the clamps, due to the corrosion observed after the heating process. Based on the experiences from the heat-press process, which was described in Section 3.1, the sample was heated in an oven at 350°C for 3 hours. It was then allowed to cool in the oven naturally to avoid any unbalanced thermal expansion. Five types of meshes were chosen which are listed in Table 3.2. and the microscopy are shown in Figure 3.12.

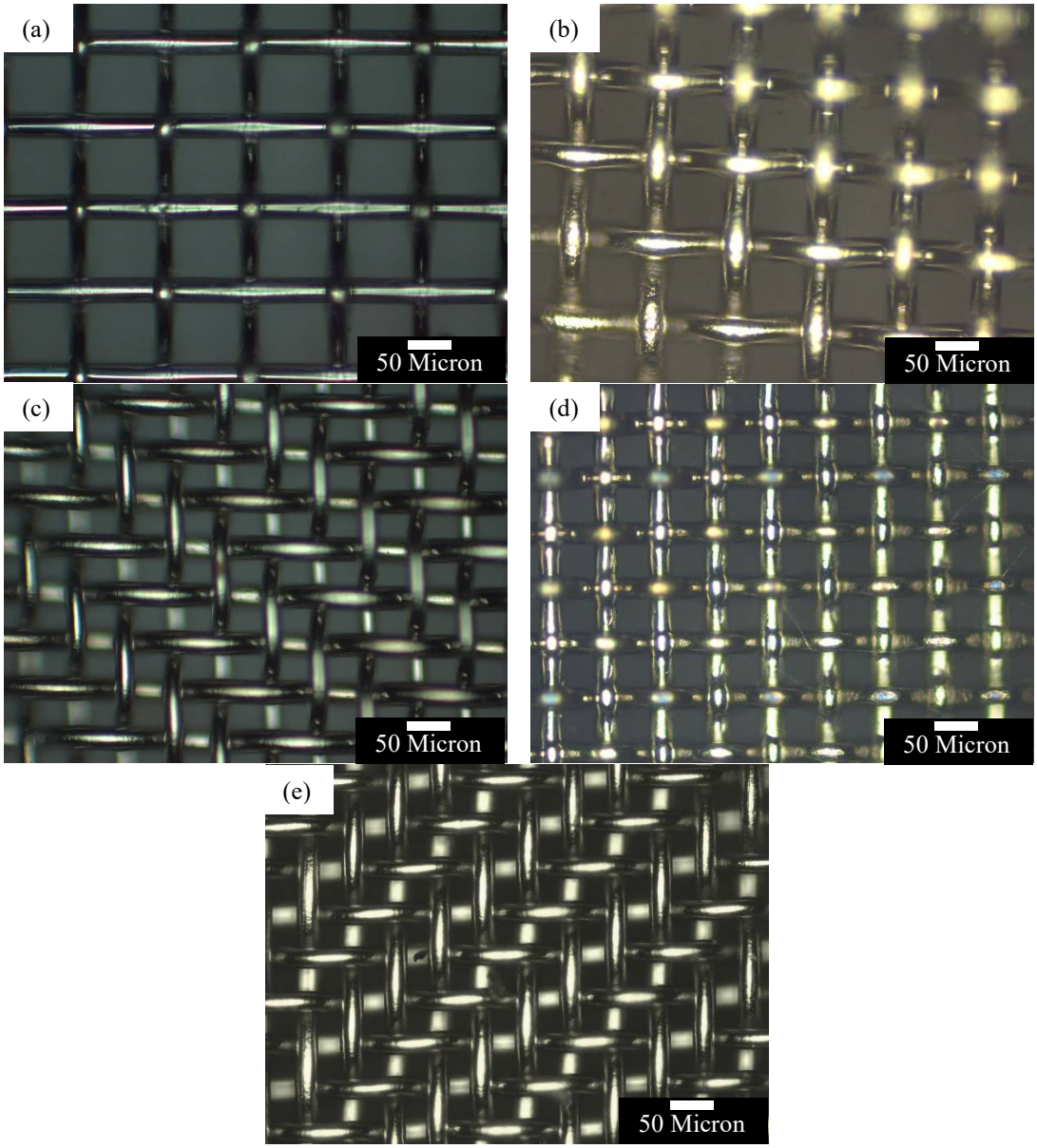

Figure 3.12. Microscopy images of the stainless steel meshes, (a) 30030, (b) 30040 (c) 40025, (d) 40030 and (e) 50025, at 200x magnification. (The definition of the mesh names are seen in Table 3.2.)

Table 3.2 Mesh parameters

Mesh type^	Number of wires per inch	Wire diameter (μm)	Aperture (μm)	Open area ratio
30030	300	30	55	46%
30040	300	40	45	28%
40025	400	25	39	37%
40030	400	30	34	28%
50025	500	25	26	28%

^The meshes are referred as mesh type number which combined with the number of wires per inch and the wire diameter.

These very fine stainless steel meshes are commercially available and bought from The Mesh Company (Warrington, Cheshire, UK). These meshes are widely used as filter or atomizer. The aperture size in Table 3.2 indicate the space between each wire, and the area of the aperture against the whole area of the mesh is referred as the open area ratio. Based on the discussion in Section 2.3.2, the dimensions of the surface features should be tens of micron or smaller to create superhydrophobicity. These five types of mesh were found as the finest meshes available from the commercial market. The embossed PTFE samples using these meshes were manufactured and will be presented and discussed in following section.

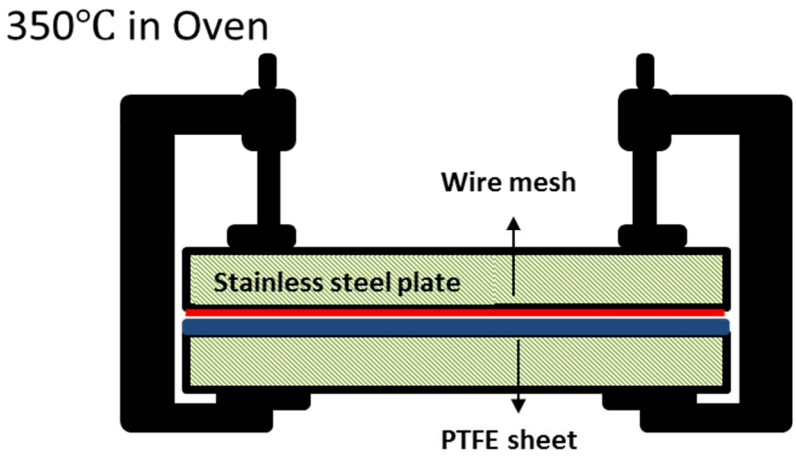

Figure 3.13. Schematic of improved heat press process.

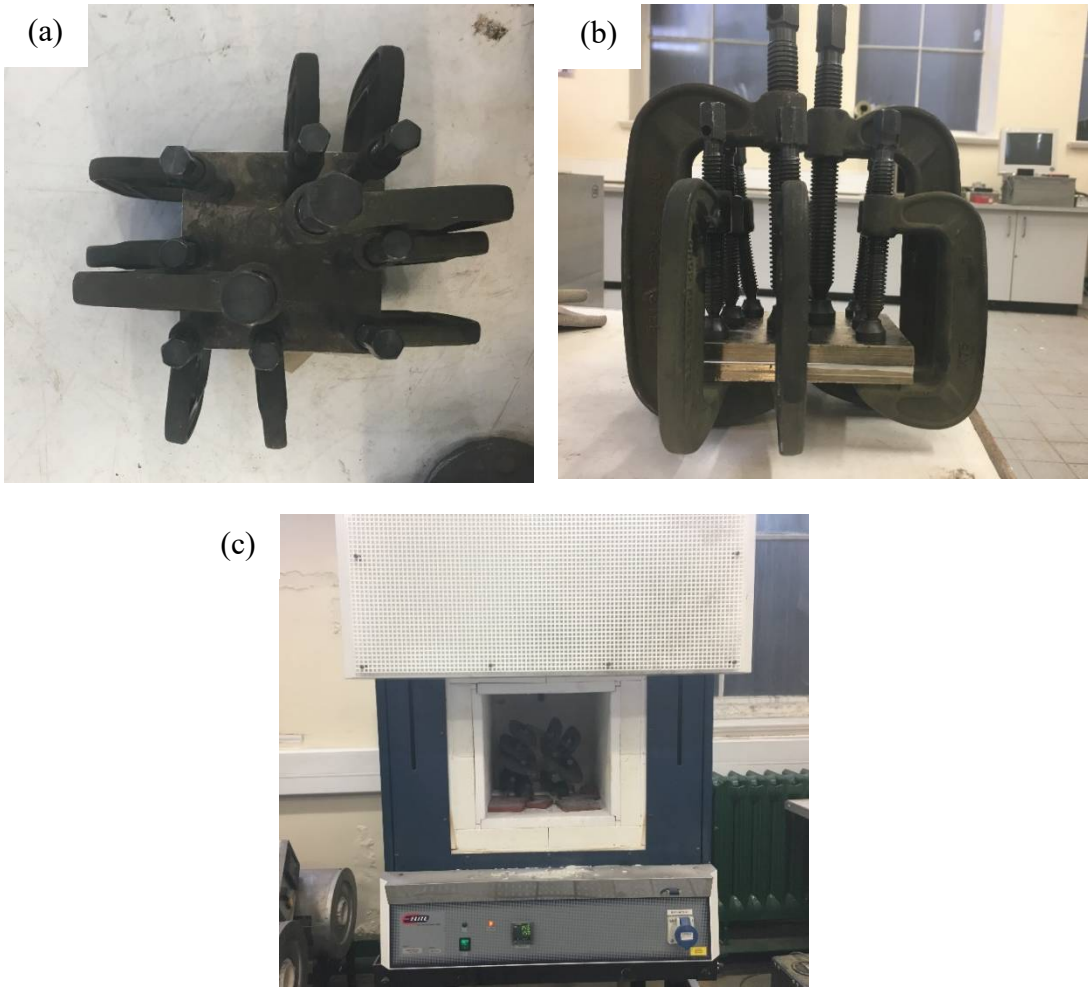

Figure 3.14. Image of the clamped sample in the furnace.

The result is better than the heat-press process, especially for the embossing uniformity. Although the size of PTFE sheet is 15 by 15 cm, only a maximum size of around 12 by 12 cm area is well embossed. The embossing quality was examined by microscopy images, and a regular brick-like structure arranged uniformly on the surface can be observed, a typical SEM image of these micro-scale structures are shown in Figure 3.15. More images will be presented and discussed in following chapter. As can be seen in Figure 3.15, the quality within the embossed area seems decent and reasonably uniform. Water drops roll off easily on the whole surface, often called “lotus effects”, as shown in Figure 3.16. The embossed superhydrophobic PTFE surfaces are referred to as “xPTFE” for the remainder of this thesis.

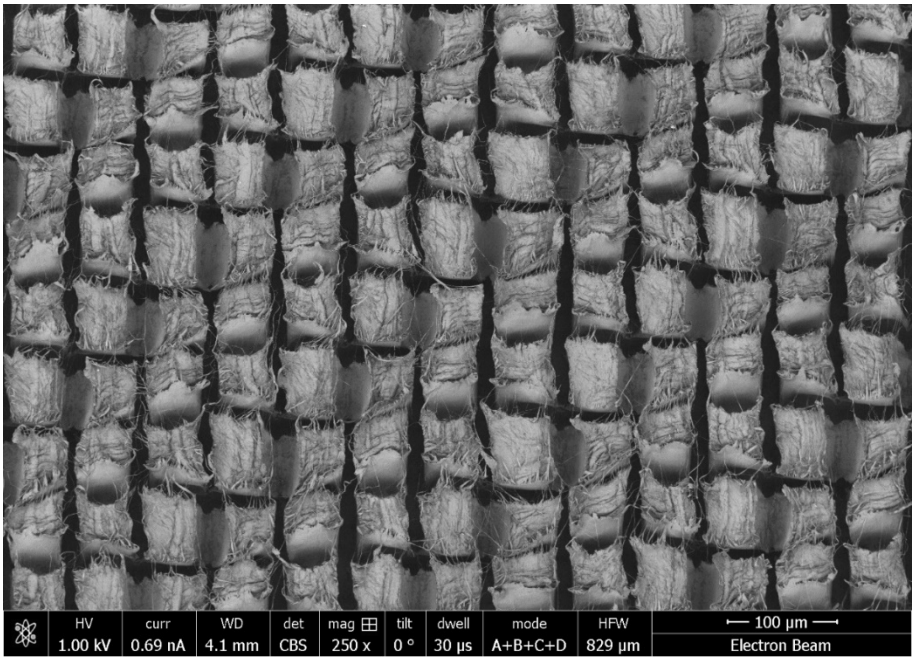

Figure 3.15. SEM image of microstructure of the embossed PTFE sheet at 200x magnification.

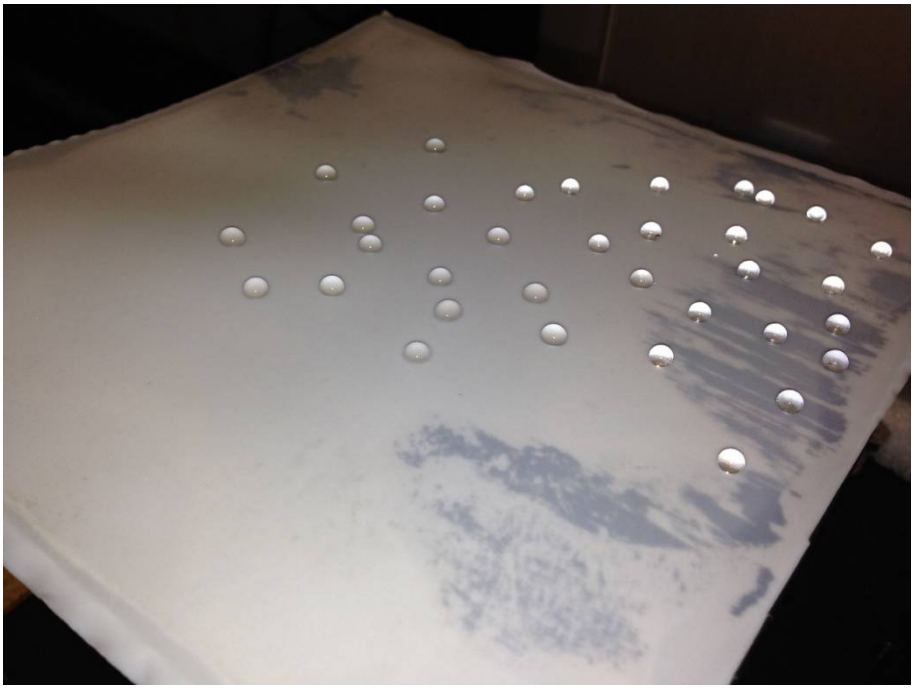

Figure 3.16. Water drops on embossed PTFE surface.

3.3 Conclusions

Using microscale diameter stainless steel meshes to emboss PTFE sheets to create superhydrophobic surfaces has been shown to be successful. This method is relatively simple, inexpensive and has potentially wide applications for industrial manufacture. In this method, the key point is to control the applied pressure and find a way to optimise the uniformity of the pressure distribution. Only a uniform pressure in combination with the correct temperature and time can provide a large and homogeneously-embossed surface.

In our laboratory, superhydrophobic PTFE sheets with “brick-like” regular micro-structure and overall maximum size of 12cm by 12cm are created after this hot-embossing process. This maximum size is only limited by the oven available. An easy visual test shows that water drops can easily roll-off the xPTFE surface due to the superhydrophobicity as expected. Static contact angles for water on the xPTFE surface

were measured as above 145°, and the contact angle hysteresis is about 15°. Additional characteristics will be introduced and discussed in the following chapter.

Some of the problems for this method are: limited by the equipment in the laboratory, the quality of the sample from different batches can be variable, it could be solved by using higher standard manufacture equipment and process on a more industrial scale. Furthermore, considering the cost of each embossing, the stainless steel meshes should be re-used after each embossing. Which would require a cleaner manufacturing environment and a more careful method to separate them from the PTFE sheet in order to avoid damaging and twisting of samples. Despite these issues, the manufacturing technique is sufficiently reliable to enable a wide range of tests to be conducted on a range of different features as will be discussed in the following chapter.

Chapter 4 Characterisation of superhydrophobic surfaces

After manufacturing the xPTFE superhydrophobic surfaces as described in Chapter 3, the wetting properties and other features of the superhydrophobic surfaces are introduced and characterised in this chapter. One of the most direct ways to characterise a superhydrophobic surface is to measure how easily water drops move on it, much as like observing the famous "lotus effect". As introduced in Chapter 2, we can use the drop contact angle hysteresis to partly describe the movability of a drop on a surface. The static contact angle is also a fundamental wetting property of the quoted surfaces as well, De Gennes et al. (2013), despite the ill-posedness of this condition as described in Section 2.1.2. A water drop bouncing test is introduced in this chapter as a definition of superhydrophobicity, as it provides the most convincing and clear boundary between hydrophobic and superhydrophobic surfaces, as seen in Crick and Parkin (2011). Finally, the slip-length and the degree of drag reduction in laminar flow over superhydrophobic surfaces are discussed and measured. Introducing effective slip (introducing a drag reduction) is one of the most important features of superhydrophobic surfaces due to its enormous potential in industrial applications. The slip-lengths of our xPTFE surfaces and for comparison TiO_2 surfaces, Lu et al. (2015), were both measured in this work.

4.1 Wetting properties

Wetting is the ability of a liquid to maintain contact with a solid surface. It is caused by the intermolecular interaction when they contact each other. Wetting includes three

phases of gas, liquid and solid, the details of which were introduced in Section 2.1.1. The wetting properties are the most distinctive features of the superhydrophobic surface in comparison with other surfaces. Superhydrophobic surfaces have high static contact angles and low contact angle hysteresis. These properties of the xPTFE surfaces, which were manufactured following the procedures described in Chapter 3 will be measured and discussed in this section.

4.1.1 Static contact angle

For an "ideal" surface which is wetted by a pure liquid drop, contact angle theory predicts only one thermodynamically stable contact angle from the force balance between gravity and surface tension, and this static contact angle is given by Young's equation, details given in Section 2.1.1. But in the real world, a drop has a series of metastable states on the surface due to the barriers of surface free energy of non-perfect surfaces. The static contact angle in a real equilibrium state is difficult to observe in practice. The apparent static contact angle could be affected by both the physical and chemical surface inhomogeneity, and the physical process of placing the drop on the surface. It could be any value from the maximum advancing contact angle to the minimum receding contact angle. Hence, many researchers claim that the hysteresis value is more important than the absolute static contact angle value to properly describe the wetting property of a surface (Schellenberger et al. (2016)).

As introduced in Chapter 2, superhydrophobic surfaces have two states: Wenzel and Cassie-Baxter states. The Wenzel states describes when the surface is completely wetted by the drop, and the Cassie-Baxter states describes the drop standing on the surface features. The small contact area between the drop and surface leads to a very small contact angle hysteresis, which allows the drop to roll off easily on the surface.

Consequently, in this case, the variation of static contact angle due to the deposition process is relatively small. The value of the static contact angle of a water drop is none the less significant and iconic for the superhydrophobic surfaces. A value of 150° is often claimed by many studies as a boundary between a hydrophobic and superhydrophobic surfaces (e.g. Erbil et al. (2003), McHale et al. (2004), Shirtcliffe et al. (2005), Kim et al. (2005), Zhang et al. (2008), Kim (2008), Shirtcliffe et al. (2010), Busse and Sandham (2012), Mammen et al. (2014), Brassard et al. (2015), Guo et al. (2015) and Wen et al. (2017)).

Five xPTFE surfaces were manufactured with five different stainless steel meshes (as discussed in Chapter 3). The mesh was embossed onto flat PTFE surfaces as a model, and created a "brick-like" surface structure. The surface feature properties were estimated by the dimensions of the embossing meshes, as can be seen in Table 4.1, and these xPTFE surfaces are referred to via the mesh types which were used to emboss them. The "brick-like" structure resulted from the printing of the mesh. The brick size could be estimated using the aperture between the mesh wires, the distance between bricks could be estimated from the mesh wire diameter, and the open area ratio indicated the ratio of area excluding the bricks over the whole area. The static contact angles were measured first to provide a rough approximation of their hydrophobicity.

Table 4.1 xPTFE surface parameters (estimated from the meshes).

Mesh type^	Brick size	Aperture	Open area ratio
30030	55 μm	30 μm	54%
30040	45 μm	40 μm	71%
40025	39 μm	25 μm	63%
40030	34 μm	30 μm	72%
50025	26 μm	25 μm	74%

^ The first three figures of the mesh type number represent the wire density of the mesh (wire number/inch), the last two figures represent the wire diameter of the mesh wire(μm).

To measure the static contact angle, a 50 µL distilled water drop was placed on the sample surface by a syringe controlled by a syringe pump. Digitalized images were taken using a camera (Nikon D5300), and processed by *ImageJ*, a schematic of measurement set-up is shown in Figure 4.1(a) and representative analysed images for different xPTFE samples are shown in Figure 4.1 (b)~(d). All reported values represent the average of ten contact angle values per sample, corresponding to the "left" and "right" contact angles of five drops, the results are shown in Figure 4.2. As discussed in Section 2.3.2, superhydrophobicity increases with the open area ratio (the area of trapped air vs the whole surface area) of superhydrophobic surfaces. The larger liquid air interface provides higher superhydrophobicity but can sustain lower pressure for maintaining the Cassie-Baxter state (Lee et al. (2008)).

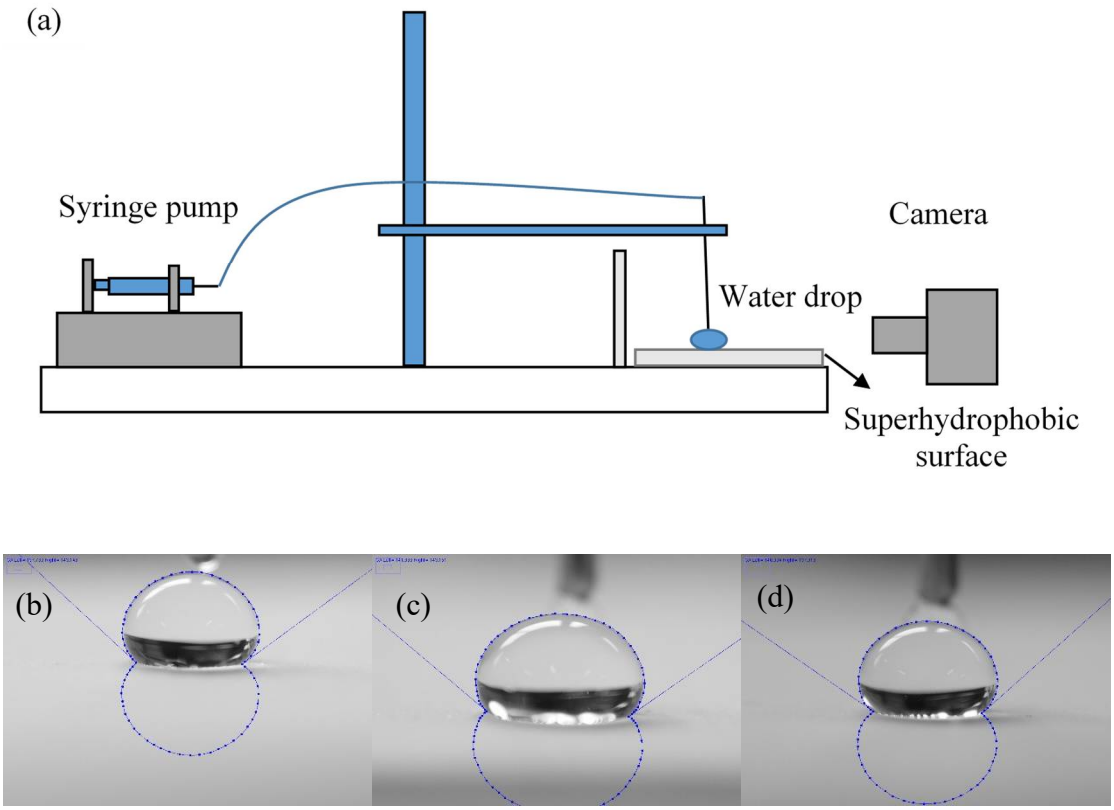

Figure 4.1. Schematic of contact angle measurement set-up (a) and analysed images for different xPTFE samples, (b) 30040, (c) 40030 and (d) 50025.

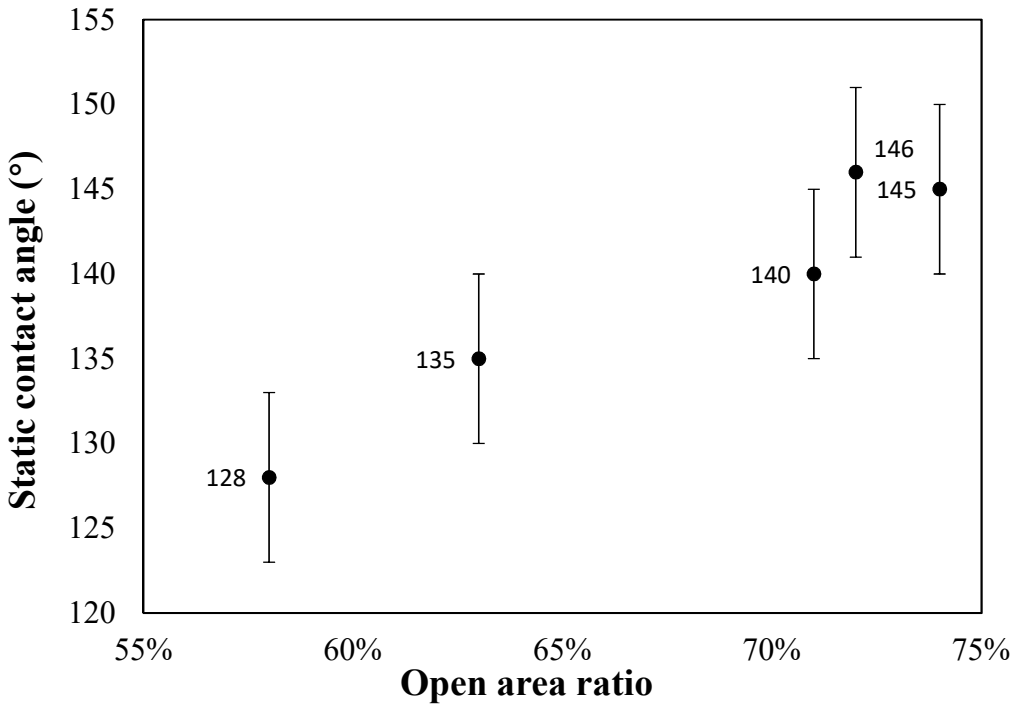

Figure 4.2. Static contact angle vs open area ratio of xPTFE surfaces.

Using equation 2.3, the static contact angle for a Cassie-Baxter state can be estimated by knowledge of the surface material and structure. As the static contact angle for a water drop on a smooth PTFE surface is ~110°, assuming the drop is in a fully Cassie-Baxter state and the top of the surface structure is smooth and flat (r_f=1). The static contact angles can be estimated as 136°, 139° and 144° for 58%, 63% and 72% open area ratios respectively. From the results shown in Figure 4.2, the measured static contact angle increases with the surface open area ratio and the results agree reasonably well with the estimation above. When the open area ratio is around 72%, the static contact angle is approaching the boundary of superhydrophobicity (i.e. 150° of static contact angle). The static contact angles measured on the xPTFE surfaces embossed by meshes 30030 and 40025 are lower than 140°. That indicates the less hydrophobic nature of these surfaces in comparison with the other three surfaces. However, their hydrophobicities are still higher than untreated smooth PTFE surfaces (the static

contact angle is measured around 110°). Therefore, only the other three xPTFE surfaces embossed by meshes 30040, 40030 and 50025 were studied in the remainder of this work as these are the most hydrophobic. These three xPTFE surfaces have a similar open area ratio and static contact angles around 145°±5°. Because of our manufacturing process, the quality of the sample varies between batches. For a limited number of samples, a static contact angle was measured higher than 150°, for the "bad" samples it was between 140° to 145°. If we consider the static contact angle of 150° as a definition of superhydrophobic surface, these three xPTFE surfaces just stand on the boundary between hydrophobic and superhydrophobic surfaces.

4.1.2 Contact angle hysteresis

Contact angle hysteresis is defined as the difference between advancing and receding contact angles (Eral et al. (2013)). For superhydrophobic surfaces, the contact angle hysteresis can be used to describe how easily the drop will move on the surface. This hysteresis occurs due to the wide range of metastable states which can be observed as the liquid sits on the solid at the solid/liquid/air interface. Because of the surface free energy barriers between these metastable states, the real equilibrium static contact angle is not strictly possible to measure. Consequently, to characterize the superhydrophobic surfaces, it is important to measure both advancing and receding contact angles and report the difference as the contact angle hysteresis.

The contact angle hysteresis can be measured by a few methods experimentally, e.g. Bourges-Monnier and Shanahan (1995), Di Mundo and Palumbo (2011), Strobel and Lyons (2011) and Eral et al. (2013). The first of these methods is the tilted plane method. In this method, a droplet is placed on an inclined plane and the contact angles are measured when the drop starts moving on the surface. Another method modified from

the tilted plane method is the centrifugal force balance method （Tadmor et al. (2009)). This method uses two rotating axes to create centrifugal forces. Manipulating these forces can decouple the tangential and parallel components of the adhesion force. This method can give any combination of lateral and tangential force as the drops rotate on an inclined plane.

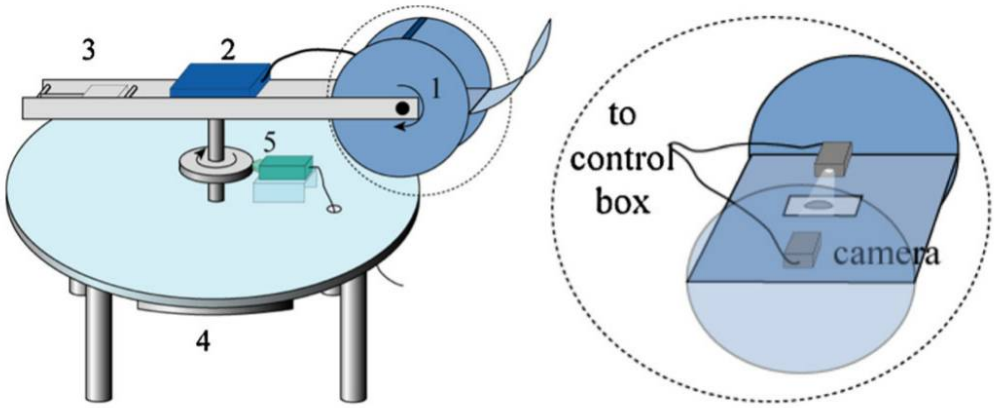

Figure 4.3. The experimental setup of the centrifugal force balance method. A rotating arm has a closed chamber (1) at one end and a counterbalance. (3) at the other. The chamber, drawn with its door open, holds a light source and a camera between which the drop is placed as shown in the right inset. The signal from the camera is transferred to a control box (2) which runs on battery and which further transfers the signal wirelessly to a computer placed nearby outside the rotating assembly (not shown). The angular velocity is monitored using an encoder (5) that touches a round enlargement in the shaft which in turn is connected to a dc motor (4). Thus force measurements are coupled with the in situ video signal of the sliding object (drop in this study). By independent manipulation of the angular velocity (measured in 5) and the tilt angle (1), this method allows for any combination of normal and lateral forces. This figure is taken from Tadmor et al. (2009).

A second method is the sessile drop method. In this method, liquid/gas is pumped into and out of a droplet/bubble to determine the advancing and receding contact angles. A modification of this method is using the evaporation effect. The advancing contact

angle is measured as air is pumped into a droplet as well, but the receding contact angle is measured as a droplet evaporates.

The third method is the so-called Wilhelmy plate method, and it also used to measure the surface tension of a liquid. In this method, a plate is forced into or pulled out of a bath to the advancing and receding angles, respectively.

The fourth method is the “add and remove” volume method. The liquid is added onto a surface dynamically to the maximum volume permitted without increasing the three-phase contact line. The maximum contact angle measured in this process is referred to the advancing contact angle. The volume can then be removed without resulting in the three-phase contact line retreating. This contact angle is the “receding” contact angle.

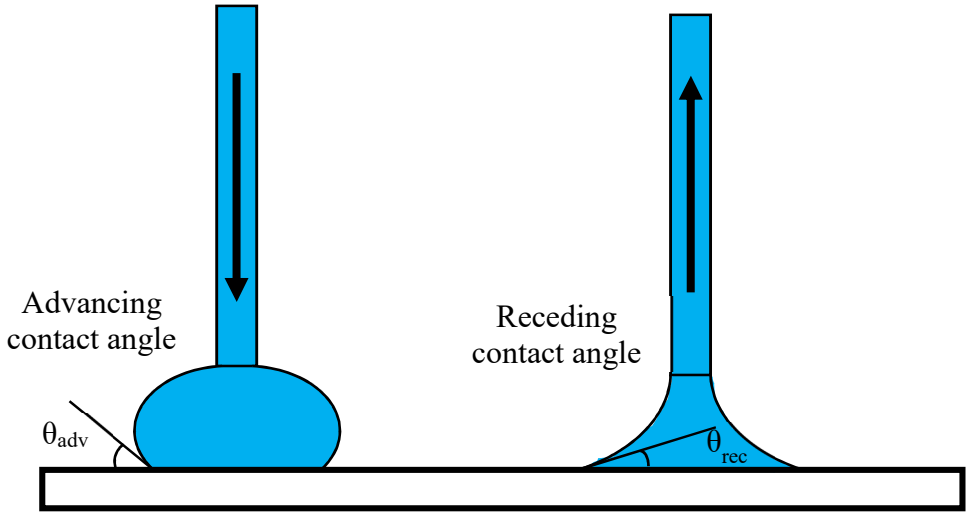

Figure 4.4. Schematic of static contact angle and contact angle hysteresis measurement.

The method used to measure the contact angle hysteresis in this work is the “add and remove” volume method, a schematic of this method can be seen in Figure 4.4. The experimental set-up is developed from the static angle measurement. A needle was

fixed above the testing superhydrophobic surface with a gap above the surface of ~1 mm. The distilled water was injected/withdrawn by a syringe pump with a flow rate of 1 μL/s. A video was taken by a camera and the advancing and receding contact angles were measured using *ImageJ*. All reported values represent the average of ten contact angle values per sample, corresponding to the "left" and "right" contact angles of five drops, typical analysed images are shown in Figure 4.5 and measured contact angle hysteresis are shown in Table 4.2.

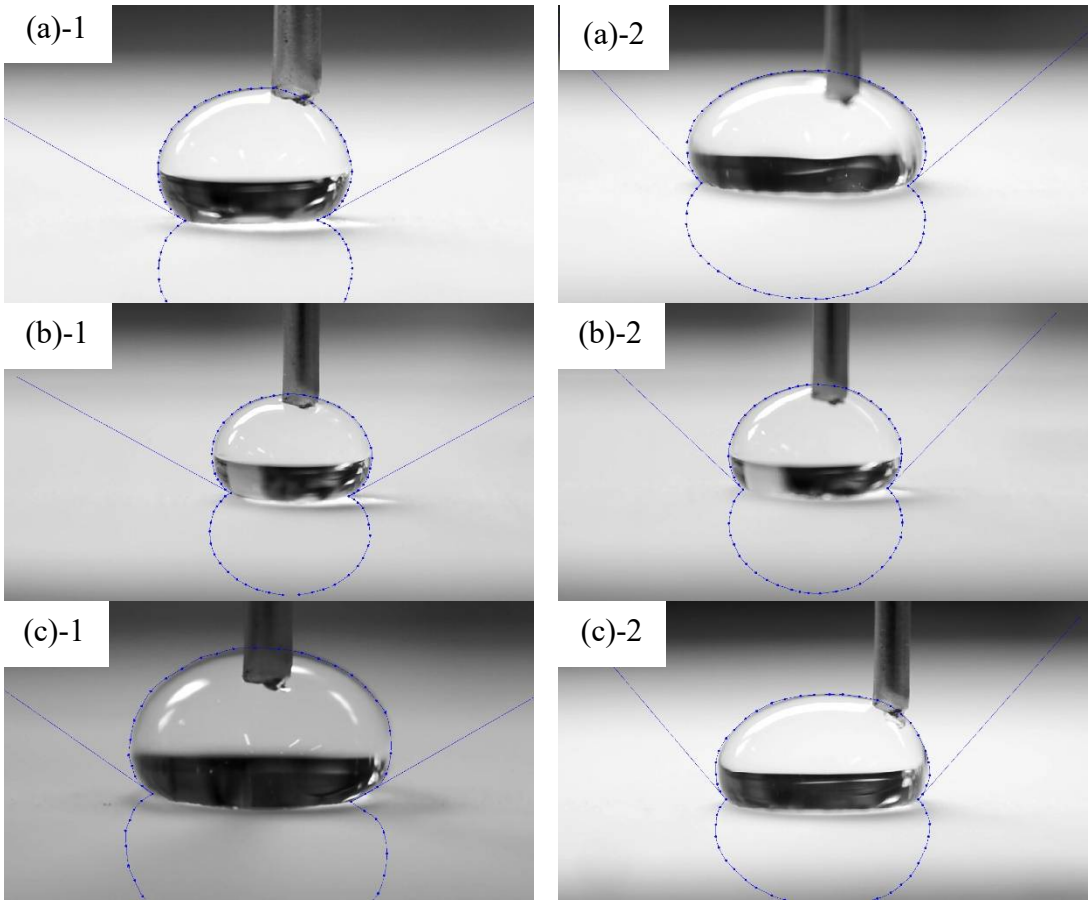

Figure 4.5 Images of contact angle hysteresis measurements on different xPTFE surfaces, (a)30040, (b)40030 and (c)50025. (1) Advancing contact angle. (2) Receding contact angle.

The average contact angle hysteresis for all three types of xPTFE are close to 15° and varies about 3° for different samples (which is within the measurement accuracy). This

small value can lead to a drop moving very easily on these surfaces and a highly water-repellent effect. In addition, similar static contact angles and contact angle hysteresis indicates that the three xPTFE surfaces have similar hydrophobicity due to the similar open area ratio despite their different surface topography.

Table 4.2 Contact angle hysteresis

Mesh type	30040	40030	50025
Static Contact angle	140°±5°	146°±5°	145°±5°
Advancing Contact Angle	152°±5°	152°±5°	148°±5°
Receding Contact Angle	137°±5°	136°±5°	132°±5°
Contact Angle hysteresis	15±3°	16±3°	16±3°

4.2 Morphology of xPTFE surface

As introduced in Section 2.1, the superhydrophobicity is created by a combination of micro/nano-scale surface structure and the low surface free energy material. The surface structures are essential to form the Wenzel and Cassie-Baster states, and the size and shape of these are the dominant factors of the resulting superhydrophobicity. Therefore, the investigation of the surface morphology is significant for understanding superhydrophobic surfaces. Firstly, the xPTFE surfaces were observed under an optical microscope (Nikon Epiphot TME). For an optical microscope, the depth of field increases with a narrowing of the aperture, but also results in a darker image. Due to the surface structure being inherently a 3D feature, the correct depth of field is important to obtain an image with good quality, but on the other hand, a darker image loses detail of the surface structure. A typical optical microscopy image can be seen in Figure 4.6. The surface was observed with a 200x magnification, the micro-scale structure can be observed from this image, however, the features of the 3D structures

and finer details are difficult to observe. The optical microscopy images can provide a preliminary observation to identify the surface structure, the “brick-like” post structures are seen clearly. It is also a good way to examine the superhydrophobic surface due to its convenience, availability and low running cost, but more fine-scale details require a more effective method.

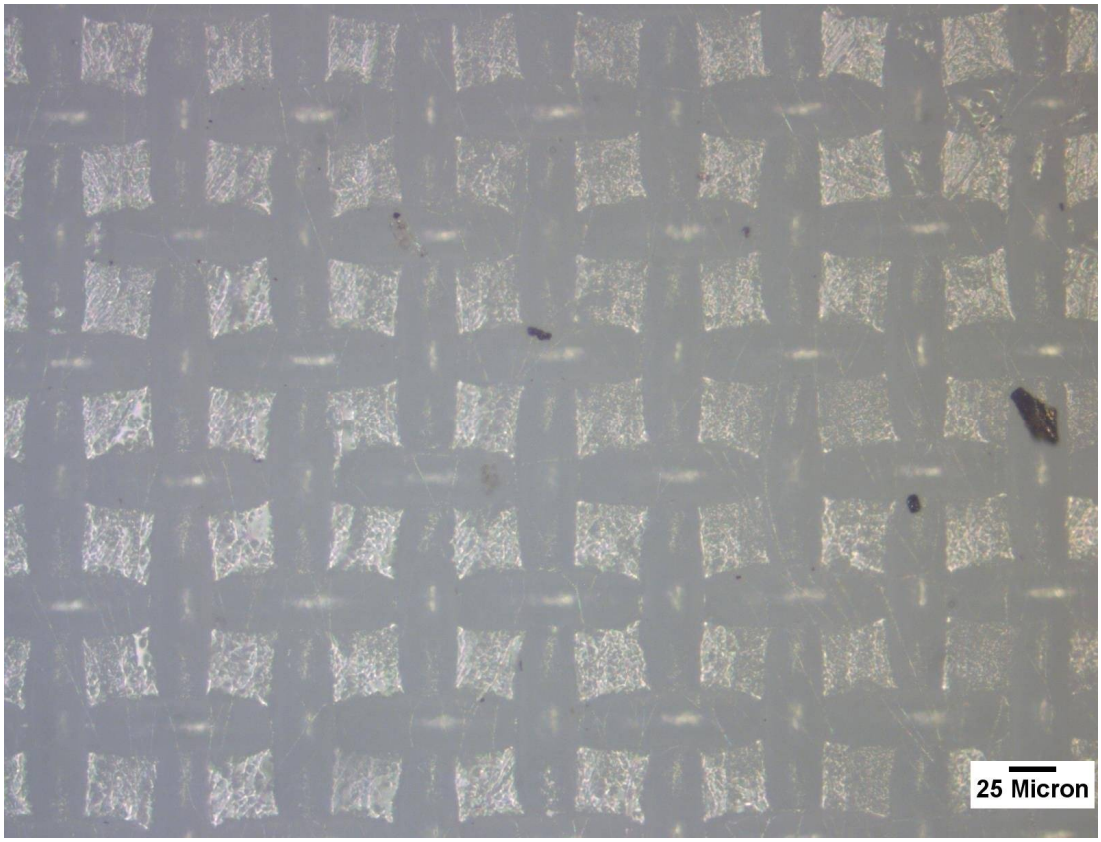

Figure 4.6. Optical microscopy image of a 40030 surface with 200x magnification.

The scanning electron microscope (SEM) can give a much better field of depth and higher resolution for the images, Flegler et al. (1993). The SEM is a type of electron microscope which uses a focused beam of electrons to scan the sample surface to produce images. In the scanning, the electrons interact with atoms of the sample surface, producing various signals that contain information about the sample's surface topography and composition. To enhance the interaction between the electron beam and

the atoms of the surface, the surface should be conductive or coated with conductive material (e.g. carbon, chromium, gold or other metals, carbon and chromium are used in this work). SEM can provide a resolution better than 1 μm. In addition, to avoid ionization, the electron beam must be working in a vacuum or low-pressure chamber. A series (from 200x to 5000x magnification) images of 40030 xPTFE are shown in Figure 4.7 and Figure 4.8, and more images of the other (30040 and 50025) xPTFE surfaces are shown in Figure 4.9 and Figure 4.10.

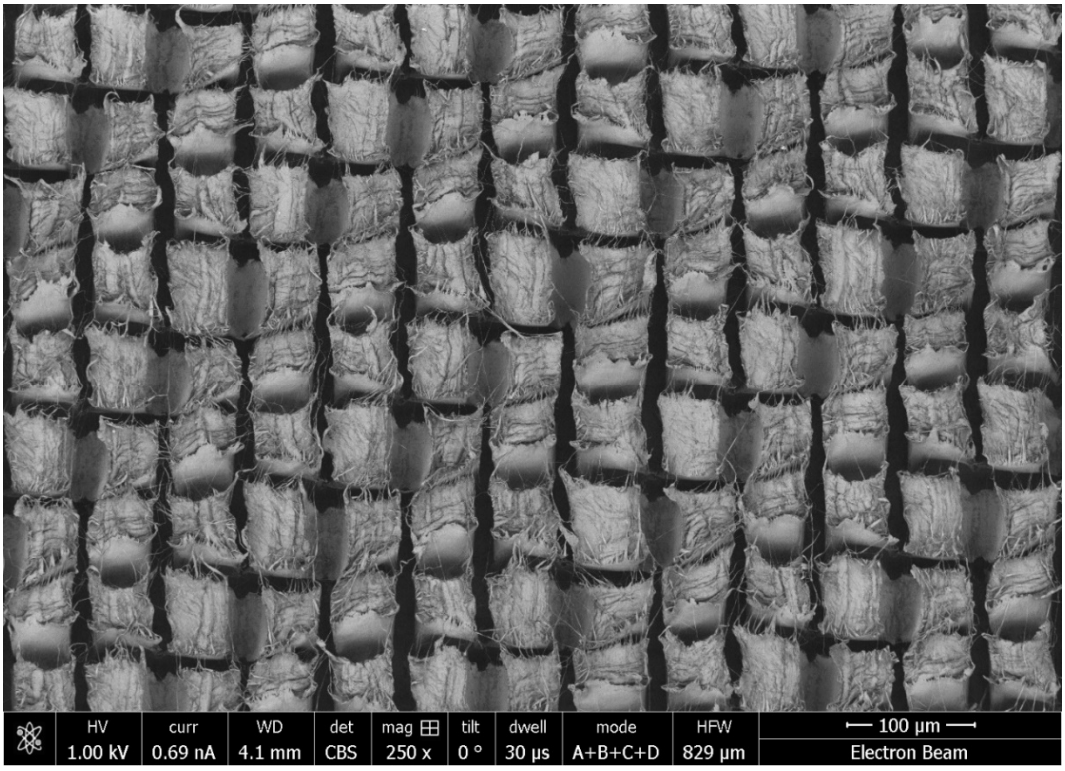

Figure 4.7. SEM images of a 40030 xPTFE surface at 250x magnification.

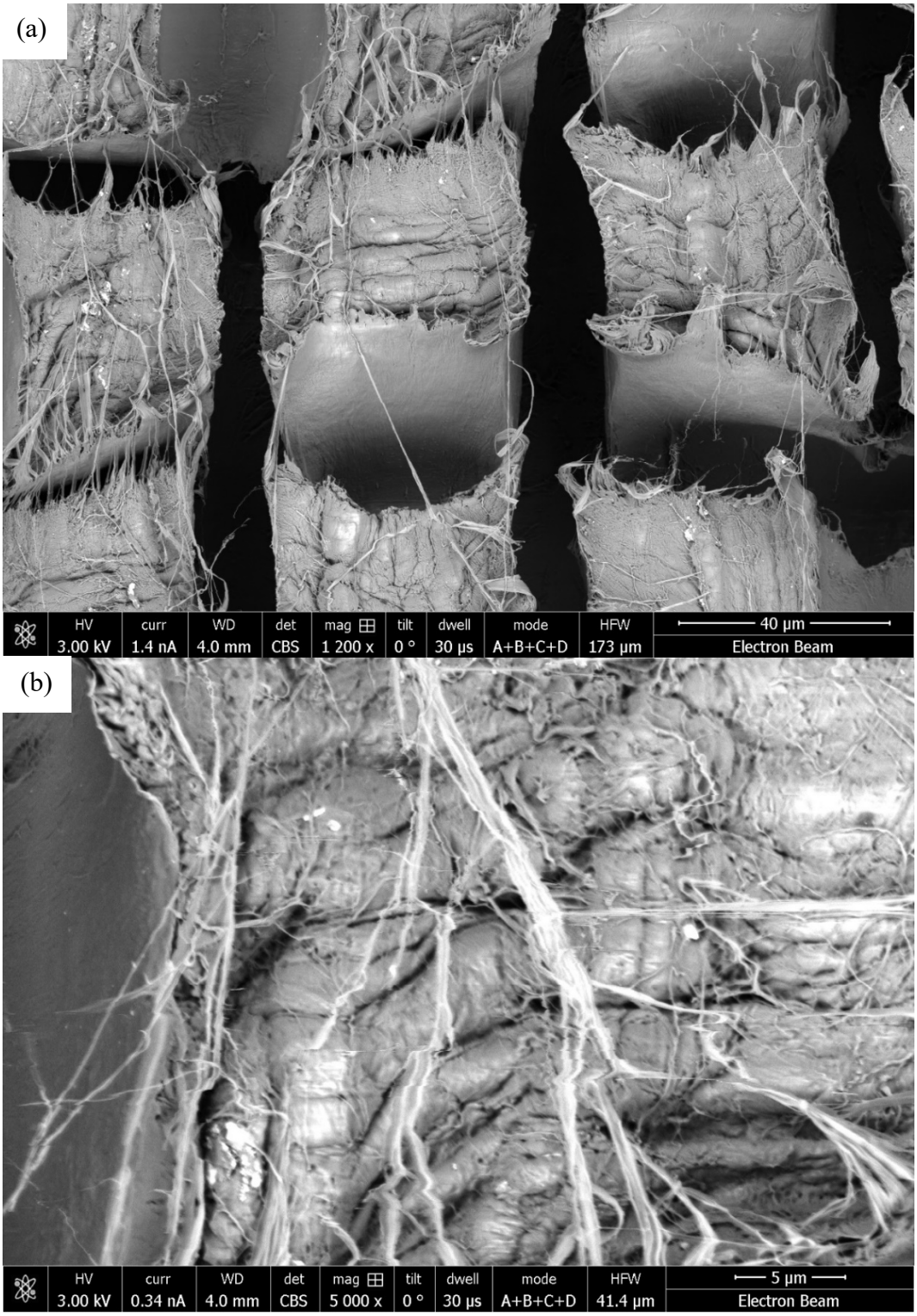

Figure 4.8. More detailed SEM images of a 40030 xPTFE surface at (a) 1200x, (b)5000x magnification.

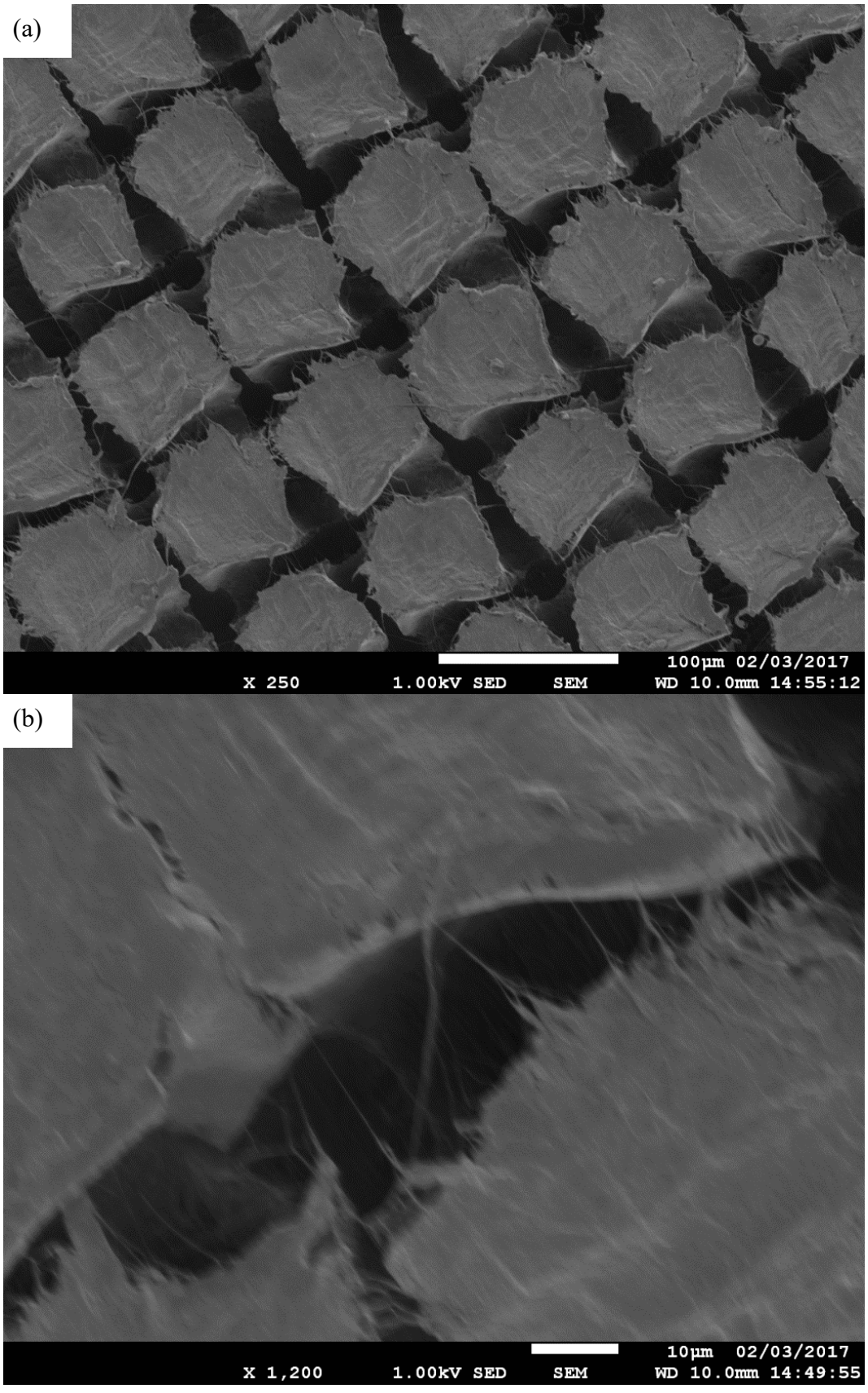

Figure 4.9. SEM images of the 30040 xPTFE surface, at (a) 250x and (b) 1200x magnification.

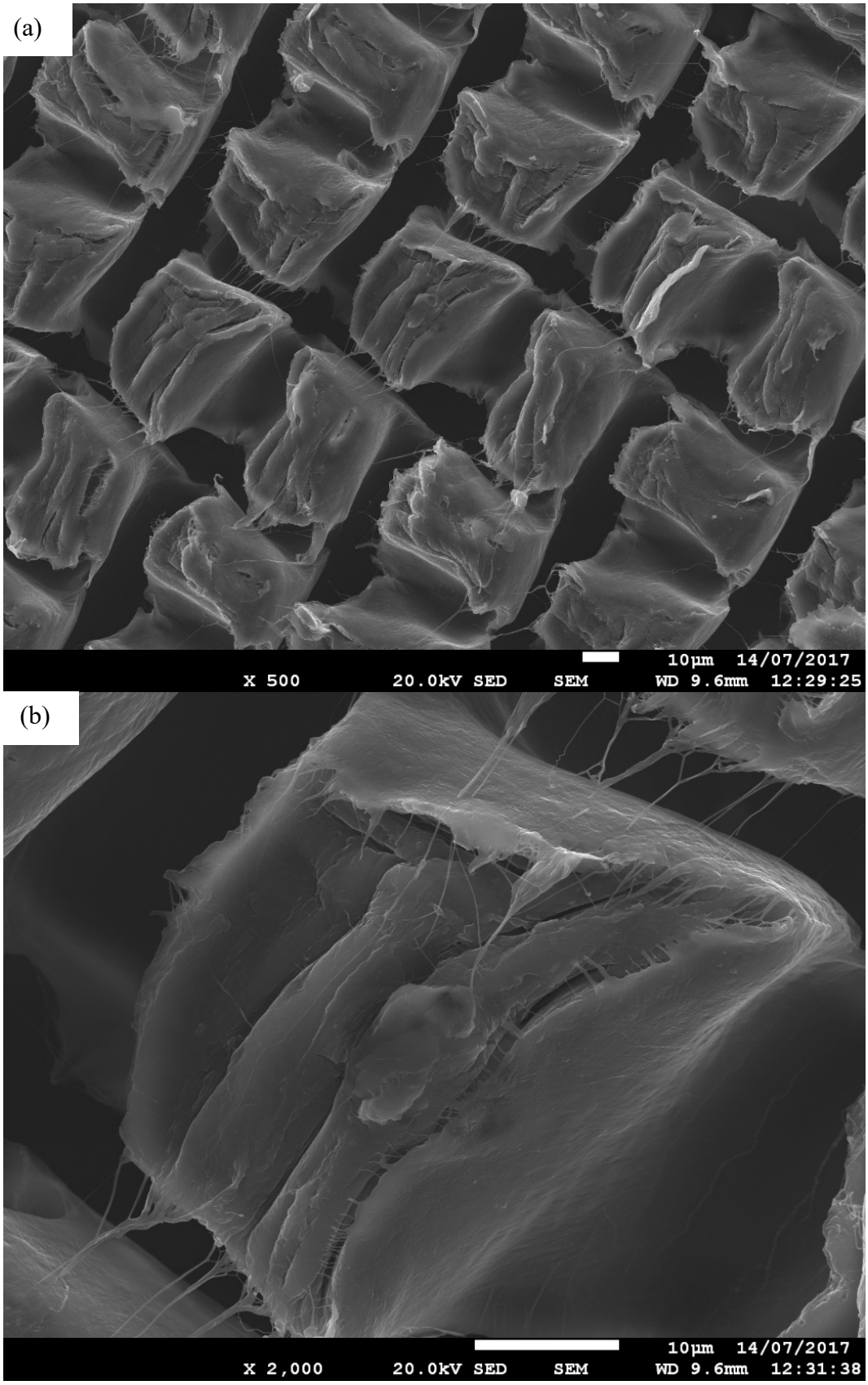

Figure 4.10. SEM images of the 50025 xPTFE surface at (a) 500x and (b) 2000x magnification.

From the images above, the highest resolution of the SEM images is about 1 μm (Figure 4.8(b)) and it can be clearly seen the quality is far better than the optical microscopy images shown in Figure 4.6. From this high resolution, a dual-scale structure can be observed on the surface. In the ten-micrometres-scale (Figure 4.7), the regular "brick-like" structure is created directly via the embossing of the meshes as a negative printed from the stainless steel meshes. On the top of the bricks, scratches were observed as a result of the sanding before the hot embossing process. In addition, on the one-micrometre-scale (Figure 4.8), some "hair-like" fibres with a diameter around 1 micrometre which stand on the edges of each "bricks" can be observed. We suggest that these fibres were created by separating the meshes from the PTFE surfaces. The PTFE was partly melted during the embossing, and sticks to the wires of the meshes after the cooling process. When the meshes were separated from the PTFE surfaces, the attached PTFE surfaces were pulled out and extended to form these fibres. As these fibres are only created at the edges of each "brick", increasing the density of the bricks can increase the density of these fibres as well. Consequently, this dual-scale structure could give a significant contribution to the surface superhydrophobicity (reported in many cases, details of which were introduced in Section 2.2). This dual-scale structure could be the reason for the higher superhydrophobicity of 40030 and 50025 xPTFE surfaces than the 30040 xPTFE surface. The size, open area ratio and density of embossed "bricks" are listed in Table 4.3.

Table 4.3. Dimensions of virgin embossed xPTFE surfaces

Mesh type		30040	40030	50025
Brick size	[1]	40 μm	34 μm	26μm
	[2]	59 ± 3 μm	32.4 ± 3 μm	23.3 ± 3 μm
Brick density	[1]	140/mm^2	250/mm^2	388/mm^2
	[2]	116 ± 2/mm^2	262 ± 2/mm^2	393.6 ± 2/mm^2
Open area ratio	[1]	72%	72%	74%
	[2]	42%	54%	55%

[1] Estimated from the dimensions of the embossing meshes.

[2] Average value measured from the SEM images.

From the SEM images, the dimensions of these surface structures on the xPTFE roughly agree with the estimation made using data from the embossing meshes. However, due to the 3D structure of the meshes, the spaces between each "bricks" are smaller than the diameter of the mesh wire and the shapes of "bricks" are not as regular as expected. This may be the reason for the open area ratios observed via SEM imaging are lower than the estimation using the mesh dimensions. In general, this observation indicates that the embossing process successfully transferred the shape of the meshes to the PTFE surfaces and provided a size of regular "brick-like" surface structure around 30 microns as expected. Furthermore, the one-micrometre-size "hair-like" structure created a dual-scale structure for the surface and offered an unanticipated "bonus" to the surface superhydrophobicity.

4.3 Water bouncing experiments

Because of the arguments regarding the static contact angle measurement which were discussed in Section 4.1. being highly dependent on the surface preparation, it cannot be solely used to characterize a surface's properties. Here another method, using a water drop bouncing on the surface to examine the surface property is implemented. This

method can probe many of the surface's properties and is especially useful for evaluating a surface's superhydrophobicity (Crick and Parkin (2011)). As introduced in Section 2.1.2, Crick and Parkin (2011) and (2013) originally reported this method and suggested using the number of water droplet bounces on a surface to evaluate its superhydrophobicity (for a fixed volume of droplet and height of drop). They suggested that such water drop bouncing experiments incorporates the surface's fundamental hydrophobicity and dynamic interaction with that surface.

Following the measurement in Section 4.1, the static contact angles of the xPTFE surfaces is around 145° which indicates the xPTFE surfaces stand on the boundary between hydrophobic and superhydrophobic surfaces. In this section, the water bouncing experiments were undertaken to examine the xPTFE surface's superhydrophobicity and provided a more obvious and convenient definition for that boundary. The experimental set-up required a levelled platform and a high-speed camera (1000fps, SONY RX10). An 8 μL coloured distilled water droplet from a 27 gauge dispensing tip fell from a height of 20 mm above the surface. This height was suggested by Crick and Parkin (2011), as the maximum height for the droplet to suffer no break up. The 8 μL droplet volume was determined as minimum drop size that could fall under its own weight from a 27 gauge dispensing tip (i.e. the weight is sufficient to overcome surface tension). Larger droplets required a lower drop height to avoid fragmentation that reduced the chance of, and the maximum number of bounces. Smaller droplets allowed for higher drop heights without fragmentation and also increased the maximum number of bounces, but it also increased the velocity when the drop contacted the surface. Such high velocity could result in the droplet penetrating in to the surface structure and damaging the Cassie-Baxter state. The series of images

showing water droplet bouncing on the 30040, 40030 and 50025 xPTFE surfaces are shown in Figure 4.11, Figure 4.12, and Figure 4.13, respectively.

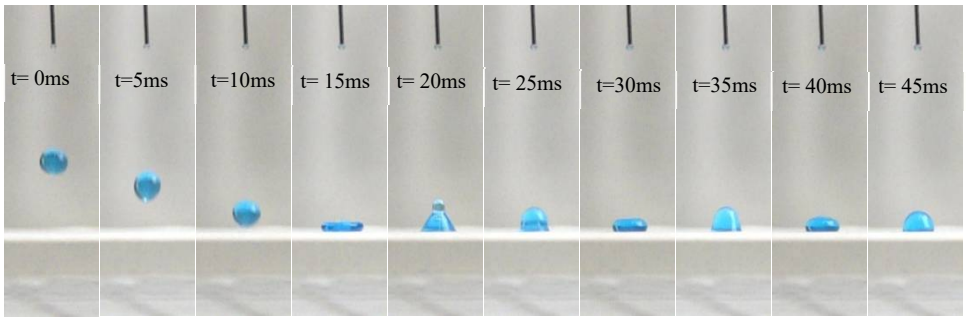

Figure 4.11. The images of a water drop hitting the 30040 xPTFE.

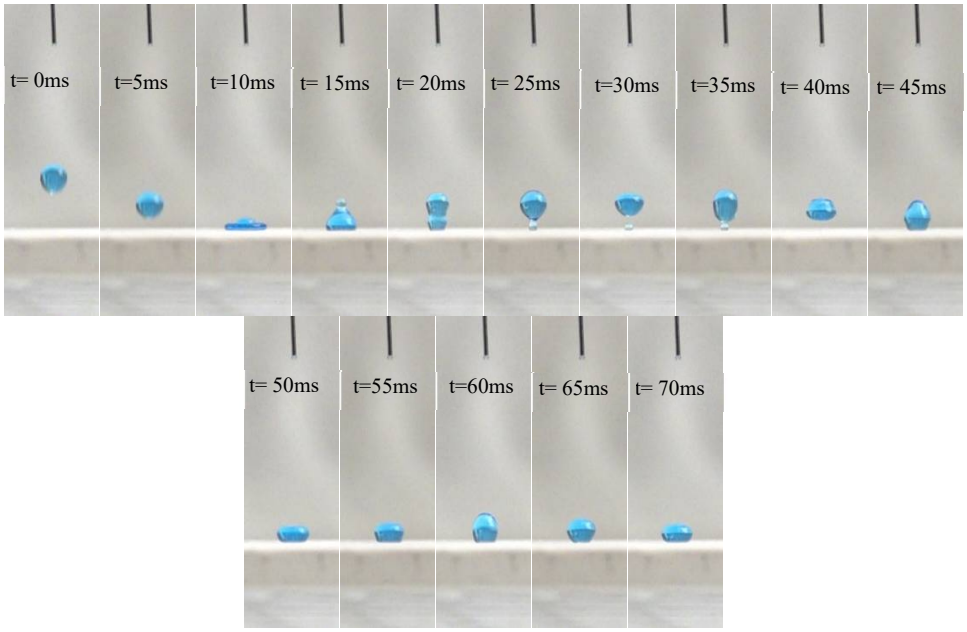

Figure 4.12. The images of a water drop bouncing on the 40030 xPTFE.

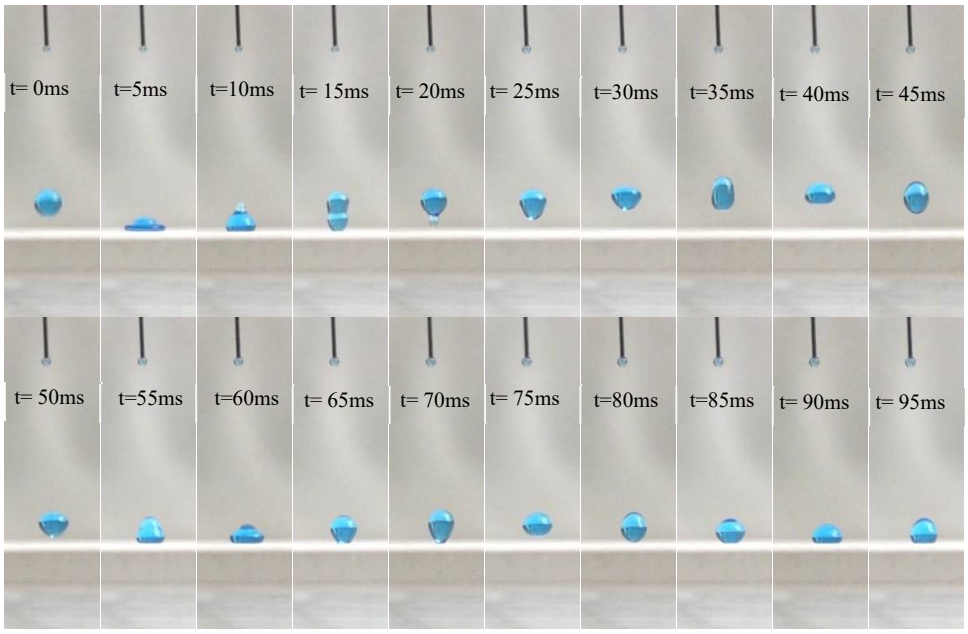

Figure 4.13. The images of a water drop boucing the 50025 xPTFE.

From the recorded videos and the images shown in Figure 4.10 - 4.12 the water droplets bounced on the 40030, 50025 xPTFE surfaces but no bouncing was observed on the 30040 xPTFE surface. When the water droplet touched the 30040 xPTFE surface, the droplet separated and deformed into a flat shape, then the surface tension forced the droplet to reform to a spherical shape in about 10 ms. During this receding process, a receding contact angle lower than 90° (time = 20 ms in Figure 4.11) was observed, which was much lower than the receding contact angle measured in Section 4.1.2. This is an indication that the surface has lost its superhydrophobicity during the droplet impact, due to the water drop penetrating into and pinned on the surface structure resulting in a loss of the Cassie-Baxter state. Consequently, the kinetic energy of the drop was consumed in this process and no bounce occurred. On the 40030 xPTFE surface, when the water droplet was bouncing back, the receding contact angle is still higher than 90° (time = 15 ms and 20 ms in Figure 4.12) unlike what happens on the 30040 xPTFE surface. The high receding contact angle provides a sufficiently large

force resulting in a bounce back. In addition, before the droplet fully bounced back, a small sub-drop separated from the main drop because of a slight pinning on the surface. A part of their kinetic energy is lost in this process and only one bounce occurred. For the 50025 xPTFE surface, two bounces occurred and showed a higher superhydrophobicity than the other two surfaces. The reasons for its higher superhydrophobicity may be that the higher brick density and smaller space between each brick in comparison with the other surfaces. The narrow space between the bricks decreases the chance of the water drop penetrating the surface structure. This idea agrees with the morphology analysis in Section 4.2 that the 50025 xPTFE surfaces have a higher superhydrophobicity due to a higher density of the one-micrometer-scale "hair-like" structures.

Crick and Parkin (2011) suggested that exceptionally hydrophobic surfaces which pin water can reduce the efficiency of "Lotus-effect" self-cleaning and even prevent water rolling as it moves over a surface. Hence, a surface capable of achieving one or more bounces (occurred on the static contact angle higher than 150°, the relationship between number of bounces and static contact angle is shown in Figure 2.7) can be judged to be superhydrophobic. The results of our water bouncing experiments proved that the 40030 and 50025 surfaces can be judged as superhydrophobic surfaces, and 30040 could be called weakly-superhydrophobic as it exhibits a similar static contact angle and contact angle hysteresis to other surfaces without bouncing occurring.

4.4 Slip-length measurements

As introduced in Section 2.3, superhydrophobic surfaces can provide considerable drag reduction in both laminar and turbulent flows. After successfully manufacturing superhydrophobic xPTFE surfaces, the drag reduction provided from these surfaces

was investigated by measuring the slip-length as will be presented in this Section. Measuring the slip-length requires a well-designed flow set-up, a sensitive and accurate experimental equipment. In the literature review, there are two methods based on two different types of flow: rotating-disk method and channel-flow method.

4.4.1 Rotating disks methods

Following the concept of the slip-length and previous studies regarding the surfaces which have the same type of surface features (details discussed in Section 2.3.2), the potential slip-length of xPTFE surfaces could be expected to be about tens of micrometres (i.e. the order of the "large" scale surface structure). For this small scale, a rheometer is the best choice for this measurement due to its high accuracy and well-controlled viscometric flow field. The rheometer used here is a torque controlled, compressed air bearing system and measures the angular velocity (at fixed torque) to measure the fluid viscosity. The available rheometer in our laboratory is an Anton Paar MCR 302 rheometer which has a measurable torque range from 1 to 200 nN·m with a resolution of 0.1 nN·m, seen in Figure 4.14. A theoretical analysis and experimental results of the slip-length measurements on xPTFE surfaces using two geometries: cone-and-plate and parallel-plates, are presented in the sections below.

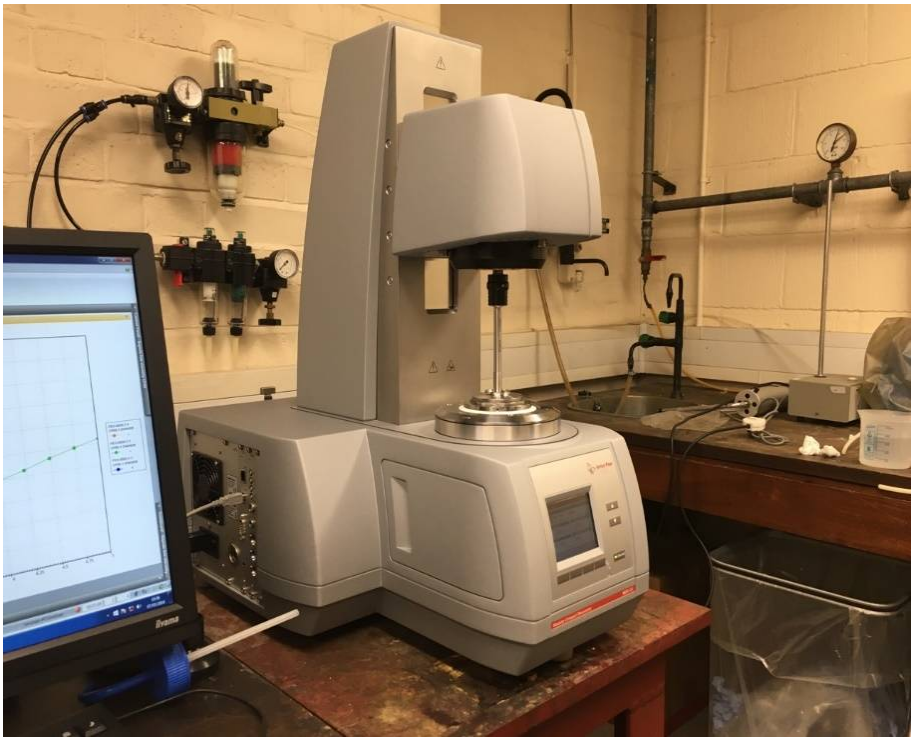

Figure 4.14. Anton Paar MCR 302 rheometer.

4.4.1.1 Drag reduction on a cone-and-plate geometry

The cone-and-plate is a commonly used geometry for rheometric experiments which is shown in Figure 4.15. The cone-and-plate system includes a rotating cone which was driven by the rheometer and a fixed stainless steel bottom plate. The driving force/torque and rotating velocity were measured and recorded to investigate the flow field between the cone-and-plate. In a cone-and-plate, the shear rate is constant, resulting in a Couette flow which is simple and can be calculated analytically neglecting any inertial or edge effects.

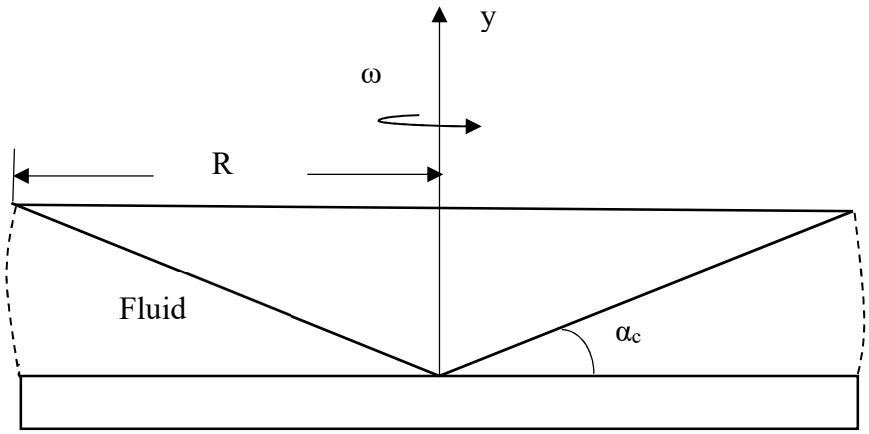

Figure 4.15 A schematic of cone-and-plate system.

Because the shear rate of the fluid flow between the cone and plate is constant, the shear stress τ can be calculated as:

$$\tau=\mu\frac{du}{dy}=\mu\frac{\omega\cdot r}{\tan\alpha_c\cdot r}=\mu\frac{\omega}{\tan\alpha_c}. \qquad 4.1$$

The torque T acting on the cone-and-plate can be calculated as follows:

$$T=\int_0^R 2\pi r\cdot\tau\cdot dr\cdot r. \qquad 4.2$$

Replacing the shear stress $\tau=\mu\frac{\omega}{\tan\alpha_c}$ gives:

$$T=\int_0^R 2\pi r\cdot\mu\frac{\omega}{\tan\alpha_c}\cdot dr\cdot r. \qquad 4.3$$

After integration:

$$T=\frac{2}{3}\pi\mu\frac{\omega}{\tan\alpha_c}R^3 \qquad 4.4$$

where T is the torque of the cone-and-plate, μ is the viscosity of the fluid, ω is the angular velocity, α_c is the angle of cone and R is the radius of the cone-and-plate. This is the classical equation for cone-and-plate system to calculate the viscosity of the fluid when tested in a rheometer (Barnes et al. (1989)). If we apply the slip-length b into

equation 4.3 above, the shear rate will no longer be constant, and the shear stress τ will become a function of r:

$$\tau = \mu \frac{\omega \cdot r}{\tan\alpha_c \cdot r + b}. \tag{4.5}$$

Then replacing the shear stress τ in equation 4.1, the torque with slip T_s will be:

$$T_s = \int_0^R 2\pi r \cdot \mu \frac{\omega \cdot r}{\tan\alpha_c \cdot r + b} \cdot dr \cdot r. \tag{4.6}$$

After integration:

$$T_s = \frac{2}{3}\pi\mu \frac{\omega}{\tan\alpha_c} R^3 \cdot \left[\begin{array}{l} 1 - \frac{3}{2} \cdot \frac{b}{\tan\alpha_c \cdot R} + 3\left(\frac{b}{\tan\alpha_c \cdot R}\right)^2 \\ -3\left(\frac{b}{\tan\alpha_c \cdot R}\right)^3 \times \ln\left(1 + \frac{\tan\alpha_c \cdot R}{b}\right) \end{array} \right]. \tag{4.7}$$

Setting $s_f = \frac{b}{\tan\alpha_c \cdot R}$ and defining the torque without slip to be $T_0 = \frac{2}{3}\pi\mu \frac{\omega}{\tan\alpha_c} R^3$,

$$T_s = T_0 \cdot \left[1 - \frac{3}{2} \cdot s_f + 3{s_f}^2 - 3{s_f}^3 \cdot \ln\left(1 + \frac{1}{s_f}\right) \right]. \tag{4.8}$$

The drag reduction *Dr* provided by a slip-length *b* is:

$$Dr = \frac{T_0 - T_s}{T_0} = \frac{3}{2} \cdot s_f - 3{s_f}^2 + 3{s_f}^3 \cdot \ln\left(1 + \frac{1}{s_f}\right). \tag{4.9}$$

According to equation 4.9 above, the drag reduction is a function of the geometric factor $s_f = \frac{b}{\tan\alpha_c \cdot R}$, and s_f is determined by the slip-length and the geometry of the cone-and-plate. Hence, the drag reduction should be independent of the shear rate. To

estimate the experimental results, this theoretical drag reduction of different geometries for various slip-lengths was calculated and the results are shown in Figure 4.16.

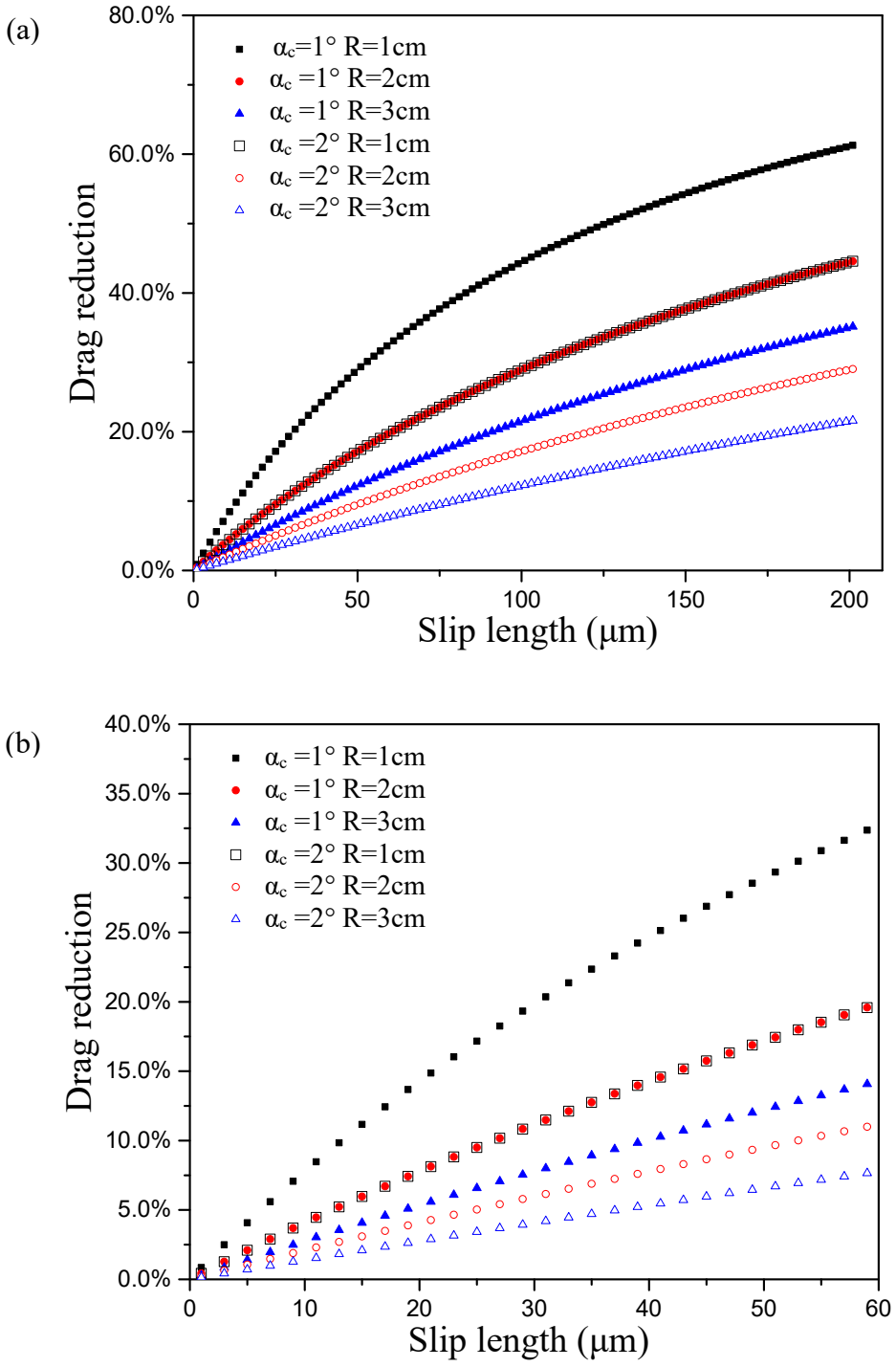

Figure 4.16 Theoretical drag reduction of the superhydrophobic surface vs slip-length ((a) 0~200 μm, (b) 0~60 μm) measured by cone-and-plate.

From Figure 4.16 above, the drag reduction increases with increasing s_f. That means the drag reduction increases with an increase of the slip-length b and a decrease of the plate radius and the angle of the cone-and-plate. For the surface with a certain slip-length, the drag reduction increases with a decrease of cone angle and its radius. On the other hand, a large torque which means higher accuracy can be measured by the rheometer from a smaller cone angle and larger cone radius. Hence, the choice of the geometry is a significant issue for accurate experiments. As introduced in the Section 2.3, the slip-length is also a function of fluid viscosity. If the drag reduction is caused by a pure layer of gas, the slip-length follows the equation 2.6: $b = l_g\left(\frac{\mu_l}{\mu_a}-1\right)$. Hence increasing the fluid viscosity is also a potential method to increase the drag reduction and make the results more easier to measure as was done by Choi & Kim (2006) and Srinivasan et al. (2013). The larger slip-lengths were measured using higher viscosity fluid and will be in introduced in Section 4.4.1.6.

4.4.1.2 Drag reduction on a parallel-plates geometry

The parallel-plates geometry is similar to the cone-and-plate system of the rheometer, but the rotating cone is replaced by a flat plate and the two plates are separated by a controllable gap of distance h. The parallel plates can provide larger torque at the same angular velocity than the cone-and-plate by setting the gap between the plates to a small value. However, the shear rate between the parallel plates is no longer constant. A schematic of the parallel plates geometry is shown in Figure 4.17.

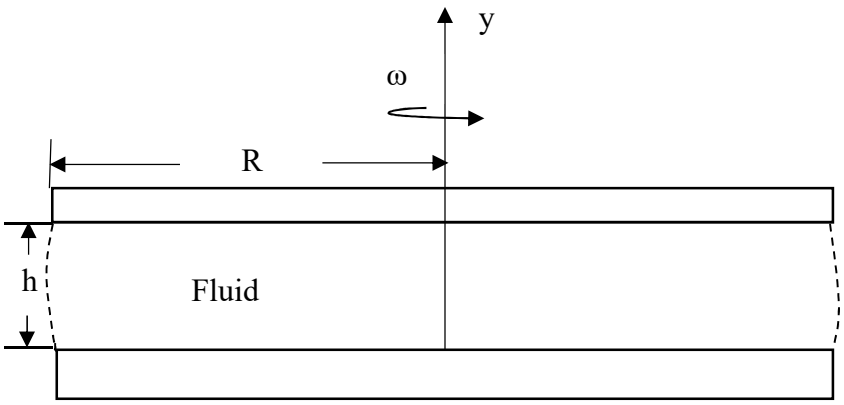

Figure 4.17 Schematic of parallel plates system.

The torque T acting on the parallel plates can be as follows:

$$T = \int_0^R 2\pi r \cdot \tau \cdot dr \cdot r \,. \tag{4.10}$$

Replacing the shear stress $\tau = \mu \frac{du}{dy} = \mu \frac{\omega \cdot r}{h}$ in equation 4.10:

$$T = \int_0^R 2\pi r \cdot \mu \frac{\omega \cdot r}{h} \cdot dr \cdot r \,. \tag{4.11}$$

After integration, the torque of parallel plates without slip T_0 is

$$T_0 = \frac{\pi \mu \omega}{2h} R^4 \,. \tag{4.12}$$

Equation 4.12 is a well-known classical equation to calculate the torque of the parallel-plates geometry (Barnes et al. (1989)). Applying the slip-length b into this classical equation, the gap distance h can be simply replaced by the gap distance plus the slip-length: $h+b$. Hence, the torque with slip T_s is:

$$T_s = \frac{\pi \mu \omega}{2(h+b)} R^4 \,. \tag{4.13}$$

The drag reduction Dr from parallel plates is then:

$$Dr = \frac{T_0 - T_s}{T_0} = \frac{1}{1 + \frac{h}{b}}. \qquad 4.14$$

From equation 4.14, it can be seen that determining the slip-length using parallel-plates is different to the cone-and-plate geometry. For the cone-and-plate geometry, the drag reduction only depends on the slip-length and the dimensions of the geometry, hence it is a constant for an experiment with a certain test surface and cone-and-plate system. For parallel plates, the drag reduction can be magnified by decreasing the gap distance between the parallel plates. This is an important result, especially for investigating small slip-lengths on the order of tens of microns. For example, given 5cm diameter parallel plates with a 500μm gap, a superhydrophobic surface with 20μm slip-length can provide 3.85% drag reduction from equation 4.14. If the gap is decreased to 200μm, the drag reduction will be increased to 9.1%. A controlled-stress rheometer is typically accurate to ± 2% (Escudier et al. (2001)), hence, the 3.85% drag reduction is very close to its inherent resolution. The calculation of the equations above with a typical geometry of 5 cm parallel plates for different gaps is shown in Figure 4.18.

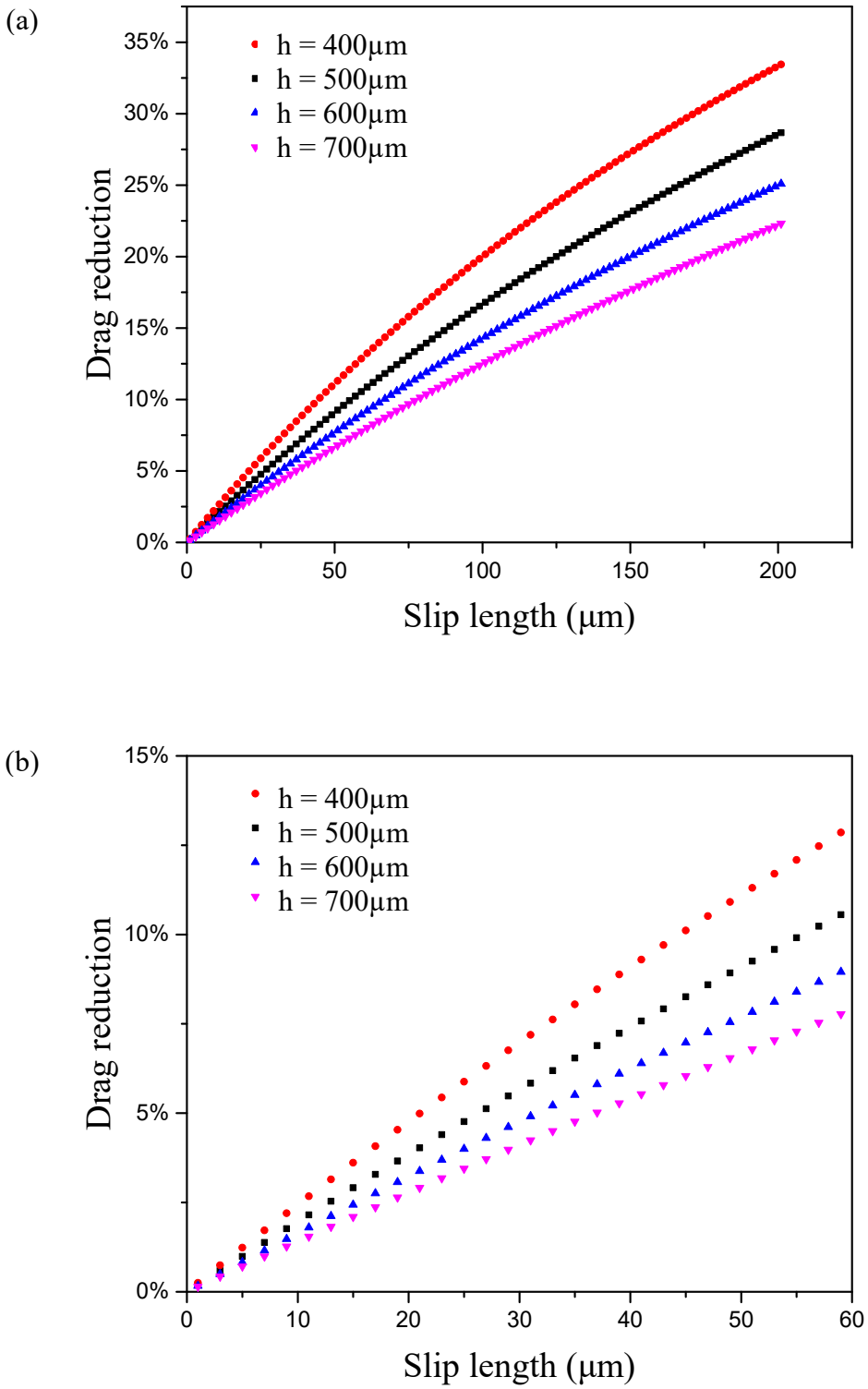

Figure 4.18. Theoretical drag reduction of the superhydrophobic surface vs slip-length ((a) 0~200 µm, (b) 0~60 µm) measured by a 5 cm parallel-plates for different gap heights.

4.4.1.3 Discussion

From the analytical calculations detailed above, the following can be understood: the flow of water flow between rotating disks is a direct method to measure slip and the resulting flow is similar to many maritime applications. The rheometer is an accurate system which can apply torques on the order of nN·m. The slip-lengths could be measured via a proper experimental technique, and can be used to predict the drag reduction in many other applications. The two types of geometry, cone-and-plate and parallel plates are the most commonly used on the rheometer. From the calculations shown above, the drag reduction is independent of the shear rate and only related with the slip-length and the geometric characteristics of the device. For the cone-and-plate, the drag reduction increases with increasing slip-length and decreasing plate radius and the angle of the cone-and-plate. That means for the same superhydrophobic surface and geometry, the drag reduction is constant.

The parallel-plates geometry is different to the cone-and-plate. For a certain cone-and-plate, the drag reduction is only related to the slip-length which is determined by the surface characteristics. The gap distance between the parallel plates can be decreased to magnify the drag reduction, it is important for the experiments with small slip-lengths which can make the drag reduction sufficiently large to be measured. From sample calculations, for the same radius of the plate, the torque of the parallel plates for a gap of 200 μm is about 3 times greater than the 1° cone-and-plate. The larger torque essentially means more accurate results. But on the other hand, the drag reduction measured by the cone-and-plate for the same slip-length is higher than the parallel-plates. In addition, for a cone-and-plate, the system only measures the angular velocity for a given torque. For the parallel plates, the gap distance should be considered and that additional variable increases the uncertainty of the system especially for small gaps.

Considering all these factors, an appropriately selected geometry is essential for an accurate slip-length measurement as will now be discussed.

4.4.1.4 Experimental set-up

Following the theoretical analysis above, there are several issues that should be considered when bringing the theory into practice. An appropriate choice of experimental conditions including the type of working fluids, measuring system geometry and the flow conditions (shape of free surface and flow shear rate) is required. Firstly, a working fluid of pure distilled water is selected because a number of working environments for superhydrophobic surfaces are related with water. Because the slip-length increases with the viscosity of the working fluid, discussed in section 4.4.1.1, the slip-length results from other fluids may not represent the most common working conditions for the superhydrophobic surfaces.

Secondly, there are four aspects we need to consider for choosing and setting the appropriate measuring system geometry and the flow conditions: potential secondary flows, edge effects, the range of torque and drag reduction which can be measured. The analytical calculation in the last section is based on a pure steady laminar flow without any secondary flow. Hence the experiment should be conducted at a low shear-rate and Reynolds number, (the critical Reynolds number for secondary flow in rotating-disks flow can be seen in Imayama et al. (2014)). From several experiments with water, when the shear rate is lower than 500 1/s for a cone-and-plate system ($\alpha_c = 2°$, R = 3 cm) and 100 1/s for a parallel-plates system (R = 2.5 cm, Gap = 500 μm), no secondary flow occurs as shown in Figure 4.19. In addition, when using smaller con-and-plate and parallel-plates systems at the same shear rate, due to the smaller characteristic lengths,

lead to corresponding smaller Reynolds numbers and as a result no secondary flows effect will occur.

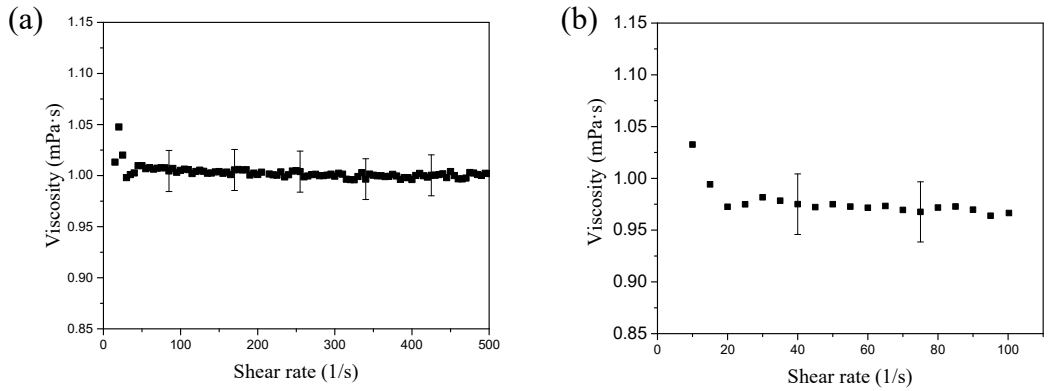

Figure 4.19. Viscosity of water measured via (a) cone-and-plates and (b) parallel-plates at 20°C.

Besides the effects from any potential secondary flow, it is also important to minimize the edge effect for the rotating disks measurement, especially in the low-torque measurement. The edge effect is caused by the unbalanced forces from an underfilled or overfilled free surface, a schematic of which is shown in Figure 4.20. The systematic errors from the edge effects could be 3% of the final result (Choi and Kim (2006), Bocquet et al. (2006), Ming et al. (2011) and Srinivasan et al. (2013)).

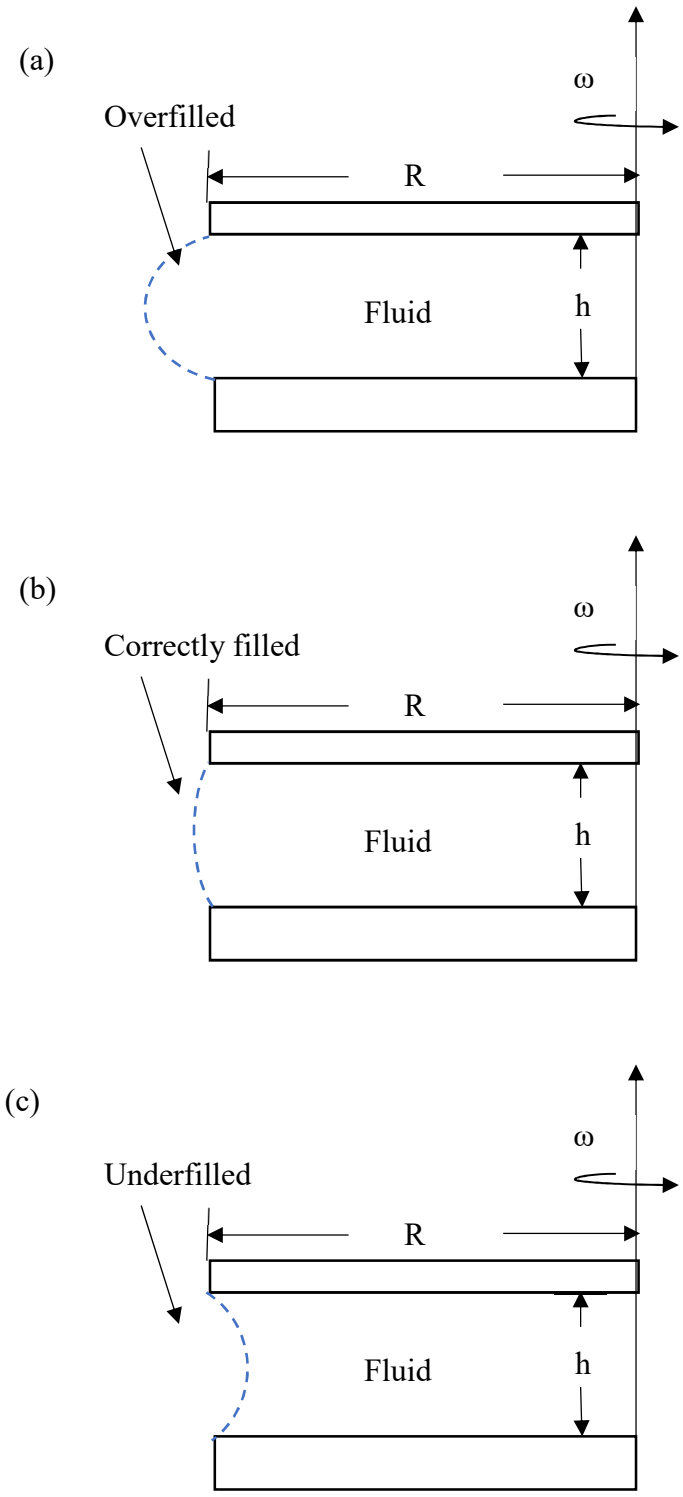

Figure 4.20. A schematic of edge effects of rotating disks measurement.

The most direct way to reduce edge effects is by reducing the size of the edge. For cone-and-plate systems that means a smaller cone angle and cone radius. From Figure 4.16, smaller cone angles means higher torques and higher drag reduction as well. Hence, a small cone angle is positive for all aspects of the measurement. Regarding the cone radius, a larger radius leads to a large torque, larger edge effect, and smaller drag reduction. According to the geometry available in our laboratory, and considering all the factors discussed above, the $\alpha_c = 1°$, radius R = 3 cm cone-and-plate system was chosen for the slip-length measurement. For parallel-plates, the larger radius provides larger torque and drag reduction and the size of the edge are all related to the gap height between the two plates, hence the largest (R = 2.5 cm) parallel-plates system was chosen in our laboratory. Then, a smaller gap gives a larger toque, the larger drag reduction and smaller size of free surface. Such a scenario benefits all the aspects of the experiments discussed above, but it also magnifies the uncertainty caused by the zero-gap position setting. This systematic error is due to the difference between the real distance and the distance measured by the rheometer. When the gap is small enough, this error can become significant and an appropriate gap has to be found by a water baseline test as determined in the following section.

Rather than carefully selecting the geometry of the measuring systems, there are two experimental methods which can be applied to reduce the edge effects as shown in Figure 4.21.

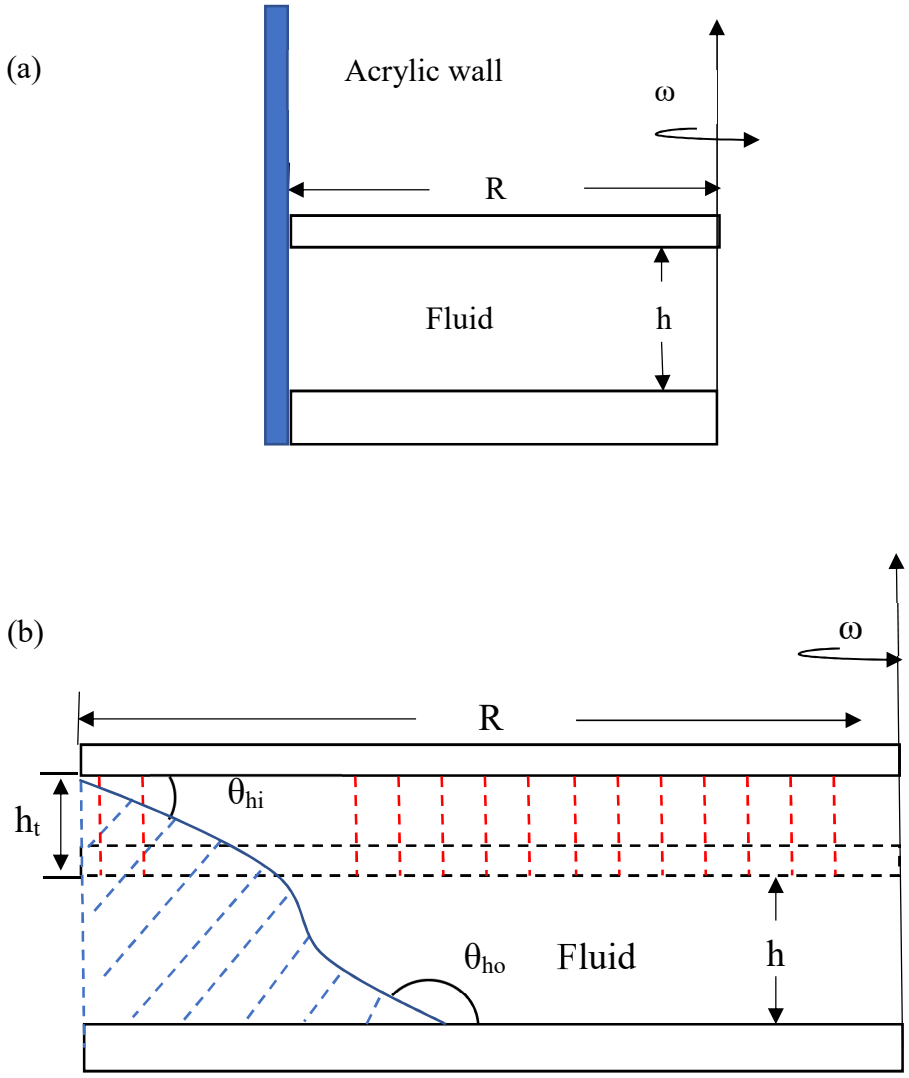

Figure 4.21. Schematics of two methods to reduce the free surface effects.

The first method is using an acrylic ring to form a fixed wall to trim the free surface during loading and the ring is then removed after loading to avoid a resulting increased torque, as seen in Figure 4.21(a). The consistent free surfaces of fluid between rotating disks were achievable using this method to reduce the uncertainty in the measurement. This method worked well for the surfaces which are not highly superhydrophobic, e.g. the xPTFE surfaces. However, it did not work for the surface with an extremely high contact angle, e.g. TiO_2 surfaces. The free edge is in an unstable state when the using the acrylic wall to force the fluid to maintain a “correctly-filled” state. The removal of

the wall could disturb this state and the fluid of the free edge area would flow away due to the surface tension force tend to reform the contact angle back to the equilibrium state. When applying the acrylic wall on an extremely high contact angle surface, this surface tension effect is too large to maintain a "correctly-filled" state during the removal of the wall. Hence, a method suggested here is using the trim space to achieve a "correctly-filled" free edge, presented in Figure 4.21(b). During loading the working fluid, the upper disk (cone for cone-and-plate system) is approaching to the bottom disk. If the fluid between two plates is more than the final expected sample volume, at some point the fluid would start to flow out of the space between the two disks while the plates close into each other. During this process, the fluid only flowed out from a certain radical location rather than axisymmetrically. In this situation, the free surface reached a balanced state and its curvature was determined by the static contact angles of both the upper and bottom disks. If this connecting point was removed/swept, the upper disk could move close to the bottom one before the fluid flowed out again. This volume between the two disks corresponding to this distance is called the maximum trim volume, which could be used to trim an underfilled free edge to a "correctly-filled" edge. The trim distance h_t could be determined by estimating the position of the upper disk at which the trim volume (crossed by red dash lines) is equivalent to the volume which we want to fill for a "correctly-filled" state (crossed by red dash lines), Figure 4.21(b). Because the curvature of the free surface is complicated and determined by the metastable static contact angles, h_t can be estimated by assuming there is no curvature (i.e. a straight line), and that the contact angle of the hydrophilic upper disk, θ_{hi}, and the contact angle of the hydrophobic bottom disk, θ_{ho} follow the relationship:

$$(90° - \theta_{hi}) + (180° - \theta_{ho}) + 90° = 180° . \qquad 4.15$$

Actually, the real θ_{hi} and θ_{ho} do not match this relationship, we only use the real value of θ_{ho} for the estimation here. The trim distance h_t can be estimated by the following relationship:

$$2\pi R^2 h_t = 2\pi R \frac{1}{2}(h+h_t)(h+h_t) / \tan(1-\theta_{ho}) = \pi R(h+h_t)^2 / \tan(1-\theta_{ho}) \qquad 4.16$$

Hence, the trim distance could be estimated and adjusted according to the experiments as 15μm for the xPTFE surfaces (contact angle around 145°) and 17 μm for the TiO_2 surfaces (contact angle around 165°).

In general, because of the small torque (tens of mN·m) and drag reduction (estimated as 5% ~ 15%), the slip-length measurements required very precise experiments. The experimental conditions had to be carefully selected and controlled to get reliable results. Distilled water was chosen as the working fluid for the measurements. The measuring system for the rotating disks method were chosen as follows: α_c = 1°, R = 3 cm for the cone-and-plate system and R = 2.5 cm for the parallel-plates with gaps ranging from 400 to 700 μm. The secondary flow and free surface effects are considered and could be solved by corresponding experimental setting and calibration techniques. The validation of the experiments is examined by a baseline test of the viscosity of water in the following section.

4.4.1.5 Baseline test

After all the aspects discussed in the last Section, the precise experimental conditions were established. The viscosity of distilled water at 20°C was measured to examine the accuracy of our experimental method and used as a baseline to calculate the potential drag reduction of xPTFE surfaces. The results contain 40 repeat tests with α_c = 1°, R = 3 cm cone-and-plate system is shown in Figure 4.22.

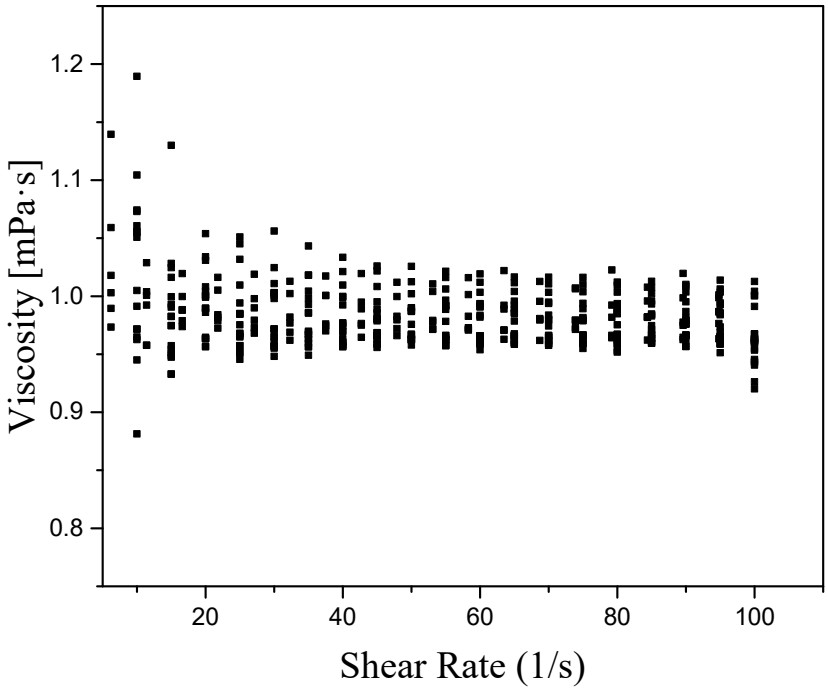

Figure 4.22. Baseline measurement for cone-and-plate (α_c=1°, R=3 cm at 20°C) geometry.

From the results shown in Figure 4.22, the average value of the viscosity of water is 1.00082 mPa·s which is close to the text book value which is 1.0016 mPa·s (Cooper and Dooley (2008)), with a difference of 0.08%. However, it needs to be noted that the error of results in the lower shear-rate range (< 20 1/s) is significantly higher due to the smaller torque at these rates. The error of these experiments in the test range of shear-

rate showed a 3.38% variation within repeats, which should be considered as a systematic error of these experiments at low shear rates.

Results of measuring water viscosity at 20°C using parallel-plates with different gaps (400μm ~700μm) are shown in Figure 4.23, each figure including 10 repeats.

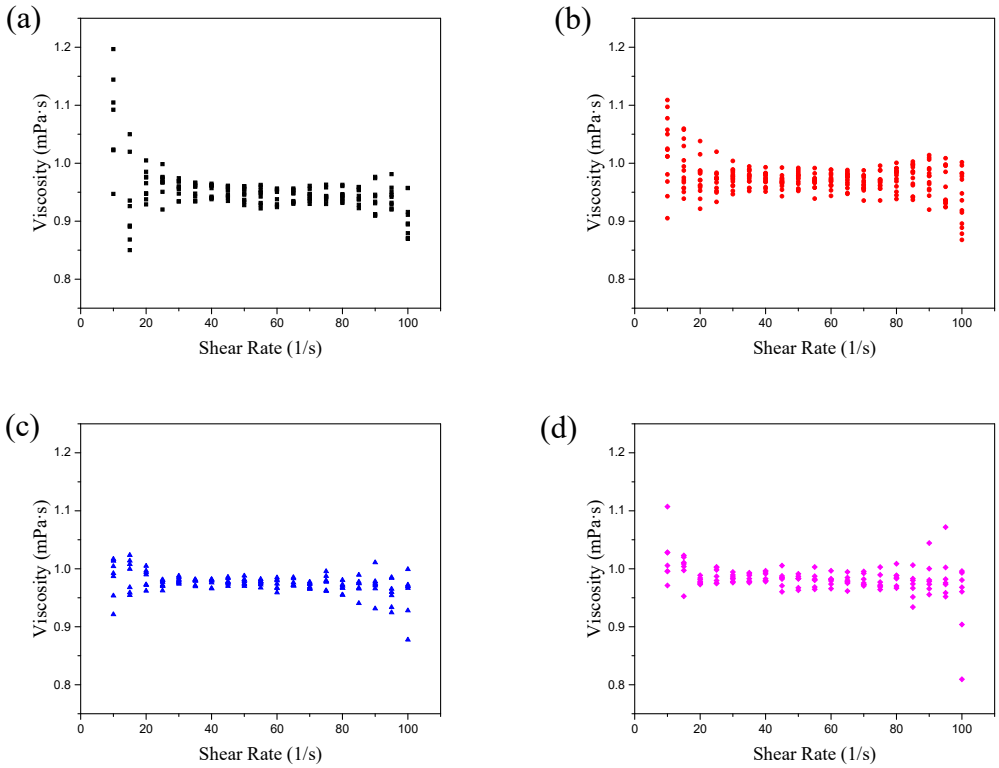

Figure 4.23. Baseline measurement for parallel-plates (R=2.5 cm) geometry at 20°C with different gaps: (a) 400 μm, (b) 500 μm, (c) 600 μm, (d) 700 μm.

The average viscosities of different gaps and the variations of repeats are listed in Table 4.4.

Table 4.4. Water baseline test for 5 cm parallel-plate system

Gap	400 μm	500 μm	600 μm	700 μm
Average viscosity	0.9510 mPa·s	0.9772 mPa·s	0.9410 mPa·s	0.9861 mPa·s
Variation of repeats	5.82%	2.87%	2.15%	2.23%

From the results, the variation of the repeats is close to the higher gap settings when the gap is selected as 500 μm. Since increasing the gap can reduce the uncertainty from the gap setting but decreasing the gap can provide larger potential drag reduction. Considering the above and the table value of the viscosity of water at 20°C, a gap of 500 μm was selected for measurements using parallel-plate system.

Including all the aspects discussed and considered above, the water baseline test results showed that our experiment is sufficiently accurate even for a low-viscosity fluid, such as water. The systematic error is within 3% which, although not negligible, is lower than the drag reduction level expected to be 5% ~ 15%, these analysis and preliminary tests works built a solid foundation for the following slip-length measurements.

4.4.1.6 Cone-plate geometry measurement

Following the discussion above and the experience gained from the baseline tests, the slip-lengths of the xPTFE surfaces were measured using an α_c = 1°, R = 3 cm cone-and-plate system. The free surfaces were "trimmed" to maintain a "correct-filled" condition using the acrylic wall method previously described. The experiments were conducted at room temperature which varied from 19°C to 23°C, because the working fluid temperature cannot be precisely controlled and measured by the rheometer when the lower plate is replaced with the superhydrophobic surface. From equations 4.4 and 4.9, the apparent viscosity μ_{ap} measured by the rheometer follows: $T = \frac{2}{3}\pi\mu_{ap}\frac{\omega}{\tan\alpha_c}R^3$, and drag reduction $Dr = \frac{T_0 - T_s}{T_0}$. Hence $Dr = \frac{\mu_{ba} - \mu_{ap}}{\mu_{ba}}$, where μ_{ba} is the viscosity of the distilled water as measured from the baseline test. In addition, considering temperature effects, the measured apparent viscosities were adjusted to the equivalent values at 20°C by using a linear relationship according to tabulated values from Cooper and

Dooley (2008). The apparent viscosities are shown in Figure 4.24, and the slip-lengths were determined from these results using equation 4.9.

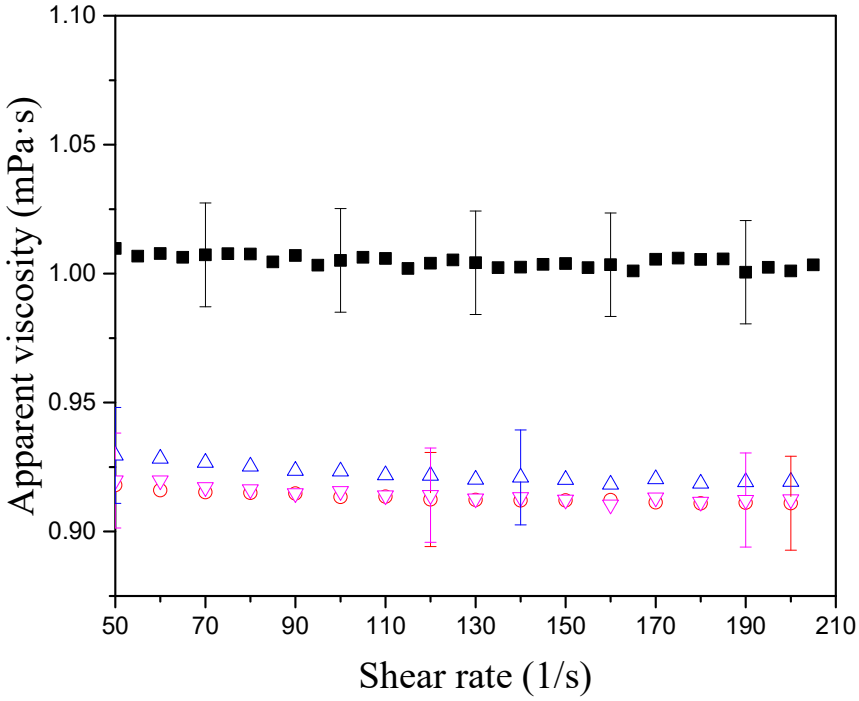

Figure 4.24. Apparent viscosities of water measured using cone-and-plate on (△) 30040, (○) 40030 and (▽) 50025 xPTFE surfaces ((■) water viscosity from baseline tests). The error bars represent the variation of the repeats.

The apparent viscosities measured on the xPTFE surfaces are significantly lower than the value measured from the baseline test, showing a drag reduction of around 7%. This drag reduction is also independent of the shear rate in agreement from the prediction in Section 4.4.1.1. In the three surfaces, the 30040 xPTFE surface showed the lowest superhydrophobicity, agreeing with the contact angle and the water drop bouncing experiments. The drag reduction of this surface measured from the cone-and-plate experiment was 6.03% which indicates a slip-length of 23 μm. The 40030 xPTFE surface provided a drag reduction of 7.1%, which is equivalent to a 27 μm slip-length. The 50025 xPTFE surface is the most superhydrophobic surface of the three, that was

also supported by the results of the contact angle measurement and the water bouncing experiment. It showed the highest drag reduction, 8%, and slip-length, 31 μm, of the three types of xPTFE surfaces. The slip-length measured by the cone-and-plate shows that the xPTFE surfaces provide a slip-length of around 30 μm which is of the same order as the dimensions of their surface features.

Furthermore, the slip-length of the TiO_2 surfaces was measured using the same method. These surfaces were manufactured by spraying mixed polymer and TiO_2 particles on an acrylic plate. The details of these surfaces were introduced in Section 2.2.6, and seen in Crick and Parkin (2011), (2013), Lu et al. (2015). These surfaces have a static contact angle higher than 165° and achieved 12 bounces in the water bouncing experiments. Our slip-length measurement also shows this surface's extraordinary superhydrophobicity, providing a drag reduction of 13.3%, which indicates a slip-length of 55 μm, the results are shown in Figure 4.25.

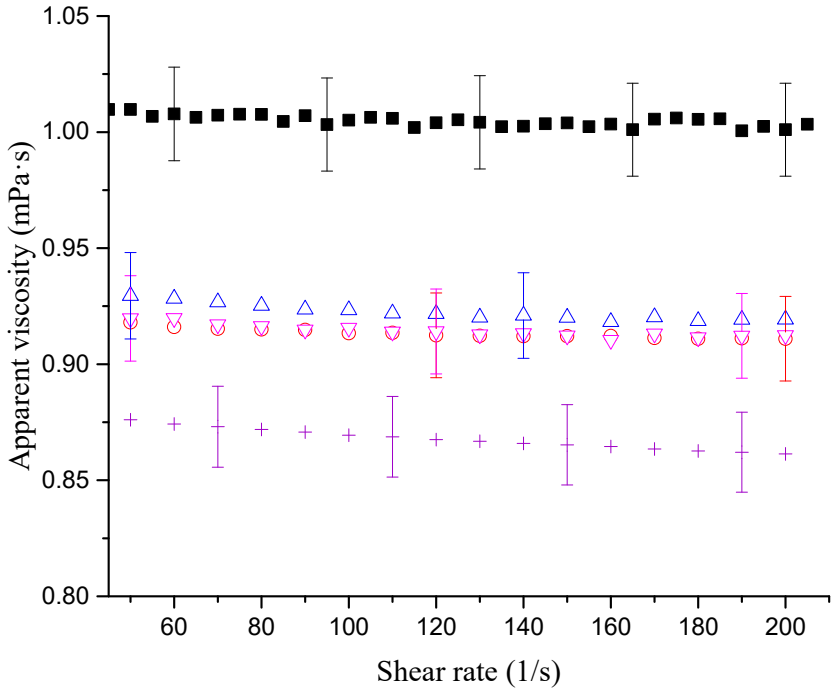

Figure 4.25. Apparent viscosities of water measured using cone-and-plate on on (△) 30040, (○) 40030, (▽) 50025 xPTFE surfaces and (+) TiO_2 surfaces. ((■) water viscosity from baseline tests). The error bars represent the variation of the repeats.

Finally, the drag reduction with two different working fluids, polyethylene glycol (PEG, molecular weight is 8000 g/mol) solutions with different concentrations (12% and 47%, w/w), were preliminary measured on 40030 xPTFE surfaces and TiO_2 surfaces. These two fluids are Newtonian and their shear viscosities were measured as 7.1 mPa·s and 285 mPa·s at 20°C respectively. The drag reduction at 20°C was measured as 10.2% ± 1.5% on 40030 xPTFE surface via an $\alpha_c = 1°$, R = 3 cm cone-and-plate. The equivalent slip-length is 40 μm ± 8 μm which is 1.48 times of the slip-length measured using water. The drag reduction on TiO_2 surfaces were measured as 24.1% ± 2% and 34.4% ± 2% for the 12% and 47% PEG solutions respectively using an $\alpha_c = 1°$, R = 3 cm cone-and-plate system. The equivalent slip-lengths are 88 μm ± 10 μm and 130 μm ± 10 μm, respectively, which are 1.6 and 2.36 times of the slip-length measured using water.

These results agreed with the discussion in Section 2.3.1: increasing the viscosity of the working fluid can magnify the drag reduction and the slip-length, as seen in Figure 4.26.

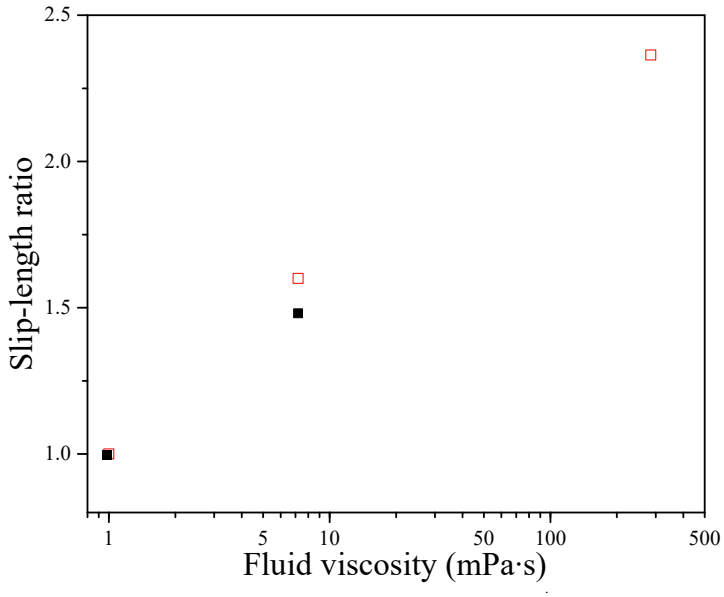

Figure 4.26. The ratio of actual slip-length over the slip-length of water vs fluid viscosity on (■) xPTFE, (□) TiO_2 surfaces.

4.4.1.7 Parallel-plates geometry measurement

As discussed in Section 4.4.1.5, the R = 2.5 cm parallel-plates was chosen to measure the slip-length with a gap of 500 µm. From the theoretical analysis in Section 4.4.1.2, the drag reduction of this geometry is smaller than the result of cone-and-plate method we used in the previous section. The slip-length can be calculated using the drag reduction following equation 4.14: $Dr = \frac{T_0 - T_s}{T_0} = \frac{\mu_{ba} - \mu_{ap}}{\mu_{ba}} = \frac{1}{1 + \frac{h}{b}}$. The measured apparent viscosities are shown in Figure 4.27.

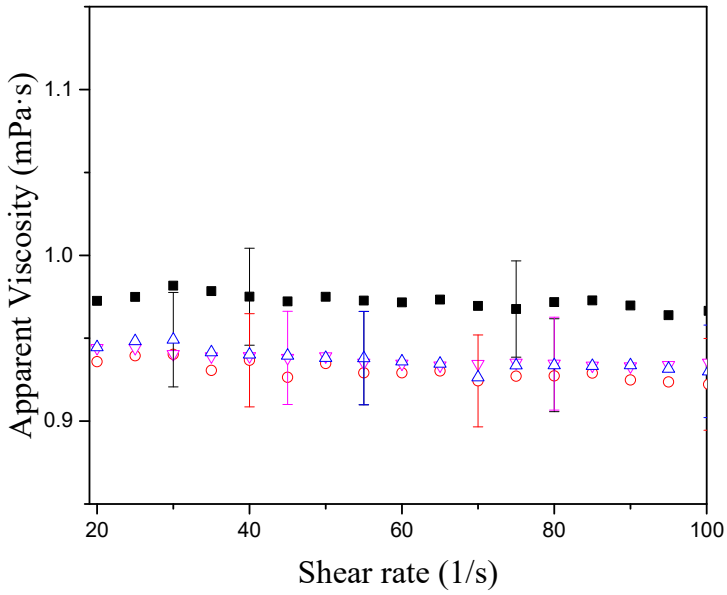

Figure 4.27. Apparent viscosities of water measured using parallel-plates on xPTFE surfaces.

Using the parallel-plates, the apparent viscosities of water measured on the xPTFE surfaces are lower than the baseline, indicating drag reductions of around 5%. The values are 4.5%, 5.3% and 5.4% for the 30040, 40030 and 50025 xPTFE surfaces respectively, which is equivalent to 24 µm, 28 µm and 29 µm slip-length. The slip-length results are close to those measured by the cone-and-plate, this repeatability providing confidence in the validity of our experiments. However, considering the larger variation of the experimental results, the smaller theoretical drag reduction, and a higher systematic error of the parallel-plates, which was discussed in Section 4.4.1.4, these slip-length measurement results of the parallel-plates should be viewed with more caution. The slip-length values discussed in the remainder of this work are those determined using the cone-and-plate method.

4.4.1.8 Conclusions for rotating disks methods

The slip-length measurements using the rotating-disks methods were analyzed and conducted using a rheometer in this section. From the theoretical analysis, the slip-length as a characteristic of the surface itself is independent of the precise flow conditions (i.e. flow geometry and shear rate). Before the slip-length measurement, the viscosity of distilled water was carefully measured using the rheometer to determine a "baseline". From several repeats of this test, a number of techniques were developed for ensuring a high accuracy of the experiments, and the accuracy of the measurement was evaluated as sufficient to investigate the slip-length. The measured viscosity of distilled water was used as a baseline value to determine the drag reduction. Furthermore, from the theoretical analysis and the experimental experience gained, the optimized geometries in our laboratory were selected as follows: for cone-and-plate, cone angle is 1° and cone radius is 3 cm and for parallel-plates, radius is 2.5 cm with 500 μm gap. Using these two measuring systems, the slip-lengths of the xPTFE surfaces were measured, and the results are shown in Table 4.5.

Table 4.5. Slip-length of xPTFE surfaces.

Mesh type	30040	40030	50025
Open area ratio	[1] 72%	72%	74%
	[2] 42%	54%	55%
Drag reduction by parallel-plates	4.5%±1.4%	5.3%±1.4%	5.4%±1.4%
Slip-length (μm)	24±8	28±8	29±8
Drag reduction by cone-and-plate	6.0%±1.6%	7.1%±1.5%	8.0%±1.5%
Slip-length (μm)	23±6	27±6	31±6

[1] Estimated by the dimensions of meshes.
[2] Measured from microscopy images.

The drag reductions were measured around 5% and 7% using parallel-plates and cone-and-plate respectively. The equivalent slip-lengths were around 30 μm for the xPTFE surfaces which are on the same order of its surface features. The results also show that the 50025 xPTFE surface has the highest and the 30040 xPTFE the lowest superhydrophobicity, respectively. This result agrees with the results from contact angle and water bouncing experiments. In addition, the slip-length of the TiO_2 surface was measured as 55 μm, which shows an extraordinary superhydrophobicity (Lee et al. (2016)) corresponding to its high static contact angle (~165°). These measured slip-length results can be used for applications to estimate the potential drag reduction or other flow effects.

4.4.2 Channel-flow method

Besides the rotating disks methods, the slip-length can be measured using a channel-flow method as well. The channel-flow is a kind of simple pressure driven flow, the working fluid is driven by pressure to flow through the channel. The driving pressure drop is equal to the friction or drag force between the fluid and the channel walls. Measuring the pressure difference between two points along the channel, the drag force can be calculated. The superhydrophobic surface can provide a slip boundary condition and therefore reduce the flow drag. The slip-length of superhydrophobic surfaces can be determined by measuring the difference of the pressure over a certain length of channel, the so-called pressure drop, with and without superhydrophobic coating. This method was reported in many studies for measuring the slip-length of superhydrophobic surfaces, e.g. Ou et al. (2004), Choi et al. (2006), Maynes et al. 2007, Daniello et al. (2009), Tsai et al. 2009, Jung and Bhushan (2010) and Song et al. (2014).

A schematic of the slip-length measurement using a channel-flow method is shown in Figure 4.28.

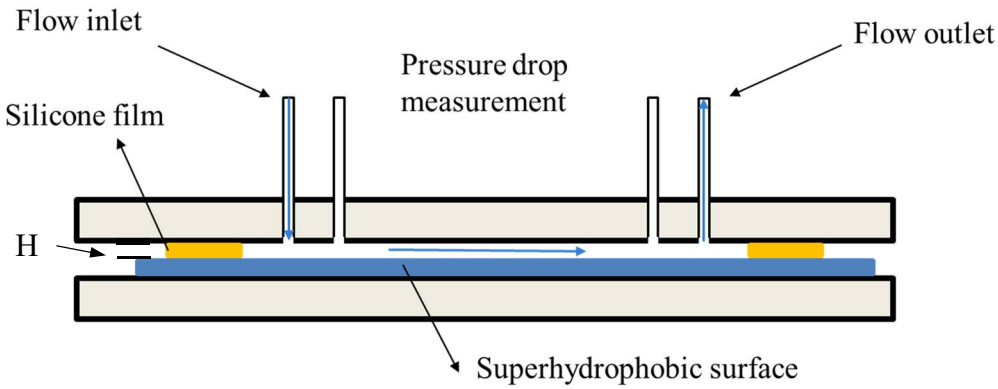

Figure 4.28. A schematic of slip-length measurement using channel-flow method.

Due to the small value, around tens of micrometres, of the slip-length, the channel height should be designed comparably to it for sufficient drag reduction which can then be easily measured. To simplify the channel-flow to a 2D condition, the width of the channel should be more than 25 times of the channel height (Ou et al. (2004) and Durst (2008)). The flow rate of a 2D channel with channel height H and channel length L in laminar flow can be determined by:

$$Q = \frac{H^3}{12\mu}\left(\frac{\Delta P}{L}\right). \tag{4.17}$$

where μ is the viscosity of the working fluid and ΔP is the pressure drop. The flow rate of a 2D channel where one side of wall is a superhydrophobic surface with slip-length b, should be as follows (Ou et al. (2004)):

$$Q = \frac{H^3}{4\mu}\left(\frac{\Delta P_{slip}}{L}\right)\left(\frac{1}{3} + \frac{b}{b+H}\right) \tag{4.18}$$

The slip-length can be calculated from equation 4.18 using the determined pressure drop, flow rate and channel dimensions (H and L).

In this work, an 8 cm long, 1 cm wide channel was cut on an ultra-thin silicon film with a nominal thickness of 200 μm, brought from SILEX Ltd, Hampshire, UK. The silicon film was then held between two acrylic plates, the upper plate has four holes drilled into it to be used as flow inlet and outlet and measuring positions of the pressure drop. The low modulus (~1.8 MPa) of the silicon film allows the device to make a seal that was experimentally verified to be leak free but also needing only a relatively light, even a consistent clamping force. Due to the deformation from this clamping, the height of the channel is no longer the nominal thickness of the silicon film and needs to be measured before measuring superhydrophobic surface. The working fluid, distilled water, flows into the channel from the first hole and out from the last hole driven by a syringe pump. The pressure drop of the channel was measured by recording the height difference between two manometer columns attached to the second and third holes which are 6 cm apart. Then the height of the channel was calculated using equation 4.17. The channel height was measured in this manner as 187.5 μm and the relationship between pressure drop and the flow rate is shown in Figure 4.29.

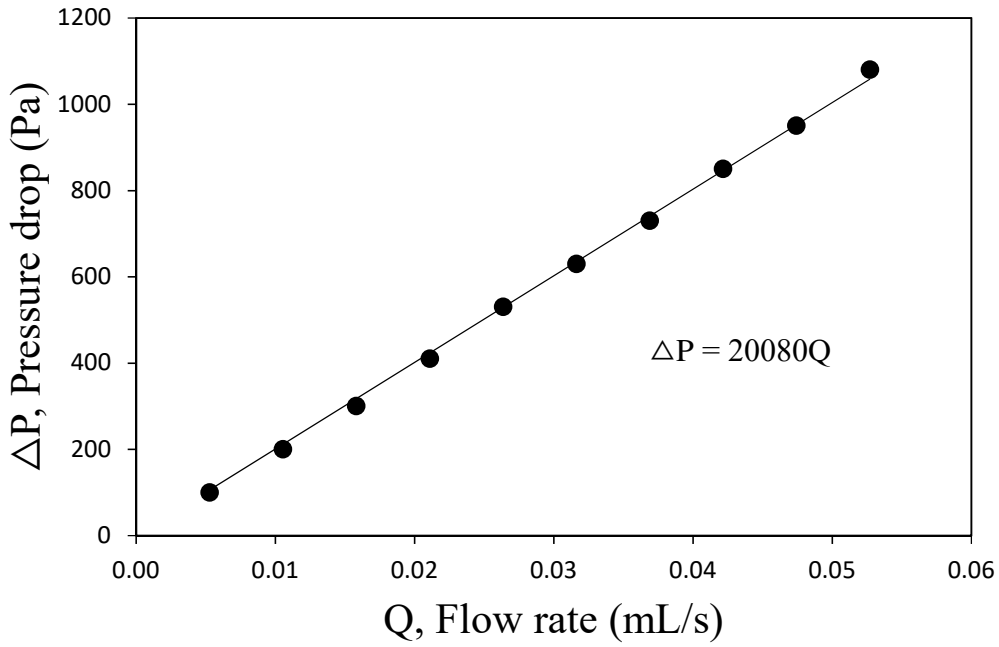

Figure 4.29. Pressure drop vs flow rate for the channel without superhydrophobic surface used to determine acturel channel height.

Subsequently, once the exact channel height was determined, one side of the channel wall was replaced by a xPTFE surface. Unfortunately, after many repeats of such experiments, no stable and repeatable slip-lengths were measurable on the xPTFE surfaces. The slip-length occasionally was measured at the beginnings of the experiment and then disappeared after a relatively short time, typically a couple of minutes. A typical slip-length lose process measured on a 40030 xPTFE surface with a constant flow rate (20 μL/s) is shown in Figure 4.30.

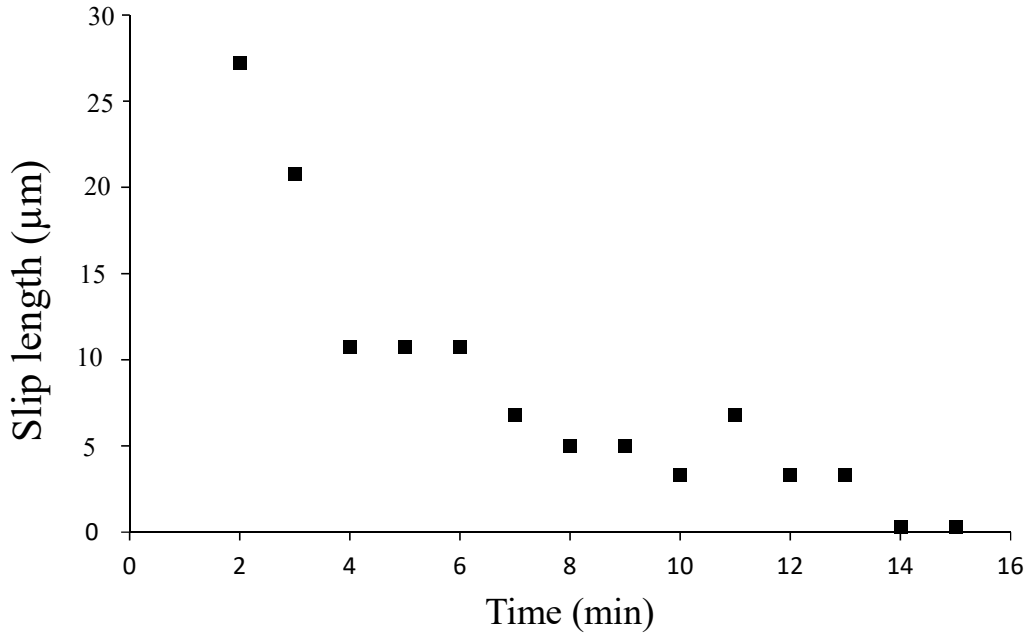

Figure 4.30. Lose of slip-length losting with time, measured on a 40030 xPTFE, the flow rate is 0.02 mL/s.

In Figure 4.30, the slip-length was initially measured as 27 μm, which is similar to the results using the rotating-disks method, but lasted for only about 2 minutes before rapidly losing any slip effects over a 15 minutes period to zero in 15 minutes. As discussed in section 2.3.2, there is a theoretical limitation of the hydraulic pressure for a stable Cassie-Baxter state which is approximately determined by equation 2.7. This limitation was estimated to be 1270 Pa using the static contact angle for a flat PTFE surface (110°) in combination with a surface feature size of 30 μm. This pressure is close to the pressure at the inlet of our channel-flow. Thus it is likely that the pressures required to drive the flow through the channel results in a loss of the Cassie-Baxter state and the air-water interface cannot be maintained for a prolonged period of time.

4.5 Conclusions

In this chapter, the properties of xPTFE surfaces were investigated and characterized using different methods including contact angle measurements, morphology

investigation using SEM, water droplet bouncing experiments and slip-length measurement. The details of their characteristics are shown in Table 4.6.

Firstly, the contact angles and contact angle hysteresis of water were measured. Of all 5 surfaces, there are three types of xPTFE surfaces which can be safely classified as superhydrophobic surfaces. These surfaces are the 30040, 40030 and 50025 xPTFE surfaces which have the highest open area ratios resulting in the largest liquid-gas interface when the drop remains in a Cassie-Baxter state on them. The static contact angles on them are about 145°, which on the 40030 and 50025 xPTFE surfaces are slightly higher than the 30040 xPTFE surface. The contact angle hysteresis of all three surfaces is about 15°.

Secondly, the morphology of the surface structures was investigated. From the SEM images, a structure as a negative model of the very fine stainless steel meshes was observed to be printed on the virgin PTFE surface to form a “brick-like” structure with a dimension of 30 μm. In addition, a secondary “hair-like” structure on a secondary scale (one-micrometre-scale), was observed and which was believed can enhance the superhydrophobicity of the surface. Because the 50025 xPTFE surface has the highest density of these “hair-like” structures, it is determined as the most hydrophobic surface in the xPTFE surfaces.

Thirdly, the water droplet bouncing experiments were implemented on the xPTFE surfaces to examine their superhydrophobicity. We consider if a water droplet can bounce or not on a surface is a definition of superhydrophobicity, there are one and two bounces, within our experimental conditions, occurring on the 40030 and 50025 xPTFE surfaces respectively, but no bounce is observed on the 30040 xPTFE surface. These results indicate that the 40030 and 50025 xPTFE surfaces are superhydrophobic but

30040 can only be called a “weakly-superhydrophobic surface” despite its similar static contact angles to the 40030 and 50025 surfaces.

Fourthly, the slip-lengths of these xPTFE surfaces were successfully measured using a rotating-disks method. These measurements were conducted using both cone-and-plate and parallel-plates geometries. It is worth stating that a few techniques for ensuring the accuracy of the experiments were developed. Such efforts are key to measure the slip-length to an acceptable accuracy. The slip-lengths of these xPTFE surfaces are 23 μm, 27 μm and 31 μm for 30040, 40030 and 50025 xPTFE surfaces, respectively. Details are given in Table 4.6. In addition, the slip-length of the extraordinarily superhydrophobic TiO_2 surfaces was measured for the first time as 55 μm, which corresponds to its very high static contact angle (~165°).

Finally, slip-length measurements were attempted using a channel-flow method. Unfortunately, there was no stable and repeatable slip-length measurable on the xPTFE surfaces. The slip-length was occasionally measurable at the start of the experiments but then disappeared in a relatively short time. This result raises a number of questions: why do these surfaces lost their superhydrophobicity, how fast is this process and how resilient are they? Further investigation regarding the resilience of the superhydrophobic surfaces will be studied in the following chapter.

Table 4.6. Characteristics of xPTFE surfaces.

Mesh type	30040	40030	50025
Brick size	[1] 40 μm	34 μm	26μm
	[2] 59 μm	32.4 μm	23.3 μm
Brick density	[1] 140/mm^2	250/mm^2	388/mm^2
	[2] 116/mm^2	262/mm^2	393.6/mm^2
Open area ratio	[1] 72%	72%	74%
	[2] 42%	54%	55%
Static Contact angle	140°±5°	146°±5°	145°±5°
Advancing Contact Angle	152°±5°	152°±5°	148°±5°
Receding Contact Angle	137°±5°	136°±5°	132°±5°
Contact Angle hysteresis	15±3°	16±3°	16±3°
Drag reduction by parallel-plates	4.5%±1.4%	5.3%±1.4%	5.4%±1.4%
Slip-length (μm)	24±8	28±8	29±8
Drag reduction by cone-and-plate	6.0%±1.6%	7.1%±1.5%	8.0%±1.5%
Slip-length (μm)	23±6	27±6	31±6

[1] Estimated from the dimensions of the embossing meshes.

[2] Measured from SEM images.

Chapter 5 Resilience of superhydrophobic surfaces

As introduced in Section 2.4, many superhydrophobic surfaces achieve limited success in practice primarily as a consequence of mechanical wear and long-term durability issues. These problems have resulted in a scarcity of commercial and industrial applications and attracted a large number of studies focused on improving the resilience of the superhydrophobicity against various types of wear damage. The nature of superhydrophobic surfaces is a combination of low surface free energy material and micro/nano scale surface structure. Most low surface free energy materials are polymers and not mechanically tough (Landel and Nielsen (1993)). Hence, there is an unavoidable natural contradiction for the superhydrophobic surface: the finer the surface structure is, the more hydrophobic it is but the weaker the resulting surface structure becomes. The superhydrophobicity of these surfaces are highly susceptible to mechanical wear, chemical corrosion or even natural light (Tian et al. (2016)). Investigating their resilience is an unneglectable part of the development of such superhydrophobic surfaces. In this Chapter, a standardized and quantifiable method is provided for identifying the resilience of superhydrophobic surfaces. As well as characterising the resilience of our surfaces, this method can also help to optimize the design of new superhydrophobic surfaces.

5.1 Introduction

The loss of superhydrophobicity may be classified as being of two different origins, schematics of which are shown in Figure 5.1. The first one is a temporary loss, that means the surface structure and the properties of the surface material are not damaged. The loss is caused by the trapped gas between the surface structures being forced out

resulting in the surface no longer being in a Cassie-Baxter state. Due to the surface being physically and chemically identical after this procedure, this kind of loss may be recoverable after cleaning the liquid from the surface. The second loss is a permanent loss, in this case, the surface structure or the properties of the surface material are damaged. Hence, this loss is considered as unrecoverable. In practice, these two kinds of losses are always combined with each other (Milionis et al. (2016)). A pulse of high workload (e.g. high hydraulic pressure or fluid shear-stress) may cause the temporary loss of the superhydrophobicity, but it also results in some degree of permanent loss, which means after drying and cleaning, the superhydrophobicity of the surface may be only partially recovered. Generally, all kinds of different types of wear will finally result in a permanent loss of the surface. However, it is still important to identify the difference between these two types of loss. Identifying temporary losses can provide the limitation of the short-time workload of the superhydrophobic surface. Investigating the permanent loss can determine the lifetime of such surfaces.

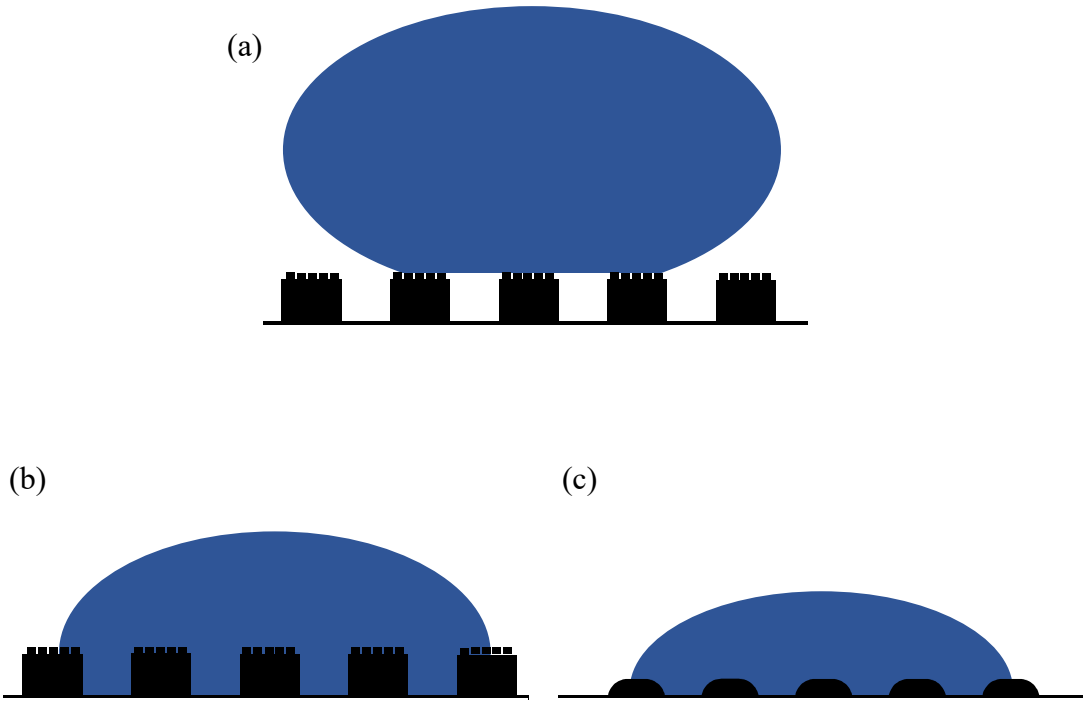

Figure 5.1. (a) A schematic of a drop stands on a fresh superhydrophobic surface in a Cassie-Baxter state. The schematics of the (b) temporary loss (the surface structureis undamaged) and (c) permanent loss (the surface structure is damaged) of superhydrophobicity.

Several methods for investigating the resilience of superhydrophobic surfaces are discussed in Section 2.4. The most commonly-existing resilience tests are conducted using different solid materials to abrade the superhydrophobic surfaces in various ways to apply mechanical wear (Milionis et al. (2016)). From these methods, the two types of losses are difficult to be identified independently. In addition, most of the working environments of the superhydrophobic surfaces are with liquids to utilize their distinct wetting properties so that it is difficult to simulate real-world wear by rubbing them with solid surfaces.

In this chapter, we provide a method which uses a commercial rheometer to create a controllable fluid shear-stress to evaluate the resilience for these two kinds of losses of the superhydrophobicity. The wear can be quantifiably controlled and the losses are described by measuring the static contact angles and slip-lengths. Besides, the changes of the surface structure are investigated using SEM imaging to provide a visual representation of how the superhydrophobic surfaces physically change during the wear process.

5.2 Experimental set-up

In this section, the experimental set-up of the resilience tests are introduced. Following the slip-length measurements, a method which can investigate the resilience of superhydrophobicity quantifiably using a rheometer with a cone-and-plate geometry is provided.

By using different fluids with different shear viscosities and varying the shear rate, a wide range (0.1 Pa to 1000 Pa) of fluid shear stress can be applied on the superhydrophobic surfaces. The shear stress can be controlled and measured precisely to quantify the wear on such surfaces. The experimental-set up is similar to the slip-length measurements: the bottom plate of the cone-and-plate system was replaced by the superhydrophobic surfaces. Three working fluids are used in the experiments for different range of shear stress including distilled water, and two polyethylene glycol (PEG) solutions with different concentrations (12% and 47%, w/w). PEG is a water-soluble polymer and has a broad range of molecular weight from thousands to millions g/mol depending on different lengths of the molecular chain. The PEG polymer used in this section has a molecular weight of 8000 g/mol (so-called PEG8000), and when dissolved in water exhibits no shear-thinning or elastic effects due to its low molecular

weight, and is basically a viscous Newtonian solution (Dontula et al. (1998)). The shear viscosities of these two fluids are 7.1 mPa·s and 285 mPa·s at 20°C for the 12% and 47% concentrations respectively. As discussed in Section 4.4.1.6, the slip-length increases with the fluid viscosity and is independent with the shear-rate. For investigating the resilience consistently, the slip-length measured with higher viscosity fluids were converted to their equivalent water "slip-length*". (i.e. the slip-length were divided by 1.48 (for xPTFE surfaces)/1.6 (for TiO_2 surfaces) and 2.36 for 12% PEG8000 and 47% PEG 8000 respectively).

Moreover, evaporation effects should be considered in these experiments due to investigating the time endurance of the surfaces over extended periods (up to 8 hours). A solvent trap was utilized to prevent potential evaporation effects, as seen in Figure 5.2. The solvent trap can provide a sealed volume for the rotating system and keep a constant humidity inside. To confirm that results are not significantly affected by this trap, the viscosity of distilled water was measured using a cone-and-plate geometry, with and without the solvent trap at a constant shear rate (50 1/s) which confirmed its validity.

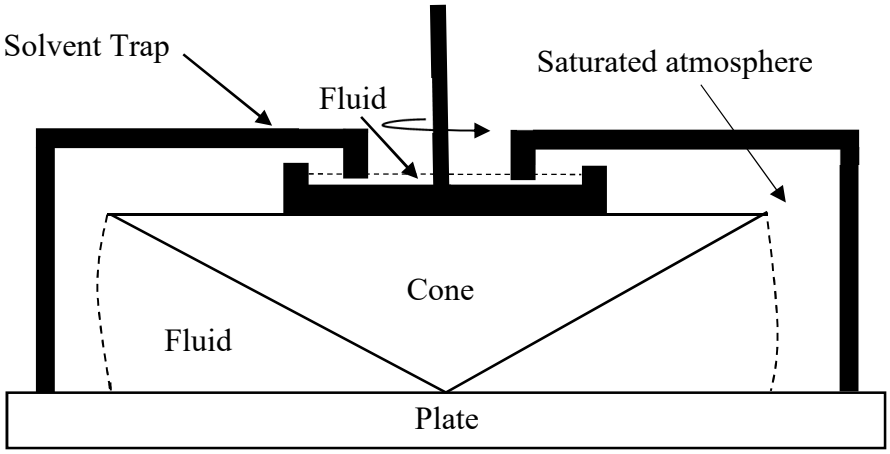

Figure 5.2. A schematic of the solvent trap.

Here we introduce two experiments to investigate possible different loss mechanisms of the superhydrophobic surfaces: the first one is the shear stress step test. A series of increasing shear stresses (0.1 Pa to 500 Pa) are applied on the superhydrophobic surface and each step lasts for 90 seconds. The slip-length of the surface was measured after every fluid shear-stress wear step to evaluate the superhydrophobicity of the sample. This experiment determined the critical shear stress which can force the air trapped between the surface structure out and destroy the Cassie-Baxter state resulting in a temporary loss of superhydrophobicity. The second experiment applies a certain shear stress on the superhydrophobic surface for an extended period of time. Then the contact angles and slip-lengths were measured to examine its remaining superhydrophobicity. This experiment aims to investigate the permanent loss of the superhydrophobicity. Using these methods, the resilience of three xPTFE (30040, 40030 and 50025) surfaces and one TiO_2 surface are examined.

5.3 Shear-stress step tests

To investigate the critical shear-stress required to cause a temporary loss of superhydrophobicity, a shear-stress step experiment was designed. This test uses steps, 90s in duration, of exposure to controlled fluid stress to wear the surfaces via a rheometer. These experiments simulate a short-time impulse of workload/stress to investigate the potential limitations of the superhydrophobic surfaces.

5.3.1 Shear-stress step tests for xPTFE surfaces

A stainless steel cone with 1° cone angle (α_c) and 3 cm cone radius (R) was used in this test. The working fluid was selected as water for the shear stress ranging from 0.06 Pa to 2.2Pa. Each shear stress was applied for 90 s then the slip-lengths were measured. The results of 30040, 40030 and 50025 xPTFE surfaces are shown in Figure 5.3. For the 40030 surfaces, the fluid shear stress was extended to 17.8 Pa using 12% PEG8000 (0.6 Pa ~ 17.8 Pa) due to its higher resilience and no slip-length loss was observed during these water tests.

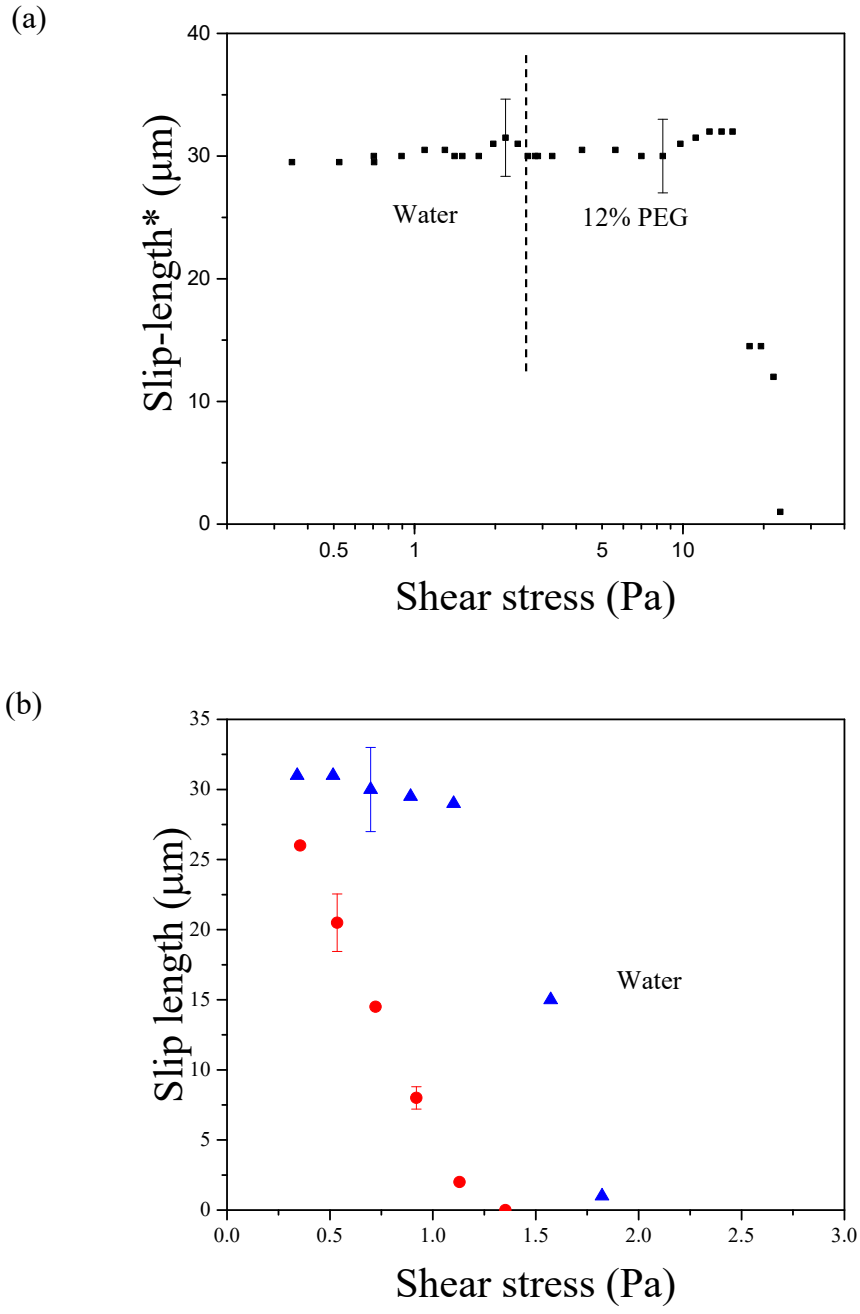

Figure 5.3. Fluid shear-stress steps experiments for xPTFE surfaces (a) 40030 (■) xPTFE (b) 30040 (●) and 50025 (▲) xPTFE using water and 12% PEG8000 solution in a cone-and-plate geometry (α_c = 1°, R = 3cm). The error bars represent the variation of repeats.

From the results shown in Figure 5.3, the 30040 surface has the lowest resilience of the three xPTFE surfaces. Its slip-length decreased rapidly after each fluid shear stress was applied from 0.3 Pa. This may be a result of its largest space between the "brick-like"

structure on the surface. The 40030 xPTFE surface has the best resilience against the short-time fluid shear-stress of the three samples, the temporary loss of the superhydrophobicity occurred when the fluid shear-stress was around 15 Pa. Its superhydrophobicity totally disappeared when the fluid shear-stress was close to 25 Pa. The 50025 xPTFE surface starts to loss its superhydrophobicity when the fluid shear stress was over 1.2 Pa, and disappeared totally after being exposed to a shear stress of 1.6 Pa. The superhydrophobicity of 30040 and 50025 xPTFE surfaces are not recoverable after the tests as the shear-stress significantly exceeds their short-time workload/stress limitation, but the slip-length of 40030 surfaces can be partially recovered to 15 ~ 20 μm after the cleaning using water and allowing to dry naturally.

In general, the critical fluid shear-stress resulting in a loss of superhydrophobicity for the 30040 xPTFE surface is lower than 0.5 Pa. The equivalent values for 40030 and 50025 xPTFE surfaces are about 15 Pa and 1.2 Pa respectively. These results indicated the limitation for their short-time workload/stress.

5.3.2 Shear-stress step tests for TiO_2 surfaces

An extraordinary high superhydrophobicity of the TiO_2 surfaces was found via slip-length measurements in Chapter 4. Such surfaces have a static contact angle around 165° and their slip-length was measured as being about 55 μm. In this section, their resilience was investigated using the same methods as were used for the xPTFE surface but with an extended range (0.1 Pa ~ 200 Pa) of fluid shear-stress. To achieve this higher shear stress, another PEG fluid was used in this section besides the two fluids used in the previous section. The concentration of this PEG fluid is 47% and its shear viscosity at 20°C is about 280 mPa·s, using this fluid, the fluid shear-stress with a cone

of 1° cone angle and 3 cm cone radius can be higher than 200 Pa. The results of these shear-stress step tests for TiO_2 surfaces are shown in Figure 5.4.

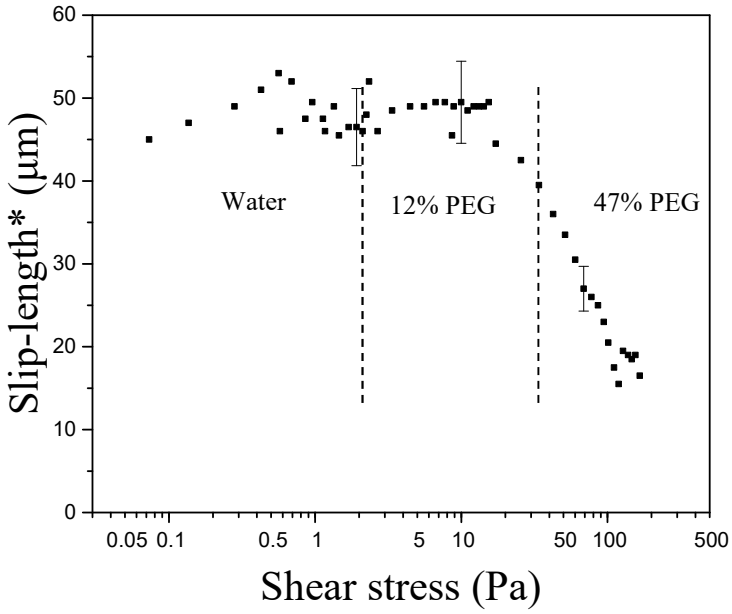

Figure 5.4. Fluid shear-stress steps experiments for TiO_2 surface using water, 12% PEG 8000 and 47% PEG 8000 solutions in a cone-and-plate geometry (α_c = 1°, R = 3cm). The error bars represent the variation of repeats.

From the results shown in Figure 5.4, the resilience against the short-time wear of the TiO_2 surface is seen to be much better than the xPTFE surfaces. Its superhydrophobicity decreases only when the fluid shear stress is over 20 Pa. Hence, the critical shear stress to cause a temporary loss of superhydrophobicity could be identified as ~25 Pa for the TiO_2 surface. It should be noticed that, even when the fluid shear stress is increased to around 200 Pa, this surface can still maintain a slip-length of around 15 μm. That suggests not all of the surface structure are damaged under the same shear-stress. The superhydrophobic TiO_2 paint contains two different size ranges of particles (~60 to 200nm and ~21 nm), and the random size of the particle groups results in a more complicated surface structure. SEM images under different magnifications of the

surface in Figure 5.5 shows that the surfaces have multiple scales of surface structures, the dimensions of the surface structures vary from hundreds of nanometres to tens of microns. A certain shear-stress may damage some scale of structures, but the other part of the structures may still be able to maintain a Cassie-Baxter state. From this point of view, these multiple scales of surface structures may be beneficial for both superhydrophobicity and resilience to wear.

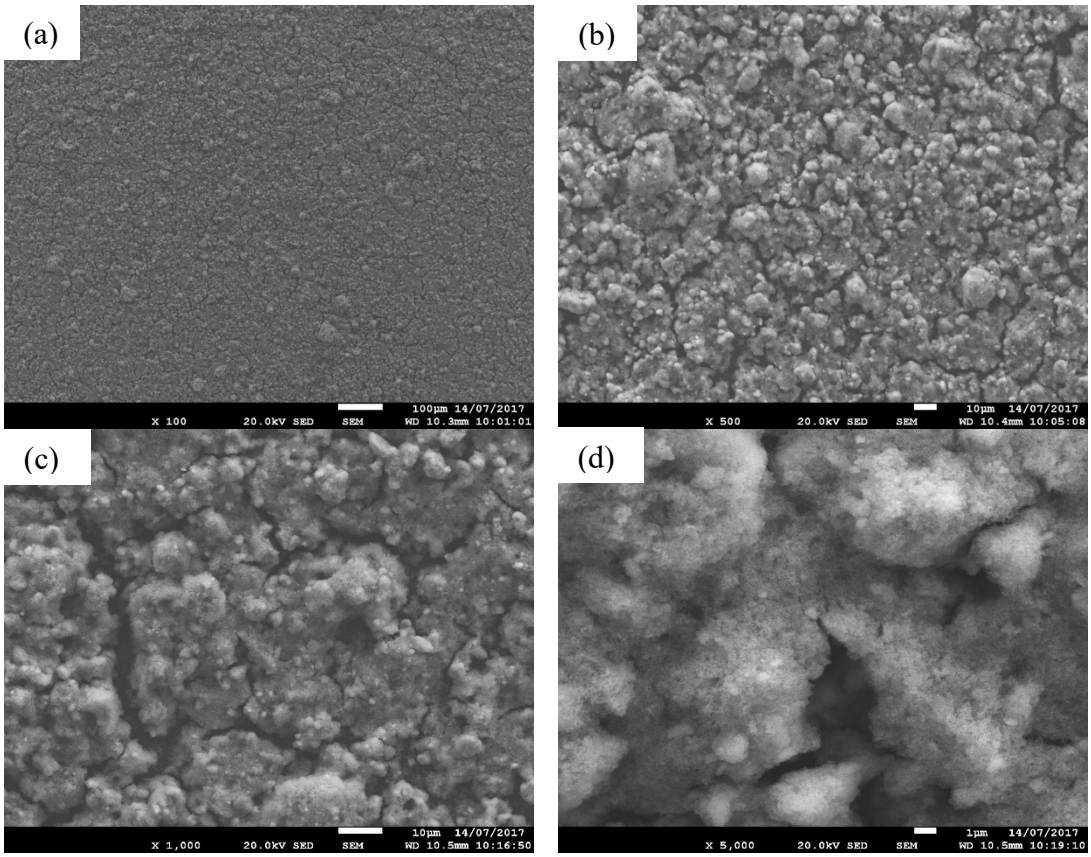

Figure 5.5. SEM images of TiO_2 surfaces at (a) 100x, (b) 500x, (c) 1000x and (d) 5000x magnifications.

5.4 Time endurance tests

After the critical shear-stresses was determined, the time endurance of the superhydrophobic surfaces were tested by applying a constant fluid shear-stress for extended periods of time. The experiments in this section used a rheometer with a

smaller (α_c = 2°, R = 1cm) cone geometry due to the limited area of samples available. The superhydrophobicity was examined by measuring the static contact angle and the slip-length. Any damage to the surface structures was observed using SEM imaging.

5.4.1 Time endurance tests for xPTFE surfaces

As the critical shear-stress was determined as around 1 Pa for the 30040 and 50025 xPTFE surfaces in Section 5.3.1, this shear-stress was selected for the time endurance tests. The three xPTFE surfaces were exposed to this 1 Pa fluid shear-stress for 8 hours. In addition, as the critical shear-stress for 40030 xPTFE surfaces was determined to be about 15 Pa, the surface was also exposed to further time endurance tests with 5 Pa and 10Pa fluid shear-stress for 8 hours. Because of the batch-to-batch variations of the xPTFE surfaces, they exhibited slightly different resilience behaviour during the time endurance tests. Representative results of slip-length verse the time are shown in Figure 5.6.

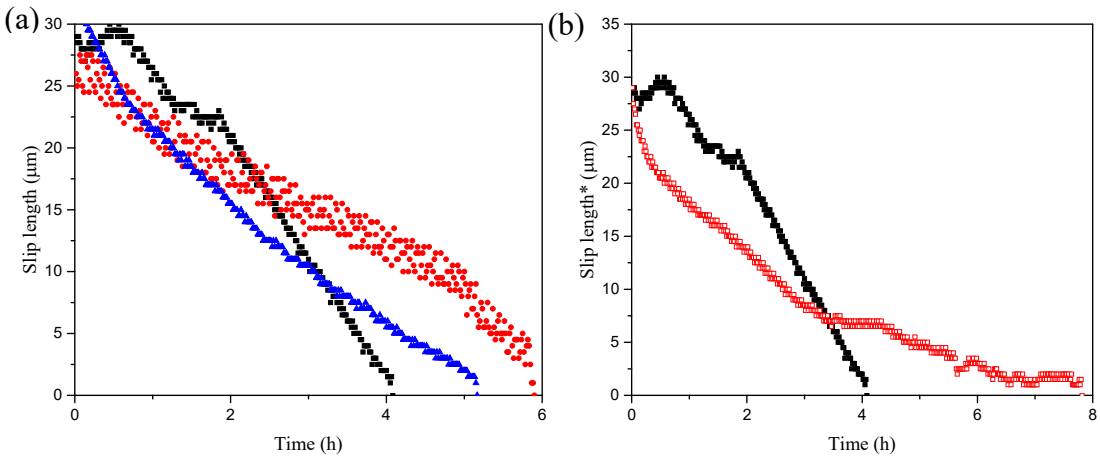

Figure 5.6. Time endurance of xPTFE surfaces (a) ▲ 30040, ■ 40030 and ● 50025 xPTFE surfaces under a 1 Pa fluid shear-stress , (b) 40030 xPTFE surfaces under ■ 1 Pa (water) and □ 10 Pa (12% PEG8000) for 8 hours.

From the results shown in Figure 5.6, it can be seen that the superhydrophobicity of the 30040 surfaces decrease with time. Their slip-length basically drops almost linearly with time, and is totally lost within 5 hours. The static contact angles for 30040 surfaces were measured as 134°±5° on fresh surfaces and decreased to 112°±8° after 8 hours exposure to a 1 Pa fluid shear-stress. The surfaces exhibited non-uniform degradation as different contact angles were measured at different positions on the surface. This result indicates that the damage is not uniform and may initiate at preferential locations (i.e. at surface defects). The SEM images of 30040 xPTFE surfaces which were taken before and after the stress tests are shown in Figure 5.7.

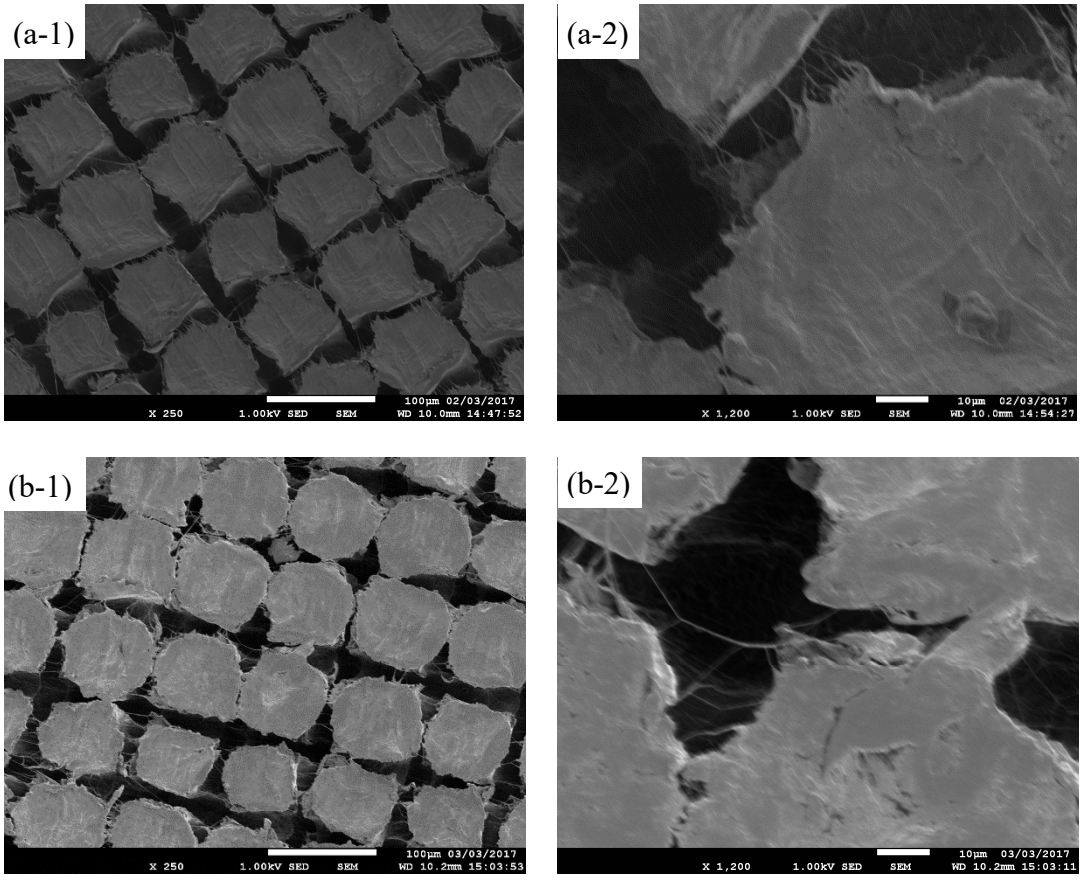

Figure 5.7. SEM images of (a) fresh surfaces and (b) after 8 hours of 1Pa fluid shear-stress for 30040 xPTFE at (1) 250 x and (2) 1200 x magnifications.

From the SEM images, comparing the images before and after the wear, the open area ratio increased from 42% to 49%, and a part of the “hair-like” structures are lost after the wear. The top of “brick-like” post was smoother than those on the fresh surfaces. A loss of the complexity of the surfaces structure results in a loss of their superhydrophobicity. Considering the dimension of the surface structures of the 30040 xPTFE are the largest in all of the three surfaces, it shows less change in morphology but a greater decrease in superhydrophobicity.

The slip-length of the 50025 xPTFE surfaces showed a similar behaviour during the application of a 1 Pa fluid shear-stress, as shown in Figure 5.6(a), compared with 30040 xPTFE surfaces. In this figure, which shows typical behaviour, the slip-length decreased linearly with time and disappeared totally in about 6 hours. The static contact angles were measured as 143°±5° for the fresh surfaces and decreased to 126°±8° after 8 hours of wear. The precise value depending on which position of the surface was measured. From the SEM images of the surfaces before and after the fluid shear-stress, as shown in Figure 5.8, the structures were obviously modified by the experiment, the “hair-like” structure are lost and the sharp corners of “brick-like” post were rounded. The wear increased the open area ratio from 55% to 63%. The surfaces structures lost their dual-scale nature and only the main surface structures at a scale of ~ 10 μm remained. These changes of the surface structure are accompanied by a loss of their superhydrophobicity (Figure 5.6).

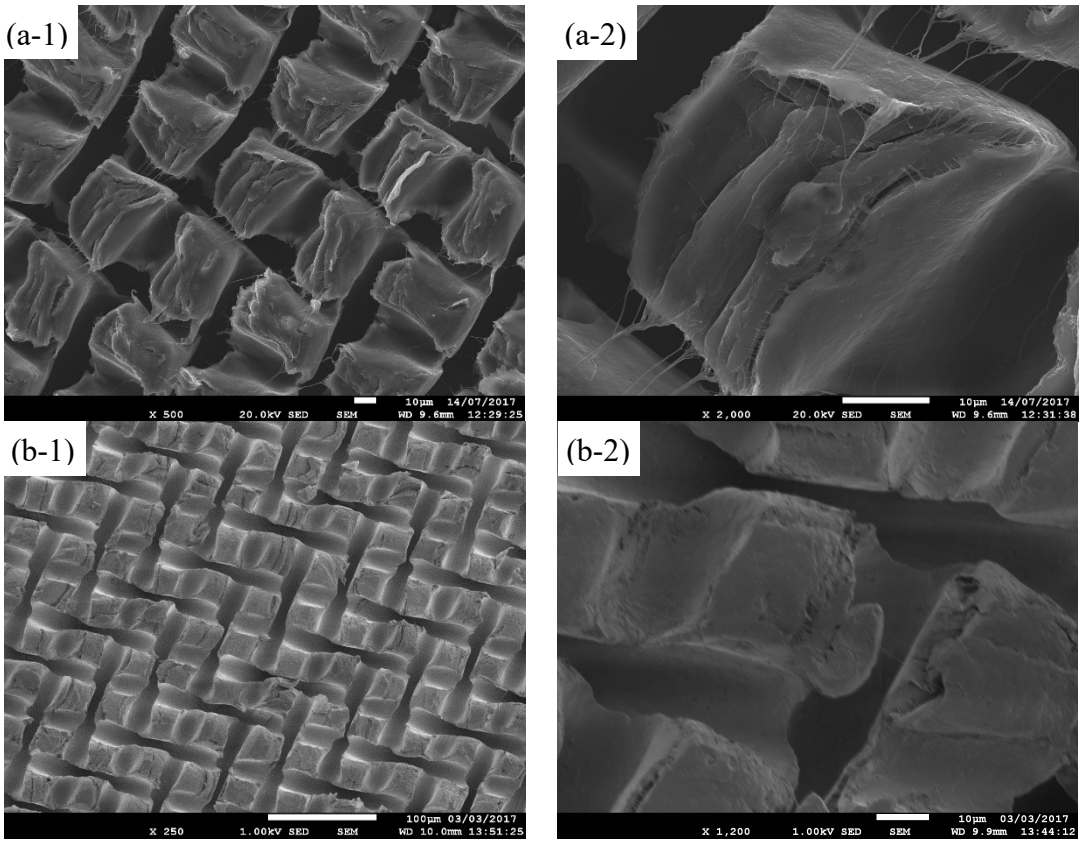

Figure 5.8. SEM images of (a) fresh surfaces and at (1) 500 x and (2) 2000 x magnifications; (b) after 8 hours if 1Pa fluid shear-stress for 50025 xPTFE at (1) 250 x and (2) 1200 x magnifications.

The 40030 xPTFE surfaces showed the best resilience in the shear-stress step test, as discussed in Section 5.3, exhibiting a critical shear-stress of around 15 Pa. Hence, in the time endurance tests, the surfaces were exposed to three different fluid shear-stresses (1 Pa, 5Pa and 10Pa) for 8 hours. Representative slip-length verses time plots during the wear of 1 Pa and 10 Pa are shown in Figure 5.6(b). During the fluid shear-stress of 1 Pa, the surfaces maintained its superhydrophobicity in the first hour, then its slip-length decreased rapidly and disappeared within 4 hours. The static contact angle angles were measured as 145°±5° for fresh surfaces and these decreased to 130°±10° after the wear. The static contact angle varied greatly at different positions on the surface, indicating that the loss of superhydrophobicity is spatially non-uniform and that, some part of the surface was still superhydrophobic. Therefore, the non-uniformity

of the surfaces resulted in a loss of slip-length. The changes of the surface structures, observed via SEM after 8 hours of 1 Pa fluid shear-stress, are shown in Figure 5.9.

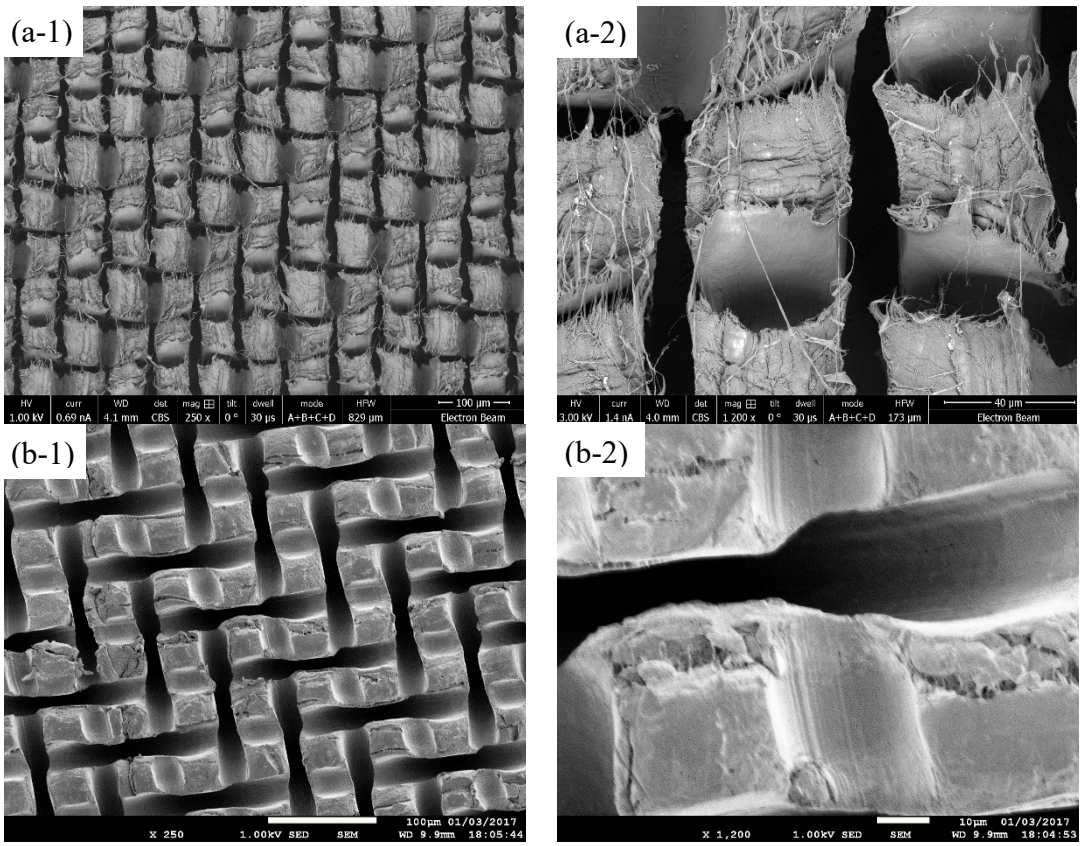

Figure 5.9. SEM images of (a) fresh surfaces and (b) after 8 hours if 1Pa fluid shear-stress for 40030 xPTFE at (1) 250 x and (2) 1200 x magnifications.

From Figure 5.9, the changes to the surface structure of the 40030 xPTFE surfaces after wear is similar to those observed on the 50025 xPTFE surfaces. The "hair-like" structures vanish after the wearing process, and the scratches due to the sanding process on the top of each "brick" became worn away and smooth. The open area ratio increased from 54% to 66%. These changes indicate a permanent loss of superhydrophobicity. More SEM images of xPTFE surfaces exposed to different fluid shear-stress for different lengths of time are shown in Figure 5.10.

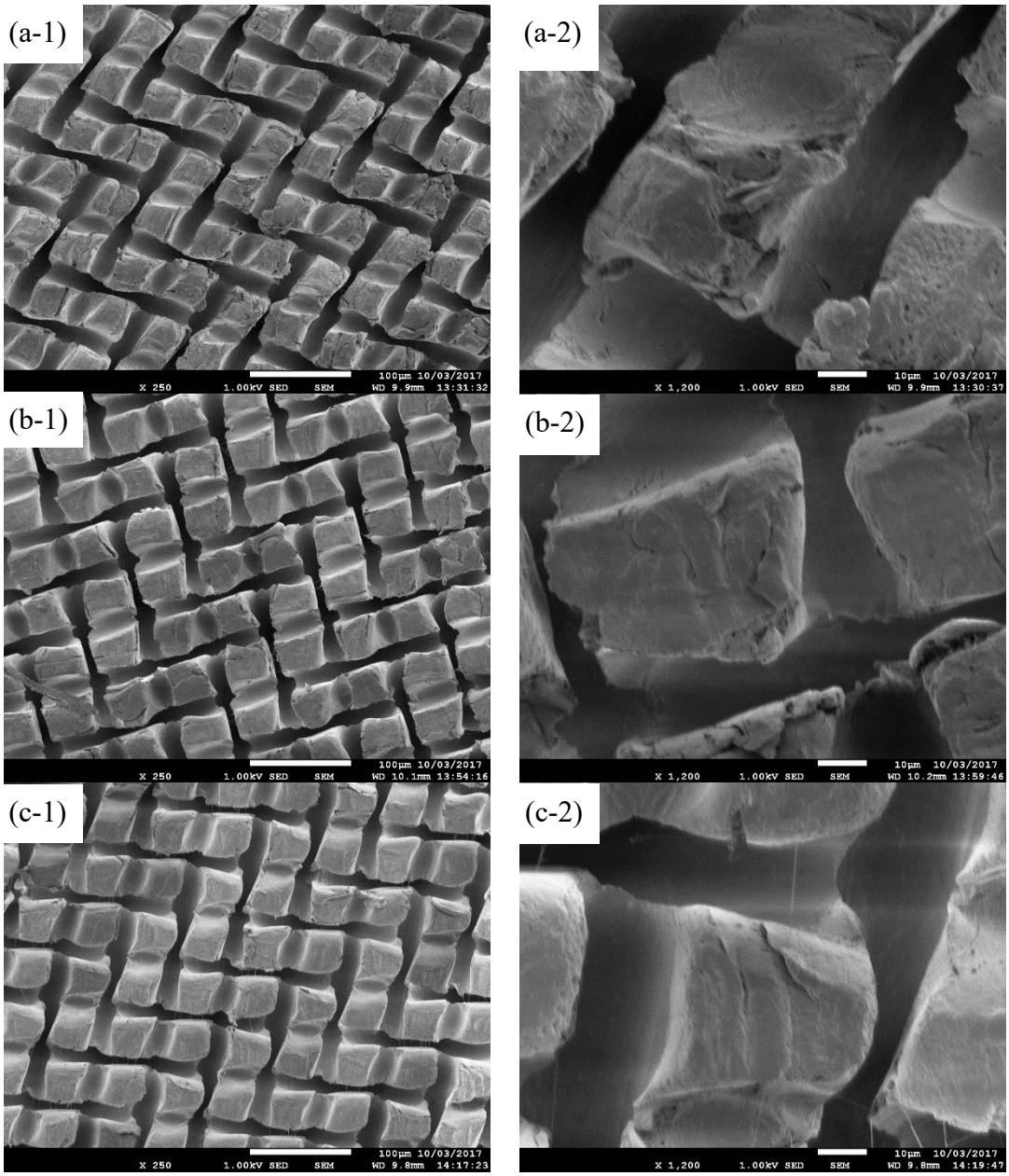

Figure 5.10. Further SEM images after various shear stress and time on 40030 xPTFE surfaces. (a) 5 Pa fluid shear stress for 8 hours. (b) 10 Pa fluid shear stress for 4 hours. (c) 10 Pa fluid shear stress for 8 hours, at (1) 250 x and (2) 1200 x magnification.

From the SEM images, similar but different degrees of change after the different fluid shear-stress and time were observed. In the most abraded case, as shown in Figure 5.10(c), the edges and the top of the posts were polished, the “hair-like” structures and scratches caused by the sandpaper have basically disappeared. The open area ratios increased from 54% to 62%, 65% and 66% after a 5 Pa shear stress for 8 hours, 10 Pa

shear stress for 4 hours and 10 Pa shear stress for 8 hours respectively. The static contact angles were measured as 115°±20°, 131°±5° and 122°±22° after 5 Pa shear stress for 8 hours, 10 Pa shear stress for 4 hours and 10 Pa shear stress for 8 hours respectively. From the static contact angle measurement and the SEM images, the resilience of xPTFE surfaces seems to be more sensitive to time than the fluid shear-stress applied. The 8 hours of 5 Pa fluid shear-stress resulted in a greater degree of loss of superhydrophobicity than 4 hours of a stress of 10 Pa. A significant difference between these cases is the uniformity of the surfaces. The static contact angles were measured as 131°±5° on the surface which was abraded after 4 hours of 10 Pa fluid shear-stress, the result is even better than the 1 Pa 8 hours sample (the static contact angles were measured from 120° to 140° on this). To quantify the loss of superhydrophobicity, the slip-length loss per unit time verses fluid shear-stress were calculated, as shown in Figure 5.11. Basically, this quantity increases with the fluid shear-stress. In addition, the slip-length loss rate presented a large variation for each fluid shear-stress due to the different quality of the xPTFE surfaces from different batches. The wear of 1 Pa shear-stress resulted in a loss of slip-length ranging from 1 to 6 μm/h and the average value is around 3 μm/h which indicates that the surface could lose all of its superhydrophobicity within about 10 hours. When the shear-stress increased to 5 Pa, the average and the maximum value of the slip-length loss rate reached 6 μm/h and 9 μm/h respectively. The time endurance of its superhydrophobicity decreases to between 3 to 5 hours under this condition. For the 10 Pa fluid shear-stress, the average and the maximum value of the slip-length loss rate increased to 14 μm/h and 27 μm/h respectively, the superhydrophobicity of the 40030 xPTFE surfaces at this stress can be maintained for 1 to 2 hours.

In general, the 40030 xPTFE surfaces have the best resilience of the three xPTFE surfaces. For a low working load (< 1Pa fluid shear-stress) it can maintain superhydrophobicity for a relatively long time (around 10 hours). When the fluid shear-stress increased to 5 Pa or 10 Pa, their slip-lengths decreased rapidly and the lifetime is only for 1 to 3 hours or less. Because of the limitation of the number of repeat measurements possible, a more systematic analysis regarding the slip-length loss rates of the xPTFE surfaces was not conducted. However, the presented results provide a quantitative indication of the resilience of the xPTFE surfaces.

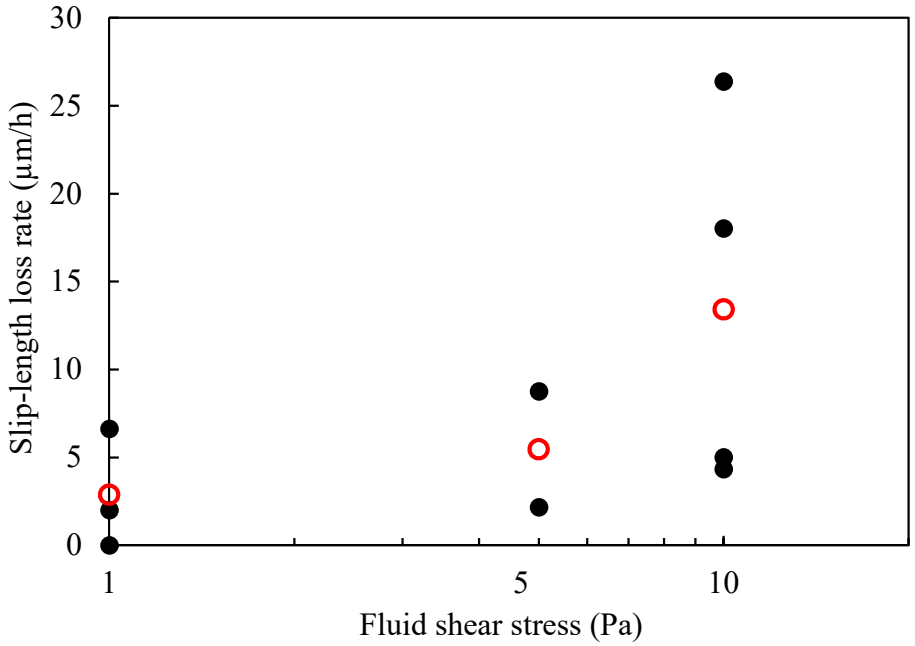

Figure 5.11. Slip-length loss rate vs fluid shear stress of 40030 xPTFE surface, (○) represent the average value.

5.4.2 Time endurance tests for TiO_2 surfaces

The critical fluid shear-stress was determined as 20 Pa in Section 5.3.2 for TiO_2 surfaces. This surface indicated a higher resilience than the xPTFE surface, hence the time endurance tests used higher fluid shear-stres. Distilled water, 12% PEG and 47% PEG fluids were used to create 1 Pa, 10 Pa and 100 Pa fluid shear stresses in this test

respectively. A representative plot of slip-length verses time under the constant shear-stresses is shown in Figure 5.12.

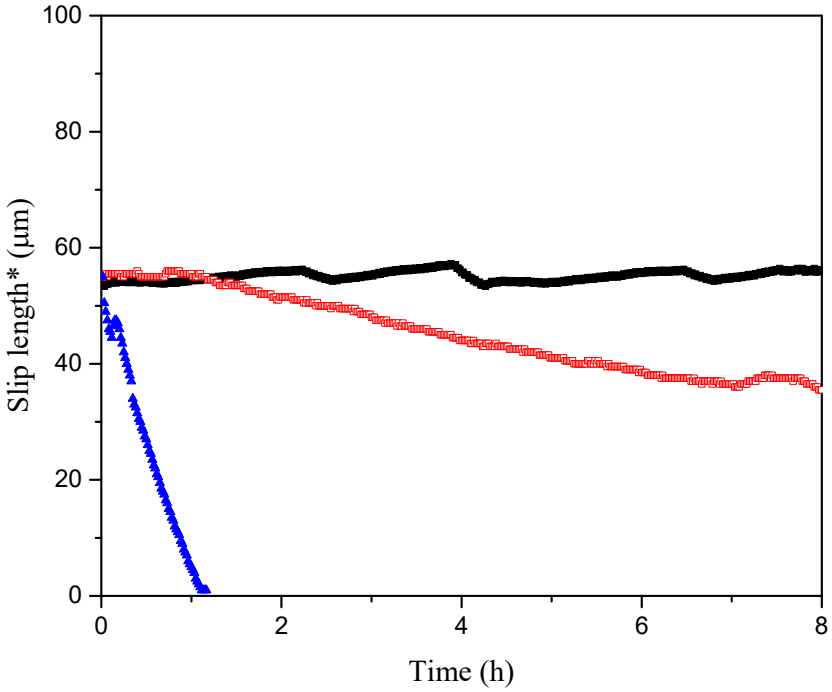

Figure 5.12. Time endurance of TiO_2 surface in different fluid shear-stress (■) 1 Pa, (○) 10 Pa and (▲) 100 Pa for 8 hours.

From the results, the slip-length of the TiO_2 surfaces essentially kept the same during the application of a 1 Pa fluid shear-stress wear. Comparing the SEM image of the surface after the wear, as shown in Figure 5.13, with the fresh surfaces (Figure 5.5), there is no notable change of the surface structure. The static contact angles were measured as 162°±3° on the surfaces after the wear, which were very close to the value of the static contact angles on fresh surfaces. In general, the 1 Pa fluid shear-stress could not damage the superhydrophobicity of the TiO_2 surface even over an eight-hour period.

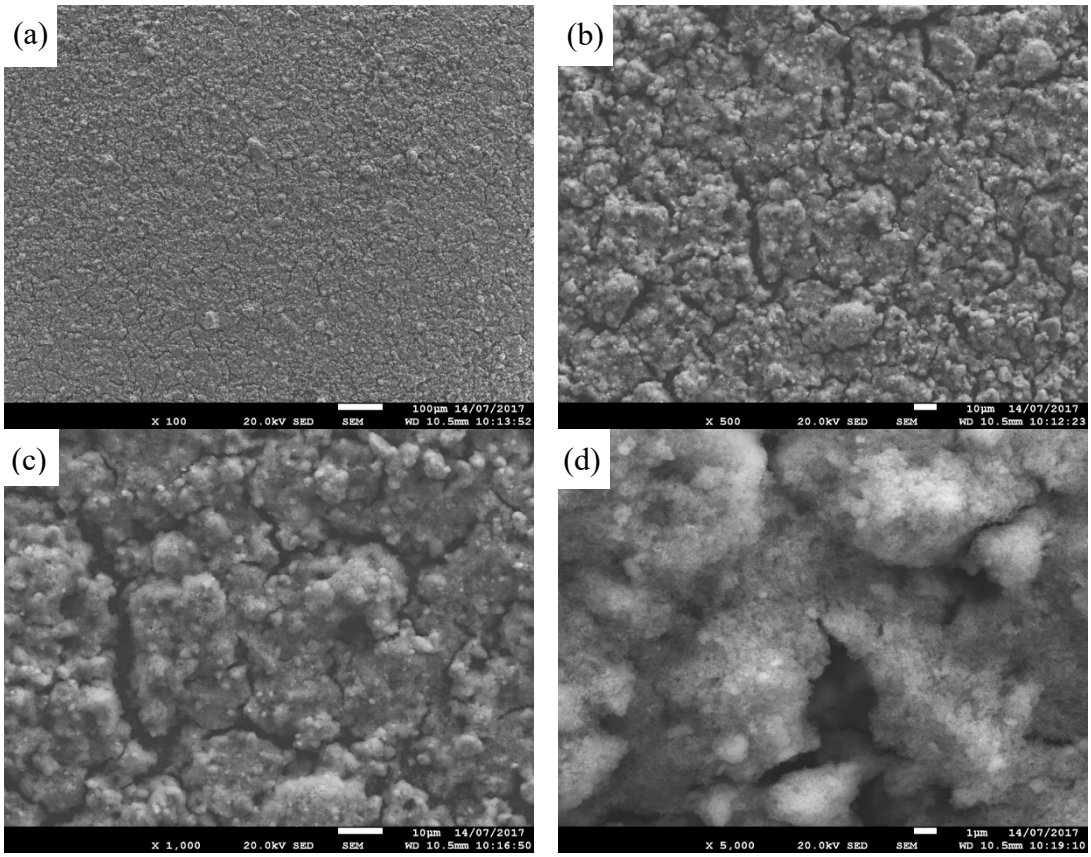

Figure 5.13. The SEM images of TiO_2 surfaces after 1 Pa fluid shear-stress for 8 hours at (a) 100 x, (b) 500 x, (c) 1000 x and (d) 5000 x magnifications.

When the fluid shear-stress increased to 10 Pa, which was close to the critical shear-stress for TiO_2 surfaces, identified in Section 5.3.2, the slip-length started to decrease linearly with time after 1 hour of stress. After 8 hours, the slip-length was measured as around 40 μm. The static contact angles were 157°±3° and no significant variations were observed at different positions on the surface. From the SEM images, as shown in Figure 5.14, an increased roughness was observed on the surface at the hundred-micrometre scale. A few cracks with a width around 5 μm were observed. In addition, at the 10 μm scale and 100 nm scale, complicated multiple-scale structures were slightly smoothed, e.g. at some of the sharp corners. In general, after 8 hours of 10 Pa fluid shear-stress, the surface only partly lost its superhydrophobicity, and the remaining structures were still uniform.

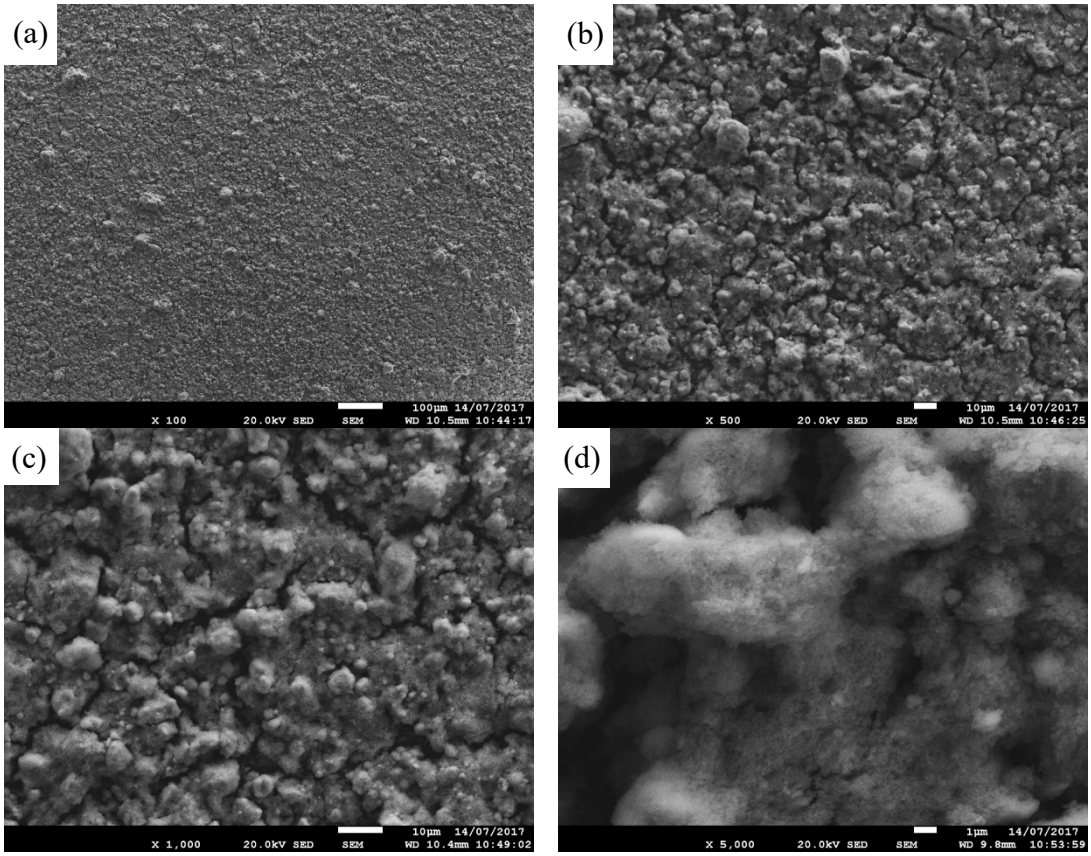

Figure 5.14. The SEM images of TiO_2 surfaces after 10 Pa fluid shear-stress for 8 hours at (a) 100 x, (b) 500 x, (c) 1000 x and (d) 5000 x magnifications.

When the fluid shear-stress increased to 100 Pa, the slip-length decreased rapidly and vanished in about 1 hour. The static contact angles were measured as 91°~157° after the test, which indicated that some parts of the surface had entirely lost its superhydrophobicity and the surface was no long uniform. The change to the surfaces were obvious after the experiments, a few "large" scratches on the surface were observed even by the naked-eye. From the SEM images at different magnifications, as shown in Figure 5.15, the widths of these obvious scratches can be measured as hundreds of microns. The TiO_2 paint was totally abraded at these positions on the surface resulting in a considerable damage to the surface structure. The images with higher magnification at these locations showed the micro/nano scale structures were

smoothed and damaged, and the remaining roughness of the surface was no longer providing superhydrophobicity.

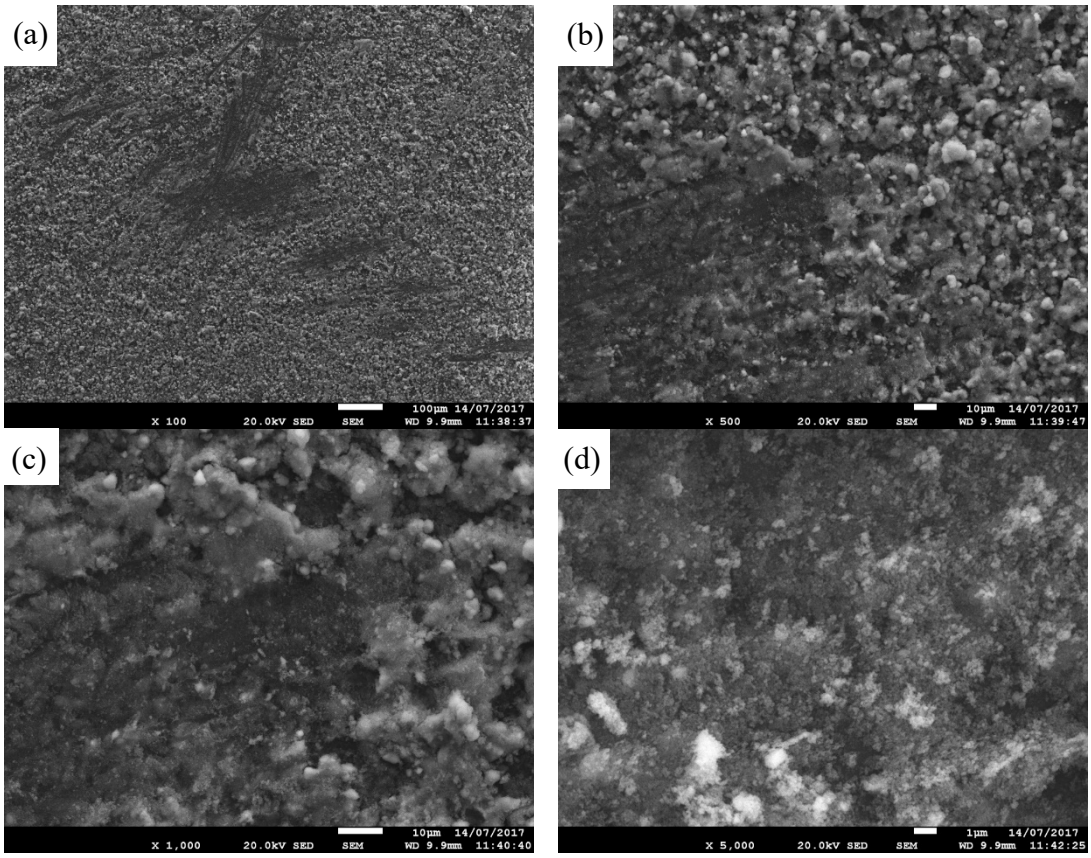

Figure 5.15. The SEM images of TiO_2 surfaces after 100 Pa fluid shear-stress for 8 hours at (a) 100 x, (b) 500 x, (c) 1000 x and (d) 5000 x magnifications.

To evaluate the loss of superhydrophobicity on TiO_2 surfaces, the slip-length loss per unit time is plotted in Figure 5.16. Because of the different quality of these surfaces for different batches, they exhibited variation of the slip-length loss rate. There was no loss of the slip-length observed during the 1 Pa fluid shear-stress wear, but it increased with the higher fluid shear-stress. When the shear-stress increased to 10 Pa, the average and the maximum value of the slip-length loss rate reached 9 µm/h and 17 µm/h respectively. These surfaces showed a better resilience than the xPTFE surfaces in the same condition. For the 100 Pa fluid shear-stress, the average and the maximum value of the slip-length

loss rate increased to 32 μm/h and 46 μm/h respectively, their superhydrophobicity could only remain for 1 to 2 hours.

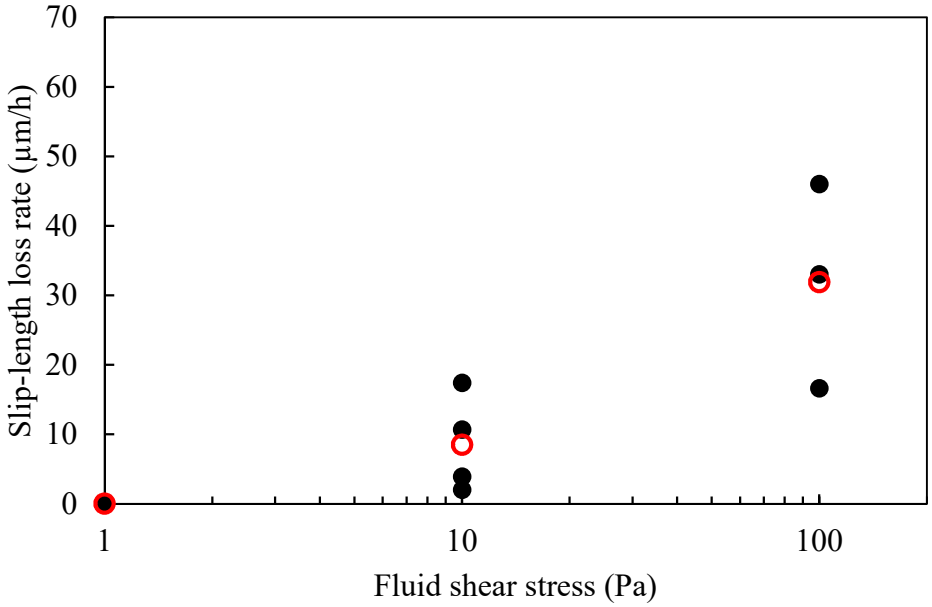

Figure 5.16. Slip-length loss rate vs fluid shear stress of TiO_2 surface, (○) represent the average value.

5.5 Conclusions

In this Chapter, the loss of superhydrophobicity was classified as being of two types: a temporary loss and permanent loss. Two methods using the rheometer to create a controllable fluid shear-stress to evaluate the resilience for these two kinds of loss are provided and implemented on both the xPTFE surfaces and TiO_2 surfaces.

The critical shear-stress which results in a temporary loss of the superhydrophobicity were investigated using a shear-stress step method. This method created a series of impulse workloads to determine the limitation of the working environments of the superhydrophobic surfaces. The results showed that the 40030 xPTFE surfaces has the best resilience of the three xPTFE surfaces, its critical shear-stress is around 15 Pa. The critical shear-stress for 30040 and 50025 xPTFE surfaces are less than 0.5 Pa and 1.2

Pa, respectively. The TiO_2 surfaces not only have a better superhydrophobicity but also have a higher critical fluid shear-stress than the xPTFE surfaces which is around 20 Pa.

Following the shear-stress step experiments, the time endurance tests were implemented. The superhydrophobic surfaces received a constant fluid shear-stress for extended periods of time. Then their superhydrophobicity was examined by measuring the static contact angle, and the changes of the surface structures were observed using SEM images. Finally, their resilience was described using the slip-length loss rate. The 40030 xPTFE surfaces have the best resilience of the three xPTFE surfaces. In a low fluid shear-stress (<1Pa fluid shear-stress) this surface can maintain superhydrophobicity for about 10 hours, the other two surfaces can only last up to 5 hours. The one-micrometer scale "hair-like" surface structures on the xPTFE surfaces were seriously damaged by the wearing process. When the fluid shear-stress increased to 5 Pa or 10 Pa, the surfaces' slip-lengths decreased rapidly and the lifetime is only 1 to 3 hours or less. The slip-length loss rates of the 40030 xPTFE surface was measured as being around 3 μm/h, 6 μm/h and 14 μm/h for stresses 1 Pa, 5 Pa and 10 Pa respectively.

In comparison to the xPTFE surface, the TiO_2 surfaces have a much better time endurance as well as a higher critical fluid shear-stress. Considerable damage on the surface structures occurred only when the fluid shear-stress increased to 100 Pa. There was no loss of slip-length for a fluid shear-stress of 1 Pa, and their slip-length loss rate was found to be 9 μm/h and 32 μm/h for 10 Pa and 100 Pa fluid shear-stress respectively.

Chapter 6 Viscoelastic drops moving on superhydrophobic surfaces[1]

6.1 Introduction

As introduced and discussed previously in Chapter 2, one of the most famous and easily observed phenomenon of a superhydrophobic surface, the so-called "lotus effect" (Neinhuis and Barthlott (1997)), is that small liquid drops can stand on such surfaces as an almost perfect spherical shape and very easily roll off. Although this phenomenon is easy to observe, it is difficult in practice to measure how easily the drops roll off. There are a few studies which investigated the sliding (i.e. Kim et al. (2002), Hodges et al. (2004), Le Grand et al. (2005), Morita et al. (2009) and Varagnolo et al. (2015)) or rolling (i.e. Richard & Quéré (1999); Hodges et al. (2004) and Mognetti et al. (2010)) of drops on various surfaces, but no study has investigated viscoelastic drops moving on superhydrophobic surfaces in detail so far. Note that, throughout this chapter we shall refer to the drops "moving" rather than attempt to categorise the motion as rolling or sliding. Le Grand et al. (2005) studied millimeter-sized Newtonian drops (silicon oil) on partially wetting surfaces with a static contact angle around 50°. The shape and motion of drops are characterized in four stages with increasing velocity or capillary number ($Ca = \eta U / \sigma$, where U is velocity, μ is viscosity, σ is surface tension). At low velocity, the drops essentially maintain a round shape called the "oval" stage. With increasing velocity, the drop shape becomes more complex including a so-called "corner" transition stage and then onto "cusps" and then "pearling" at higher droplet velocities. Morita et al. (2009) conducted a similar study but using two polymer solutions, a polystyrene of molecular weight M_w=280,000 g/mol in acetophenone. A small difference observed with the comparator Newtonian fluid is that the polymer drop

[1]Some results from this chapter have been published in Xu et al. (2016), (2018)

moves faster at equivalent capillary number, which may be due to the shear-thinning nature of the solutions but the use of the zero shear rate viscosity in the estimation of the capillary number.

In this chapter, the moving viscoelastic drops on superhydrophobic and other surfaces were investigated in detail. In so doing, an interesting phenomenon is observed while viscoelastic fluid drops are moving on the superhydrophobic surfaces. For water and other Newtonian fluid drops, the embossed structure on our superhydrophobic surfaces can reduce the friction by trapping air to form an air-liquid interface when a drop moves over as which can be described as the "slip-length", as measured and discussed in Section 4.4, meanwhile the large contact angle of our surfaces lead to a small contact area between the fluid drops and the surface. In addition, the low contact angle hysteresis for these Newtonian drops on the xPTFE surfaces allow rapid movement when the surface is inclined (at angle α) above the rolling-off angle, as expected (Cassie and Baxter (1944)). In this study, viscoelastic effects on moving drops are studied using constant-viscosity viscoelastic liquids, so-called Boger fluids (Boger (1977), Dontula et al. (1998) and James (2009)). These have particular advantages for studying the effect of fluid elasticity independently of shear-thinning. By careful design, Boger fluids and a comparison Newtonian fluid can have essentially the same properties such as shear viscosity μ, surface tension σ, density ρ, and advancing/receding contact angle $\theta_{adv}/\theta_{rec}$ on a given surface. When the drop moves on a hydrophilic surface, for example smooth glass, no difference between the motion of these elastic liquids at identical capillary number and effective Bond number ($Bo = (V^{2/3}\rho g \cdot \sin\alpha)/\sigma$), where g is the gravitational acceleration is observed. However, when a Boger fluid drop moves on our superhydrophobic surfaces, the velocity is significantly reduced in comparison with the

Newtonian fluid at equivalent viscosity, and complex "branch-like" patterns, "beads-on-a-string" like phenomenon, (e.g. seen in capillary-thinning experiments in Oliveira and McKinley (2005)), are left on the surface. Such profound differences imply a complex mechanism during the motion of viscoelastic drops on superhydrophobic surfaces. In this chapter, this phenomenon was investigated in detail and on various scales (μm ~ mm).

This chapter is structured as follows. Firstly, the experimental set-up is described, including the chosen xPTFE surfaces and the rheology of the working fluids. Subsequently, we describe results on a hydrophilic surface using a broad range of fluids and results on a weakly hydrophobic surface followed by data for the xPTFE surfaces. A broad range of both surfaces and viscoelastic fluids confirms the robustness of the observed effects. In addition, SEM imaging is utilized to obtain greater insight into the surface structure and the underlying physical mechanism supporting standard light microscopy. Finally, this chapter ends with a conclusions section.

6.2 Experimental set up

In this chapter, the experiments were primarily focused on the 40030 xPTFE surfaces due to its relevantly higher superhydrophobicity and resilience in comparison to the other xPTFE surfaces. The xPTFE surfaces used in this chapter were after slight wear by water, with fewer "hair-like" structures remaining for the repeat measurement required, the SEM images of the 40030 xPTFE surfaces are presented in Figure 6.1. The drops of Newtonian and Boger fluids have similar advancing/receding contact angles on the xPTFE surface being measured as about 150°/135° respectively, giving a contact angle hysteresis of about 15° for both fluids, as shown in Table 6.1. In order to isolate any potential effects of the surface structure, a weakly hydrophobic surface, a

polycarbonate, was also embossed using the same mesh as used to emboss the xPTFE but at a lower temperature (~125°C). The resulting surface, SEM image shown in Figure 6.1 (e), has an advancing contact angle (~92°) and contact angle hysteresis (~38°) for both Newtonian and Boger fluids, which is not significantly different to the untreated polycarbonate surface, as is also shown in Table 6.1.

Table 6.1: Contact angles

	Boger fluid			Newtonian fluid		
Surface	Advancing contact angles θ_{Adv}	Receding contact angles θ_{Rec}	Contact angle hysteresis	Advancing contact angles θ_{Adv}	Receding contact angles θ_{Rec}	Contact angle hysteresis
Smooth glass	54°±5°	11°±5°	43°±10°	58°±5°	12°±5°	46°±10°
Smooth polycarbonate	90°±5°	55°±5°	35°±10°	88°±5°	55°±5°	32°±10°
Embossed polycarbonate	92°±5°	54°±5°	38°±10°	94°±5°	54°±5°	40°±10°
xPTFE	152°±5°	136°±5°	16°±10°	151°±5°	136°±5°	15°±10°

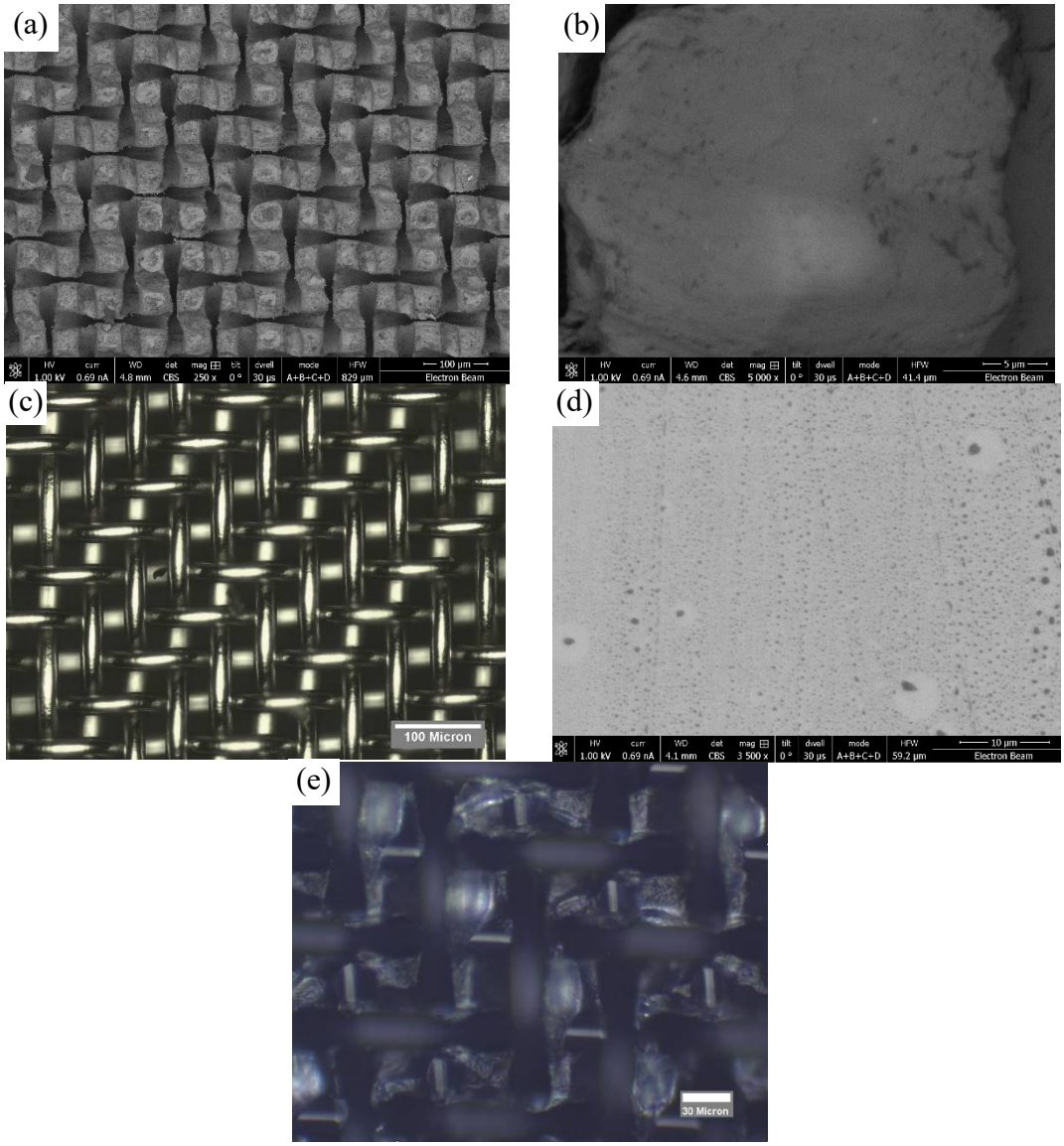

Figure 6.1. (a) and (b) SEM image of embossed xPTFE; (c) Optical microscope image of stainless steel mesh; (d) SEM image of smooth xPTFE; (e) Optical microscope image of embossed polycarbonate surface.

6.2.1 Preparation of Water-PEG-PEO solution

Three Boger fluids, referred to as Fluids B1, B2 and B3, and a comparator Newtonian fluid, referred to as Fluid N1, were prepared in this study based on polyethylene glycol (PEG). Polyethylene glycol is a water-soluble polymer and has a large range of molecular weight from thousands to millions g/mol depending on different lengths of the molecular chain. If the polymer has a molecular weight below $M_w < 20{,}000$ g/mol

it is referred to as polyethylene glycol "PEG", and if the molecular weight is above $M_w >$ 20,000 g/mol it is referred to as polyethylene oxide "PEO". The PEG solution exhibits practically no shear-thinning or elastic effects due to its low molecular weight, and can basically produce a viscous Newtonian solution when dissolved in water. After adding a small amount of PEO polymer to a high concentration PEG solution, the water-PEG-PEO solution becomes a strongly-elastic Boger fluid (Dontula et al. (1998)).

The three Boger fluids were prepared by adding three different high-molecular-weight polymers to a 42.9% w/w PEG (M_w=8000 g/mol) solution. Fluid B1 is based on a $M_w=2\times10^6$ g/mol PEO at 1000 ppm (w/w) concentration, whereas Fluids B2 and B3 were made using two different brands of nominally-identical $M_w=4\times10^6$ g/mol PEO at 500 ppm (w/w) concentration. The different brands of nominally-identical molecular weight produced fluids of varying elasticity due perhaps to different molecular weight distributions. Hence, these different M_w distributions have similar shear viscosity but significantly different elasticity as has been observed elsewhere (Zilz et al. (2014)). The Fluids B1 and B2 were prepared using $M_w=2\times10^6$ g/mol PEO and one grade of $M_w=4\times10^6$ g/mol PEO, which are both provided by polysciences and the other $M_w=4\times10^6$ g/mol PEO used in Fluid B3 was provided by Sigma Aldrich. The Newtonian comparator, referred to as Fluid N1, is 47% w/w PEG (M_w=8000 g/mol) solution which has approximately the same viscosity as the Boger fluids. The mixing of PEO in the PEG solution requires a long time due to the high molecular weight of PEO and the high viscosity of the PEG solution. Therefore, PEO polymer was added into distilled water first and mixed to a homogeneous solution after 24 hours gentle mixing using a magnetic stirrer. Then the PEG polymer powder was added into the water-PEO solution to create the Boger fluid after another 24 hours mixing. The

prepared fluids were stored in the refrigerator at 4°C to prevent any potential thermal or bacteriological degradation.

Because the moving drop experiments were conducted at room temperature which varied slightly day to day (17-20°C), the rheological profiles at different temperatures were measured in order to match exactly the experimental conditions. The shear viscosities of the four fluids were measured by an Anton Paar MCR 302 controlled stress rheometer using a 60 mm diameter 1° cone-plate geometry at 17°C and 20°C, shown in Figure 6.4.

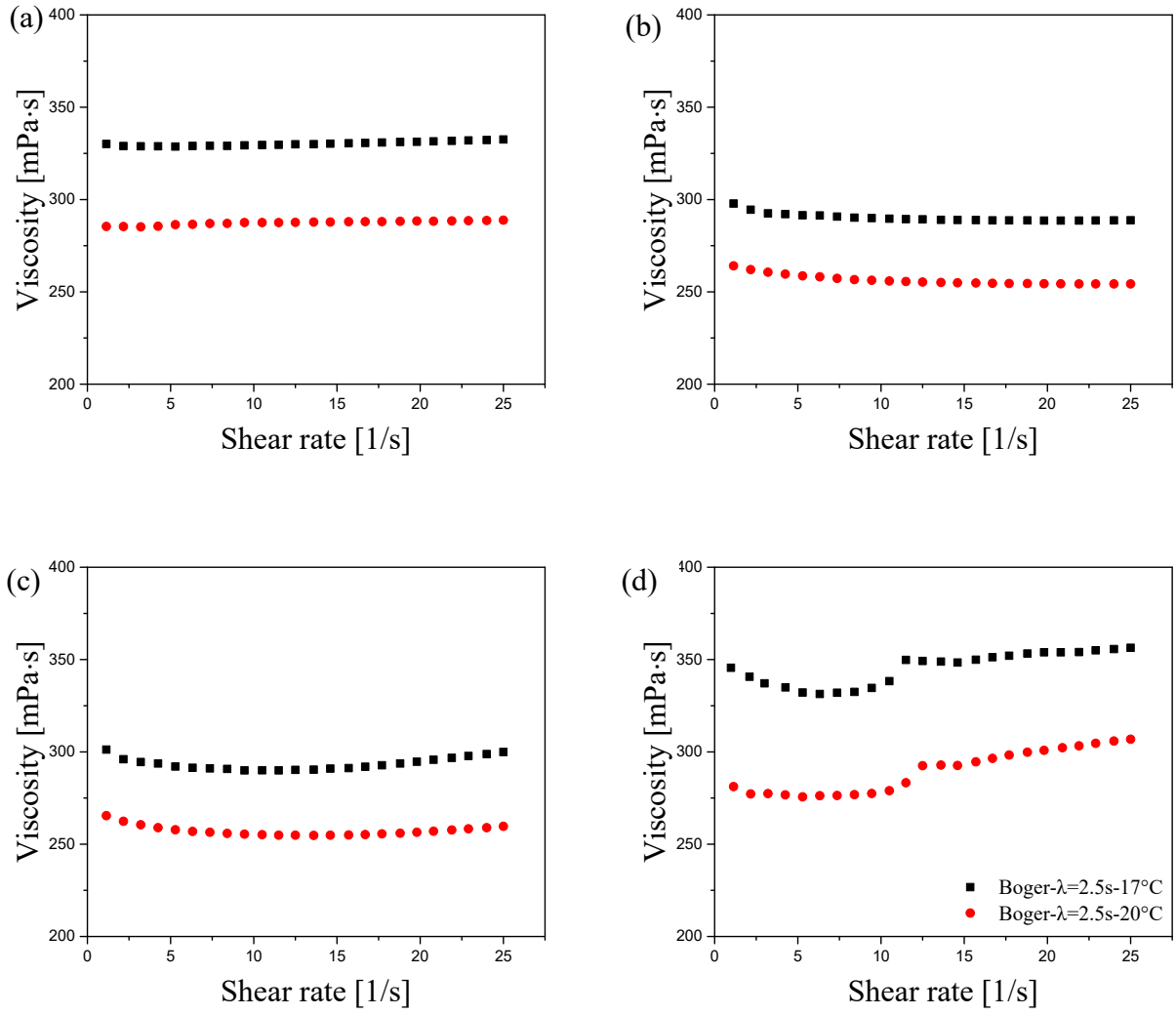

Figure 6.2. Viscosity vs shear rate of working fluids at 17°C (■) and 20°C (●). (a) fluid N1; (b) fluid B1; (c) fluid B2; (d) fluid B3. Note onset of a purely-elastic instability for fluid 3 at a shear rate ~ 11 s^{-1}.

The relaxation time of the Boger fluids were measured using a Capillary Break Up Extensional Rheometer (CaBER) (Rodd et al. (2005)) at different temperatures. In the CaBER technique, a liquid bridge is initially maintained by its capillary force between two cylindrical plates of 4 mm diameter. A sudden axial strain is then applied which results in the formation of an unstable elongated liquid thread. The diameter of the

thread is measured and recorded by a laser micro-meter of 10μm resolution. The balance of elastic and capillary force on this uniform cylindrical fluid thread of radius R_0 then predicts that the filament radius decays exponentially in time as:

$$\frac{R_{mid}(t)}{R_0} = \left(\frac{GR_0}{2\sigma}\right)^{1/3} exp\left(\frac{-t}{3\lambda}\right) \qquad 6.1$$

where t is time, $R_{mid}(t)$ is the radius of mid-point of the fluid thread at time t, G is the elastic modulus, σ is the surface tension and λ is the relaxation time, Entov and Hinch (1997) and Rodd et al. (2005). Using equation 6.1 the relaxation time of the Boger fluid can be determined by fitting an exponential to the diameter vs time plot in the elasto-capillary region as shown in Figure 6.4.

The working fluid characterisation includes viscosities, densities, surface tensions, and relaxation time of the four experimental fluids and are listed in Table 6.2. As can be seen in Table 6.2, the four fluids have similar viscosities around 285 mPa·s at 20°C when the shear rate is above about 5 s^{-1}. The CaBER measurements show the relaxation time λ of these Boger fluids have a large range from 0.2s to 2.5s and the extensional viscosity (shown in Figure 6.3) also increases with the polymer molecular weight from 500 Pa·s for fluid B1 to over 10000 Pa·s for fluid B3 (i.e., for fluid B3 very similar to that measured in Oliveira et al. (2006)).

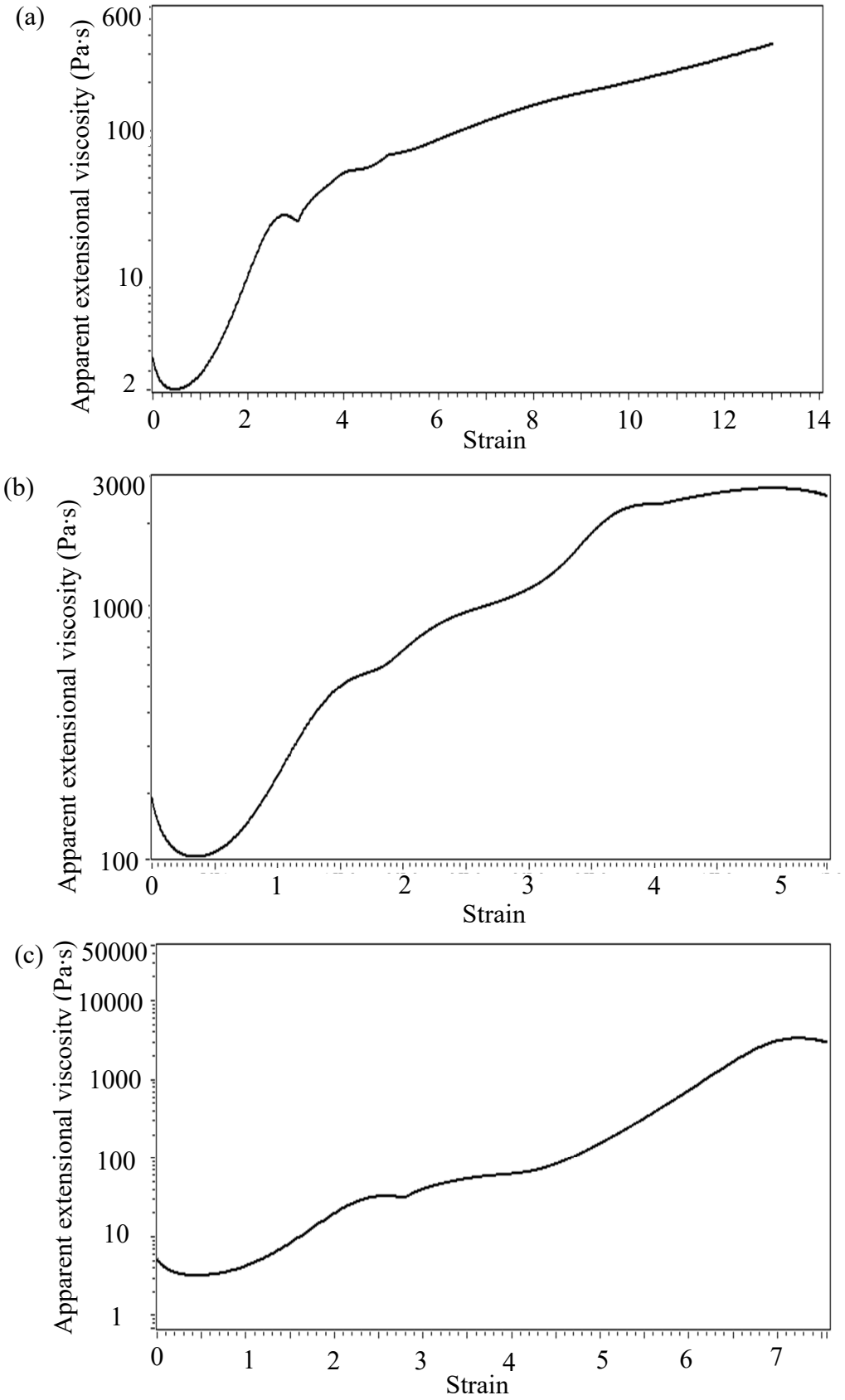

Figure 6.3. Extentional viscosities vs strain measured via CaBER of (a) Fluid B1, (b) Fluid B2 and (c) Fluid B3.

Fluids B2 and B3 which have high molecular weight show a high elasticity and slight shear thinning especially at low shear rates. Meanwhile, the densities and surface tensions are very similar for all fluids due to the similar concentration of PEG and the same chemical component of the four solvents.

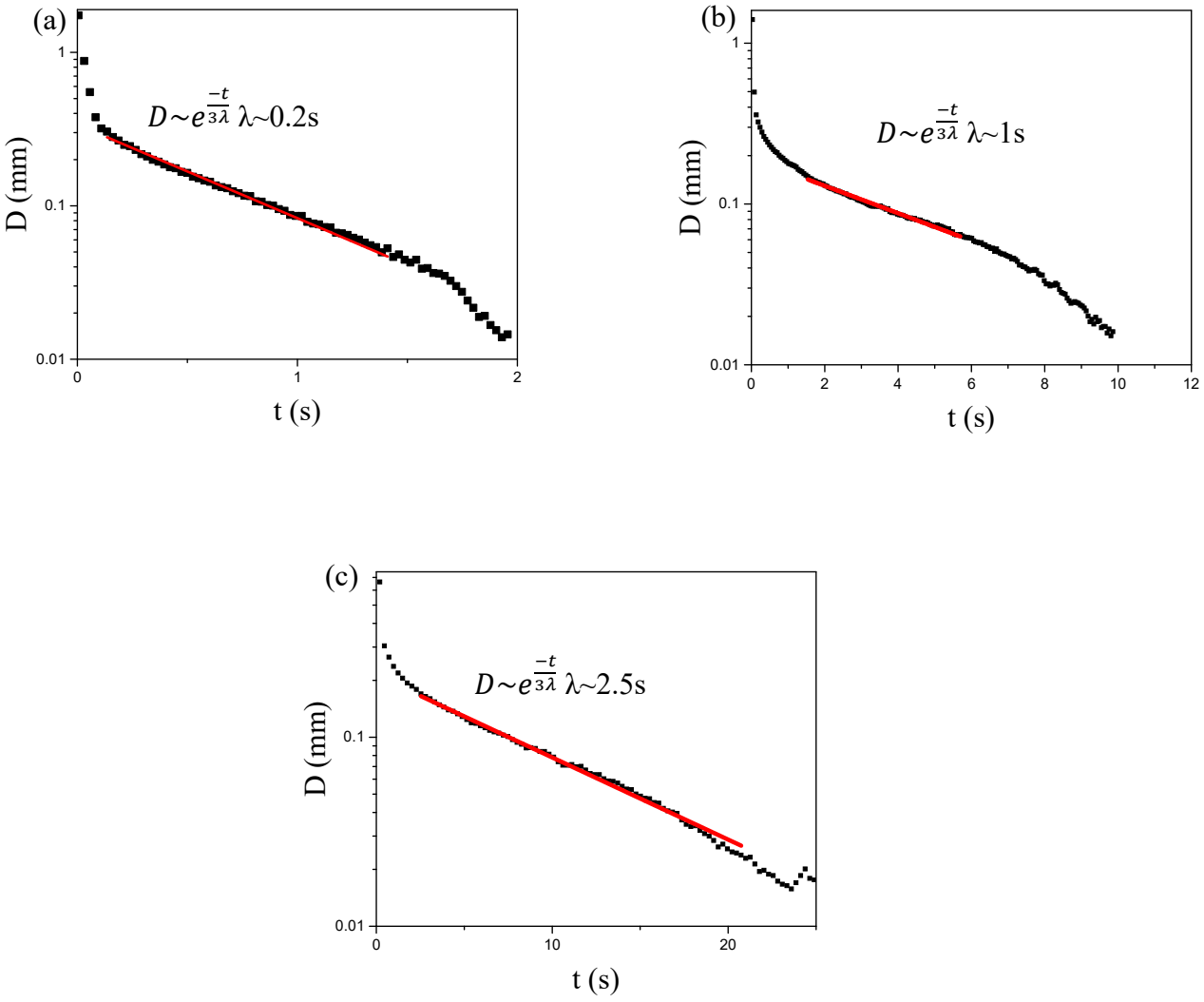

Figure 6.4. Diameter vs time from CaBER measurement (a) fluid B1; (b) fluid B2; (c) fluid B3.

Table 6.2: Rheology properties of fluids.

Fluid	Shear Viscosity μ (mPa·s @20°C)	Surface tension σ (mN/m)	Fluid density ρ(kg/m^3)	CaBER relaxation time λ (s)
Fluid B1: PEG/PEO (Boger λ~0.2s)	255±2	53.3^	1080	0.2±0.1
Fluid B2: PEG/PEO (Boger λ~1s)	285±5	53.3^	1080	1±0.5
Fluid B3: PEG/PEO (Boger λ~2.5s)	285±5	53.3^	1080	2.5±0.5
Fluid N1: PEG (Newtonian)	285±2	53.3	1082	-

6.2.2 Inclined plate and drop motion recording system

An adjustable acrylic inclination platform was built to conduct the moving-drop experiments. The platform is fixed on a table and adjusted to the desired angle. Then the drops were placed on the test surface using a syringe pump to accurately control the drop volume. The flow rate of the syringe pump is carefully controlled at a very slow speed (10 μL/s) to prevent any potential degradation of the polymer solutions via shear. The surface is then impulsively tilted and the droplet motion recorded using a camera (Nikon D5300) at 30 frames per second. The recording continues for at most 5 minutes, which avoids any significant influence of evaporation, and each experiment is repeated at least three times a schematic of the setup is shown in Figure 6.5. The recorded videos were post-processed using “Tracker”, details can be seen in Brown and Cox (2009), to determine the steady-state droplet velocity. Hydrophilic smooth glass surfaces, microscope slides (purchased from AmScope) which were pre-cleaned and single use “as delivered”, were used to directly compare with the hot-embossed superhydrophobic xPTFE surfaces. The advancing and receding contact angles for all of the test fluids on

these glass surfaces are 54° and 11° respectively, as shown in Table 6.1. In addition, a weakly hydrophobic surface, a polycarbonate but embossed by the same mesh as used to emboss the xPTFE, was investigated as well to isolate any potential effect of the surface structure on the observed phenomena.

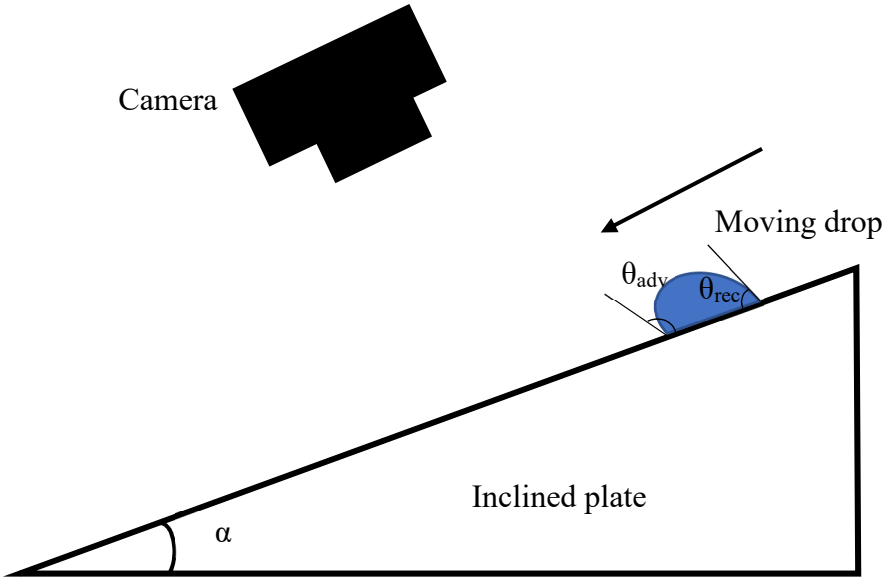

Figure 6.5. Schematic of inclined plate and drop motion recording system.

6.3 Results and discussion

6.3.1 Drops moving on hydrophilic surfaces

Most surfaces in nature are hydrophilic (Drelich et al. (2011)), for example smooth glass surfaces, for such surfaces the contact angle is lower than 90°. Two Boger fluids, fluids B2 and B3, and the Newtonian comparator, fluid N1, with different controlled volumes of 50, 75 and 100 μL were tested on the smooth glass surface. The inclination angle of the surfaces was varied from 19° to 27°. In general, the Newtonian and Boger fluid drops behave very similarly on the smooth glass surfaces: they flow slowly, and

leave a wide thin-film behind which indicates a close to zero receding contact angle. The velocity of the "drop" ranges from 0.05mm/s for the lowest inclination angle and smallest volume to 0.8 mm/s for the highest inclination angle and largest volume. The data is plotted as velocity verses inclination angle in Figure 6.6. From Figure 6.6, the velocity of the drops which have the same volume varies linearly with the inclination angle.

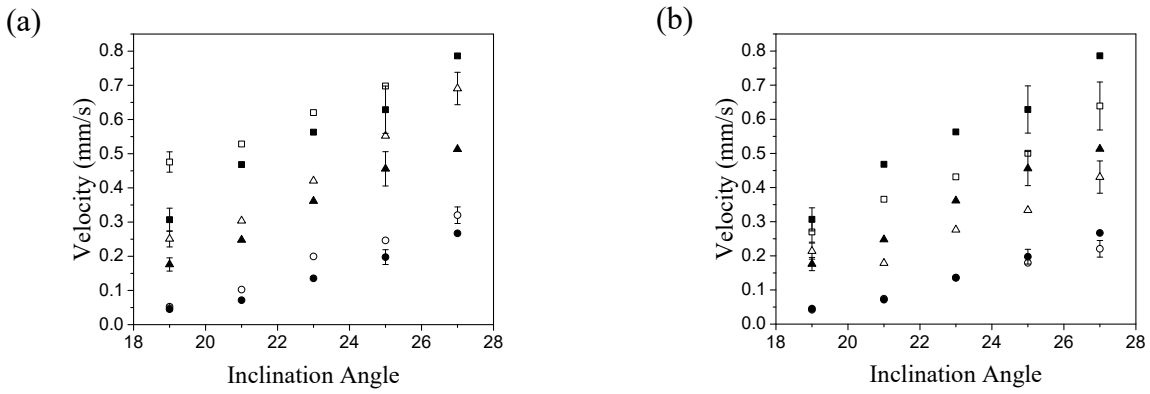

Figure 6.6. Velocity vs Inclination angle for Newtonian (fluid N1, ■ 100 μL, ▲ 75 μL, ● 50 μL.) and Boger fluid (a) fluid B2, λ~1s; (b) fluid B3, λ~2.5s, (□ 100 μL, △ 75 μL, ○ 50 μL.) drops on smooth glass surface; drops on smooth glass surface. Error bars represent the spread of data from repeat experiments.

Although the viscosity of the Boger fluid is approximately constant against shear rate in most cases, a slight shear-thinning effect can be observed at very low shear rate (< 5 s^{-1}). By adjusting the viscosity value based on a shear rate corresponding to the drop's moving speed and size (~ 0.01s^{-1}), we can plot the data as capillary number versus Bond number, shown in Figure 6.7, and all the data sets approximately collapse. This result is in agreement with previous studies (Le Grand et al. (2005) and Morita et al. (2009)), and this linear relationship between *Ca* and *Bo* with a non-zero intercept indicates a force balance between viscous force, gravitational and resistance caused by contact angle hysteresis. Even though the flow field inside the drop is complicated (Hodges et

al. (2004)) while the drop is moving on the surface, under the relatively slow velocities observed here, the flow field can be considered as laminar and steady. For a deformed drop as it slides, it is possible to use either of the two primary axis to calculate an appropriate length scale (or an average of the two). However, for a drop leaving a film behind, as seen here, such calculations will likely be poor estimates. As a consequence, for simplicity we assume the drop is a hemisphere of radius *r*. Although we expect that the shear rate increases to infinity as you approach the contact line (because the height goes to zero), we try to capture that effect here by saying that the drop's velocity will vary over some small distance δ which is proportional to this radius (expecting the constant of proportionality *c* to be << 1):

$$\dot{\gamma} \sim U/\delta \sim U/cr. \tag{6.2}$$

And the contact area is:

$$A \sim \pi r^2. \tag{6.3}$$

The viscous force can then be roughly estimated as

$$F_V \sim \mu \dot{\gamma} A = \frac{\eta U}{cr} \cdot \pi r^2 = \frac{\pi \mu U r}{c}. \tag{6.4}$$

If we assume the volume of the drop is a hemisphere, the gravitational force is then:

$$F_g \sim \rho g V \sin\alpha = \rho g \frac{2}{3} \pi r^3 \sin\alpha. \tag{6.5}$$

The resistance caused by contact angle hysteresis F_h is:

$$F_h \sim 2\sigma r(\cos\theta_{rec} - \cos\theta_{adv}). \tag{6.6}$$

If the viscous force balances with the gravitational force and contact angle hysteresis force, $F_g = F_v + F_h$, hence:

$$\rho g \frac{2}{3}\pi r^3 \sin\alpha \sim \frac{\mu U \pi r}{c} + 2\sigma r(\cos\theta_{rec} - \cos\theta_{adv}) \qquad 6.7$$

then if we divide both sides by $\pi\sigma r$, we have the relationship:

$$\frac{(\frac{2}{3}\pi)^{\frac{1}{3}}}{\pi}\frac{V^{2/3}\rho g \sin\alpha}{\sigma} \sim \frac{\mu U}{c\sigma} + \frac{2}{\pi}(\cos\theta_{rec} - \cos\theta_{adv}) \qquad 6.8$$

which is equivalent to $Ca \sim cC_1Bo - cC_2(\cos\theta_{rec} - \cos\theta_{adv})$, where C_1 is $\frac{(\frac{2}{3}\pi)^{\frac{1}{3}}}{\pi} \sim 0.407$ and C_2 is $\frac{2}{\pi} \sim 0.6366$ (and $c << 1$). This result demonstrates that under this experimental condition, the capillary number should be approximately proportional to the Bond number, and the slope is a constant for a particular surface somewhat analogous to a "friction coefficient", independent with the size or viscosity of the drop. The non-zero intercept of this linear curve is caused by the contact angle hysteresis. Based on this analysis the linear variation shown in Figure 6.7 indicates the dominant forces achieved on the drop for these conditions are gravity, contact angle hysteresis and viscosity. Fitting the data shown in Figure 6.7 can be used to estimate the value of the constant "*c*" and, as it can be determined separately from both the slope and the intercept, provide an indication of the internal consistency of the scaling analysis above. Doing so, assuming the receding contact angle is zero, gives values of *c* equal to 0.00916 and 0.0104, calculated from the slope and interception respectively.

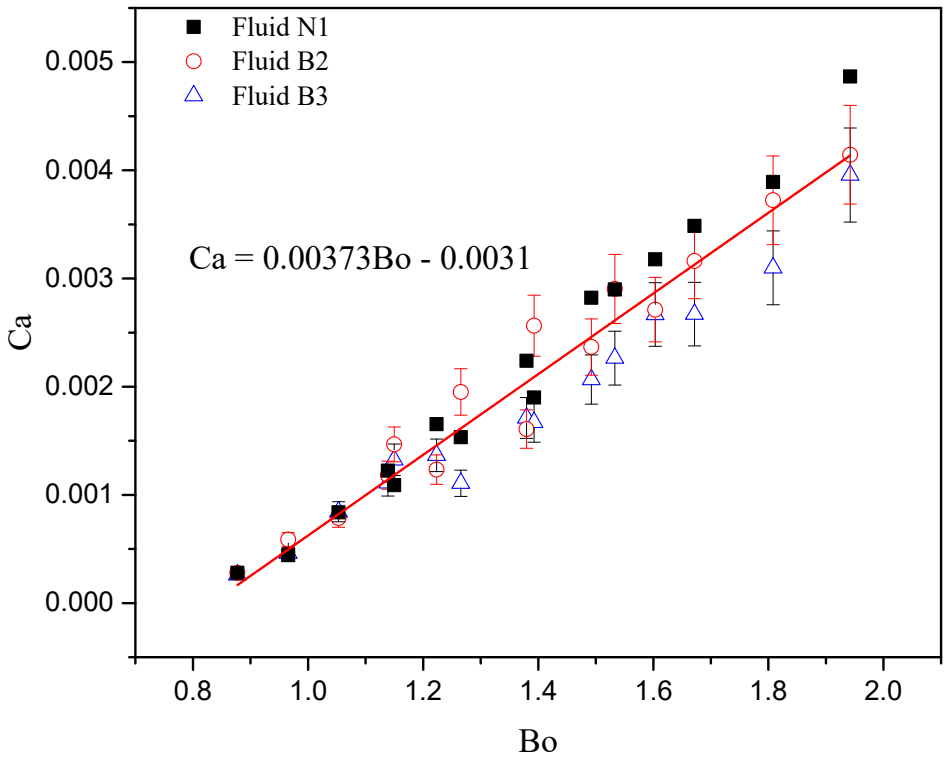

Figure 6.7. Capillary number versus Bond number for Newtonian (fluid N1) and Boger fluid (fluid B2, λ~1s, and B3, λ~2.5s.) drops on smooth glass surface including linear fit to the complete data set. Error bars represent the spread of data from repeat experiments.

When a structure is created on a hydrophilic surface, the so-called "Wenzel" state liquid-solid interface makes the surface more hydrophilic and could introduce some additional "friction" while drops move on the surface, acting like structural "roughness" elements (Whyman et al. (2008) and Lee et al. (2016)). To compare with the xPTFE surfaces which have a micro-scale brick-like surface structure, a polycarbonate plate was embossed by an identical mesh using a similar hot-embossing technique. The surface structure was observed using a microscope, and was found to be similar to the xPTFE structure as already shown in Figure 6.1(e). The velocity data for this embossed

polycarbonate surface is shown in Figure 6.8, and the velocities can be seen to be slower compared to the results on the smooth glass surface. The Boger fluid drops, much as was observed on the smooth glass surfaces, behave no differently to the Newtonian drops. In addition, all the data sets collapse in an approximately linear way when plotted as *Ca* versus *Bo* despite the non-linear results caused by the uncertainty in low *Ca* values, as shown in Figure 6.9. The intercept of the curve is close to the smooth glass data due to the similar level of contact angle hysteresis for the two surfaces (~38° for polycarbonate and ~43° for glass), but the slope is lower compared with the smooth glass results which is expected given the additional roughness introduced.

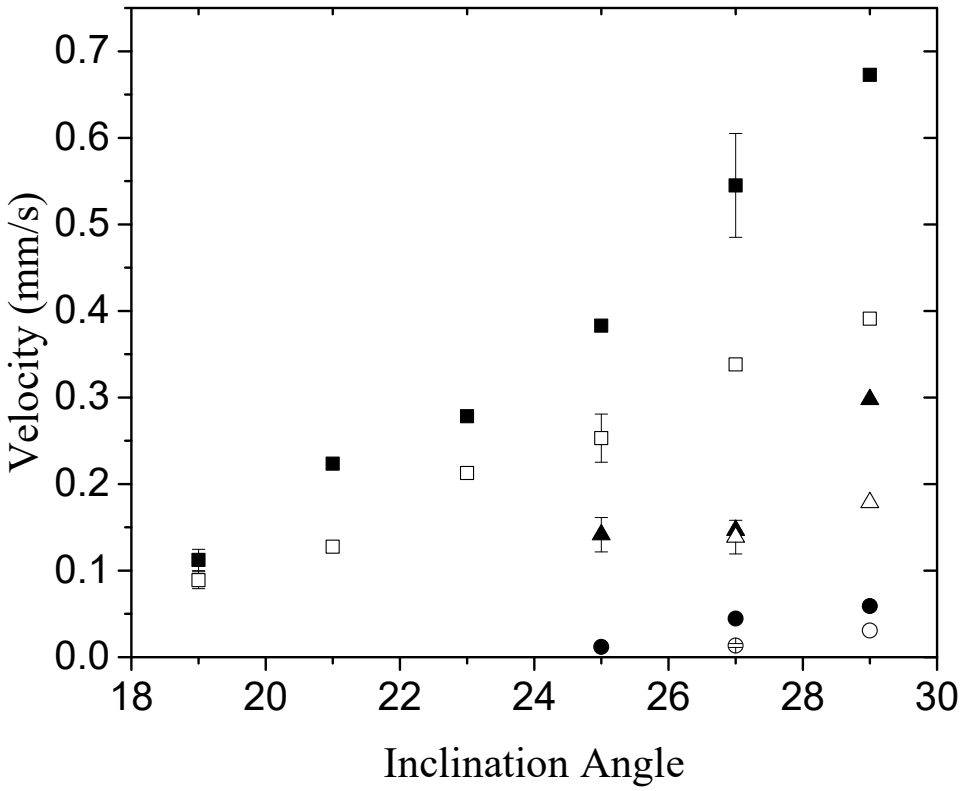

Figure 6.8. Velocity vs Inclination angle for Newtonian (fluid N1, ■ 100 μL, ▲ 75 μL, ● 50 μL.) and Boger fluid (fluid B3, λ~2.5s, □ 100 μL, △ 75 μL, ○ 50 μL.) drops on embossed polycarbonate surface. Error bars represent the spread of data from repeat experiments.

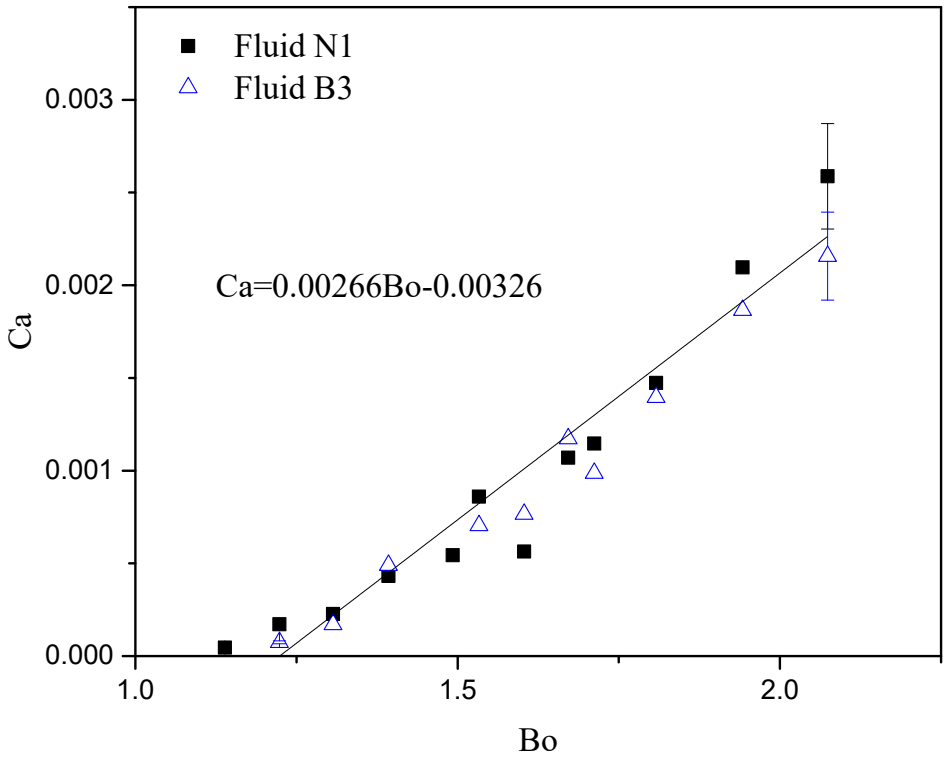

Figure 6.9. Capillary number versus Bond number for Newtonian (fluid N1) and Boger fluid (fluid B3, λ~2.5s) drops on embossed polycarbonate surface including linear fit to the complete data set. Error bars represent the spread of data from repeat experiments.

6.3.2 Drops moving on hydrophobic surfaces

In contrast to hydrophilic surfaces, the contact angles on superhydrophobic surfaces are much higher than 90°, therefore the surface tension acts to reduce the contact interface area. In addition, the contact angle hysteresis is quite small (< 15°) and, as a consequence, the drops can move much easier than on hydrophilic and weakly hydrophobic surfaces such as those discussed in Section 3.1. This is especially so on superhydrophobic surfaces which have typical contact angles higher than 150°

(Shirtcliffe et al. (2010)), the moving speed is often over 10 times greater than that on hydrophilic surfaces. As we discussed in the previous section, the Boger and Newtonian fluid behave equivalently on such hydrophilic surfaces, or stated in another way, the elasticity does not significantly affect the drop's velocity (at least under the parameter range studied). On the superhydrophobic xPTFE surfaces, the velocities of our Newtonian drops were slower than the maximum wetting speed (Blake & Ruschak (1979) and Le Grand et al. (2005)) hence no instability is observed and no threads are left behind for these drops. In contrast, the Boger fluid drops are slowed down significantly compared to the Newtonian drops and there are complex "branch-like" and "beads-on-tail" structures left behind, as shown in Figure 6.10, which indicates a distinctive mechanism for such elastic fluids on superhydrophobic surfaces in comparison to equivalent Newtonian fluids.

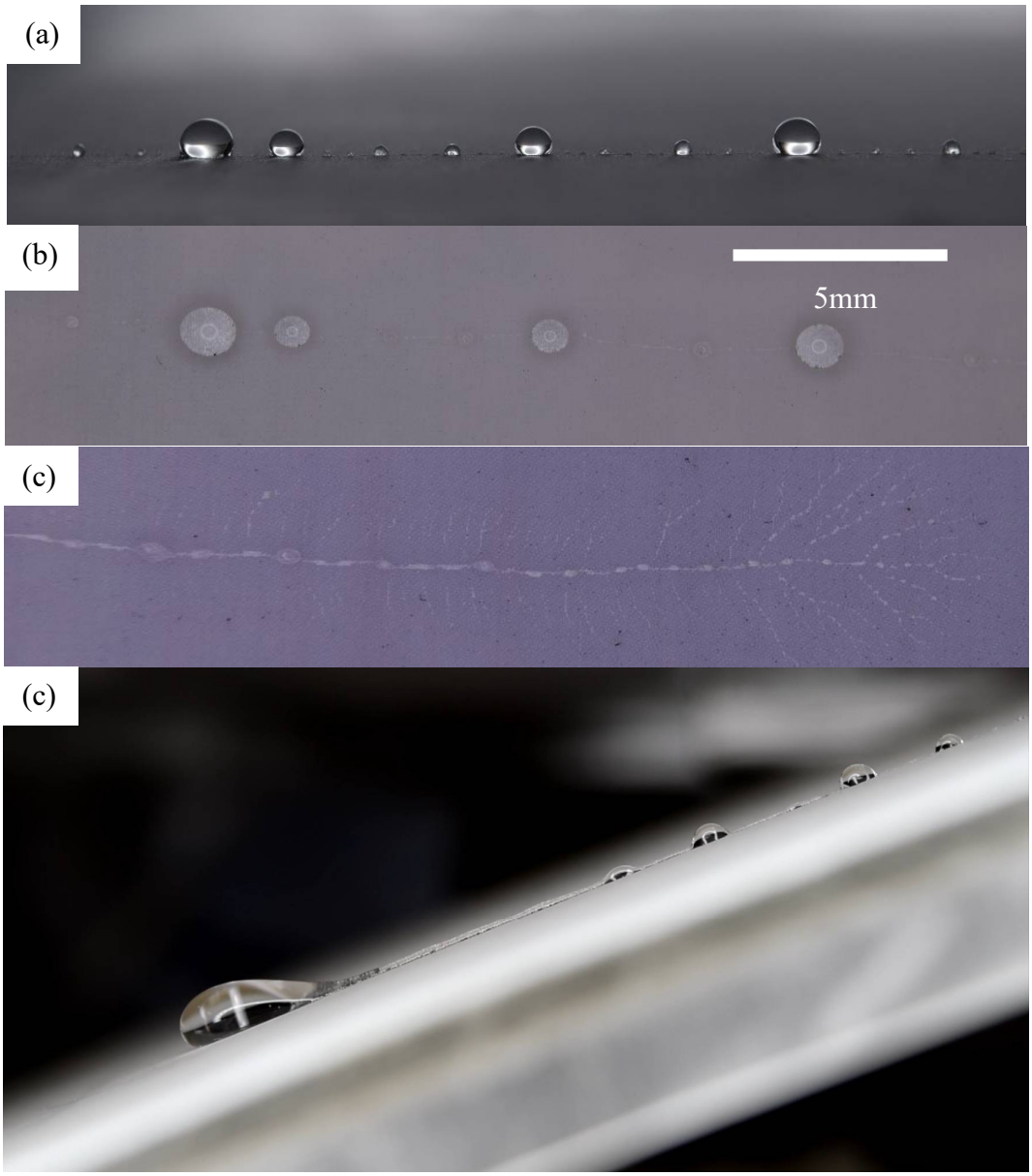

Figure 6.10. (a) Side view of "Beads-on-tail" phenomenon; (b) Top view of "Beads-on-tail" phenomenon; (c) Top view of "Branch-like" structure left behind moving Boger fluid drop; (d)A Boger fluid drop moving on the xPTFE surface and "Beads-on-tail" forming behind. Scale bar representative for all images.

Three Boger fluids, fluids B1, B2 and B3, and a Newtonian comparator fluid N1 were tested on the 40030 xPTFE surfaces which have the best superhydrophobicity and resilience of the three xPTFE introduced in Chapter 3. The volumes of the drop were controlled via a syringe pump as 50, 75 and 100 μL and the inclination angle of the surfaces is varied from 19° to 27°. The velocity versus inclination angle data is shown

in Figure 6.11. The velocity of the Newtonian drops is much higher than that of equivalent volume drops on hydrophilic surfaces, the range is from 2 mm/s, at lowest inclination angle and smallest volume, to 15mm/s at the highest inclination angle and largest volume. For the Boger fluid drops, the velocity is much lower than the Newtonian drops, being reduced by nearly 50% for the low elasticity fluid (Fluid B1) and 85% for the highly-elastic fluid (Fluid B2 and B3).

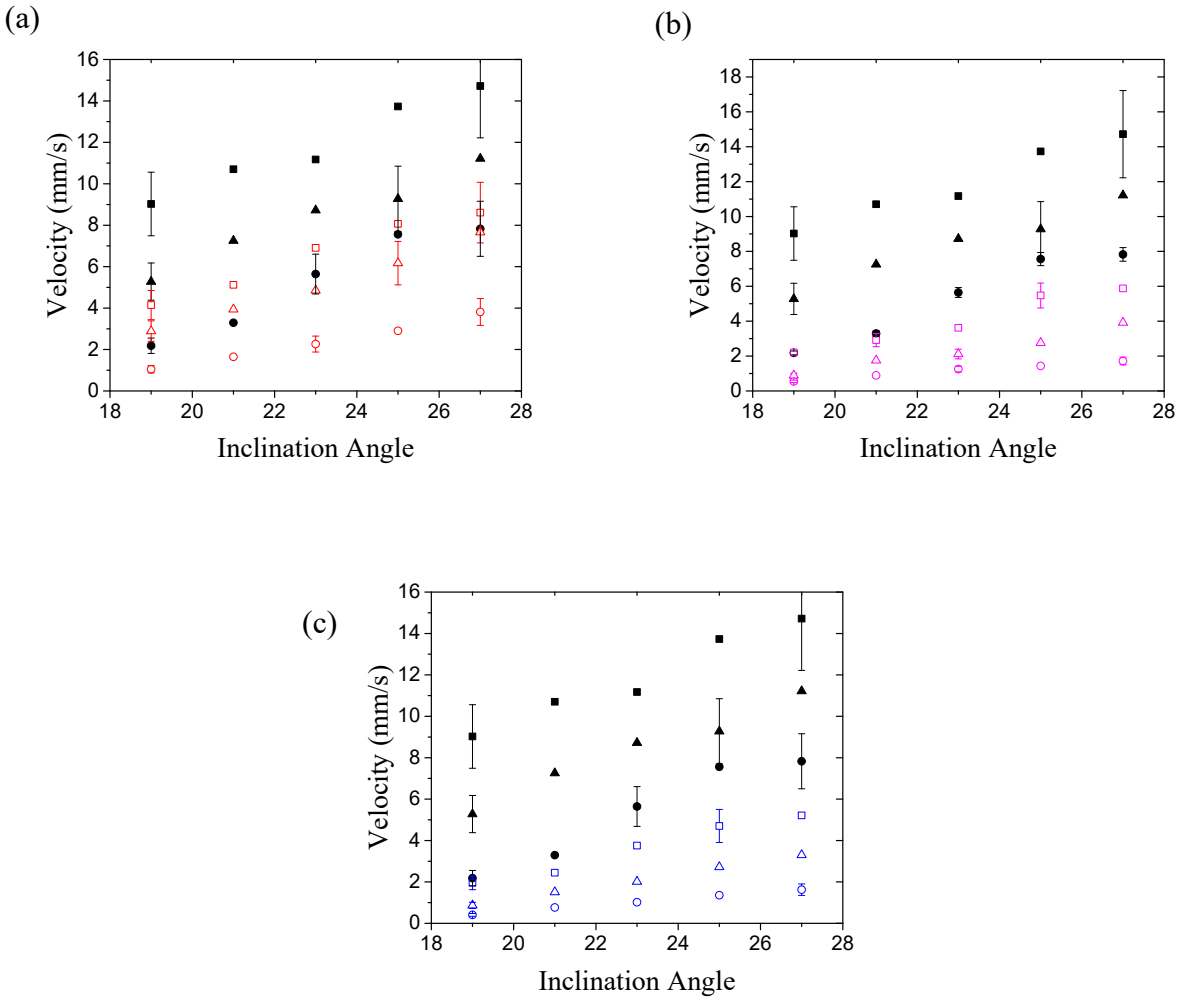

Figure 6.11. Velocity vs Inclination angle for Newtonian (fluid N1, ■ 100 µL, ▲ 75 µL, ● 50 µL.) and Boger fluid, (a) fluid B1, λ~0.2s; (b) fluid B2, λ~1s, (□ 100 µL, △ 75 µL, ○ 50 µL.) (c) fluid B3, λ~2.5s, (□ 100 µL, △ 75 µL, ○ 50 µL.) drops on xPTFE surface. Error bars represent (n=3) the spread of data from repeat experiments.

If plotted as *Ca* versus *Bo*, shown in Figure 6.12, the data sets collapse for each type of fluid respectively, but the data from different fluids do not collapse onto a single master curve as was observed for the smooth and rough hydrophilic surfaces. Assuming identical viscous forces, the four slopes indicate three different "friction coefficients" on the same surface, and the only difference between these fluids is the level of elasticity. Comparing the data of fluid B1 and fluid B3 which have different elasticity, the larger elasticity exhibits a larger "friction coefficient", which means the elasticity essentially increases the "friction" and slows the drops down more.

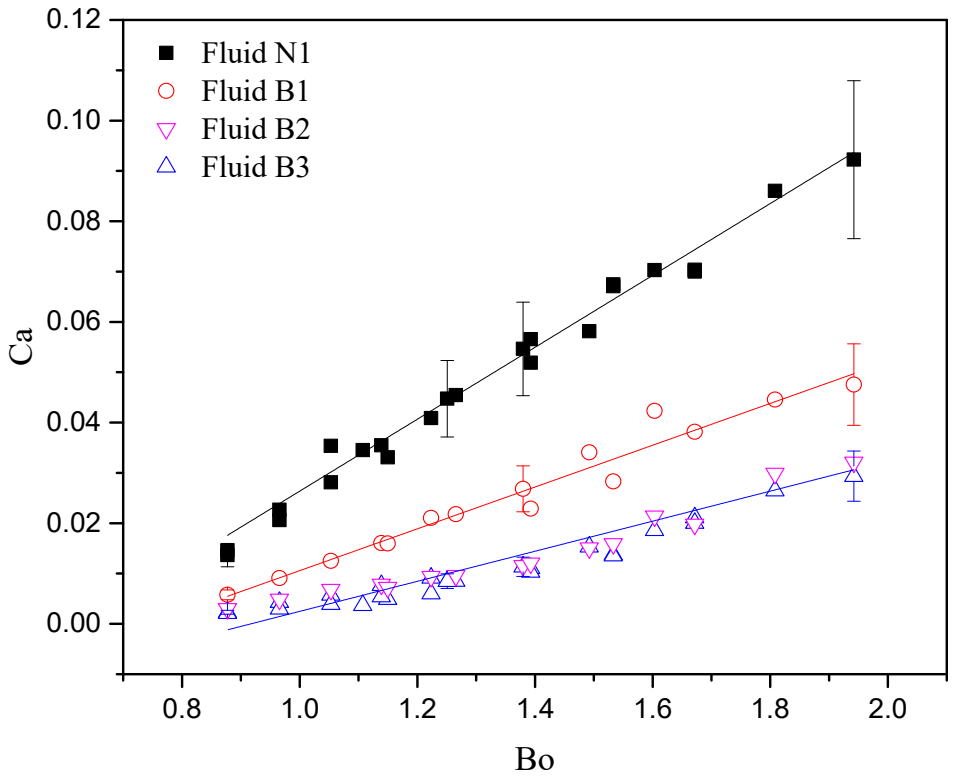

Figure 6.12. Capillary number versus Bond number for Newtonian (Fluid N1) and Boger fluid (Fluid B1, λ~0.2s, B2 λ~1s and B3, λ~2.5s.) drops on xPTFE including representative error bars and linear fits to each of the data sets. Error bars represent the spread of data from repeat experiments.

In addition, the same experiments using Fluid N1 and B1 were implemented on the 30040 and 50025 xPTFE surfaces to investigate the effects from the surface structures, the Ca vs Bo data are plotted in Figure 6.13. From the results, the both fluid drops behaved similarly on the 50025 xPTFE due to its similar superhydrophobicity (static contact angle, contact angle hysteresis and slip-length) to the 40030 xPTFE surfaces, details shown in Table 4.6. However, the slopes of Ca vs Bo plot on the 30040 surfaces are lower than the other surfaces for both of the Newtonian and Boger fluid drops due to its lower superhydrophobicity than the other xPTFE surfaces. This result indicates that the higher superhydrophobicity can make both the Newtonian and Boger fluid drop move easier (critical *Bo* is lower) and faster (slope is higher).

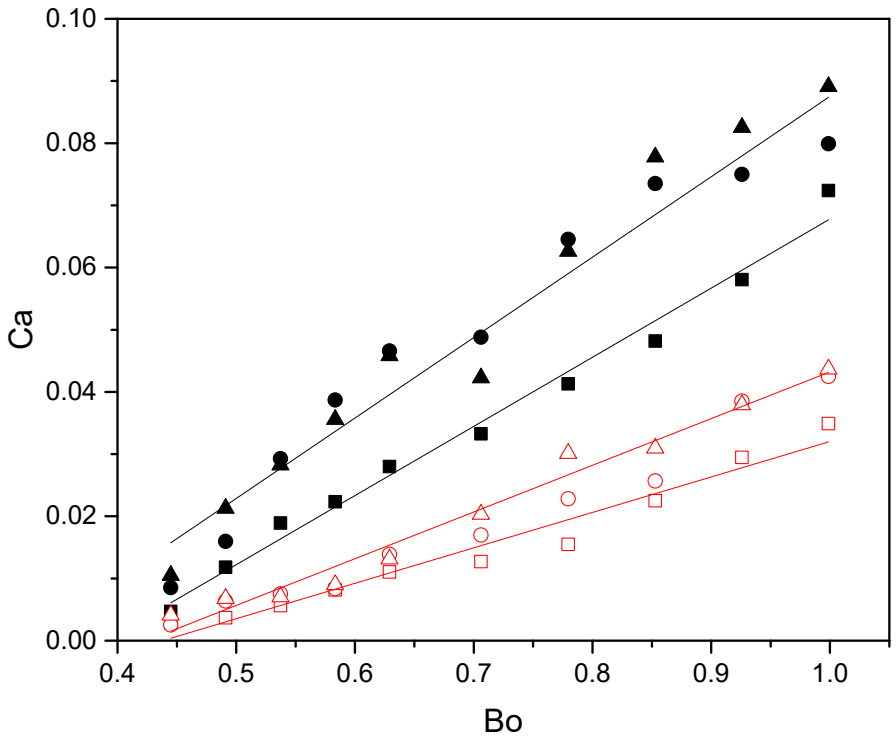

Figure 6.13. Capillary number versus Bond number for Newtonian (Fluid N1, filled symbles) and Boger fluid (Fluid B1 λ~0.2s, open symbles) drops on different ■ 30040, ● 40030 and ▲ 50025 xPTFE.

After calculating the apparent viscosity from the results of 40030 xPTFE surfaces, shown in Figure 6.14, by comparing the moving velocity of Boger fluid drops to the Newtonian drops (assuming the resistance is caused solely by higher apparent "viscosity"), for the lower molecular weight Boger fluid (fluid B1) its apparent viscosity is almost 2.5 times the Newtonian one, for the higher molecular weight Boger fluid (fluid B3) its apparent viscosity is as high as 7 times the Newtonian drop at low speeds and decreasing to 2.5 times when the Bond number is over 1.4. Meanwhile, if we estimate a Weissenberg number ($Wi = \dot{\gamma} \cdot \lambda$) to examine the effect of elasticity, we note that the speed of smaller Boger drops on the xPTFE surface is roughly similar to large drops on smooth glass surface. This suggests that they have the same range of "global" Weissenberg number Wi (~ 0.8), which based on drop speed and drop radius (~2-4 mm) or capillary length (~2.2 mm) in these experiments, but as we have demonstrated in Section 6.3.1, there is no effect of elasticity observed on either smooth glass or embossed polycarbonate surfaces. This suggests elastic effects, which were only observed on the xPTFE surfaces, cannot be explained as a "bulk" effect even though the Weissenberg number is order one on both smooth glass, embossed polycarbonate and superhydrophobic surfaces.

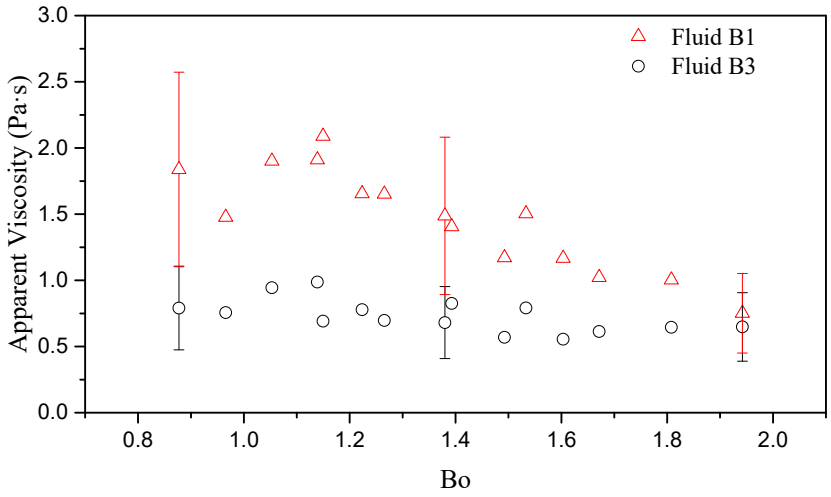

Figure 6.14. Apparent viscosity vs Bond number on the xPTFE surface for Boger fluids B1 and B3. Error bars represent the spread of data from repeat experiments.

Considering the micro-scale structure of the xPTFE surface and the "branch-like" tail of the Boger fluid left by the moving drop, we suspect that the strong elastic effect might possibly be caused by a micro-scale mechanism i.e. interaction between the fluid and the surface on the scale of the brick-like structure (~30μm). In order to gain more insight into this phenomenon, we used both light microscope (Nikon Epiphot TME) and SEM to investigate the "branch-like" structures on the drop's "tail", as is shown in Figure 6.15.

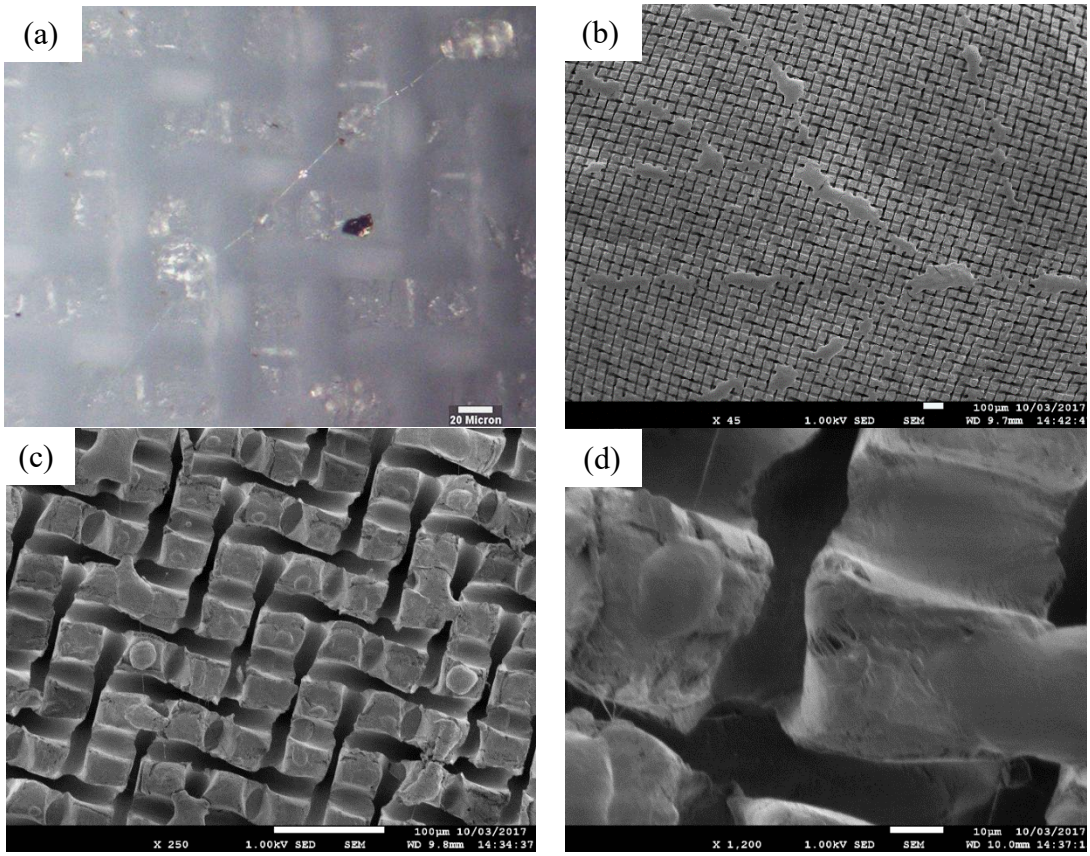

Figure 6.15. (a) Branch structure left on the xPTFE surface observed under optical microscope (200x magnification) illustrating islands of elastic fluid marooned on pillars of structure connected by very thin (~1 micron) fluid bridges. (b) 45x magnification; (c) 250x magnification; (d) 1200x magnification, observed under SEM, polymer "blobs" attached on the pillars and filaments connected between them.

6.3.3 Micro-scale ligament extension

Using microscopy to investigate the "branch-like" structure which is left behind the drop, under the optical microscope, it is shown that filaments connect the isolated micro-scale size droplets pinned to the pillars that form the surface structure (size on the order of 30 μm), as can be seen in Figure 6.15(a). Using SEM, which benefits from higher resolution and better depth of field, the surface structure and droplets were more clearly observed. However, the solvent evaporates due to the fact that the samples have to be placed in a vacuum chamber during the SEM investigation. Although only dried polymer was observed, the drops and the filaments connecting between them are still

clearly observable as shown in Figure 6.15(b)-(d). This suggests that during the drop's movement on the xPTFE surface, while the drop is passing over the pillar, some of the fluid is "pinned" on the sharp corner of the pillar to form a separate droplet still connected to the main drop via a filament. We posit that, within this stretching filament, the local strain rate is sufficient to extend the polymer chains between the micro scale drop and the main drop. The extending chains increase the extensional viscosity locally in this filament, slowing down the drop and leaving behind the "branch-like" structure when the filaments finally breaks due to capillarity. Krumpfer and McCarthy (2011) studied a comparable mechanism on similar superhydrophobic surfaces, but only for water. Their study shows the microdroplets can be produced at pinning sites on this kind of surface and then rapidly evaporate corroborating this picture. The extension of the filaments provides a tensile resistive force to the main drop and that is the reason why the Boger fluid drops are significantly slowed down compared to the Newtonian drops, very much akin to a series of "bungy" ropes pulling against the main drop. For this to be true, the filament break-up time $\tau_b \approx \eta_E d / \sigma$ must be longer than the time for the drop to reach to the next pillar, $\tau_c = w/U$. Here $w = 2d$ is the spacing between pillars. Therefore, a minimum extensional viscosity of $\eta_E > 2\sigma / U \approx 100$ Pa·s is required for this to form stable filaments between the pillar and main drop, from the CaBER measurements the extensional viscosities (500 Pa·s and 10,000 Pa·s) of the two Boger fluid used in this study are much larger than this requirement. To estimate the resistance force from the extension of these filaments, as shown in the cartoon in Figure 6.16, the resistance force resulting from extensional viscosity can be approximated as $F_{EV} = \eta_E \dot{\varepsilon} k A$, where $\dot{\varepsilon} = U / w$ is the extension rate, k is the probability of Boger fluid attaching on the pillars of the surface structure, and $A = \pi d^2 n / 4$ is the total area of the

pillars through the receding contact line of the drop, where n=D/2w is the number of pillars along that line. Then the force becomes $F_{EV} = (\pi UkD\eta_E)/16 = (\pi k\sigma D/16)TrCa$ where $Tr = \eta_E/\eta$ is the Trouton ratio. From microscope images, it can be seen that k is on the order of 0.1 and the resulting extensional force from the extension of the filaments is then on the same order of magnitude as the gravitational force and shear viscosity force. The extension process of these filaments causes some of the fluid to be slowed down, and form an elongated tail. The resulting "beads-on-a-tail" phenomenon then occurs possibly by a similar instability mechanism as observed in capillary break-up experiments (Oliveira et al. (2006)) and ink-jetting processes (Duineveld (2003), Davis (1980)). Experiments on the weakly hydrophobic (polycarbonate) surface with a similar micro-scale structure, discussed in section 6.3.1, do not exhibit these phenomena.

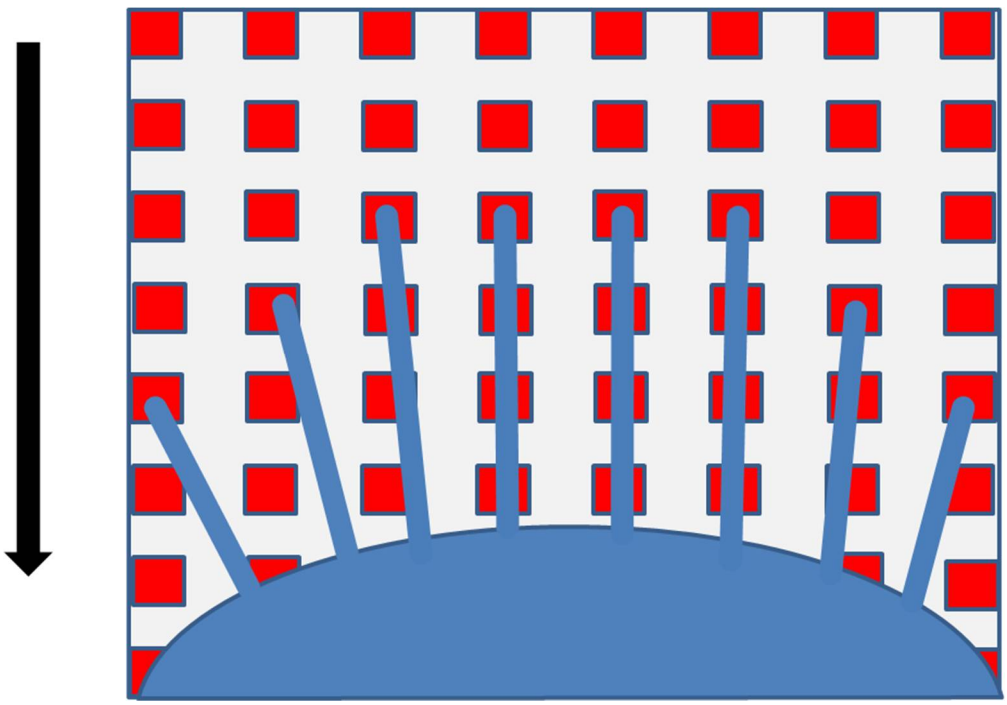

Figure 6.16. Cartoon of possible polymer extension mechanism on xPTFE.

In addition, similar experiments were conducted on a TiO_2 superhydrophobic surface. Similar phenomena, i.e. slowed down Boger fluid drops and "beads-on-tail" residue, were observed on these superhydrophobic surfaces also indicating the robustness of our observations for different superhydrophobic surfaces. The preliminary results of the *Ca* vs *Bo* plot are shown in Figure 6.17. In totality, these combined results indicate that roughness alone is insufficient to create this mechanism but that the combination of hydrophobicity with surface topography (the hallmark of superhydrophobic surfaces), are *both* required to observe such striking phenomena.

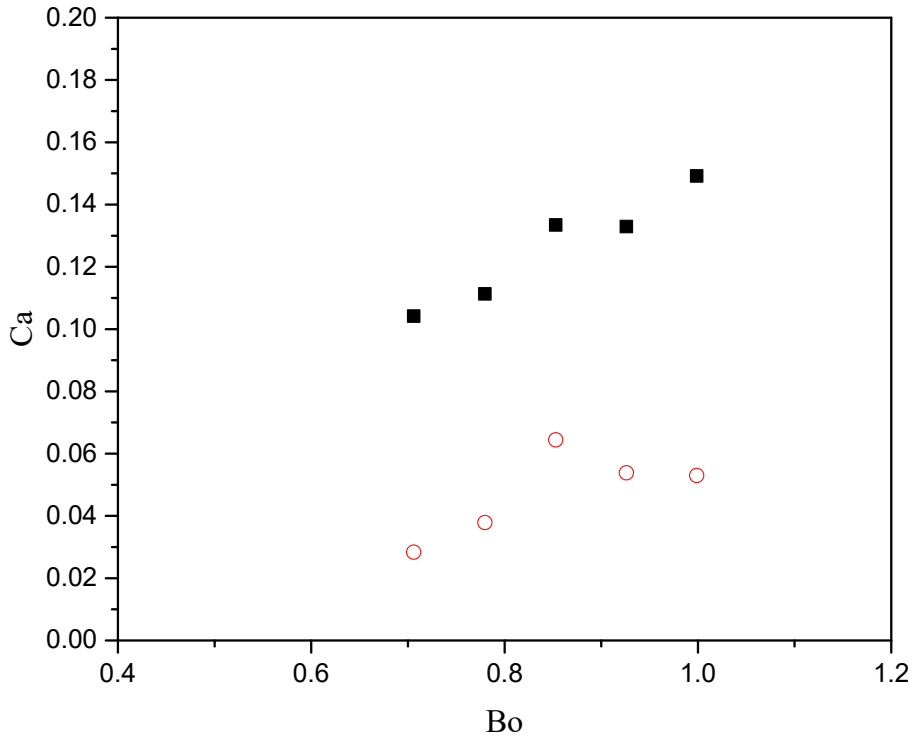

Figure 6.17. Capillary number versus Bond number for Newtonian (Fluid N1, filled symbles) and Boger fluid (Fluid B3 λ~2.5s, open symbles) drops on TiO_2 Surfaces

6.4 Conclusions

Under the experimental conditions studied, Boger fluid drops with very high elasticity but otherwise identical properties show no difference compared to Newtonian fluid drops while moving on hydrophilic glass surfaces. The main force balance in such cases is between viscosity, gravity and contact angle hysteresis. In addition, embossing structure on a weakly hydrophobic polycarbonate surface only increases the "friction", retarding the drops, but is otherwise unremarkable.

On superhydrophobic surfaces (hot-embossed xPTFE and a TiO_2 surface), the elastic drops move at a significantly reduced rate (up to ~ 85% reduction). "Branch-like" structures were left behind the drop and a "beads-on-tail" instability forms on that tail. Even though a "global" Weissenberg number, based on drop speed and droplet radius or the capillary length, is order one this cannot fully explain such pronounced viscoelastic effects as at similar Weissenberg numbers on other surfaces no differences were seen. Using microscopy, a phenomenon was observed which indicates the local extension of single filaments between the main drop and micro drops pinned on individual surface pillars producing significant resistance to the drop's motion. This phenomenon requires the combination of both surface topography and hydrophobicity (i.e. the surface to be superhydrophobic). In addition, the higher elasticity provides a larger resistance force from this effect. In addition to the interesting pattern formations observed here, these results may have significant technological applications as many fluids used in practical coating flows are viscoelastic, as are many biological liquids.

Chapter 7 Conclusions

This chapter summaries the contributions to the manufacturing and characterisation of superhydrophobic surfaces and the novel investigations regarding viscoelastic fluid drops interacting with such superhydrophobic surfaces.

7.1 Manufacturing of xPTFE surfaces

From the literature review in Chapter 2, it is clear that many of the current methods for manufacturing superhydrophobic surfaces are expensive for "large" scale surfaces (Tian et al. (2016)). In Chapter 3, a relatively simple, inexpensive method was described, and it has potential applications for industrial scale manufacture. PTFE has very low surface free energy that means great potential to achieve superhydrophobicity by creating surface roughness on it (Zhang et al. (2004),Falah Toosi et al. (2015) and Kim and Rothstein (2016)). Microscale diameter stainless steel meshes were used as a model to emboss the PTFE sheets to create superhydrophobic surfaces. The sanded PTFE sheet was covered by a stainless steel mesh, then they were held by two stainless steel gauge plates and tightened using several G-clamps. A uniform arrangement of the G-clamps and consistent tightening force on each clamp was used to provide a uniform pressure force distribution. The sample was then heated in an oven at 350°C for 3 hours, and was allowed to cool in the oven naturally. As a result, "brick-like" regular micro-structures were printed on to the PTFE sheet and made the resulting surfaces superhydrophobic. The overall maximum size of a well-printed area was about 12cm by 12cm which is only limited by the size of oven employed.

Five types of PTFE surfaces were manufactured using this method with different types of meshes. An easy visual observation to check the process is to see if water drops can easily roll-off the PTFE surfaces due to the superhydrophobicity as expected. Static

contact angles for water on the PTFE surfaces were measured as being above 145°, and the contact angle hysteresis is about 15°.

7.2 Characteristics of xPTFE surfaces

The properties of five xPTFE surfaces manufactured in Chapter 3 were investigated and characterized in Chapter 4, including measurements of the static contact angle and contact angle hysteresis, a morphology investigation using SEM imaging, water droplet bouncing experiments and slip-length measurements.

Firstly, the static contact angles and contact angle hysteresis of water were measured on all five xPTFE surfaces. Three of the xPTFE surface types (30040, 40030 and 50025), all with open area ratios of around 72%, showed a high static contact angle and low contact angle hysteresis. These three surfaces can be classified as superhydrophobic. The static contact angles were measured as around 145° on the 40030 and 50025 xPTFE surfaces and 140° on the 30040 xPTFE surface. In addition, the contact angle hysteresis of all three surfaces are about 15°.

Secondly, the morphology of the surface structures was investigated at different scales using the SEM technique. On the tens-micrometre-scale, the “brick-like” structures were observed with dimensions around 30 μm. These structures were expected as a result from the shape of the meshes after the embossing process. In addition, a “hair-like” structure on a one-micrometre-scale was observed on the edge of each “brick”. These “hairs” were suggested to be the result of separating the meshes from the PTFE surfaces. These two scales of structures formed a dual-scale structure, which provides a greater contribution to the surface superhydrophobicity than the “brick-like” structure

alone. The 50025 xPTFE surfaces have the highest density of these structures and they also have the highest superhydrophobicity as indicated from the other measurements.

Thirdly, the water droplet bouncing experiments were implemented as an additional definition of superhydrophobicity, following Crick and Parkin (2011), and this definition is one of the most clear and convincing definitions of superhydrophobicity. There are one and two bounces, within our experimental conditions, occurring on the 40030 and 50025 xPTFE surfaces respectively, but no bounce was observed on the 30040 xPTFE surface. This result suggested that the 40030 and 50025 xPTFE surfaces are superhydrophobic, and the 50025 xPTFE surface has a higher superhydrophobicity despite their static contact angle being slightly lower than 150° which claimed by many studies (Watanabe et al. (1999), Erbil et al. (2003), McHale et al. (2004), Lee et al. (2008), Kim (2008), Busse and Sandham (2012), Deng et al. (2012), Mammen et al. (2014) and Kondrashov and Rühe (2014)) as a boundary between superhydrophobic and hydrophobic surfaces. The 30040 surfaces can only be called a "weakly-superhydrophobic surface" despite the similar static contact angles to the other surfaces.

Fourthly, the slip-length of the three xPTFE surfaces and an additional surface created from TiO_2 for comparison were successfully measured using the rotating-disks methods. A commercial rheometer with cone-and-plate and parallel-plates geometries was utilized in this measurement. It is worth noticing that, an appropriate selection of geometries, a correct shear rate range to avoid secondary flow and a few novel techniques for preventing free surfaces effects are key elements for an accurate measurement of the slip-length. The slip-lengths of these xPTFE surfaces are measured as 23 μm, 27 μm, 31 μm and 55 μm for the 30040, 40030, 50025 xPTFE surfaces and the TiO_2 surfaces respectively. This result is close to the previous studies with similar

surface structure dimensions (Lee et al. (2016)), and proved that the 50025 xPTFE have the highest superhydrophobicity of the xPTFE surfaces, and the TiO_2 surfaces have an even higher superhydrophobicity than the xPTFE surfaces which corresponds to its very high static contact angle (~165°).

Finally, the channel-flow method for determining the slip-length was also attempted, but unfortunately, there was no stable and repeatable slip-length measured. The results of the channel-flow method indicated a potential loss of superhydrophobicity of the xPTFE surfaces during the experiments. A further investigation about the resilience of the superhydrophobic surface was therefore conducted and described in Chapter 5.

7.3 Resilience of superhydrophobic surfaces

Most superhydrophobic surfaces are made by low surface free energy material (i.e. polymers) which are not mechanically tough (Landel and Nielsen (1993)). Hence, the superhydrophobicity of these surfaces are highly susceptible to mechanical wear, chemical corrosion or even natural light (Verho et al. (2011),Wu et al. (2014),Tian et al. (2016) and Milionis et al. (2016)). In Chapter 5, the two types of losses of superhydrophobicity, either a temporary loss or a permanent loss, for xPTFE surfaces and the TiO_2 surface were investigated. The temporary loss means the gas trapped between the surface features is forced out, and any liquid on the surface is no longer in a Cassie-Baxter state. In most cases, the superhydrophobicity can be recovered by cleaning the surfaces. A permanent loss implies the surface structures were damaged physically or chemically: the surface structures are lost or the surface free energy of the material is modified.

Two tests are designed to investigate these two losses of superhydrophobicity. The first one is a shear-stress step test. This test was designed to determine the limitation of the

working environments of the superhydrophobic surfaces using impulse workloads/stress. An increasing ramp of fluid shear-stress was applied via a rheometer to wear the superhydrophobic surfaces, the slip-lengths were measured to examine its superhydrophobicity after each shear-stress. The critical shear-stresses, which are the limitation for the surface to be in a Cassie-Baxter state, for different surfaces were found in this experiment. From these results, the 40030 xPTFE surfaces have the best resilience of the three xPTFE surfaces, its critical shear-stress is around 15 Pa. The critical shear-stresses for 30040 and 50025 xPTFE surfaces are <0.5 Pa and around 1.2 Pa respectively. In addition, the TiO_2 surfaces not only have a better superhydrophobicity than the xPTFE but also have a higher critical fluid shear-stress which is around 20 Pa.

The second test is the time endurance test. In this test, the superhydrophobic surfaces received a constant fluid shear-stress, which was selected as the critical shear-stress determined previously, for a certain period of time (4 or 8 hours). Then the superhydrophobic surfaces were examined by the static contact angles, slip-lengths, and SEM imaging. The 40030 xPTFE surfaces showed the best resilience of the three xPTFE surfaces as well as the shear-stress step test. At a fluid shear-stress of less than 1Pa, its superhydrophobicity can remain about 8 hours and the other two surfaces can only last about 5 hours. At the higher fluid shear-stress (5 Pa or 10 Pa), the slip-length of the 40030 xPTFE surface decreased rapidly and their lifetime was reduced to only about 1 to 3 hours. This loss can be described as the slip-length loss rate, the result for 40030 xPTFE surfaces is measured as about 3 μm/h, 6 μm/h and 14 μm/h at different fluid shear-stress: 1 Pa, 5 Pa and 10 Pa respectively. In addition, from the SEM images, the one-micrometer scale “hair-like” surface structures are totally removed after the 8 hours of wear. The TiO_2 surfaces not only has a higher critical fluid shear-stress but

also have a better time endurance than the xPTFE surfaces. Obvious damage to the surface structures was only observed when the fluid shear-stress increased to 100 Pa. Their slip-length loss rates were measured as 9 μm/h and 32 μm/h for 10 Pa and 100 Pa fluid shear-stress respectively, and no loss was observed for 1 Pa fluid shear-stress.

In general, 40030 xPTFE surfaces have the best resilience of the xPTFE surfaces and comparable superhydrophobicity with the 50025 surfaces. Given this better resilience, it was considered as the first choice for further applications. The TiO_2 surfaces have a better resilience and superhydrophobicity due to their more delicate surface structures, however its sensitivity to light, currently limits its applications (Lu et al. (2015)).

7.4 Viscoelastic drops moving on superhydrophobic surfaces

After the study of the superhydrophobic surfaces interacting with Newtonian fluids, the different behaviour of complex non-Newtonian fluids was instigated in this work because of the potential applications in chemical and food industry where such fluids are common. A novel phenomenon regarding constant-viscosity viscoelastic (Boger) fluid drops moving on superhydrophobic surfaces was studied. Under our experimental conditions, Boger fluid drops with very high elasticity but otherwise identical properties show no difference compared to Newtonian fluid drops while moving on hydrophilic glass surfaces. The main force balance in such cases is between viscosity, gravity and contact angle hysteresis. In addition, embossing structure on a weakly hydrophobic polycarbonate surface only increases the “friction”, retarding the speed of the drops, but is otherwise unremarkable. These results are in approximate agreement with the limited previous results of droplet motion of non-Newtonian fluids (Morita et al. (2009), Varagnolo et al. (2015)) on such surfaces.

On the basis on many previously reported studies (e.g. Shirtcliffe et al. (2010), Cheng and Rodak (2005), Neinhuis and Barthlott (1997)) of the wetting properties of so-called superhydrophobic surfaces it would be anticipated that fluid droplets placed on the surface would rapidly roll-off the surface when impulsively tilted above some critical angle (Richard and Quéré (1999), Mognetti et al. (2010)). Work presented in this thesis has highlighted that, although this is true even for quite viscous Newtonian droplets (~280 mPa·s or 280 times more viscous than water), it is certainly not true for highly-elastic viscoelastic fluids even when the shear viscosity, density and surface tension are matched to the Newtonian fluid drop. On superhydrophobic surfaces (hot-embossed xPTFE), the elastic drops move at a significantly reduced rate (up to ~ 85% reduction). "Branch-like" structures were left behind the drop and a "beads-on-tail" instability forms on that tail. Thus significant fluid residue is left on surfaces which are nominally "non-wetting". Even though a "global" Weissenberg number, based on drop speed and droplet radius or the capillary length, is order one this cannot fully explain such pronounced viscoelastic effects as at similar Weissenberg numbers on other surfaces no differences were seen. Using optical microscopy and SEM, a phenomenon was observed which indicates the local extension of single filaments between the main drop and micro drops pinned on individual surface pillars producing significant resistance to the drop's motion. This phenomenon requires the combination of both surface topography and hydrophobicity (i.e. the surface to be superhydrophobic). In addition, the higher elasticity provides a larger resistance force from this effect.

The results of Chapter 6 are the first to indicate that "superhydrophobic" surfaces may not be so for elastic fluids. The limited previous studies (Morita et al. (2009), Varagnolo et al. (2015)) of droplet motion of non-Newtonian fluids, admittedly only on smooth hydrophobic and weakly hydrophobic surfaces, would not have suggested any such

extravagant effects with non-Newtonian fluids with these cases indicating only subtle differences. The results indicate that, even if for such viscoelastic fluids they exhibit high contact angles and low contact angle hysteresis, such surfaces may not be "non-wetting" for viscoelastic fluids as significant fluid residue is left behind. Given the large interest in such superhydrophobic surfaces (e.g. Shateri Khalil-Abad and Yazdanshenas (2010), LeClear et al. (2016), Wen et al. (2017) and Zhao et al. (2017)), and their many potential practical applications, the results from this thesis should be of wide interest as these surfaces may not respond as expected when interacting with viscoelastic fluids. This is especially important for any potential applications as many fluids used in practical coating flows are viscoelastic (e.g. paints, inks), as are many biological liquids.

7.5 Future works

The future works are suggested as follows:

1. There are potential improvements for the hot-embossing procedure used in the manufacturing process. The method used in this work suffers from the quality variations of different batches. The fine stainless steel meshes could be replaced by a flat metal plate which have pre-curved patterns, or a roll milling system with micro-structure for large-scale manufacturing.

2. The "dual-scale" surface structures are observed to be quite weak during the resilience experiments, carbon-nano-tubes could be a potential method to create more resilient and enhanced one-micrometer-scale "hair-like" structures.

3. A potential 3D optical measurement from alicona (Danzl et al. (2011)) could be used to provide the 3D information on the surface structures, e.g. the height of the "brick". Preliminary results of such an approach are shown in Appendix A.

4. The drag reduction of the superhydrophobic surfaces could be tested in different types of flows for its potential maritime applications. For example, an external flow: such as flow over the flat plate, cylinder or hull body; or on internal flow: such as flow in an open channel with different channel cross-section. The relationship between the flow drag reduction and slip-length in turbulent flow is also an interesting subject which requires further study (Daniello et al. (2009)).

5. Future work regarding the viscoelastic fluid drops on superhydrophobic surfaces should investigate a broader range of superhydrophobic surfaces and viscoelastic fluids (including, for example, shear-thinning effects) to determine the ubiquity of the phenomena observed here. Furthermore, it may be possible to utilise this striking phenomenon to quantify viscoelastic effects by relating speed reduction on the surface at a given angle to, say, the fluid's extensional viscosity.

References

Acatay, K., Simsek, E., Ow-Yang, C. & Menceloglu, Y.Z., (2004). Tunable, superhydrophobically stable polymeric surfaces by electrospinning. *Angewandte Chemie (International ed. in English)*, 43(39), pp.5210–3.

Afferrante, L. & Carbone, G., (2014). The effect of drop volume and micropillar shape on the apparent contact angle of ordered microstructured surfaces. *Soft matter*, 10(22), pp.3906–14.

Barnes, H.A., Hutton, J.F. & Walters, K., (1989). *An Introduction to Rheology* K. Walters, ed., Elsevier Science.

Barrat, J.L. & Bocquet, L., (1999). Large slip effect at a nonwetting fluid-solid interface. *Physical Review Letters*, 82(23), pp.4671–4674.

Bixler, G.D., (2013). *Bioinspired Surface for Low Drag, Self-Cleaning, and Antifouling: Shark Skin, Butterfly and Rice Leaf Effects*.

Bixler, G.D. & Bhushan, B., (2013a). Bioinspired micro/nanostructured surfaces for oil drag reduction in closed channel flow. *Soft Matter*, 9(5), p.1620.

Bixler, G.D. & Bhushan, B., (2013). Fluid drag reduction and efficient self-cleaning with rice leaf and butterfly wing bioinspired surfaces. *Nanoscale*, 5(17), pp.7685–7710.

Bixler, G.D. & Bhushan, B., (2013b). Fluid Drag Reduction with Shark-Skin Riblet Inspired Microstructured Surfaces. *Advanced Functional Materials*, 23(36), pp.4507–4528.

Blake, T.D. & Ruschak, K.J., (1979). A maximum speed of wetting. *Nature*, 282(5738),

pp.489–491.

Bocquet, L., Tabeling, P. & Manneville, S., (2006). Comment on “Large Slip of Aqueous Liquid Flow over a Nanoengineered Superhydrophobic Surface” by C-H Choi and C Kim. *Physical Review Letters*, 66001(September), p.66001.

Boger, D. V., (1977). A highly elastic constant-viscosity fluid. *Journal of Non-Newtonian Fluid Mechanics*, 3(1), pp.87–91.

Bourges-Monnier, C. & Shanahan, M.E.R., (1995). Influence of Evaporation on Contact Angle. *Langmuir*, 11(7), pp.2820–2829.

Brassard, J.D., Sarkar, D.K. & Perron, J., (2015). Studies of drag on the nanocomposite superhydrophobic surfaces. *Applied Surface Science*, 324, pp.525–531.

Brown, D. & Cox, A.J., (2009). Innovative Uses of Video Analysis. *The Physics Teacher*, 47(3), pp.145–150.

Busse, A. & Sandham, N.D., (2012). Influence of an anisotropic slip-length boundary condition on turbulent channel flow. *Physics of Fluids*, 24(5), pp.55111–20.

Busse, A., Sandham, N.D., Mchale, G. & Newton, M.I., (2013). Change in drag, apparent slip and optimum air layer thickness for laminar flow over an idealised superhydrophobic surface. *J. Fluid Mech*, 727, pp.488–508.

Cassie, A.B.D. & Baxter, S., (1944). Wettability of porous surfaces. *Transactions of the Faraday Society*, 40(5), pp.546–551.

Cheng, Y.T. & Rodak, D.E., (2005). Is the lotus leaf superhydrophobic? *Applied Physics Letters*, 86(14), pp.1–3.

Choi, C.-H., Ulmanella, U., Kim, J., Ho, C.-M. & Kim, C.-J., (2006). Effective slip and

friction reduction in nanograted superhydrophobic microchannels. *Physics of Fluids*, 18(8), p.87105.

Choi, C.H. & Kim, C.J., (2006). Large slip of aqueous liquid flow over a nanoengineered superhydrophobic surface. *Physical Review Letters*, 96(6), p.66001.

Coghill, W.H. & Anderson, C.O., (1923). US, Bur. *Mines, Tech. Paper*, 47, p.262.

Cooper, J. & Dooley, R., (2008). Release on the IAPWS Formulation 2008 for the Thermodynamic Properties of Seawater. In *The International Association for the Properties of Water and Steam*. pp. 1–19.

Coulson, S.R., Woodward, I.S., Badyal, J.P.S., Brewer, S. a. & Willis, C., (2000). Ultralow surface energy plasma polymer films. *Chemistry of Materials*, 12(23), pp.2031–2038.

Crick, C.R. & Parkin, I.P., (2013). Relationship between surface hydrophobicity and water bounces – a dynamic method for accessing surface hydrophobicity. *J. Mater. Chem. A*, 1(3), pp.799–804.

Crick, C.R. & Parkin, I.P., (2011). Water droplet bouncing—a definition for superhydrophobic surfaces. *Chemical Communications*, 47(44), p.12059.

Cui, Y., Paxson, A.T., Smyth, K.M. & Varanasi, K.K., (2012). Hierarchical polymeric textures via solvent-induced phase transformation: A single-step production of large-area superhydrophobic surfaces. *Colloids and Surfaces A: Physicochemical and Engineering Aspects*, 394, pp.8–13.

Daniello, R., Muralidhar, P., Carron, N., Greene, M. & Rothstein, J.P., (2013). Influence of slip on vortex-induced motion of a superhydrophobic cylinder.

Journal of Fluids and Structures, 42, pp.358–368.

Daniello, R.J., Waterhouse, N.E. & Rothstein, J.P., (2009). Drag reduction in turbulent flows over superhydrophobic surfaces. *Physics of Fluids*, 21(2009).

Danzl, R., Helmli, F. & Scherer, S., (2011). Focus variation - A robust technology for high resolution optical 3D surface metrology. *Strojniski Vestnik/Journal of Mechanical Engineering*, 57(3), pp.245–256.

Davis, A., Yeong, Y.H., Steele, A., Loth, E. & Bayer, I.S., (2014a). Nanocomposite coating superhydrophobicity recovery after prolonged high-impact simulated rain. *RSC Adv.*, 4(88), pp.47222–47226.

Davis, A., Yeong, Y.H., Steele, A., Loth, E. & Bayer, I.S., (2014b). Spray impact resistance of a superhydrophobic nanocomposite coating. *AIChE Journal*, 60(8), pp.3025–3032.

Davis, S.H., (1980). Moving contact lines and rivulet instabilities. Part 1. The static rivulet. *Journal of Fluid Mechanics*, 98(2), pp.225–242.

Deng, X., Mammen, L., Butt, H.-J. & Vollmer, D., (2012). Candle Soot as a Template for a Transparent Robust Superamphiphobic Coating. *Science*, 335(6064), pp.67–70.

Dontula, P., Macosko, C.W. & Scriven, L.E., (1998). Model elastic liquids with water-soluble polymers. *AIChE Journal*, 44(6), pp.1247–1255.

Drelich, J., Chibowski, E., Meng, D.D. & Terpilowski, K., (2011). Hydrophilic and superhydrophilic surfaces and materials. *Soft Matter*, 7(21), p.9804.

Duineveld, P.C., (2003). The stability of ink-jet printed lines of liquid with zero

receding contact angle on a homogeneous substrate. *Journal of Fluid Mechanics*, 477, pp.175–200.

Dupont, (1996). *Teflon PTFE*,

Durst, F., (2008). *Fluid mechanics: an introduction to the theory of fluid flows*, Springer Science & Business Media.

Entov, V.M. & Hinch, E.J., (1997). Effect of a spectrum of relaxation times on the capillary thinning of a filament of elastic liquid. *Journal of Non-Newtonian Fluid Mechanics*, 72, pp.31–53.

Eral, H.B., 't Mannetje, D.J.C.M. & Oh, J.M., (2013). Contact angle hysteresis: a review of fundamentals and applications. *Colloid and Polymer Science*, 291(2), pp.247–260.

Erbil, H.Y., Demirel, A.L., Avcı, Y. & Mert, O., (2003). Transformation of a Simple Plastic into a Superhydrophobic Surface. *Science*, 299(5611), pp.1377–1380.

Escudier, M.P., Gouldson, I.W., Pereira, A.S., Pinho, F.T. & Poole, R.J., (2001). On the reproducibility of the rheology of shear-thinning liquids. *Journal of Non-Newtonian Fluid Mechanics*, 97(2–3), pp.99–124.

Falah Toosi, S., Moradi, S., Kamal, S. & Hatzikiriakos, S.G., (2015). Superhydrophobic laser ablated PTFE substrates. *Applied Surface Science*, 349, pp.715–723.

Feng, L., Li, S., Li, Y., Li, H., Zhang, L., Zhai, J., Song, Y., Liu, B., Jiang, L. & Zhu, D., (2002). Super-Hydrophobic Surfaces: From Natural to Artificial. *Advanced Materials*, 14(24), pp.1857–1860.

Flegler, S.L., Heckman Jr, J.W. & Klomparens, K.L., (1993). Scanning and transmission electron microscopy: an introduction. *Oxford University Press(UK),*

1993,, p.225.

Gao, L. & McCarthy, T.J., (2006). A Perfectly Hydrophobic Surface (θ A /θ R = 180°/180°). *Journal of the American Chemical Society*, 128(28), pp.9052–9053.

De Gennes, P.-G., Brochard-Wyart, F. & Quéré, D., (2013). *Capillarity and wetting phenomena: drops, bubbles, pearls, waves*, Springer Science & Business Media.

Gogte, S., Vorobieff, P., Truesdell, R., Mammoli, A., van Swol, F., Shah, P. & Brinker, C.J., (2005). Effective slip on textured superhydrophobic surfaces. *Physics of Fluids*, 17(2005), pp.1–4.

Le Grand, N., Daerr, A. & Limat, L., (2005). Shape and motion of drops sliding down an inclined plane. *Journal of Fluid Mechanics*, 541(2005), pp.293–315.

Gu, Z.-Z., Uetsuka, H., Takahashi, K., Nakajima, R., Onishi, H., Fujishima, A. & Sato*, O., (2003). Structural Color and the Lotus Effect. *Angewandte Chemie (International ed. in English)*, 34(8), pp.891–894.

Guo, C., Feng, L., Zhai, J., Wang, G., Song, Y., Jiang, L. & Zhu, D., (2004). Large-area fabrication of a nanostructure-induced hydrophobic surface from a hydrophillic polymer. *ChemPhysChem*, 5(5), pp.750–753.

Guo, Y., Wang, Z., Wu, H. & Zhang, X., (2015). Facile fabrication of superhydrophobic polyimide/polytetrafluoroethylene composite coatings with high water adhesion. *Journal of Applied Polymer Science*, 132(46), p.42810.

Han, J.T., Zheng, Y., Cho, J.H., Xu, X. & Cho, K., (2005). Stable Superhydrophobic Organic−Inorganic Hybrid Films by Electrostatic Self-Assembly. *The Journal of Physical Chemistry B*, 109(44), pp.20773–20778.

Hensel, R., Finn, A., Helbig, R., Braun, H.G., Neinhuis, C., Fischer, W.J. & Werner, C., (2014). Biologically inspired omniphobic surfaces by reverse imprint lithography. *Advanced Materials*, 26(13), pp.2029–2033.

Hodges, S.R., Jensen, O.E. & Rallison, J.M., (2004). Sliding, slipping and rolling: the sedimentation of a viscous drop down a gently inclined plane. *Journal of Fluid Mechanics*, 512, pp.95–131.

Hosono, E., Fujihara, S., Honma, I. & Zhou, H., (2005). Superhydrophobic perpendicular nanopin film by the bottom-up process. *Journal of the American Chemical Society*, 127(39), pp.13458–9.

Imayama, S., Lingwood, R.J. & Alfredsson, P.H., (2014). The turbulent rotating-disk boundary layer. *European Journal of Mechanics, B/Fluids*, 48, pp.245–253.

James, D.F., (2009). Boger Fluids. *Annual Review of Fluid Mechanics*, 41(1), pp.129–142.

Jiang, L., Zhao, Y. & Zhai, J., (2004). A lotus-leaf-like superhydrophobic surface: a porous microsphere/nanofiber composite film prepared by electrohydrodynamics. *Angewandte Chemie (International ed. in English)*, 43(33), pp.4338–41.

Johnson, R.E. & Dettre, R.H., (1964). Contact Angle Hysteresis. In pp. 112–135.

Joseph, P., Cottin-Bizonne, C., Benoît, J.-M., Ybert, C., Journet, C., Tabeling, P. & Bocquet, L., (2006). Slippage of Water Past Superhydrophobic Carbon Nanotube Forests in Microchannels. *Physical Review Letters*, 97(15), p.156104.

Jung, Y.C. & Bhushan, B., (2010). Biomimetic structures for fluid drag reduction in laminar and turbulent flows. *Journal of physics. Condensed matter : an Institute of Physics journal*, 22(3), p.35104.

Khorasani, M.T., Mirzadeh, H. & Kermani, Z., (2005). Wettability of porous polydimethylsiloxane surface: morphology study. *Applied Surface Science*, 242(3–4), pp.339–345.

Kim, H.-Y., Lee, H.J. & Kang, B.H., (2002). Sliding of liquid drops down an inclined solid surface. *Journal of colloid and interface science*, 247(2), pp.372–380.

Kim, J.H. & Rothstein, J.P., (2016). Droplet Impact Dynamics on Lubricant-Infused Superhydrophobic Surfaces: The Role of Viscosity Ratio. *Langmuir*, 32(40), pp.10166–10176.

Kim, S.H., (2008). Fabrication of Superhydrophobic Surfaces. *Journal of Adhesion Science and Technology*, 22(3–4), pp.235–250.

Kim, S.H., Kim, J.-H., Kang, B.-K. & Uhm, H.S., (2005). Superhydrophobic CFx coating via in-line atmospheric RF plasma of He-CF4-H2. *Langmuir : the ACS journal of surfaces and colloids*, 21(26), pp.12213–7.

Kondrashov, V. & Rühe, J., (2014). Microcones and Nanograss: Toward Mechanically Robust Superhydrophobic Surfaces. *Langmuir*, 30(15), pp.4342–4350.

Krumpfer, J.W. & McCarthy, T.J., (2011). Dip-coating crystallization on a superhydrophobic surface: A million mounted crystals in a 1 cm 2 array. *Journal of the American Chemical Society*, 133(15), pp.5764–5766.

Kunugi, Y., Nonaku, T., Chong, Y.B. & Watanabe, N., (1993). Electro-organic reactions on organic electrodes. Part 18. Electrolysis using composite-plated electrodes. Part VII. Preparation of ultrahydrophobic electrodes and their electrochemical properties. *Journal of Electroanalytical Chemistry*, 353(1–2), pp.209–215.

Lafuma, A. & Quéré, D., (2003). Superhydrophobic states. *Nature materials*, 2(7), pp.457–60.

Landel, R.F. & Nielsen, L.E., (1993). *Mechanical properties of polymers and composites*, Crc Press.

Lau, K.K.S., Bico, J., Teo, K.B.K., Chhowalla, M., Amaratunga, G. a. J., Milne, W.I., McKinley, G.H. & Gleason, K.K., (2003). Superhydrophobic Carbon Nanotube Forests. *Nano Letters*, 3(12), pp.1701–1705.

Lauga, E. & Stone, H., (2003). Effective slip in pressure-driven Stokes flow. *J. Fluid Mech*, 489, pp.55–77.

LeClear, S., LeClear, J., Abhijeet, Park, K.C. & Choi, W., (2016). Drop impact on inclined superhydrophobic surfaces. *Journal of Colloid and Interface Science*, 461, pp.114–121.

Lee, C., Choi, C.-H. & Kim, C.-J., (2008). Structured Surfaces for a Giant Liquid Slip. *Physical Review Letters*, 101(6), p.64501.

Lee, C., Choi, C.H. & Kim, C.J., (2016). Superhydrophobic drag reduction in laminar flows: a critical review. *Experiments in Fluids*, 57(12), pp.1–20.

Lu, Y., Sathasivam, S., Song, J., Crick, C.R., Carmalt, C.J. & Parkin, I.P., (2015). Robust self-cleaning surfaces that function when exposed to either air or oil. *Science*, 347(6226), pp.1132–1135.

Lum, K., Chandler, D. & Weeks, J.D., (1999). Hydrophobicity at Small and Large Length Scales. *J. Phys. Chem.*, 103(22), pp.4570–4577.

Luo, C., Zuo, X., Wang, L., Wang, E., Wang, J.J.J.J.J., Wang, J.J.J.J.J., Fan, C., Cao, Y., About, M. & Article, T., (2008). Flexible Carbon Nanotube#Polymer

Composite Films with High Conductivity and Superhydrophobicity Made by Solution Process. *Nano Lett*, 8(12), pp.4454–4458.

Mammen, L., Bley, K., Papadopoulos, P., Schellenberger, F., Encinas, N., Butt, H.-J., Weiss, C.K. & Vollmer, D., (2014). Functional superhydrophobic surfaces made of Janus micropillars. *Soft matter*, 11(3), pp.506–15.

McHale, G., (2007). Cassie and Wenzel: Were they really so wrong? *Langmuir*, 23(15), pp.8200–8205.

McHale, G., Shirtcliffe, N.J. & Newton, M.I., (2004). Contact-angle hysteresis on super-hydrophobic surfaces. *Langmuir*, 20(23), pp.10146–10149.

Milionis, A., Loth, E. & Bayer, I.S., (2016). Recent advances in the mechanical durability of superhydrophobic materials. *Advances in Colloid and Interface Science*, 229, pp.57–79.

Ming, Z., Jian, L., Chunxia, W., Xiaokang, Z. & Lan, C., (2011). Fluid drag reduction on superhydrophobic surfaces coated with carbon nanotube forests (CNTs). *Soft Matter*, 7(9), p.4391.

Mognetti, B.M., Kusumaatmaja, H. & Yeomans, J.M., (2010). Drop dynamics on hydrophobic and superhydrophobic surfaces. *Faraday discussions*, 146(March), p.153–65;

Morita, H., Plog, S., Kajiya, T. & Doi, M., (2009). Slippage of a droplet of polymer solution on a glass substrate. *Journal of the Physical Society of Japan*, 78(1), pp.1–4.

Morra, M., Occhiello, E. & Garbassi, F., (1989). Contact angle hysteresis in oxygen plasma treated poly(tetrafluoroethylene). *Langmuir*, 5(3), pp.872–876.

Di Mundo, R. & Palumbo, F., (2011). Comments Regarding "An Essay on Contact Angle Measurements." *Plasma Processes and Polymers*, 8(1), pp.14–18.

Muralidhar, P., Ferrer, N., Daniello, R. & Rothstein, J.P., (2011). Influence of slip on the flow past superhydrophobic circular cylinders. *Journal of Fluid Mechanics*, 680, pp.459–476.

Navier, C., (1823). Memoire surles du movement des. *Mem Acad. Sci. Inst. France*, 1(6), pp.414–416.

Neinhuis, C. & Barthlott, W., (1997). Characterization and Distribution of Water-repellent, Self-cleaning Plant Surfaces. *Annals of Botany*, 79(6), pp.667–677.

Nilsson, M.A., Daniello, R.J. & Rothstein, J.P., (2010). A novel and inexpensive technique for creating superhydrophobic surfaces using Teflon and sandpaper. *Journal of Physics D: Applied Physics*, 43(4), p.45301.

Nosonovsky, M. & Hejazi, V., (2012). Why Superhydrophobic Surfaces Are Not Always Icephobic. *ACS Nano*, 6(10), pp.8488–8491.

Oliveira, M.S.N. & McKinley, G.H., (2005). Iterated stretching and multiple beads-on-a-string phenomena in dilute solutions of highly extensible flexible polymers. *Physics of Fluids*, 17(7), pp.1–4.

Oliveira, M.S.N., Yeh, R. & McKinley, G.H., (2006). Iterated stretching, extensional rheology and formation of beads-on-a-string structures in polymer solutions. *Journal of Non-Newtonian Fluid Mechanics*, 137(1–3), pp.137–148.

Ollivier, H., (1907). Recherches sur la capillarité. *Journal de Physique Théorique et Appliquée*, 6(1), pp.757–782.

Onda, T., Shibuichi, S., Satoh, N. & Tsujii, K., (1996). Super-Water-Repellent Fractal

Surfaces. *Langmuir*, 12(9), pp.2125–2127.

Ou, J., Perot, B. & Rothstein, J.P., (2004). Laminar drag reduction in microchannels using ultrahydrophobic surfaces. *Physics of Fluids*, 16(12), p.4635.

Ou, J. & Rothstein, J.P., (2005). Direct velocity measurements of the flow past drag-reducing ultrahydrophobic surfaces. *Physics of Fluids*, 17(10), p.103606.

Papadopoulos, P., Mammen, L., Deng, X., Vollmer, D. & Butt, H., (2013). How superhydrophobicity breaks down. *Proceedings of the National Academy of Sciences of the United States of America*, 110(9), pp.3254–3258.

Qian, B. & Shen, Z., (2005). Fabrication of superhydrophobic surfaces by dislocation-selective chemical etching on aluminum, copper, and zinc substrates. *Langmuir : the ACS journal of surfaces and colloids*, 21(20), pp.9007–9.

Resound, G.N., (2012). Super-repellent surfaces by plasmachemical functionalization.Case study, *REF 2014, Assessment 8, Durham University.*

Richard, D. & Quéré, D., (1999). Viscous drops rolling on a tilted non-wettable solid. *Europhysics Letters (EPL)*, 48(3), pp.286–291.

Rodd, L.E., Scott, T.P., Cooper-White, J.J. & McKinley, G.H., (2005). Capillary break-up rheometry of low-viscosity elastic fluids. *Applied Rheology*, 15(1), pp.12–27.

Ryan, M.E., Hynes, A.M. & Badyal, J.P.S., (1996). Pulsed Plasma Polymerization of Maleic Anhydride. *Chemistry of Materials*, 8(1), pp.37–42.

Schellenberger, F., Encinas, N., Vollmer, D. & Butt, H.J., (2016). How Water Advances on Superhydrophobic Surfaces. *Physical Review Letters*, 116(9), pp.2–7.

Schutzius, T.M., Jung, S., Maitra, T., Graeber, G., Köhme, M. & Poulikakos, D., (2015).

Spontaneous droplet trampolining on rigid superhydrophobic surfaces. *Nature*, 527(7576), pp.82–85.

Shateri Khalil-Abad, M. & Yazdanshenas, M.E., (2010). Superhydrophobic antibacterial cotton textiles. *Journal of Colloid and Interface Science*, 351(1), pp.293–298.

Shirtcliffe, N.J., McHale, G., Atherton, S. & Newton, M.I., (2010). An introduction to superhydrophobicity. *Advances in Colloid and Interface Science*, 161(1–2), pp.124–138.

Shirtcliffe, N.J., McHale, G., Newton, M.I., Chabrol, G. & Perry, C.C., (2004). Dual-Scale Roughness Produces Unusually Water-Repellent Surfaces. *Advanced Materials*, 16(21), pp.1929–1932.

Shirtcliffe, N.J., McHale, G., Newton, M.I. & Perry, C.C., (2003). Intrinsically superhydrophobic organosilica sol-gel foams. *Langmuir*, 19(14), pp.5626–5631.

Shirtcliffe, N.J., McHale, G., Newton, M.I. & Perry, C.C., (2005). Wetting and wetting transitions on copper-based super-hydrophobic surfaces. *Langmuir : the ACS journal of surfaces and colloids*, 21(3), pp.937–43.

Shiu, J.-Y., Kuo, C.-W. & Chen, P., (2004). Fabrication of Tunable Superhydrophobic Surfaces A. R. Wilson, ed. *Chemistry of Materials*, 5648, pp.325–332.

Simpson, J.T., Hunter, S.R. & Aytug, T., (2015). Superhydrophobic materials and coatings: A review. *Reports on Progress in Physics*, 78(8), p.86501.

Song, D., Daniello, R.J. & Rothstein, J.P., (2014). Drag reduction using superhydrophobic sanded Teflon surfaces. *Experiments in Fluids*, 55(8), p.1783.

Song, X., Zhai, J., Wang, Y. & Jiang, L., (2005). Fabrication of Superhydrophobic

Surfaces by Self-Assembly and Their Water-Adhesion Properties. *The Journal of Physical Chemistry B*, 109(9), pp.4048–4052.

Srinivasan, S., Chhatre, S.S., Mabry, J.M., Cohen, R.E. & McKinley, G.H., (2011). Solution spraying of poly(methyl methacrylate) blends to fabricate microtextured, superoleophobic surfaces. *Polymer*, 52(14), pp.3209–3218.

Srinivasan, S., Choi, W., Park, K.-C., Chhatre, S.S., Cohen, R.E. & McKinley, G.H., (2013). Drag reduction for viscous laminar flow on spray-coated non-wetting surfaces. *Soft Matter*, 9(24), p.5691.

Starkweather, H.W., Zoller, P. & Jones, G.A., (1983). The heat of fusion of poly(ethylene terephthalate). *J. Polym. Sci.: Polym. Phys. Ed.*, 21(4), pp.295–299.

Strobel, M. & Lyons, C.S., (2011). An Essay on Contact Angle Measurements. *Plasma Processes and Polymers*, 8(1), pp.8–13.

Tadmor, R., Bahadur, P., Leh, A., N'guessan, H.E., Jaini, R. & Dang, L., (2009). Measurement of Lateral Adhesion Forces at the Interface between a Liquid Drop and a Substrate. *Physical Review Letters*, 103(26), p.266101.

Thompson, P. a. & Troian, S.M., (1997). A general boundary condition for liquid flow at solid surfaces. *Nature*, 389(September), pp.360–362.

Tian, X., Verho, T. & Ras, R.H.A., (2016). Moving superhydrophobic surfaces toward real-world applications. *Science*, 352(142), pp.142–143.

Tretheway, D.C. & Meinhart, C.D., (2004). A generating mechanism for apparent fluid slip in hydrophobic microchannels. *Physics of Fluids*, 16(5), p.1509.

Turska, E. & Janeczek, H., (1979). Liquid-induced crystallization of a bisphenoI-A

polycarbonate. *Polymer*, 20(December 1978), pp.855–858.

Varagnolo, S., Mistura, G., Pierno, M. & Sbragaglia, M., (2015). Sliding droplets of Xanthan solutions: A joint experimental and numerical study. *European Physical Journal E*, 38(11), pp.1–8.

Verho, T., Bower, C., Andrew, P., Franssila, S., Ikkala, O. & Ras, R.H.A., (2011). Mechanically Durable Superhydrophobic Surfaces. *Advanced Materials*, 23(5), pp.673–678.

Vinogradova, O.I., (1999). Slippage of water over hydrophobic surfaces. *International Journal of Mineral Processing*, 56(1), pp.31–60.

Voronov, R.S., Papavassiliou, D. V. & Lee, L.L., (2008). Review of Fluid Slip over Superhydrophobic Surfaces and Its Dependence on the Contact Angle. *Industrial & Engineering Chemistry Research*, 47(8), pp.2455–2477.

Wang, H., Xue, Y., Ding, J., Feng, L., Wang, X. & Lin, T., (2011). Durable, self-healing superhydrophobic and superoleophobic surfaces from fluorinated-decyl polyhedral oligomeric silsesquioxane and hydrolyzed fluorinated alkyl silane. *Angewandte Chemie - International Edition*, 50(48), pp.11433–11436.

Wang, H., Zhou, H., Gestos, A., Fang, J. & Lin, T., (2013). Robust, superamphiphobic fabric with multiple self-healing ability against both physical and chemical damages. *ACS Applied Materials and Interfaces*, 5(20), pp.10221–10226.

Watanabe, K., Udagawa, Y. & Udagawa, H., (1999). Drag reduction of Newtonian fluid in a circular pipe with a highly water-repellent wall. *Journal of Fluid Mechanics*, 381, pp.225–238.

Wen, Q., Guo, F., Yang, F. & Guo, Z., (2017). Green fabrication of coloured

superhydrophobic paper from native cotton cellulose. *Journal of Colloid and Interface Science*, 497, pp.284–289.

Wenzel, R.N., (1936). Resistance of solid surfaces to wetting by water. *Journal of Industrial and Engineering Chemistry (Washington, D. C.)*, 28(8), pp.988–994.

Whyman, G., Bormashenko, E. & Stein, T., (2008). The rigorous derivation of Young, Cassie–Baxter and Wenzel equations and the analysis of the contact angle hysteresis phenomenon. *Chemical Physics Letters*, 450(4–6), pp.355–359.

Wu, L., Zhang, J., Li, B., Fan, L., Li, L. & Wang, A., (2014). Facile preparation of super durable superhydrophobic materials. *Journal of Colloid and Interface Science*, 432(October), pp.31–42.

Xu, H., Clarke, A., Rothstein, J.P. & Poole, R.J., (2016). Sliding viscoelastic drops on slippery surfaces. *Applied Physics Letters*, 108(24), p.241602.

Xu, H., Clarke, A., Rothstein, J.P. & Poole, R.J., (2018). Viscoelastic drops moving on hydrophilic and superhydrophobic surfaces. *Journal of Colloid and Interface Science*, 513(Supplement C), pp.53–61.

Yabu, H. & Shimomura, M., (2005). Single-Step Fabrication of Transparent Superhydrophobic Porous Polymer Films. *Chemistry of Materials*, 11(4), pp.5231–5234.

Ybert, C., Barentin, C., Cottin-Bizonne, C., Joseph, P. & Bocquet, L., (2007). Achieving large slip with superhydrophobic surfaces: Scaling laws for generic geometries. *Physics of Fluids*, 19(2007), pp.17–19.

Young, T., (1805). An Essay on the Cohesion of Fluids. *Philosophical Transactions of the Royal Society of London*, 95(0), pp.65–87.

Zhang, J., Li, J. & Han, Y., (2004). Superhydrophobic PTFE Surfaces by Extension. *Macromolecular Rapid Communications*, 25(11), pp.1105–1108.

Zhang, X., Shi, F., Niu, J., Jiang, Y. & Wang, Z., (2008). Superhydrophobic surfaces: from structural control to functional application. *Journal of Materials Chemistry*, 18(6), p.621.

Zhang, Y., Ge, D. & Yang, S., (2014). Spray-coating of superhydrophobic aluminum alloys with enhanced mechanical robustness. *Journal of Colloid and Interface Science*, 423, pp.101–107.

Zhao, N., Weng, L., Zhang, X., Xie, Q., Zhang, X. & Xu, J., (2006). A lotus-leaf-like superhydrophobic surface prepared by solvent-induced crystallization. *ChemPhysChem*, 7(4), pp.824–827.

Zhao, X., Yu, B. & Zhang, J., (2017). Journal of Colloid and Interface Science Transparent and durable superhydrophobic coatings for. , 501, pp.222–230.

Zilz, J., Schäfer, C., Wagner, C., Poole, R.J., Alves, M.A. & Lindner, A., (2014). Serpentine channels: micro-rheometers for fluid relaxation times. *Lab Chip*, 14(2), pp.351–358.

Appendix A Optical 3D Measurement for 40030 xPTFE surface

The InfiniteFocus system from alicona is a 3D micro coordinate measurement machine and surface roughness measurement device. It has an unlimited range of measurable surfaces using the coaxial lightning and optimized LED ring light. The measurement can provide high resolution, high repeatability and high accuracy. This method uses the focus variation information and post-process to build a 3D map of the surface roughness, the details are seen in Danzl et al. (2011). Preliminary results are shown in Figure A.1 and A.2 for an 40030 xPTFE surfaces.

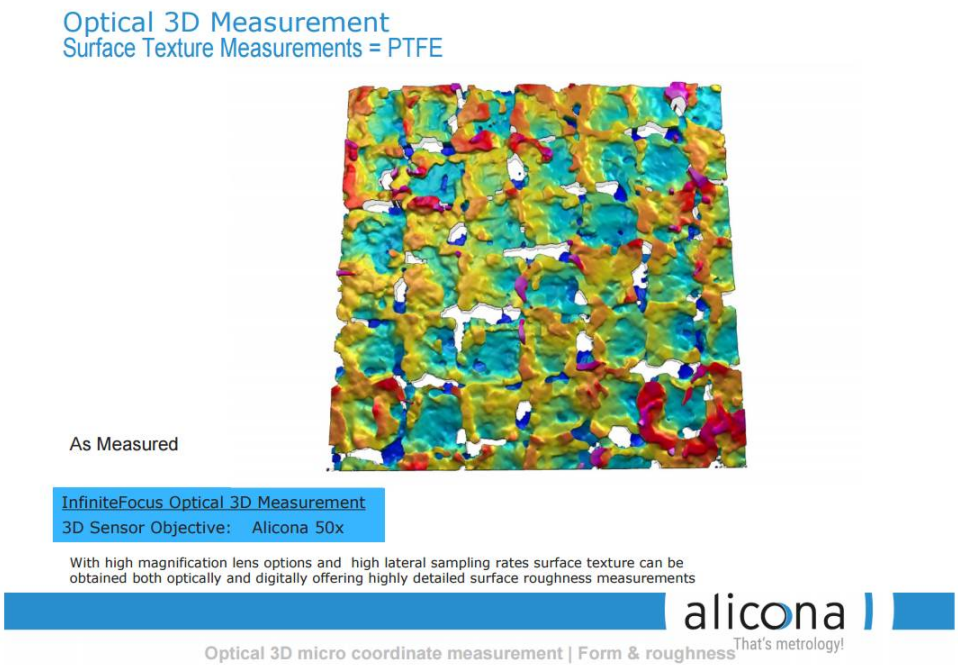

Figure A.1. Optical 3D measurement of 40030 xPTFE surface.

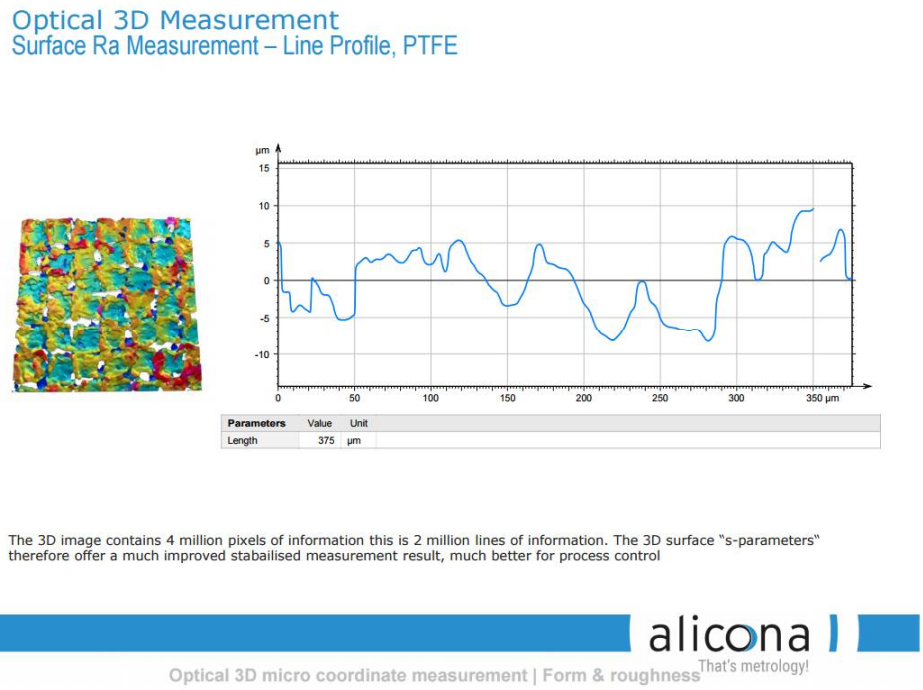

Figure A.2. Surface roughness measurement by optical 3D measurement.